Developments and applications of the aluminium-[^{18}F]fluoride method for biomolecule radiolabelling

By

Jin Hui Teh

A thesis submitted in partial fulfilment of the requirements of the degree of

Doctor of Philosophy in Chemistry

July 2023

Department of Chemistry

Imperial College London

Statement of originality

The work described in this thesis was conducted between October 2019 and July 2023, either at the Department of Chemistry, Imperial College London, or at the Department of Surgery and Cancer, Imperial College London. Unless otherwise stated, through cited reference or acknowledgement, it is entirely my own and has not been submitted for a degree at this university, or any other university.

Copyright declaration

Abstract

The development of novel methods to efficiently synthesise new radiotracers is an active area of research in nuclear medicine. One major advancement is the development of the aluminium-[^{18}F]fluoride ([^{18}F]AlF) method, which has enabled facile and efficient radiofluorination reactions. The [^{18}F]AlF^{2+} complex, described as a pseudo-radiometal, combines the convenience of radiometal-based synthetic approaches with the favourable decay characteristics of fluorine-18. These advantages have led to the widespread implementation of the [^{18}F]AlF method for producing new radiotracers, with an array of clinical trials already being reported. This thesis aims to further expand on the applications of the [^{18}F]AlF method and develop new approaches to allow its incorporation into biomolecules.

Firstly, the utility of the [^{18}F]AlF method in enabling facile ^{18}F-labelling of microbubbles was developed to enable their whole-body distributions to be tracked. An [^{18}F]AlF-labelled tetrazine was synthesised in excellent radiochemical yield and used to radiolabel *trans*-cyclooctene-functionalised microbubbles *via* the efficient inverse-electron-demand Diels-Alder (IEDDA) reaction. To further improve the accessibility of ^{18}F-labelled microbubbles, a kit-based approach was successfully developed. This approach allows microbubbles to be radiolabelled with minimal radiochemical expertise, which potentially facilitates the development of new lipid-based microbubble formulations. In addition, the [^{18}F]AlF-labelled microbubbles were also successfully applied for evaluating the effects ultrasound-mediated microbubble destruction and sonoporation in enhancing the delivery of radioactivity to tumours, further demonstrating the utility of the [^{18}F]AlF method in enabling different biological phenomena to be studied.

This thesis also investigated the potential to improve on the current [^{18}F]AlF-labelling methodologies. To facilitate [^{18}F]AlF-labelling under milder conditions, the development of new chelators was undertaken. Whilst initial studies using aluminium-salen complexes showed their potential for ^{18}F-labelling, conclusive evidence on the formation of an Al-F bond was not obtained, necessitating further optimisation of the ligand structure and fluorination conditions.

Finally, the ability to site-selectively radiolabel biomolecules by [^{18}F]AlF was explored using the *π*-clamp-mediated cysteine conjugation method. Two approaches were developed: (i) a prosthetic group approach, and (ii) a direct [^{18}F]AlF-labelling approach. Both approaches demonstrated the utility of the [^{18}F]AlF method to be used for site-selectively radiolabelling octreotate as the model peptide, providing the potential for translation to larger biomolecules.

In summary, the work presented herein provides an extension to the current toolkit of radiolabelling microbubbles and biomolecules using the [^{18}F]AlF method, which ultimately seeks to expand on the available strategies for producing new radiotracers.

Acknowledgements

First and foremost, my deepest gratitude goes to my supervisor Professor Nicholas Long for the invaluable guidance and support he has given me throughout last 4 years. Thank you for providing me with the opportunity to work on such a diverse range of projects and the resources to develop my own ideas. Most of all, thank you for your understanding, encouragement, and advice when times were tough, which has always steered me in the right direction.

I would also like to thank my co-supervisor Professor Eric Aboagye for the help and support he has given me throughout this project. Your passion for the development of new radiotracers was a source of motivation to me, and thank you for teaching me so much about a field I knew so little of when I started this PhD.

I also owe a huge thank you to everyone who has worked with me on this project. From the Aboagye group, I would first like to thank Marta, for your patience in teaching a chemist how to do biology and for all of your advice on microbubbles. To Louis, thank you for getting me started on radiochemistry with all the tricks of the trade. To Chris, thank you for being a constant source of encouragement and positivity in the basement lab. To Ala, thank you for helping me out with the numerous biology experiments. To Joel, thank you for your help and advice on all the animal work we did. And to Jerry, thank you for your constructive suggestions throughout this journey.

Thank you also to Professor Meng-Xing Tang for your advice and collaboration. From the Tang group, thank you to Laura for persevering with me throughout our microbubble imaging experiments. To Kai Riemer, thank you for the invaluable advice, feedback and help throughout our microbubble bursting endeavours.

To all members of the Long group, thank you for all the fun and laughter throughout the years. I couldn't have asked for a better group to work in. I would like to thank a few people in particular. Special thanks to Tom, for driving me all around Hawaii and for our continued struggles with pi-clamp etc. Brad, thank you for getting me started on tacn, and more importantly, for all the noise and laughs. Shane, I definitely needed that extra bit of stress from FPL to keep myself going. Senior scientist Troy, thank you for always being a source of inspiration. Saul, thanks for being the chemistry encyclopedia that I could always tap into. Ed, thank you for reminding me of all the Malay words that I had forgotten about. Ben, I somehow look forward to your greetings. And Katharine, thank you for all the random desk chats that were usually more exciting and informative than whatever I was doing on my computer.

I would also like to thank my friends for keeping me going throughout this PhD. Special thanks to my housemates, Ning and Chen Yuan, for putting up with me for the past two years, and especially so when I was finishing up. Thank you also to Shuo Yi and Fang Wei, for helping me get through those cold and tough covid months, and for always reminding me of home.

Finally, to my family, papa, mama, Jin Wei and Jin Kai, thank you for your unconditional love, belief and support throughout my whole life. I could embark on this journey because I knew I always had a place to fall back on. Thank you for being the source of my strength. All that I have achieved, I owe it to you all.

Publications relevant to this thesis:

A kit-based aluminium-[^{18}F]fluoride approach to radiolabelled microbubbles.

Jin Hui Teh, Marta Braga, Louis Allott, Chris Barnes, Javier Hernández-Gil, Meng-Xing Tang, Eric O. Aboagye and Nicholas J. Long, *Chem. Commun.*, 2021, **57**, 11677-11680

Abbreviations

[^{18}F]FDG	[^{18}F]Fuorodeoxyglucose
[^{18}F]FEA	[^{18}F]Fluoroethylazide
[^{18}F]SFB	N-succinimidyl-4-[^{18}F]fluorobenzoate
%ID	Percentage of injected dose
%ID/g	Percentage of injected dose per gram
[^{18}F]AlF	Aluminium-[^{18}F]fluoride
A_m	Molar activity
Aq.	Aqueous
Ar	Aromatic group
Bn	Benzyl
Calc.	Calculated
CT	Computed Tomography
CuAAC	Copper-catalysed azide-alkyne cycloaddition
DCC	Dicyclohexylcarbodiimide
DIPEA	*N,N*-diisopropylethylamine
DBPC	1,2-dibehenoyl-sn-glycero-3-phosphocholine
DMF	*N,N*-Dimethylformamide
DMSO	Dimethylsulfoxide
DPPA	1,2-dipalmitoyl-sn-glycero-3-phosphate, sodium salt
DPPC	1,2-dipalmitoyl-sn-glycero-3-phosphocholine
DPPE	1,2-dipalmitoyl-sn-glycero-3-phosphoethanolamine
DSPE-PEG_{2000}-NH_2	1,2-distearoyl-sn-glycero-3-phosphoethanolamine-N-[amino(polyethylene glycol)-2000] (ammonium salt)
Doc	Docetaxel
Dox	Doxorubicin
EC	Electron capture
EDTA	Ethylenediaminetetraacetic acid
Equiv.	Equivalent(s)
ESI	Electrospray ionisation
Et	Ethyl
FDA	Food and Drug Administration
GMP	Good manufacturing practice
HBED	N,N'-bis-(2-hydroxybenzyl)ethylenediamine-N,N'dipropionic acid
HOMO	Highest occupied molecular orbital
HPLC	High-Performance Liquid Chromatography

HRMS	High-Resolution Mass Spectrometry
HSA	Human Serum Albumin
HSAB	Hard and Soft Acid and Base
ICAM-1	Intracellular adhesion molecule-1
IEDDA	Inverse-electron-demand Diels Alder reaction
^{i}Pr	*Iso*-propyl
LC	Liquid chromatography
Log P	Partition coefficient
MALDI-ToF	Matrix-assisted laser desorption/ionisation time-of-flight
mAu	Milli arbitrary unit
MRI	Magnetic resonance imaging
MBs	Microbubbles
Me	Methyl
MeCN	Acetonitrile
MS	Mass spectrometry
NaOAc	Sodium acetate
NMR	Nuclear magnetic resonance
NODAGA	1,4,7-Triazacyclononane-1-glutaric acid-4,7-acetic Acid
NOTA	1,4,7-Triazacyclononane-1,4,7-triacetic Acid
OTf	Triflate
ρ	Density
PEG	Polyethylene glycol
PFBP	Perfluorobiphenyl
p.i.	Post injection
PBS	Phosphate-Buffered Saline
PET	Positron Emission Tomography
Ph	Phenyl
ppm	Parts per million
PSMA	Prostate-Specific Membrane Antigen
RCC	Radiochemical conversion
RCP	Radiochemical purity
RCY	Radiochemical yield
RF	Radiofrequency
SiFA	Silicon fluoride acceptor
SPAAC	Strain-promoted azide-alkyne cycloaddition
T	Temperature

t	Time
^{t}Bu	*Tert*-butyl
TCO	*Trans*-cyclooctene
THF	Tetrahydrofuran
TFA	Trifluoroacetic acid
TLC	Thin Layer Chromatography
t_R	Retention time
US	Ultrasound
r.t.	Room temperature
SD	Standard deviation
S_NAr	Nucleophilic aromatic substitution
SPE	Solid-phase extraction
SPECT	Single Photon Emission Computed Tomography
UMMD	Ultrasound-mediated microbubble destruction
US	Ultrasound
UV	Ultraviolet
VEGFR	Vascular endothelial growth factor receptor
VCAM-1	Vascular cell adhesion molecule-1
v	velocity
Z	Acoustic impedance

Table of Contents

Chapter 1: Introduction

This chapter aims to provide a general introduction to biomedical imaging, with a focus on the use of fluorine-18 in positron emission tomography and microbubbles in contrast-enhanced ultrasound imaging. First, a broad overview of the different imaging modalities is discussed. This is followed by a discussion on general methods for radiolabelling by fluorine-18. Finally, the use of microbubbles as contrast agents for ultrasound imaging will be covered.

1.1 Overview of Imaging Modalities

Medical imaging is the use of techniques and processes to obtain anatomical or functional information of the body, which enables the detection of diseases and subsequent medical intervention.[1] Although some techniques, such as endoscopy, may require surgical insertion of external devices into the body, most medical imaging techniques are non-invasive, where the introduction of external instruments into the body is not required. The ability to non-invasively visualise the interior of the body relies on the difference in signals generated in the different regions of the body when an external stimulus is applied. For example, in ultrasound imaging, when ultrasound waves are being applied to the body as an external stimulus, the difference in acoustic properties of bodily tissues result in the reflection of ultrasound waves, enabling anatomical information to be acquired.[2]

Although the use of endogenous biological properties can allow imaging and evaluation of the certain physiological conditions, the introduction of contrast agents for signal amplification or generation can be beneficial. For example, the introduction of microbubbles as contrast agents in ultrasound imaging allows the rate of blood perfusion to be measured in echocardiography, which gives an indication on cardiac function.[3] Apart from ultrasound imaging, contrast agents are also used in other imaging modalities, including magnetic resonance imaging (MRI), optical imaging, computed tomography (CT), and nuclear imaging.

With the use of contrast agents, functional information such as biological mechanisms can be obtained in addition to anatomical information, which can lead to a better understanding of physiological processes. The visualisation and monitoring of these processes at a cellular and molecular level is termed molecular imaging, where the use of molecular probes enable functional biological data to be obtained with minimal perturbation to the living organism.[4] In comparison to traditional methods such as biopsies for the evaluation biochemical pathways and disease diagnosis, contrast-enhanced medical imaging has several advantages: (i) it is non-invasive; (ii) issues regarding sampling bias due to tumour or tissue heterogeneity can be avoided, since the whole region of interest can visualised; and (iii) a better representation of the biological state can be obtained, since cells and tissues are imaged in their native state.[5] These advantages make molecular imaging an exciting field, where it can facilitate the development of new drugs, personalised medicine and image-guided surgery.

In molecular imaging, the exogenous contrast agents typically comprise two essential components:[6] (i) a signal generating component, such as a radionuclide or a fluorophore; and (ii) a targeting component, such as a peptide that binds specifically to a receptor. Whilst the design of contrast agents is vital to ensure successful imaging of a biological process; the choice of imaging modality is equally important, since each imaging modality offers different spatial and temporal resolutions, with each having their own advantages and drawbacks (**Table 1.1**).[4] For example, nuclear imaging techniques such as positron emission tomography (PET) appear ideal for imaging drug distribution within the body, but are likely unsuitable for determining the localisation of drugs within cellular compartments. In contrast, optical imaging performs well for imaging cellular structures, but falls short in terms of imaging whole-body distributions due to its limited penetration depth. Therefore, selection of the appropriate imaging modality would depend on the type of information required, where a combination of two or more modalities could be beneficial. One popular combination is the use of PET/CT scanners, where the functional information provided by PET imaging is supplemented by the anatomical information provided by CT imaging, enabling better characterisation and visualisation of diseases. In the subsequent sections, an overview of each imaging modality is provided.

1.1.1 Positron emission tomography (PET)

Positron emission tomography is a nuclear imaging modality that uses unstable neutron-deficient nuclides as signal generators. These nuclides decay by positron (β^+) emission, where the emitted positron travels a few millimetres in tissues before colliding and undergoing annihilation with an electron (β^- particle) (**Figure 1.1**).[7] This phenomenon is known as an annihilation event, which generates two coincident 511 keV photons, otherwise known as gamma rays (γ-rays). The two γ-rays travel through the body simultaneously, and are being detected by a 360 ° array of gamma cameras that surround the patient. Upon tomographic reconstruction, a 3-dimensional image corresponding to the location of annihilation events can be obtained, giving information on the distribution of radionuclides in the body.

A range of radionuclides are available for imaging by PET, which can be broadly divided into two categories depending on their method of incorporation into molecules:[4,8]

(i) 'inorganic' radiometals such as ^{64}Cu, ^{68}Ga and ^{89}Zr, incorporated using chelators.

(ii) organic' p-block elements such as ^{11}C, ^{13}N, ^{15}O, ^{18}F and ^{124}I, incorporated directly onto molecular structures.

Table 1.1: Comparison of the different medical imaging modalities available.[4]

Modality	Spatial resolution	Temporal resolution	Penetration depth	Contrast agent quantity	Advantages	Disadvantages
Ultrasound	50-500 μm	Seconds	mm-cm	μg-mg $>10^6$ microbubbles per mL of blood	Real-time Affordable High sensitivity No ionizing radiation	No whole-body imaging Mostly anatomical data Clinically approved contrast agents limited to vasculature
MRI	4-100 μm	Minutes to hours	Unlimited	μg-mg	High spatial resolution No ionizing resolution Possibility of functional imaging without contrast agents	Low sensitivity – high amounts of contrast agents required
Optical	15-1000 nm	Seconds	< 1cm	μg-mg	High spatial resolution High sensitivity	Limited penetration depth
PET	1-2 mm	Minutes to hours	Unlimited	ng	High sensitivity Whole-body imaging	Low spatial resolution Ionizing radiation used Contrast agent availability might be limited
SPECT	1-2 mm	Minutes to hours	Unlimited	ng	High sensitivity Whole-body imaging	Low spatial resolution Ionizing radiation used
X-ray/CT	12-200 μm	Minutes	Unlimited	Not required	High spatial resolution	Low sensitivity Limited soft tissue contrast Ionising radiation used

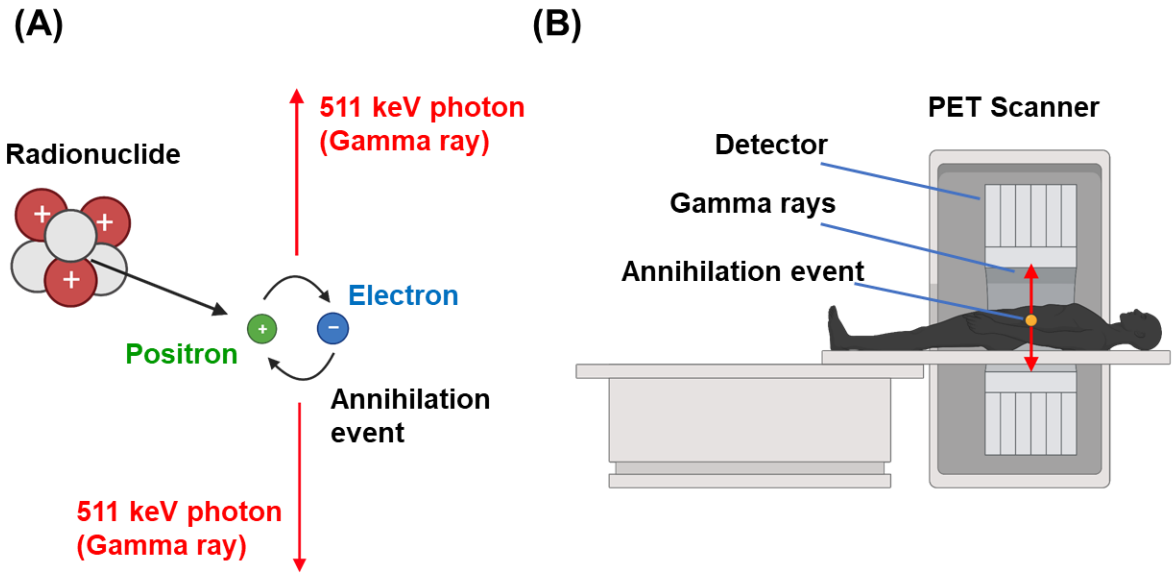

Figure 1.1: Graphical illustration of principles for positron emission tomography. (A) Schematic showing positron emission from a radionuclide, followed by an annihilation event between a positron and electron that results in the emission of two antiparallel 511 keV photons. (B) Detection of gamma rays produced in a PET scanner.

A summary of the properties of the different radionuclides for PET imaging is provided in **Table 1.2**, which can influence the choice of radionuclide to be used in a study. Firstly, the abundance of β^+ decay affects the amount of radioactivity required for administration, where radionuclides with high β^+ abundances such as ^{11}C, ^{13}N, ^{15}O and ^{18}F undergoes decay by β^+ emission >96 % of the time, resulting in a useful signal being generated for detection. In comparison, only 25.6 % of ^{124}I decay by β^+ emission, where other decay pathways could potentially generate γ-rays that negatively impacts the quality of the images obtained.[9]

Secondly, the decay half-life of the radionuclides is also an important parameter for consideration in the design of radiopharmaceuticals. Radionuclides with short half-lives such as ^{11}C, ^{13}N and ^{15}O do not allow for extensive synthetic manipulations and long imaging sessions. However, the abundance of carbon-12, nitrogen-14 and oxygen-16 in drugs and natural products make their corresponding radionuclides important for the preparation of equivalent radiolabelled compounds with identical chemical and physiological behaviour.[4,8] In contrast, longer-lived radionuclides such as ^{64}Cu and ^{89}Zr enable a longer radiosynthesis duration and imaging period, which can be useful for imaging using biological molecules with longer circulation half-lives such as antibodies.[10]

Table 1.2: Properties of radionuclides used in PET imaging.[4] β^+_{max}: Maximum positron energy, EC: electron capture

Radionuclide	β^+abundance (%)	Half-life ($t_{1/2}$)	β^+_{max} (meV)	Production method
^{11}C	100	20.4 min	0.96	Cyclotron, ^{14}N(*p*,*α*)^{11}C
^{13}N	100	9.97 min	1.19	Cyclotron, ^{16}O(*p*,*α*)^{13}N
^{15}O	100	2.04 min	1.72	Cyclotron, ^{15}N(*d*,*n*)^{15}O
^{18}F	96	110 min	0.64	Cyclotron, ^{18}O(*p*,n)^{18}F or ^{20}Ne(*d*,*α*)^{18}F
^{124}I	25.6	4.2 d	2.14	Cyclotron, ^{124}Te(*p*,*n*)^{124}I
^{64}Cu	19	12.7 h	0.65	Cyclotron, ^{64}Ni(*p*,*n*)^{64}Cu
^{68}Ga	89	68 min	1.89	^{68}Ge/^{68}Ga generator (by EC)
^{89}Zr	23	3.3 d	0.90	Cyclotron, ^{89}Y(*p*,*n*)^{89}Zr

Apart from these, the maximum positron energy (β^+_{max}) of a radionuclide affects the distance that the positron travels from its initial decay site to the annihilation event. Therefore, radionuclides with higher β^+_{max} generally result in lower spatial resolutions.[9]

In terms of production, most of the radionuclides used in PET imaging are generated using cyclotrons, where particles (proton, deuteron or $^4He^{2+}$) are accelerated for bombardment into the target nuclei, creating the unstable radionuclides. For ^{18}F production, the most common method is the bombardment of oxygen-18 enriched water using proton beams, where subsequent ejection of a neutron produces fluorine-18.[11] This nuclear reaction can be summarised by ^{18}O(*p*,n)^{18}F, which generates ^{18}F in the form of [^{18}F]fluoride ions when oxygen-18 enriched water is used as the target. Alternatively, ^{18}F can also be generated in the form of [^{18}F]F_2 gas using ^{20}Ne(*d*,*α*)^{18}F. However, due to the need for the addition of non-radioactive F_2 gas as a carrier, the molar activity of [^{18}F]F_2 is usually low, which can be suboptimal for the synthesis of radiopharmaceuticals with high molar activities. In comparison, gallium-68 is produced using ^{68}Ge/^{68}Ga generators, where ^{68}Ge undergoes electron capture (EC) to produce $^{68}Ga^{3+}$, which can be eluted in its chloride form as [^{68}Ga]$GaCl_3$ using hydrochloric acid.[12] Notably, the use of generator-produced radionuclides can improve the access to radiopharmaceuticals in areas without a cyclotron.

Upon production of the radionuclides, synthetic manipulations are usually carried out to obtain radiopharmaceuticals that enable the imaging of specific biological processes. The design considerations for these radiopharmaceuticals or radiotracers are discussed in section 1.2.1.

1.1.2 Single Photon Emission Computed Tomography (SPECT)

Similar to PET, SPECT represents another nuclear imaging technique. However, instead of the production of imaging signals through positron emission and subsequent annihilation events, signals are generated in SPECT imaging by the emission of a single γ-ray per radionuclide, which is illustrated in **Figure 1.2**. In brief, the detector is made up of an array of gamma cameras that rotates around the subject to collect signals for imaging the whole body. A collimator is used as a filter for the incoming γ-rays, which only allows γ-rays perpendicular to the camera to be captured. Tomographic reconstruction is then carried out to determine the origin of the signals, which enables a 3D image of the radiotracer distribution to be obtained.

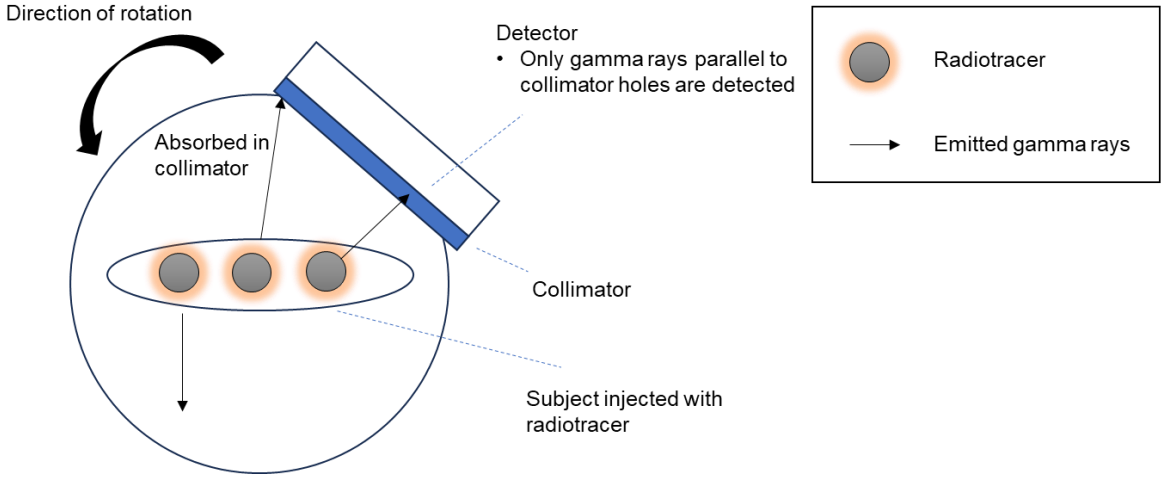

Figure 1.2: Graphical illustration of the principles of SPECT. Image adapted from Long and Wong.[4]

A range of radionuclides are also available for imaging by SPECT, such as ^{67}Ga, ^{99m}Tc, ^{111}In, ^{123}I and ^{125}I. Of these radionuclides, ^{99m}Tc is by far the most widely used, accounting for approximately 85 % of nuclear imaging scans worldwide.[13] This is mostly due to the ease of access to ^{99m}Tc from ^{99}Mo/^{99m}Tc generators, its favourable half-life of 6 h, and the facile kit-based procedures for preparing ^{99m}Tc-based radiopharmaceuticals.[13]

However, some of the drawbacks of SPECT imaging include poor image resolution and long scanning times, which can result in patient discomfort. Nevertheless, the utility of SPECT imaging for evaluating and diagnosing a broad spectrum of diseases has improved the field of medical imaging, with extensive research being carried out for the continued improvement in radiotracer design, image reconstruction, and instrument development.[4] Given that this imaging modality is not used in this work, further discussion on SPECT imaging is not carried out.

1.1.3 Magnetic Resonance Imaging (MRI)

Magnetic resonance imaging (MRI) is a medical imaging technique that makes use of the same basic principles of nuclear magnetic resonance (NMR), where nuclear spin relaxation is used to generate radiofrequency signals for detection. Given the abundance of water in the human body (approximately 60 %), MRI primarily measures the relaxation of water protons.[4]

During an MRI scan, the subject is placed in the presence of a strong magnetic field (B_0), where protons align their spins parallel to the direction of the applied magnetic field (**Figure 1.3**). Upon application of radiofrequency (RF) pulses equal to the Larmor frequency, the proton spins tilt away from the magnetic field. When application of the RF pulse is stopped, the protons relax by re-aligning their spins to the magnetic field, giving off an RF signal that can be detected.

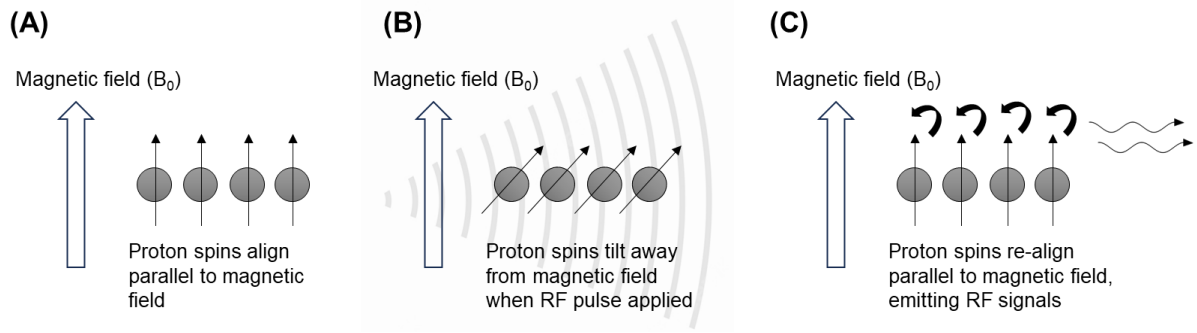

Figure 1.3: Graphical illustration of principles of MRI signal generation.

Images can then be generated by measuring either the (i) longitudinal relaxation time (T_1) required for protons to re-align their spins along the longitudinal axis to the magnetic field B_0, or (ii) transverse relaxation time (T_2) required for protons to lose their phase coherency along the transverse axis. Different signal intensities can be obtained by the inherent differences in water content in different parts of the body, thus allowing the differentiation of tissues.

To improve image quality, contrast agents can be administered to alter the T_1 and T_2 relaxation times. In general, paramagnetic contrast agents such as compounds containing Gd^{3+}, Mn^{2+}, or Fe^{3+} are used to promote T_1 relaxation, while superparamagnetic contrast agents such as iron oxide nanoparticles are used to promote T_2 relaxation.[14]

Whilst MRI offers excellent soft tissue contrast and high spatial resolution, one drawback of this imaging modality is its relatively low sensitivity. This low sensitivity arises from the small population difference between the protons in the excited state and non-excited state when the radiofrequency pulse is applied.[4] Although its sensitivity can be improved through the use of contrast agents, the requirement of relatively large doses of contrast agents can result in

toxicity issues. Nevertheless, the continued development of new contrast agents with reduced toxicity can potentially circumvent these risks. In addition, the progress in imaging protocols and instrumentation can also enable improved contrast, where developments in functional MRI (fMRI) have enabled non-invasive imaging of the brain without the need for contrast agents.[15]

1.1.4 Computed Tomography (CT)

Computed tomography (CT) is an imaging technique that uses external X-rays for the generation of cross-sectional images of the body. X-rays are electromagnetic radiation with wavelengths of 0.01-10 nm (photon energies 10-150 keV).[16] When X-rays are transmitted through the body, they travel in straight lines. These X-rays are absorbed and attenuated, but are still detectable after passing through the body. Contrast is obtained by the difference in intrinsic absorption and attenuation properties of the different matter in the body such as water, tissues, organs, fat, bone and air. In computed tomography, 2D cross section images of the body are obtained, which are then stacked and reconstructed to produce a 3D image.

One advantage of CT is that structural and anatomical information can be obtained at high resolutions, often enabling precise characterisation of the size and location of abnormal physiological conditions such as tumour growth. Although CT imaging is often limited to providing structural information, it can be used in combination with other imaging modalities such as PET or MRI, allowing enhanced visualisation and diagnosis of diseases.

1.1.5 Optical Imaging

Optical imaging utilises the different interaction of light with cellular components, tissues or contrast agents to generate contrast. When light is transmitted onto an object, it can be absorbed, emitted, reflected, polarised or scattered.[4] Whilst each of these interactions can give useful information on the system being studied, light absorption and emission are likely most widely used in biomedical imaging in the form of luminescence imaging, which will be covered in this section.[4]

Luminescence encompasses both fluorescence and phosphorescence, which can be explained using a Jablonski diagram (**Figure 1.4**). Upon light irradiation, an electron from the highest occupied molecular orbital (HOMO) can absorb a photon of energy that corresponds to the energy difference between the ground state (S_0) and an electronically excited state (S_1). In the S_1 state, electrons can undergo spontaneous relaxation back to the ground state (S_0), which emits light waves in a process termed fluorescence. In the S_1 state, intersystem crossing (ISC) can also occur to the T_1 state, and the subsequent relaxation by the emission of light is termed phosphorescence. Since spin selection rules only allow transitions without a change

in spin (ΔS = 0), phosphorescence is formally forbidden, and thus occurs at lower intensities compared to fluorescence.[17]

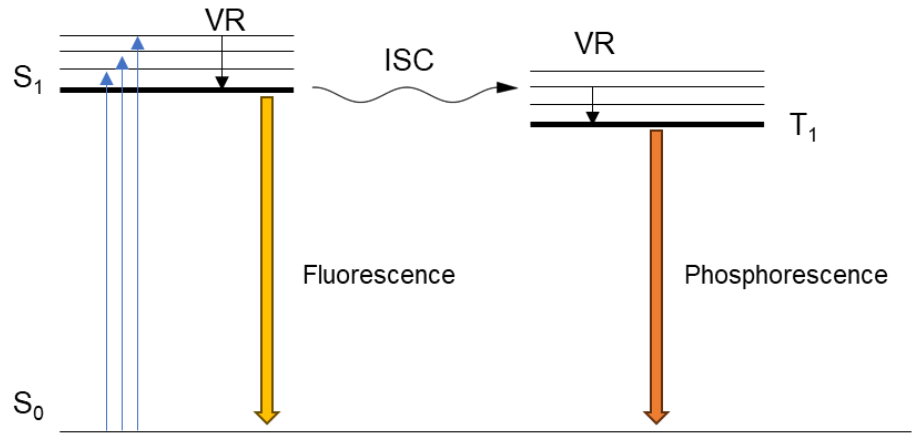

Figure 1.4: Jablonksi diagram showing the principles of fluorescence and phosphorescence. S_0: singlet ground state, S_1: singlet excited state, T_1: triplet excited state, VR: vibrational relaxation, ISC: intersystem crossing

Fluorescence imaging can be conducted using both endogenous and exogeneous fluorophores.[18] Typically, these involve the use of highly conjugated molecules such as fluorescein and cyanine dyes (**Figure 1.5**). Excellent spatial resolution can be obtained using fluorescence imaging, often enabling the discrimination between different cellular compartments. However, one major limitation of fluorescence imaging for *in vivo* applications is the limited penetration depth due to absorption by endogenous fluorophores. To address this, fluorophores that absorb and emit in near-infrared region (λ = 800-2500 nm) are being developed. In addition, molecules with different optical properties such as photoacoustic systems can also be exploited for *in vivo* imaging.[4]

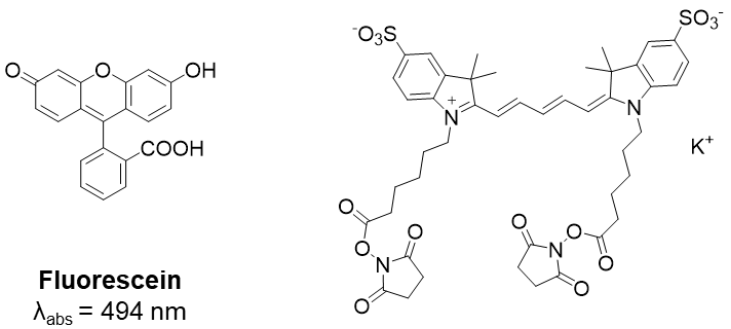

Fluorescein
λ_{abs} = 494 nm
λ_{em} = 521 nm

Cyanine-5
λ_{abs} = 649 nm
λ_{em} = 670 nm

Figure 1.5: Structures of fluorescein and N-hydrosuccinimide-functionalised cyanine-5 as fluorophores

1.1.6 Ultrasound Imaging

The potential application of ultrasound for medical diagnostics was first reported in 1941 by Austrian neurologist Karl Dussik to map brain ventricles.[19] However, signal attenuation hindered its clinical application. It was in 1953 when cardiologist Inge Edler recognized characteristic signals from mitral valve echoes that ultrasound gained recognition as a non-invasive diagnostic technique.[19]

Ultrasound (US) is defined as sound waves with frequencies higher than the typical human audible range (20 to 20000 Hz). In clinical settings, ultrasound waves with frequencies between 1 to 12 MHz are employed.[20] When ultrasound is applied to the body, the ultrasound waves travel linearly at fixed velocities, where they can be transmitted, absorbed, or reflected. Upon encountering the boundary between two tissues, parts of the ultrasound pulses are reflected as echoes, which are being detected as signals. The amplitude of the reflected waves is then used to generate ultrasound images, where a good contrast is obtained when there is a large difference in acoustic impedance between two adjacent tissue structures. Acoustic impedance (*Z*) refers to the resistance in which sound waves experience as they travel through a medium, and is defined as:

$$Z = \frac{P}{U} = \rho v \tag{1}$$

where *P* denotes pressure, *U* denotes flow, *ρ* denotes density and *v* denotes speed.

Since the density of human tissues vary, and sound waves travels at different speeds in different tissues (e.g., 1430 m/s in breast tissue, 1647 m/s in muscle),[21,22] these result in a difference in acoustic impedance between tissues. However, although contrast could be obtained in certain regions of the body, ultrasound imaging is still limited by the inherent acoustic homogeneity of the body.[4,23] In particular, there is difficulty in determining the blood-tissue interface for echocardiology and in other fields. For these reasons, microbubbles have been developed as contrast agents due to their ability to significantly improve ultrasound contrast,[20,24] which will be more extensively discussed in section 1.3.

Ultrasound imaging boasts several advantages when compared to other imaging modalities. It is affordable, portable, enables real-time imaging, and has a good safety profile without the use of ionizing radiation. Therefore, ultrasound imaging is used in a wide range of settings such cardiology, oncology, and obstetrics. As with other imaging modalities, ultrasound also has its limitations, where it does not allow for whole-body imaging, has limited penetration depth, and is mostly limited to anatomical imaging.[25] However, recent developments in microbubble contrast agents have showed the potential of ultrasound to be used for molecular imaging,[24,26,27] demonstrating the continued improvement of this imaging modality.

In summary, the different imaging modalities offer the ability to obtain different types of information, with each having their own advantages and drawbacks (summarized in **Table 1.1**). Therefore, a judicious choice of imaging modality should be made in consideration of the type of information required. To enhance the imaging capabilities of these techniques, contrast agents can also be used, which now play a vital role in the clinical diagnosis of various diseases.[23,25]

This thesis aims to improve on currently available contrast agents by (i) expanding on the methods available for producing ^{18}F-labelled microbubbles for molecular ultrasound imaging, and (ii) developing new strategies for ^{18}F-labelling of biomolecules for PET imaging. In the next section, an overview of ^{18}F-labelling strategies is discussed. This is then followed by an introduction on microbubbles as ultrasound contrast agents and their use in molecular imaging.

1.2 Radiolabelling by ^{18}F

1.2.1 Radiotracer design considerations

Apart from synthesising radiotracers that are identical to biologically relevant molecules, which can be enabled by using radionuclides such as ^{11}C (**Figure 1.6A**), the use of radionuclides such as ^{18}F, ^{68}Ga, or ^{89}Zr, which represent elements that are not typically present in biological compounds, can require more involved radiotracer design to enable accurate quantification of biological events. One strategy is to design structural analogues that closely mimic the uptake of the biologically relevant compound (**Figure 1.6B**). In this example, [^{18}F]fluorodeoxyglucose is structurally similar to its biological analogue, glucose, which is involved in many metabolic processes.

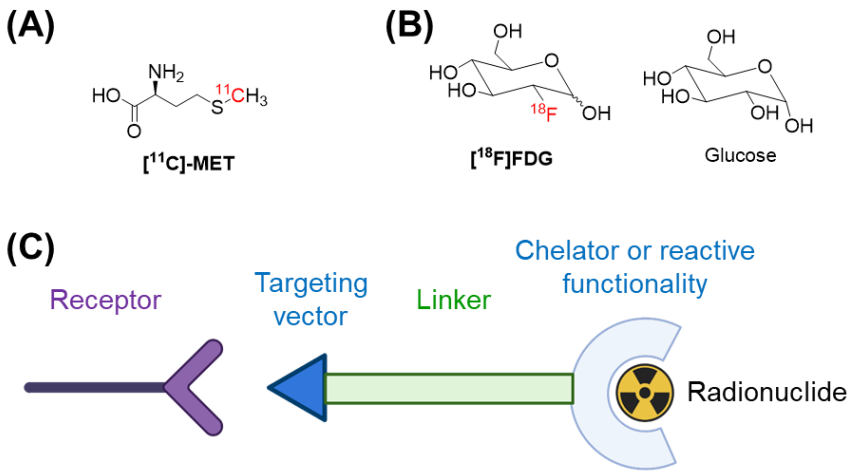

Figure 1.6: Typical design of radiopharmaceuticals. (A) Radiotracers that are identical to the biologically relevant molecules, such as ^{11}C-labelled methionine. (B) Radiotracers that are structural analogues of biologically relevant molecules, such as [^{18}F]FDG. (C) Radiotracers designed using the bifunctional chelator concept.[28]

Notably, [^{18}F]FDG is the most widely used radiotracer for PET imaging.[29] Although its uptake is non-specific, [^{18}F]FDG can be used to image pathologies where glucose uptake is upregulated. For example, it is widely used in cancer imaging, where cancer cells show increased glucose uptake when compared to normal cells.[30] Upon entering cells, [^{18}F]FDG can be phosphorylated to form 6-Phospho-[^{18}F]FDG. However, in contrast to glucose, which undergoes further metabolism, modification of the 2-hydroxy group to fluorine prevents further metabolism of 6-Phospho-[^{18}F]FDG. Since phosphorylated sugars are not transported by glucose transporter proteins, 6-Phospho-[^{18}F]FDG remains trapped in the cell.[31] This results in an increase in radioactive concentration in cancer cells, which is detectable by PET imaging. In addition, since the fluorine atom is a bioisostere of the hydrogen atom, hydroxy groups and amino groups,[32] the incorporation of ^{18}F in place of these atoms/groups have also been used in radiotracer designs.

An alternative design strategy for radiotracers involves the use of the bifunctional chelator concept.[28,33,34] Three components are usually present in radiotracers synthesised using this approach: (i) a targeting vector, (ii) a chelator or reactive handle for radionuclide incorporation, and (iii) a linker that joins the two components.

Apart from radiotracer design, another important parameter for consideration during radiotracer production is molar activity (A_m).[35] Molar activity is a measure of the ratio between the amount of radioactive molecules (n_A*) to the total amount of molecules (n_A + n_A*), where the non-radioactive molecule (n_A) is expected to dominate. Molar activity is defined by:

$$A_m = \frac{Activity_{A*}(GBq)}{n_A + n_{A*}(\mu mol)} \approx \frac{Activity_{A*}(GBq)}{n_A(\mu mol)}$$

A_m is important because non-radioactive molecules can compete with the radiolabelled molecule for binding sites, which can diminish image quality.[35] This is illustrated in **Figure 1.7**.

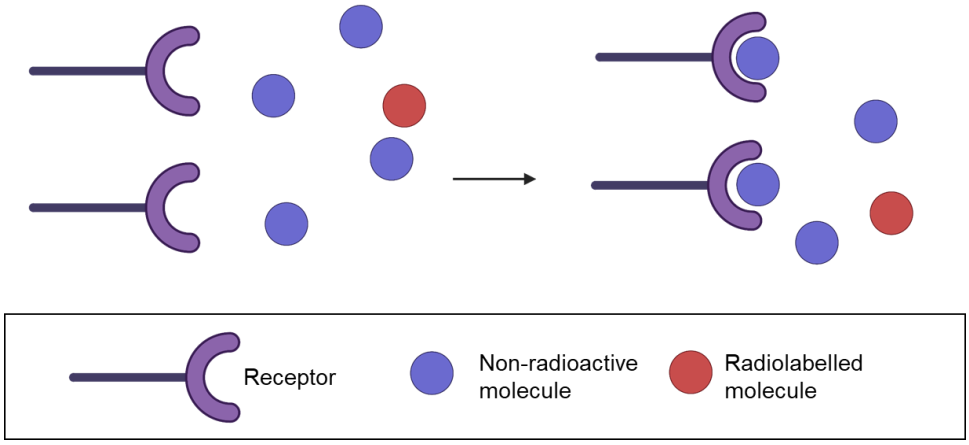

Figure 1.7: Graphical illustration in the importance of producing radiotracers with high A_m

Another consideration in producing radiopharmaceuticals is the synthetic route and duration. Typically, a radiosynthesis of <2 h is desirable for ^{18}F radiotracers, where ^{18}F should be incorporated at the latest possible step to minimise the number of reaction steps during radiosynthesis.[29] In this regard, a broad range of reactions and strategies have been developed for the incorporation of ^{18}F into molecules, which are discussed in the subsequent sections.

1.2.2 ^{18}F-labelling by C-F bond formation

^{18}F-labelling by carbon-fluorine bond formation can be divided into two types, electrophilic and nucleophilic fluorination.

Electrophilic fluorination

Whilst a range of reagents are available for electrophilic fluorination, [^{18}F]F_2 is the most widely used.[7] Due to the high reactivity of fluorine gas, these reactions must be conducted in specialised equipment, and carefully controlled at low temperatures or in inert atmospheres. Alternatively, [^{18}F]F_2 can be converted into a less reactive fluorinating agent such as [^{18}F]CH_3COOF, which was used in the first synthesis of [^{18}F]FDG (**Figure 1.8A**).[36] Apart from this, fluorine gas has also been used in the synthesis of 2-nitroimidazoles for hypoxia imaging,[37] and [^{18}F]F-DOPA through the use of organometallic reagents for increased regioselectivity during [^{18}F]fluorination.[38,39]

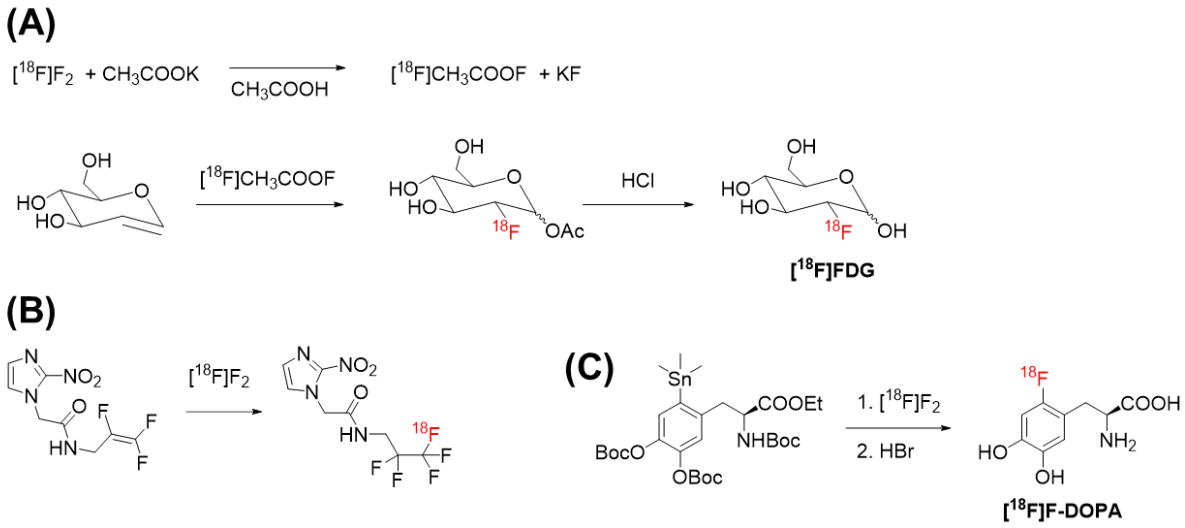

Figure 1.8: (A) Radiosynthesis of [^{18}F]FDG by electrophilic fluorination. (B) Radiosynthesis of ^{18}F-labelled 2-nitroimidazole using fluorine gas. (C) Synthesis of [^{18}F]F-DOPA by electrophilic fluorination.

Overall, despite the improved control of electrophilic fluorination reactions afforded by the use of reagents milder than $[^{18}F]F_2$, one major drawback using these methods is the low molar activity of the resulting radiotracers. For example, [^{18}F]F-DOPA is synthesised with molar activities of approximately 3.7 GBq/μmol using $[^{18}F]F_2$,[39] which is significantly lower than that afforded by nucleophilic fluorination reactions (>100 GBq/μmol).[40–42] The low molar activities obtained is mainly due to the need for F_2 as a carrier gas during the production of $[^{18}F]F_2$.

Nucleophilic fluorination

Nucleophilic fluorination using the [^{18}F]fluoride ion is perhaps the most routinely employed reaction for the synthesis of clinically important ^{18}F-labelled radiotracers.[7,43] Radiotracers prepared using nucleophilic fluorinations typically have high molar activities, since the addition of a carrier is not required during cyclotron production. $[^{18}F]F^-$ is produced by proton irradiation of ^{18}O-enriched water, resulting in an aqueous solution of $[^{18}F]F^-$. As a result of strong hydrogen bonds with water, the fluoride ion has poor nucleophilicity, which necessitates further preparation of the $[^{18}F]F^-$. Several steps are involved, which are shown in **Scheme 1.1**. Firstly, the $[^{18}F]F^-$ in water is trapped on an anion exchange. It is then eluted using a solution of Kryptofix® 222 (K2.2.2) and potassium carbonate in a mixture of water and acetonitrile. Finally, azeotropic distillation is carried out to remove water by heating the solution at 80-110 °C under a stream of nitrogen. Since kryptofix forms strong complexes with the potassium ions, this leaves 'naked' $[^{18}F]F^-$ ions with high nucleophilicities.

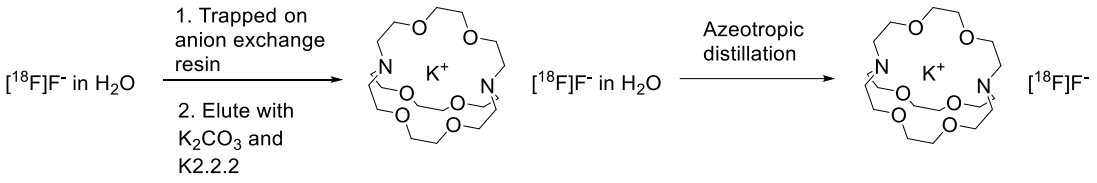

Scheme 1.1: Preparation of nucleophilic $[^{18}F]F^-$.

Upon preparation of $[^{18}F]F^-$,they can then be used in a range of [^{18}F]fluorination reactions, including aliphatic nucleophilic substitution, aromatic substitution and transition metal-mediated reactions.[7,43] Aliphatic nucleophilic substitution involves the displacement of a good leaving group (e.g. sulfonates or halides) by $[^{18}F]F^-$ through the S_N2 mechanism. The reaction is usually performed in polar aprotic solvents such as DMF, DMSO, MeCN and THF, at temperatures of 80-130 °C in 15 min.[7] This method is now being used in the synthesis of [^{18}F]FDG (**Scheme 1.2A**), producing it with molar activities exceeding 185 GBq/μmol.[29,41] Interestingly, the use of *tert*-butanol as a solvent has shown to improve the radiochemical yield (RCY) for the synthesis of [^{18}F]FLT (**Scheme 1.2B**) to 65 % compared to the 50 % obtained when using MeCN as a solvent.[44,45] The increased yield obtained was rationalised by the

reduction in competing elimination reactions and the increased entropy afforded by its de-solvation upon undergoing nucleophilic substitution.[46,47]

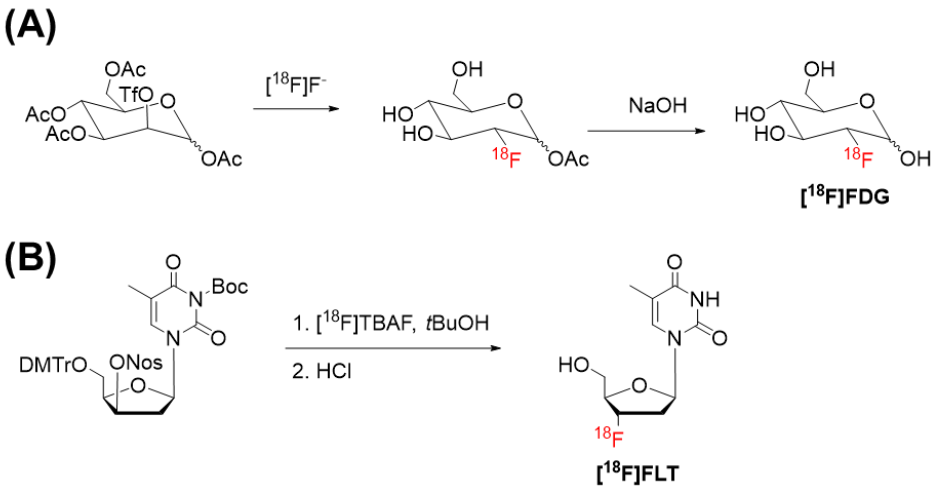

Scheme 1.2: Examples of nucleophilic aliphatic substitution reactions for the [^{18}F]fluorination

Aromatic substitution reactions are also an important class of reactions for the ^{18}F-labelling of molecules. One example is nucleophilic aromatic substitution (S_NAr) reactions using electron-deficient aryl systems with leaving groups such as halides, NO_2 and NMe_3. S_NAr reactions typically involve harsh conditions, where heating at 120-180 °C in a basic solution of DMSO is required. This is exemplified in the radiosynthesis of [^{18}F]PK14105, benzodiazepine-derived radiotracer for imaging peripheral-type benzodiazepine binding sites (**Scheme 1.3**).[48] Even under the relatively harsh conditions employed, a low RCY of 10-20% was obtained. To improve this, trimethylammonium leaving groups have been developed to afford higher RCYs, and S_NAr on heteroarenes such as pyridines have also been shown to proceed more efficiently under milder conditions.[49–51]

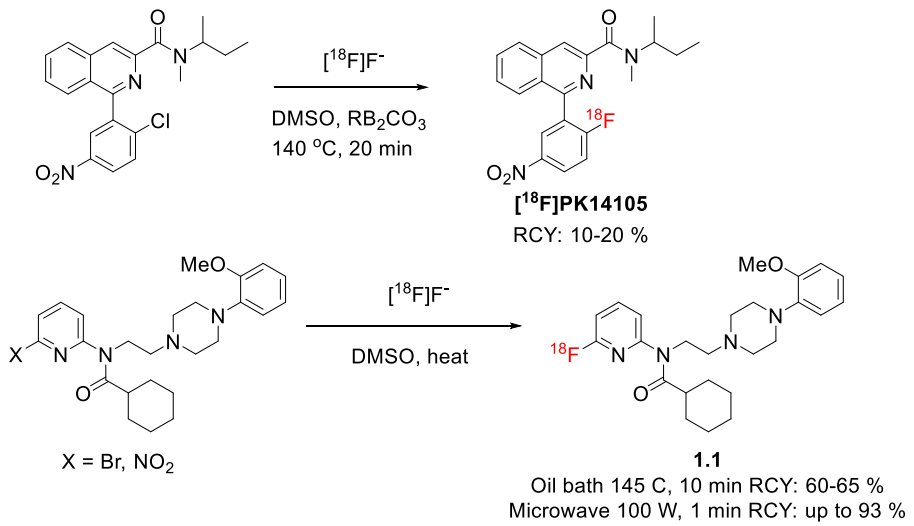

Scheme 1.3: Examples of nucleophilic aromatic substitution reactions for [^{18}F]fluorination

Apart from S_NAr, ^{18}F-labelling of aromatic compounds have also been carried out using aryl diazonium and diaryliodonium salts (**Scheme 1.4**). Limited success has been achieved by the use of diazonium salts, since the use of tetrafluoroborates as counterions limits the maximum radiochemical yield to 25 %.[43] To overcome this, alternative counterions such BCl_4^- have also been tested, but still resulted in low optimised RCYs of up to 19%.[52] As an alternative, diaryliodonium salts have been investigated for ^{18}F-labelling of aromatic compounds. Whilst regioselectivity issues can result in decreased RCY, preferred substitution of the desired aromatic ring can be achieved by tuning the substituents on the (hetero)aryl substrates. In general, reactions at *ortho*-substituted rings are preferred due to steric effects of resulting from the formation of a tricovalent iodine intermediate.[43,53,54] One example of the use of diaryliodonium salts is the radiosynthesis of **1.2**, which results in 35 % RCY within 90 min.[55]

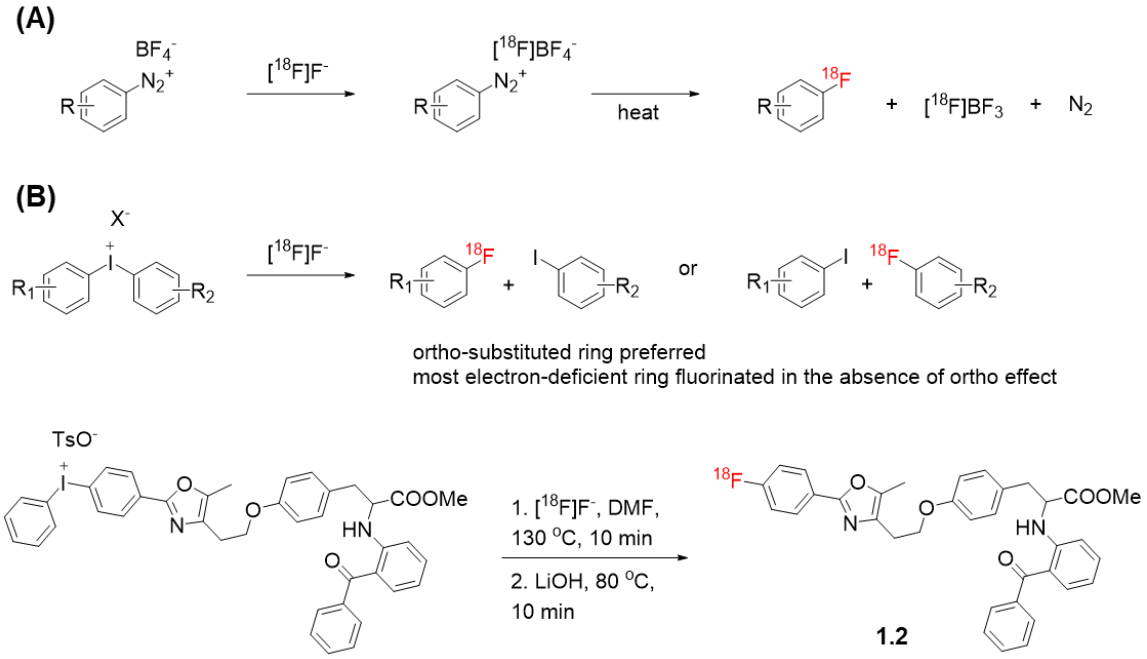

Scheme 1.4: Examples of aromatic [^{18}F]fluorination using (A) diazonium salts and (B) diaryliodonium salts.

Transition metal-mediated fluorination reactions have also been applied for the construction of carbon-fluorine bonds. One promising example is copper-mediated radiofluorination reactions (**Scheme 1.5**), which can be applied to arylboronic acids, arylboronic esters and arylstannanes with relatively good radiochemical yields and conversions (up to 83 %).[56–58]

In summary, even though there have been exciting developments in ^{18}F-labelling using carbon-fluorine bond formation, these generally still require some form of heating (above 40 °C) and the use of organic solvents, which are incompatible for the functionalisation of biomolecules. To circumvent this problem, prosthetic groups have been developed to enable

^{18}F-labelling of biomolecules under mild conditions (<37 °C, aqueous conditions), which will be briefly discussed in the next section.

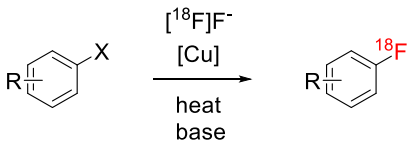

X = $B(OH)_2$: 110 °C, up to 73 % RCC
X = BPin : 110 °C, up to 84 % RCY
X = SnR_3 : 60 °C, up to 65 % RCC

Scheme 1.5: General scheme for copper-mediated radiofluorination reactions

1.2.3 Prosthetic groups for ^{18}F-labelling of biomolecules

Due to the structural complexity of some natural products and biomolecules, which can contain multiple reactive functionalities, ^{18}F-labelling is not always possible within 1-2 steps using the methods described above. As such, ^{18}F-labelled prosthetic groups, also known as bifunctional labelling agents, have been developed to enable functionalisation of these more complex molecules. Prosthetic groups are small ^{18}F-labelled molecules containing an activated functional group that is used for the modification of the compound of interest. A few common examples are shown in **Figure 1.9**.

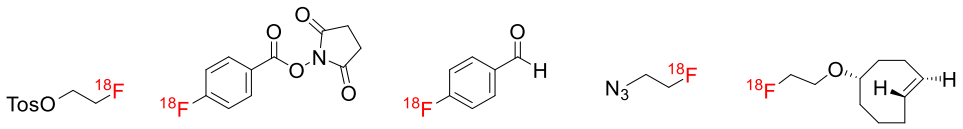

[^{18}F]FETos **[^{18}F]SFB** **[^{18}F]FBA** **[^{18}F]FEA** **[^{18}F]F-TCO**

Figure 1.9: Examples of prosthetic groups used for ^{18}F-labelling

2-[^{18}F]fluoroethyl tosylate ([^{18}F]FETos) is a widely used prosthetic group for the radiolabelling of small molecule radiotracers due to its small size, good reactivity, high stability, and convenient radiosynthesis.[59] Although [^{18}F]fluoroalkyl halides have also been reported,[60,61] the reliability of [^{18}F]FETos has resulted in its continued use for the alkylation of nucleophilic functionalities.[59]

Since alkylation reactions using [^{18}F]FETos are typically performed under aprotic conditions at high temperatures, it is less useful for the functionalisation of biomolecules such as peptides or proteins. Therefore, [^{18}F]SFB and [^{18}F]FBA have been developed as alternative prosthetic groups for the functionalisation of amines in biomolecules.[62–64]

Apart from these, the development of ‘click’ reactions (discussed next in section 1.2.4) has also resulted in the widespread application of 2-[^{18}F]fluoroethylazide ([^{18}F]FEA) for the ^{18}F-labelling of biomolecules via the copper-catalysed azide-alkyne cycloaddition (CuAAC)

reaction or the strain-promoted azide-alkyne cycloaddition (SPAAC) reaction.[65] More recently, the synthesis of ^{18}F-labelled *trans*-cyclooctenes have also been reported, enabling rapid ligation by the inverse-electron-demand Diels-Alder (IEDDA) reaction with a tetrazine counterpart.[66,67]

In summary, the development and use of prosthetic groups have enabled more complex molecules to be radiolabelled by ^{18}F, enabling their biological behaviour to be studied using PET imaging. However, it should be noted that the addition of extra functionalities onto molecules can change their biological behaviour in terms of their metabolism, toxicity and affinity (**Figure 1.10**). Therefore, careful design of the site of functionalisation should be undertaken to ensure that these parameters remain unaffected.

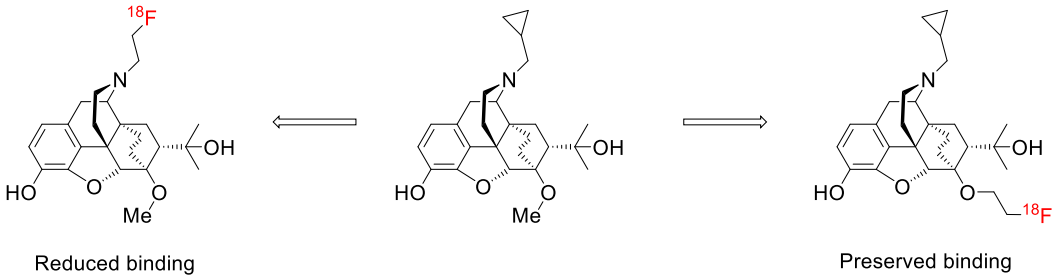

Figure 1.10: Illustration of the importance of site of functionalisation using ^{18}F-labelled derivatives of diprenorphine.[59,68]

Whilst a range of other prosthetic groups are available for the ^{18}F-labelling of biomolecules, these will instead be discussed in Chapter 5, which aims at developing new methodologies for the site-selective radiolabelling biomolecules by ^{18}F.

1.2.4 Click chemistry and bioorthogonal reactions

The term ‘click’ chemistry was first coined by Sharpless and coworkers to describe reactions that are modular, high yielding, have a wide scope, and only produce harmless and easily removable by products.[69] In addition, the reaction should be operationally simple, takes place in a benign solvent such as water, and is easily purified through non-chromatographic methods. These characteristics make click reactions ideal for radiosynthesis and is widely applied for the synthesis of ^{18}F-labelled biomolecules using [^{18}F]FEA (**Figure 1.11**).[59,70] Currently, click chemistry is synonymous with the copper-catalysed azide-alkyne cycloaddition (CuAAC) reaction, which was reported in 2002 by both the Sharpless and Meldal groups.[71,72]

However, the use of copper(I) reagents can sometimes result in toxicity issues, which led to the development of strain-promoted azide-alkyne cycloadditions (SPAAC) that enable catalyst-free click reactions. Ring strain can be introduced by the use of highly strained cyclooctynes such as dibenzocyclooctyne (DBCO) (**Figure 1.11**). However, the large size and

steric bulk of DBCO can them unfavourable for use, which resulted in the development of bicyclononynes (BCN) that retain the high reactivity of these strained systems.[73,74]

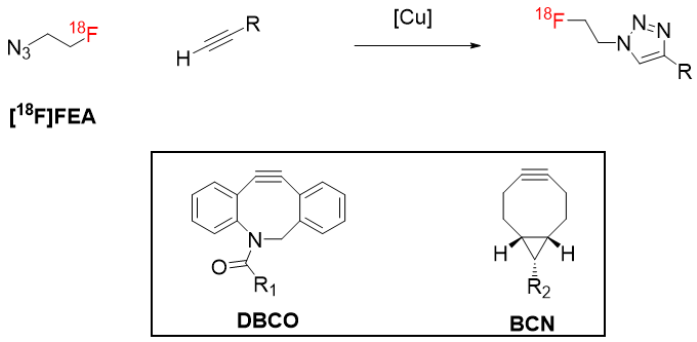

Figure 1.11: General reaction scheme for the use of CuAAC in ^{18}F-labelling. Insert shows examples of strained cyclooctynes used for SPAAC.

Building on the development of click chemistry, bioorthogonal chemistry was then introduced by the Bertozzi group, which refers to reactions that take place in biological environments without interfering or affecting the biological system.[75] The use of bioorthogonal reactions for the study of physiological processes involves the use of non-native functionalities with the following characteristics:

(i) Inert under physiological conditions
(ii) Non-toxic
(iii) Rapid and efficient reaction at low concentrations under physiological conditions

Although the Staudinger ligation was first investigated to demonstrate the utility of bioorthogonal chemistry (**Figure 1.12A**), it is not applied in ^{18}F-labelling, and is thus not discussed further. Instead, the use of the two aforementioned click reactions, oxime ligations, and tetrazine-*trans*-cyclooctene ligations have been applied for the ^{18}F-labelling of biomolecules. Examples of prosthetic groups using these approaches are included in **Figure 1.12B**, where [^{18}F]FEA and [^{18}F]F-DBCO are used for azide-alkyne cycloaddition reactions,[65,76] and [^{18}F]F-Tz and [^{18}F]F-TCO are used in tetrazine-*trans*-cyclooctene ligations.[66,77]

Of note, the fast and efficient inverse-electron-demand Diels-Alder (IEDDA) reaction between tetrazines and *trans*-cyclooctenes (TCO) (second order rate constants: 1-10^6 M^{-1} s^{-1}, *c.f.* SPAAC 0.01-1 M^{-1} s^{-1} and CuAAC 10-100 M^{-1} s^{-1}) has seen it being applied for pre-targeted PET imaging using ^{18}F.[70,77–80] Pre-targeted imaging involves two steps: (i) the subject is first injected with a targeting molecule functionalised with a bioorthogonal handle (such as TCO). After the targeting molecule is allowed to accumulate at the target site, step (ii) is conducted, where the radiolabelled complementary functional group (tetrazine) is injected. This allows

short-lived radioisotopes such as ^{18}F to be used in combination with long-circulating, high affinity biomolecules such as antibodies, which are traditionally incompatible.

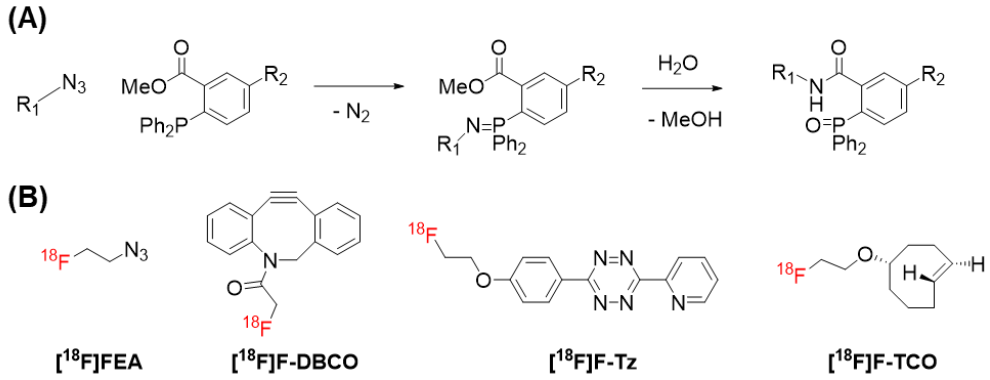

Figure 1.12: (A) Staudinger reaction. (B) Examples of ^{18}F-labelled prosthetic groups used in bioorthogonal reactions.

In short, apart from improving the methods available for the ^{18}F-labelling of molecules, the development of click and bioorthogonal chemistry has also enabled ^{18}F to be used in combination with targeting vectors that were previously incompatible. Although these represent powerful approaches that enable improved imaging of biological processes, they tend to introduce relatively large steric bulks onto radiotracers, and might be unsuitable for the ^{18}F-labelling of small molecules. Thus, ^{18}F incorporation by the formation of Si-F, B-F or metallic fluoride bonds have been investigated to enable more facile ^{18}F-labelling.

1.2.5 Inorganic approaches for ^{18}F-labelling

To enable ^{18}F-labelling under milder conditions, non-carbon elements that have high affinity for fluorine have been investigated to enable incorporation of ^{18}F. The bond dissociation energies of these systems are given in **Table 1.3**, where systems such as B-F, Al-F, Ga-F and Si-F appear attractive due to their higher bond dissociation energies compared to the C-F bond, which could indicate their ability to form single bonds with ^{18}F more readily.[81]

Table 1.3: Bond dissociation energies of selected single fluorine bonds.[81]

Bond type	Bond dissociation energy (kJ mol^{-1})
C-F	536
B-F	766
Al-F	664
Ga-F	577
Si-F	540
P-F	439
Fe-F	477

Boron is an attractive choice since the B-F bond has high thermodynamic stability. ^{18}F-labelling using boron-containing compounds is typically achieved using the organotrifluoroborate (RBF_3^-) group by fluorination of boronic esters,[82] or isotopic exchange in the presence of a Lewis acid (**Scheme 1.6**).[83,84] Although these methods allow the use for [^{18}F]fluoride under partially aqueous conditions, negating the need for azeotropic drying steps, the need for non-radioactive KHF_2 during the preparation of [^{18}F]KHF_2 reduces the ability to synthesise radiotracers with high molar activities.

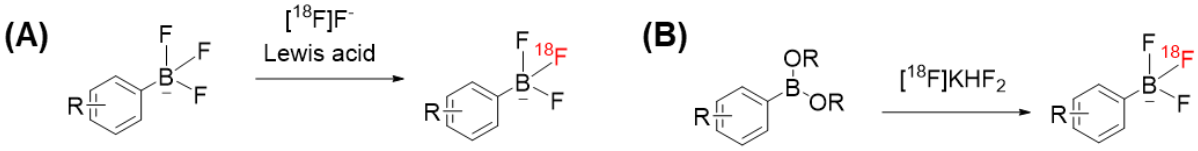

Scheme 1.6: ^{18}F-labelling by B-F bond formation by (A) isotopic exchange and (B) fluorination of boronic esters.

Nevertheless, organotrifluoroborates have enabled late-stage incorporation of ^{18}F, where it has been used in the one-step labelling of biomolecules for *in vivo* imaging.[82,83,85,86] In addition, Kim *et al*. also demonstrated the ability of ^{18}F incorporation by isotopic exchange to form BODIPY **1.3** (**Scheme 1.7**), which potentially allows dual modal PET and optical imaging of the brain.

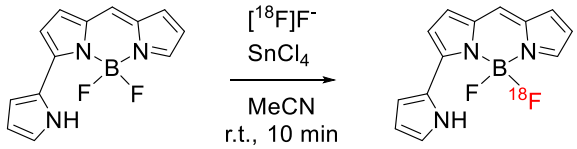

1.3

Scheme 1.7: ^{18}F-labelling of BODIPY for dual-modal PET/optical imaging

Apart from boron, organosilicons are also widely investigated as ^{18}F acceptors due to their high affinity to fluorine, where fluoride ions are used to remove trimethylsilyl protecting groups from alcohols.[87] The use of organosilicons for ^{18}F-labelling is termed silicon-fluoride-acceptor (SiFA) systems, which was first reported by the Schirrmacher Group in 2006 (**Scheme 1.8**).[88]

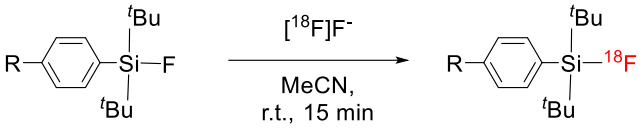

Scheme 1.8: ^{18}F-labelling by SiFA chemistry

However, one drawback of SiFA systems is the requirement of bulky *tert*-butyl groups to reduce hydrolysis, which results in increased lipophilicity of the resulting radiotracer. In

addition, although ^{18}F-labelling does not need to be conducted under strictly anhydrous conditions, azeotropic drying of [^{18}F]F$^-$ in the presence of Kryptofix® 222 is still required,[88–91] which could reduce the attractiveness of this method for the one-step ^{18}F-labelling of biomolecules.[40]

Besides these, ^{18}F-labelling at phosphorus and sulfur atoms have also been reported. ^{18}F-labelling through ^{18}F/^{19}F isotopic exchange of S-F bonds is known as the sulfur fluoride exchange (SuFEx) click chemistry, which enables high yields at room temperatures.[92] While aryl fluorosulfonyls have been found be unstable *in vivo* to defluorination (**Scheme 1.9**),[93] aryl fluorosulfates are stable *in vivo*, and have been receiving increased attention.[92] However, as with C-F bond formation, these requires the [^{18}F]fluoride to be anhydrous, thus necessitating azeotropic distillation. In comparison, although ^{18}F-labelling by P-F bond attention is less popular, recent developments have enabled fluorination reactions to be carried out in aqueous conditions at high yields. This allows one-step ^{18}F-labelling of biomolecules, showing its potential for more routine applications.[94]

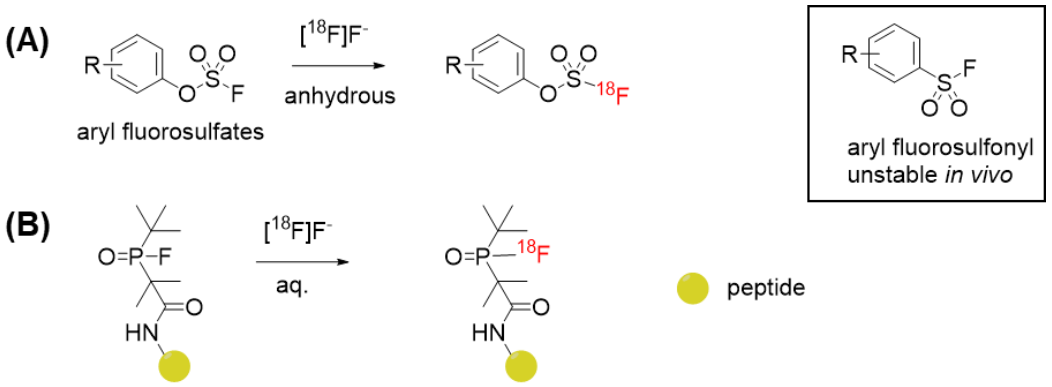

Scheme 1.9: ^{18}F-labelling by S-F and P-F bond formation.

Metal-fluoride bonds have also been investigated for ^{18}F-labelling. One example is the use of triazacyclononane (tacn)-based ligands for the formation of stable metal complexes (**Scheme 1.10A**). Whilst the trichloride precursors were initially investigated for halide exchange reactions, these required relatively large amounts of metal precursors due to hydrolysis.[95,96] Instead, using the corresponding trifluoride for ^{18}F/^{19}F isotopic exchange enabled lower amounts of precursors to be used.[97] Importantly, these systems allowed semi-aqueous conditions to be used, eliminating the need for azeotropic distillation during the preparation of [^{18}F]F$^-$. In addition, a scandium [^{18}F]fluoride complex was also reported recently, which enabled ^{18}F-labelling in high radiochemical yields and showed good *in vivo* stability when used for PSMA imaging.[98] This represents an exciting development, since it allows the same system to be used for ^{47}Sc-labelling, which is a β$^-$ emitter with the potential to be used in cancer therapy.[99] With the use of an identical system for both imaging and therapy, the precise

locations of the radiotracer can be determined since it has the same chemical composition. In comparison, using a pair of different radionuclides for imaging and therapy, such as ^{68}Ga and ^{177}Lu,[100] could result in slightly different biological distributions.

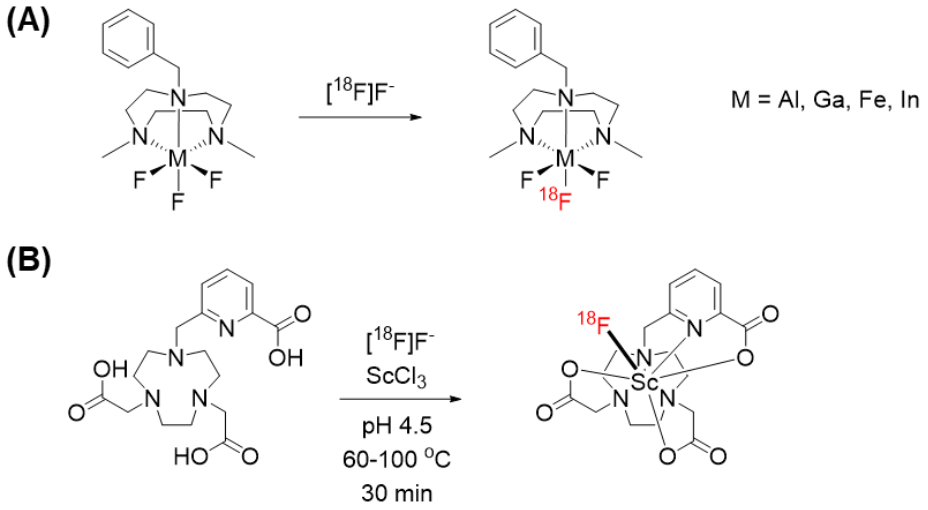

Scheme 1.10: Strategies for ^{18}F-labelling using the formation of metal-fluoride bonds.

Finally, the use of aluminium in combination with pentadentate chelators such as 1,4,7-triazacyclononane-1,4,7-triacetic acid (NOTA) has also enabled facile one-step ^{18}F-labelling of biomolecules.[101] Since this method forms the basis of the radiolabelling used in this thesis, it is introduced in more detail in the next section.

1.2.6 Radiolabelling by the aluminium-[^{18}F]fluoride method

First introduced by McBride *et al*. in 2009,[102] the aluminium-[^{18}F]fluoride ([^{18}F]AlF) method has received widespread attention from the nuclear community, with a multitude of [^{18}F]AlF-labelled radiotracers, new chelators, production protocols, and clinical trials being reported.[103,104] The [^{18}F]AlF complex can be described as a 'pseudo-radiometal', as it combines the favourable decay characteristics of ^{18}F and the convenience radiometal-based synthesis.[105] Typical conditions for [^{18}F]AlF-labelling are shown in **Figure 1.13**. Fully aqueous conditions can be used, though the addition of organic co-solvents has been shown to increase reaction yields.[106]

The ability to conduct the [^{18}F]AlF-labelling reactions in the presence of water removes the need for azeotropic drying of the cyclotron-produced [^{18}F]fluoride, where simple purification on an anionic cartridge is sufficient to remove any trace metal contaminants and cyclotron-generated impurities (**Figure 1.13A**). Upon purification of the [^{18}F]fluoride, it is added to a solution containing the precursor and aluminium trichloride in a buffer (typically NaOAc) at pH 4-5. After heating at 90-110 °C for 10-20 min, high radiochemical conversions of up to 99 %

can be achieved.[101] In cases where RCC is low, removal of any unreacted fluoride can be easily carried out through purification by solid-phase extraction, eliminating the need for extensive purification by preparative high-performance liquid chromatography (HPLC). The combination of the facile [^{18}F]fluoride preparation, one-step radiosynthesis, and simple purification procedures result in short overall radiosynthesis durations of 25-45 min.

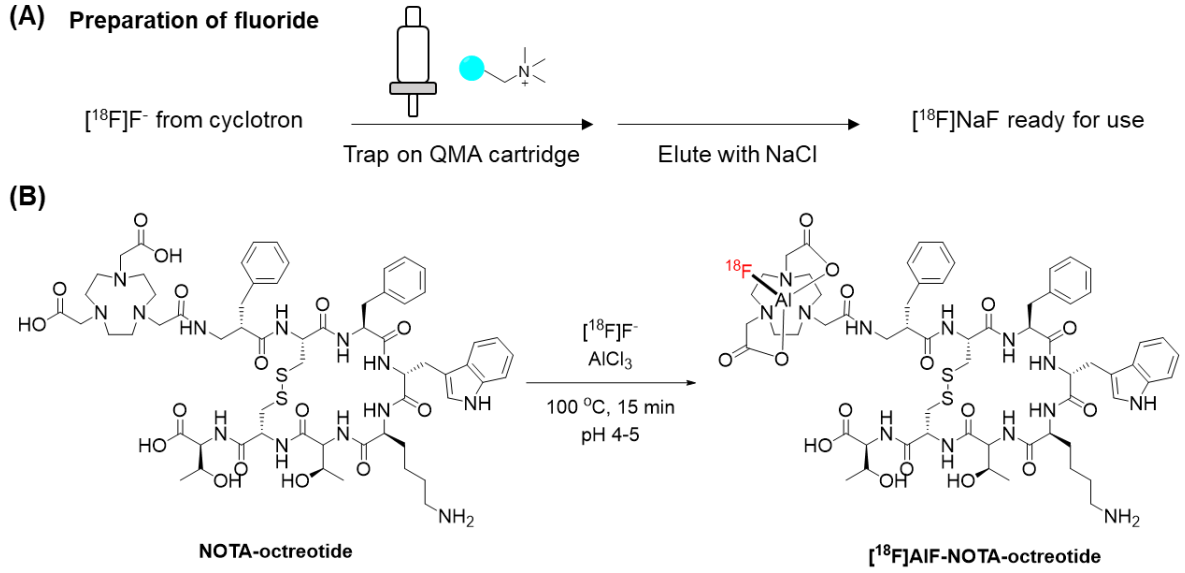

Figure 1.13: Typical procedures for radiolabelling by the [^{18}F]AlF method.

Radiolabelling by the [^{18}F]AlF method can generate radiotracers with high molar activities of up to 260 GBq/μmol,[107] making it viable for producing receptor-targeted radiopharmaceuticals. The advantages of radiolabelling by the [^{18}F]AlF method has resulted in its widespread use, with more than 20 clinical trials already being published for imaging a range of cancer types, and several clinical trials are also in progress.[101,108–115]

In addition to the late-stage ^{18}F-labelling of biomolecules, the [^{18}F]AlF method has also been used to radiolabel tetrazines with moderate to good radiochemical yields of 48-65 % in 26-108 min (**Figure 1.14**).[80,116,117] The long synthesis duration of 108 min reported for tetrazine **1.6** was largely due to an additional preparation step taken to form the [^{18}F]AlF^{2+} complex prior to radiolabelling the tetrazine, which has been shown to be unessential for [^{18}F]AlF reactions. In comparison, tetrazines produced using S_N2 reactions had significantly lower RCYs of 13.2-16 % after 90 min synthesis;[77,118] whereas those produced using copper-mediated radiofluorinations resulted in slightly higher yields of 25 %, with a similar radiosynthesis duration of 90 min.[78] The higher RCYs obtained using the [^{18}F]AlF method demonstrates that it can potentially be used as a substitute for C-F bond formation reactions in the synthesis of prosthetic groups.

Notably, for the [^{18}F]AlF-labelled tetrazines, compound **1.6** features a monosubstituted tetrazine with a 6-H group, which is more reactive than the disubstituted tetrazines featuring a

6-Me group in compounds **1.4** and **1.5** due to steric and electronic reasons.[70,119] While compound **1.5** was used in the 2-step functionalisation of an affibody,[116] compound **1.6** was used in pretargeted PET imaging,[80] demonstrating the versatility of the ^{18}F-labelled tetrazines for different applications.

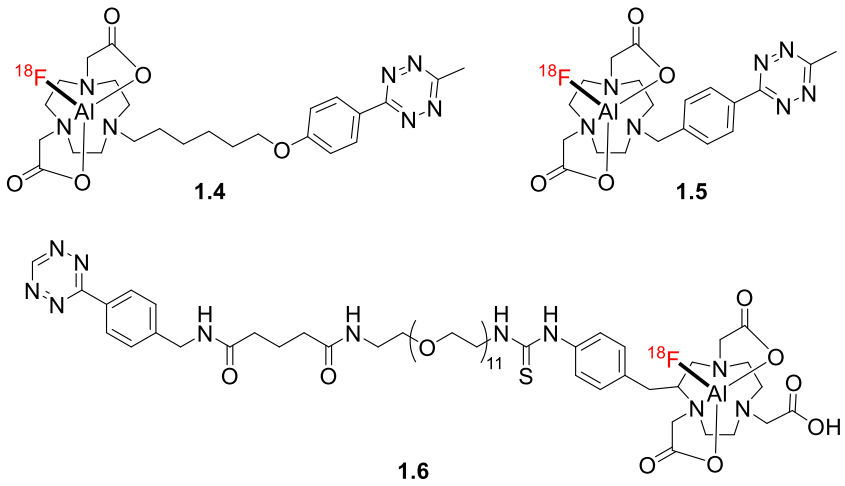

Figure 1.14: Structures of [^{18}F]AlF-labelled tetrazines

However, one drawback of the [^{18}F]AlF method is the relatively harsh reaction conditions employed (acidic pH and high temperatures), making it unsuitable for radiolabelling acid- or heat-sensitive biomolecules. To address this, the development of acyclic chelators (**Figure 1.15**) for [^{18}F]AlF^{2+} complexation are being carried out to enable radiolabelling at ambient temperatures.[120,121] Since a more in-depth discussion on the coordination of the [^{18}F]AlF complex and ligand development will provided in chapter 4, further discussion of each ligand is not undertaken in this section.

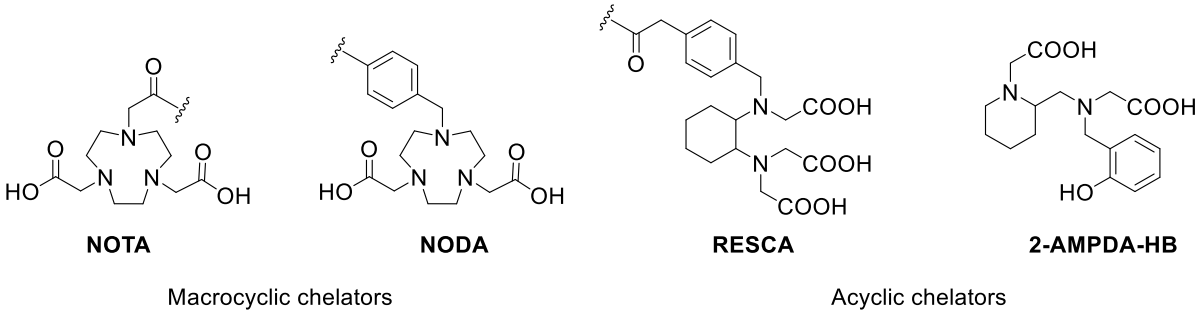

Figure 1.15: Examples of chelators used for [^{18}F]AlF-labelling

In summary, the [^{18}F]AlF method enables facile, high-yielding and late-stage ^{18}F-labelling of molecules. As such, it is being widely employed to radiolabel a range of compounds, with several biologically relevant [^{18}F]AlF-labelled radiotracers currently undergoing clinical trials to enable better diagnosis of cancer.

Since a large section of this thesis is focused on using the [^{18}F]AlF method for radiolabelling microbubbles, and the application of these microbubbles in molecular imaging and cancer therapy, the next section gives a brief introduction on the use of microbubbles as ultrasound contrast agents.

1.3 Microbubbles as contrast agents for ultrasound imaging

1.3.1 Introduction to microbubbles

The ability of microbubbles to act as ultrasound contrast agents was discovered serendipitously in 1968 by Raymond Gramiak and Pravin Shah, where they observed an enhancement in ultrasound contrast in the aorta after the injection of an agitated saline solution during cardiac catheterisation.[122] However, due to surface tension, bubbles of this size are unstable and are prone to coalesce or dissolve in the bloodstream.[123] Thus, initial research on microbubbles were aimed primarily at increasing bubble stability through improvements in the carrier gas and shell composition.[124]

Microbubbles are composed of a carrier gas encapsulated by a biocompatible shell (**Figure 1.16**), and they generally have diameters of 0.5 to 10 μm.[4,123,125] Microbubble formulations approved by the United States Food and Drug Administration (FDA) have a mean diameter of 1.1-3.3 μm, with no bubbles exceeding 20 μm in size.[126] For reference, red blood cells have a comparable diameter of 6-8 μm, which demonstrates the suitability (and restriction) of microbubbles as intravascular agents.

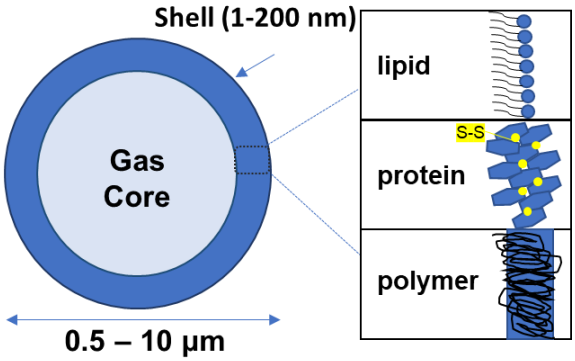

Figure 1.16: Graphical representation microbubbles with typical shell compositions, where different shell components are held together by different physical interactions. Lipid shells (3-5 nm) are held intact by hydrophobic interactions; protein shells (~15 nm) are joined by disulfide linkages; and polymer shells (100-200 nm) are covalently cross-linked or entangled. The gas core can be made of air, nitrogen, perfluorocarbons or sulfur hexafluoride.[123,125]

The enhanced ultrasound contrast afforded by microbubbles is mainly due to the carrier gas, which has a much lower density compared to water. The speed in which sound waves travel in gaseous media is also slower than that in liquids. According to equation 1 ($Z = \rho v$, Section 1.1.6), the acoustic impedance (*Z*) of microbubbles is much lower compared to that of the body tissues. Thus, strong echoes are generated in the presence of microbubbles, giving rise to a good contrast. Apart from that, the shell composition also affects the acoustic properties and stability of the microbubbles generated, which are briefly described below.

Lipid Shells: The formulation of lipid shells was inspired by lung surfactants,[123,127] where their formation is based on the principle that the ambiphilic phospholipids can spontaneously self-assemble to form a monolayer at the gas-water interface, with their hydrophilic chains facing water and hydrophoblic tails facing inwards to the non-polar gas.[123] This lowers surface tension, stabilising the microbubbles. One favourable feature of lipid shells is that they are held together by weak van der Waals forces and hydrophobic interactions, making them more flexible to contraction and expansion, which gives rise to more favourable acoustic behaviours for ultrasound imaging.[123]

Protein Shells: Protein-shelled microbubbles were first discovered by Keller in 1987,[128] and was the first commercialized US contrast agent.[129] Most formulations made use of albumin,[125,129] but formulations using lysozyme have also been reported.[130] Although the exact nature of protein shells have yet to be determined, it is suggested that the shell is made up of both native and denatured proteins.[131] Importantly, cysteine residues have been shown to be vital for protein cross-linking to form the microbubble shells,[132] and Cavalieri ***et al.*** were able to confirm the formation of disulfide bonds in their lysozyme microbubbles.[130]

Polymer Shells: Polymer shells are formed by cross-linked or entangled polymer chains. These result in rigid shells that are more resistant to compression and expansion, decreasing the microbubbles' response to ultrasound.[123] Although early efforts were focused on developing biopolymer shells,[129,133] these had problems in material contamination, size reproducibility and *in vivo* stability.[129,134] Hence, current microbubble formulations utilize synthetic polymers such as cyanoacrylates[135] and vinyl alcohols,[136,137] both of which are biocompatible.

Due to the excellent ultrasound contrast afforded by microbubbles and their good safety profile, a few formulations have been clinically approved and are commercially available (**Table 1.4**). The 'first-generation' microbubbles (Echovist, Albunex and Levovist) were all air-filled, and have been withdrawn due to their low stability in vivo.[129] This is mainly due to the high solubility of air in the blood plasma, which results in the gas core leaking into the blood.[4] Subsequent use heavy density gases such as perfluorocarbon and sulfur hexafluoride has improved

microbubble stability due to their higher molecular weight, lower solubility in blood, and lower diffusivity compared to air.

Table 1.4: Summary of clinically approved microbubble formulations.[4,125]

Name	Year approved	Shell Material	Core gas
Echovist	1991, withdrawn	Galactose	Air
Albunex	1993, withdrawn	Serum albumin	Air
Levovist	1995, withdrawn	Galactose, palmitic acid	Air
Optison	1998	Serum albumin	Octafluoropropane
Definity	2001	Phospholipid	Octafluoropropane
Imavist	2002, withdrawn	Phospholipid	Perfluorohexane, nitrogen
Luminity	2006	Phospholipid	Octafluoropropane
Sonazoid	2007	Phospholipid	Perfluorobutane
SonoVue	2014	Phospholipid	Sulfur hexafluoride

Generally, microbubbles stay in circulation for less than 20 minutes,[123,125,138] where their stability decreases from passage through the lungs due to gas diffusion. However, the functionalisation of microbubble surfaces with long polyethylene glycol (PEG) chains have been shown to increase microbubble stability by decreasing their immunogenicity and coalescence.[139,140] Notably, a poly(allylamine) hydrochloride formulation by Lentacker *et al*. showed a half-life of around 7 hours *in vivo*,[141] indicating a potential advantage of polymer-shell microbubbles.

1.3.2 Functionalised microbubbles for molecular imaging

Apart from enhancing ultrasound contrast for anatomical imaging, microbubbles can also be functionalised with targeting vectors for molecular imaging, with early examples being reported around 1997.[142–144] To functionalise microbubbles for molecular imaging, two strategies are available: (i) attaching the targeting vector to the shell material prior to microbubble formation, and (ii) attaching the targeting vector to pre-formed microbubbles.[27]

In brief, strategy (i) allows for the stepwise synthesis and purification by traditional organic chemistry methods, which allows for more precise characterisation of the modified molecules. This approach works well for attaching smaller molecules such as peptides, carbohydrates and biotin to lipid-shelled microbubbles. In contrast, strategy (ii) is generally used for materials that are unstable under high shear mixing and sonication, which are required for microbubble

formation. Therefore, it is suitable for the attachment of large biomolecules such as proteins and antibodies that can potentially denature or aggregate under harsh conditions. A more focused discussion on microbubble functionalisation is included in Chapter 2.

Upon functionalisation, microbubbles are used to visualise vascular biomarkers due to their relatively large sizes.[3,144] Popular targets include the intracellular adhesion molecule-1 (ICAM-1) and vascular cell adhesion molecule-1 (VCAM-1) for the detection of thrombosis, inflammation and atherosclerosis.[145–147] Apart from that, $\alpha_v\beta_3$ integrins and vascular endothelial growth factor receptors (VEGFR) are also targeted for imaging angiogenesis in cancer.[26,148,149] Notably, the development of BR55 in 2010,[150] which is a lipid-based microbubble formulation for targeting VEGFR2, has showed positive results for detecting different cancer types in clinical trials,[151–153] demonstrating the potential of contrast-enhanced ultrasound to be used for molecular imaging. Given the advantages of ultrasound compared to other medical imaging modalities,[4,26] this development could provide an alternative method for the safe, affordable and accessible diagnosis and monitoring of cancer.

Apart from ultrasound imaging, microbubbles can also be applied for therapeutic purposes, where the application of focused ultrasound pulses in the presence of microbubbles have been shown to increase membrane permeability for improved drug delivery.[154,155] A more in-depth discussion of the use of microbubbles for enhancing drug delivery is provided in Chapter 3.

In summary, the development of microbubbles has vastly improved the diagnostic utility of ultrasound imaging, enabling it to be used for both anatomical and molecular imaging. In addition, the application of microbubbles as therapeutic agents also demonstrates their potential for further improving current treatment capabilities. Taken together, the development of new microbubble formulations could be beneficial for both diagnostic and therapeutic purposes, which forms the basis of the first part of this thesis. The next section briefly outlines the aims of this project in relation to each chapter.

1.4 Aims and objectives

The main aim of this project was to apply and develop the [^{18}F]AlF method for biomolecule radiolabelling. In particular, developments in methodologies for the [^{18}F]AlF-labelling of peptides, lipids and microbubbles were investigated.

Chapter 2 seeks to develop facile and convenient methods to access ^{18}F-labelled microbubbles using the [^{18}F]AlF method and tetrazine-TCO ligation. This involves the design, synthesis and [^{18}F]AlF-labelling of a tetrazine-functionalised chelator, followed by its conjugation onto TCO-functionalised microbubbles. Incorporation of a targeting vector for cancer imaging was also attempted to investigate the potential of the [^{18}F]AlF-labelled microbubbles to be used in molecular imaging.

Chapter 3 then applies the [^{18}F]AlF-labelled microbubbles for studying the ability to increase radioactive accumulation in tumours after treatment using ultrasound-mediated microbubble destruction (UMMD). If successful, this could pave the way for the use of therapeutic radionuclides in combination with UMMD.

Chapter 4 explores the use of new chelators for enabling milder conditions during [^{18}F]AlF-labelling. Two classes of acyclic chelators, bisphosphonate derivatives and salen derivates, were synthesised to investigate their potential to complex the [^{18}F]AlF^{2+} ion.

Chapter 5 describes the use of a site-selective cysteine conjugation method for achieving chemo- and regioselective [^{18}F]AlF-labelling of biomolecules to minimise the issues caused by stochastic bioconjugation methodologies.

1.5 References

1 P. Suetens, *Fundamentals of Medical Imaging*, Cambridge University Press, 3rd edn., 2017.

2 R. S. C. Cobbold, *Foundations of Biomedical Ultrasound (Biomedical Engineering Series)*, Oxford University Press, USA, 2006.

3 E. Brown and J. R. Lindner, *Curr. Cardiol. Rep.*, 2019, **21**, 30.

4 N. J. Long and W. T. Wong, *The Chemistry of Molecular Imaging*, John Wiley & Sons, Inc, Hoboken, NJ, 2014.

5 L. M. Kenny and E. O. Aboagye, *Adv. Cancer Res.*, 2014, **124**, 329–374.

6 V. T. C. Tsang, X. Li and T. T. W. Wong, *Sensors (Basel).*, 2020, **20**, 1–20.

7 Z. Li and P. S. Conti, *Adv. Drug Deliv. Rev.*, 2010, **62**, 1031–1051.

8 P. W. Miller, N. J. Long, R. Vilar and A. D. Gee, *Angew. Chemie Int. Ed.*, 2008, **47**, 8998–9033.

9 M. Conti and L. Eriksson, *EJNMMI Phys.*, 2016, 3, Article no 8.

10 M. Farleigh, T. T. Pham, Z. Yu, J. Kim, K. Sunassee, G. Firth, N. Forte, V. Chudasama, J. R. Baker, N. J. Long, C. Rivas and M. T. Ma, *Bioconjug. Chem.*, 2021, **32**, 1214–1222.

11 S. Vallabhajosula, *Semin. Nucl. Med.*, 2007, **37**, 400–419.

12 J. Hernández-Gil, M. Braga, B. I. Harriss, L. S. Carroll, C. H. Leow, M.-X. Tang, E. O. Aboagye and N. J. Long, *Chem. Sci.*, 2019, **10**, 5603–5615.

13 *The Supply of Medical Isotopes: An Economic Diagnosis and Possible Solutions*, OECD Publishing, 2019.

14 Y. D. Xiao, R. Paudel, J. Liu, C. Ma, Z. S. Zhang and S. K. Zhou, *Int. J. Mol. Med.*, 2016, **38**, 1319–1326.

15 G. H. Glover, *Neurosurg. Clin. N. Am.*, 2011, **22**, 133.

16 M. Hoheisel, *Nucl. Instruments Methods Phys. Res. Sect. A Accel. Spectrometers, Detect. Assoc. Equip.*, 2006, **563**, 215–224.

17 A. Steffen, K. Costuas, A. Boucekkine, M. H. Thibault, A. Beeby, A. S. Batsanov, A. Charaf-Eddin, D. Jacquemin, J. F. Halet and T. B. Marder, *Inorg. Chem.*, 2014, **53**, 7055–7069.

18 M. W. Conklin, P. P. Provenzano, K. W. Eliceiri, R. Sullivan and P. J. Keely, *Cell Biochem. Biophys.*, 2009, **53**, 145.

19 S. Singh and A. Goyal, *Tex. Heart Inst. J.*, 2007, **34**, 431–438.

20 D. Cosgrove, *Eur. J. Radiol.*, 2006, **60**, 324–330.

21 A. Benjamin, R. E. Zubajlo, M. Dhyani, A. E. Samir, K. E. Thomenius, J. R. Grajo and B. W. Anthony, *Ultrasound Med. Biol.*, 2018, **44**, 2739.

22 P. P. Rebouças Filho, E. de S. Rebouças, L. B. Marinho, R. M. Sarmento, J. M. R. S. Tavares and V. H. C. de Albuquerque, *Pattern Recognit. Lett.*, 2017, **94**, 211–218.

23 J. K. Willmann, N. van Bruggen, L. M. Dinkelborg and S. S. Gambhir, *Nat. Rev. Drug Discov.*, 2008, 7, 591–607.

24 J. R. Lindner, *J. Nucl. Cardiol.*, 2004, **11**, 215–221.

25 M. A. Pysz, S. S. Gambhir and J. K. Willmann, *Clin. Radiol.*, 2010, **65**, 500–516.

26 A. L. Klibanov, *J. Nucl. Cardiol.*, 2007, **14**, 876-884.

27 S. Unnikrishnan and A. L. Klibanov, *Am. J. Roentgenol.*, 2012, **199**, 292–299.

28 S. Liu, *Adv. Drug Deliv. Rev.*, 2008, **60**, 1347–1370.

29 H. H. Coenen, P. H. Elsinga, R. Iwata, M. R. Kilbourn, M. R. A. Pillai, M. G. R. Rajan, H. N. Wagner and J. J. Zaknun, *Nucl. Med. Biol.*, 2010, **37**, 727–740.

30 J. W. Kim and C. V. Dang, *Cancer Res.*, 2006, **66**, 8927–8930.

31 L. Fass, *Mol. Oncol.*, 2008, **2**, 115–152.

32 N. Brown, *Bioisosteres Med. Chem.*, 2012, **54**, 1–237.

33 P. Spang, C. Herrmann and F. Roesch, *Semin. Nucl. Med.*, 2016, **46**, 373–394.

34 A. Foster, S. Nigam, D. S. Tatum, I. Raphael, J. Xu, R. Kumar, E. Plakseychuk, J. D. Latoche, S. Vincze, B. Li, R. Giri, L. H. McCarl, R. Edinger, M. Ak, V. Peddagangireddy, L. M. Foley, T. K. Hitchens, R. R. Colen, I. F. Pollack, A. Panigrahy, D. Magda, C. J. Anderson, W. B. Edwards and G. Kohanbash, *EBioMedicine*, 2021, **71**, 103571.

35 G. Luurtsema, V. Pichler, S. Bongarzone, Y. Seimbille, P. Elsinga, A. Gee and J. Vercouillie, *EJNMMI Radiopharm. Chem.*, 2021, **6**, 1–16.

36 R. E. Ehrenkaufer, J. F. Potocki and D. M. Jewett, *J. Nucl. Med.*, 1984, **25**, 333–337.

37 W. R. Dolbier, A. R. Li, C. J. Koch, C. Y. Shiue and A. V. Kachur, *Appl. Radiat. Isot.*, 2001, **54**, 73–80.

38 M. Namavari, A. Bishop, N. Satyamurthy, G. Bida and J. R. Barrio, *Int. J. Radiat. Appl. Instrumentation. Part A. Appl. Radiat. Isot.*, 1992, **43**, 989–996.

39 S. Forsback, O. Eskola, M. Haaparanta, J. Bergman and O. Solin, *Radiochim. Acta*, 2008, **96**, 845–848.

40 G. E. Smith, H. L. Sladen, S. C. G. Biagini and P. J. Blower, *Dalton Trans.*, 2011, 40, 6196–6205.

41 T. Tippayamontri, E. Betancourt-Santander, B. Guérin, R. Lecomte, B. Paquette and L. Sanche, *Front. Nucl. Med.*, 2022, **2**, 815141.

42 P. Saxena, A. K. Singh, M. Dixit, S. C. Kheruka, T. Mahmood and S. Gambhir, *Indian*

J. Nucl. Med., 2021, **36**, 120.

43 L. Cai, S. Lu and V. W. Pike, *European J. Org. Chem.*, 2008, **2008**, 2853–2873.

44 D. W. Kim, D. S. Ahn, Y. H. Oh, S. Lee, H. S. Kil, S. J. Oh, S. J. Lee, J. S. Kim, J. S. Ryu, D. H. Moon and D. Y. Chi, *J. Am. Chem. Soc.*, 2006, **128**, 16394–16397.

45 S. J. Oh, C. Mosdzianowski, D. Y. Chi, J. Y. Kim, S. H. Kang, J. S. Ryu, J. S. Yeo and D. H. Moon, *Nucl. Med. Biol.*, 2004, **31**, 803–809.

46 M. A. Vincent and I. H. Hillier, *Chem. Commun.*, 2005, **0**, 5902–5903.

47 D. Albanese, D. Landini and M. Penso, *J. Org. Chem.*, 1998, **63**, 9587–9589.

48 C. Pascali, S. K. Luthra, V. W. Pike, G. W. Price, R. G. Ahier, S. P. Hume, R. Myers, L. Manjil and J. E. Cremer, *Int. J. Radiat. Appl. Instrumentation. Part A. Appl. Radiat. Isot.*, 1990, **41**, 477–482.

49 F. Dolle, *Curr. Pharm. Des.*, 2005, **11**, 3221–3235.

50 M. Karramkam, F. Hinnen, M. Berrehouma, C. Hlavacek, F. Vaufrey, C. Halldin, J. A. McCarron, V. W. Pike and F. Dollé, *Bioorg. Med. Chem.*, 2003, **11**, 2769–2782.

51 D. E. Olberg, J. M. Arukwe, D. Grace, O. K. Hjelstuen, M. Solbakken, G. M. Kindberg and A. Cuthbertson, *J. Med. Chem.*, 2010, **53**, 1732–1740.

52 A. Knöchel and O. Zwernemann, *Int. J. Radiat. Appl. Instrumentation. Part A. Appl. Radiat. Isot.*, 1991, **42**, 1077–1080.

53 V. G. Vladimir, *Acc. Chem. Res.*, 1992, **25**, 529–536.

54 T. L. Ross, J. Ermert, C. Hocke and H. H. Coenen, *J. Am. Chem. Soc.*, 2007, **129**, 8018–8025.

55 B. C. Lee, C. S. Dence, H. Zhou, E. E. Parent, M. J. Welch and J. A. Katzenellenbogen, *Nucl. Med. Biol.*, 2009, **36**, 147–153.

56 M. Tredwell, S. M. Preshlock, N. J. Taylor, S. Gruber, M. Huiban, J. Passchier, J. Mercier, C. Génicot and V. Gouverneur, *Angew. Chemie Int. Ed.*, 2014, **53**, 7751–7755.

57 A. V. Mossine, A. F. Brooks, K. J. Makaravage, J. M. Miller, N. Ichiishi, M. S. Sanford and P. J. H. Scott, *Org. Lett.*, 2015, **17**, 5780–5783.

58 K. J. Makaravage, A. F. Brooks, A. V. Mossine, M. S. Sanford and P. J. H. Scott, *Org. Lett.*, 2016, **18**, 5440–5443.

59 R. Schirrmacher, B. Wängler, J. Bailey, V. Bernard-Gauthier, E. Schirrmacher and C. Wängler, *Semin. Nucl. Med.*, 2017, **47**, 474–492.

60 V. T. Lien and P. J. Riss, *Biomed Res. Int.*, 2014, 2014, Article ID 380124.

61 S. Comagic, M. Piel, R. Schirrmacher, S. Höhnemann and F. Rösch, *Appl. Radiat. Isot.*, 2002, **56**, 847–851.

62 P. Mäding, F. Füchtner and F. Wüst, *Appl. Radiat. Isot.*, 2005, **63**, 329–332.

63 R. Iwata, C. Pascali, A. Bogni, G. Horvath, Z. Kovács, K. Yanai and T. Ido, *Appl. Radiat. Isot.*, 2000, **52**, 87–92.

64 Y. S. Chang, J. M. Jeong, Y. S. Lee, H. W. Kim, G. B. Rai, S. J. Lee, D. S. Lee, J. K. Chung and M. C. Lee, *Bioconjug. Chem.*, 2005, **16**, 1329–1333.

65 M. Glaser and E. Årstad, *Bioconjug. Chem.*, 2007, **18**, 989–993.

66 Z. Li, H. Cai, M. Hassink, M. L. Blackman, R. C. D. D. Brown, P. S. Conti and J. M. Fox, *Chem. Commun.*, 2010, **46**, 8043–8045.

67 R. Selvaraj, S. Liu, M. Hassink, C. W. Huang, L. P. Yap, R. Park, J. M. Fox, Z. Li and P. S. Conti, *Bioorganic Med. Chem. Lett.*, 2011, **21**, 5011–5014.

68 P. L. Chesis, D. R. Hwang and M. J. Welch, *J. Med. Chem.*, 1990, **33**, 1482–1490.

69 H. C. Kolb, M. G. Finn and B. K. Sharpless, *Angew. Chem. Int. Ed.*, 2001, **40**, 2004–2021.

70 B. L. Oliveira, Z. Guo and G. J. L. Bernardes, *Chem. Soc. Rev.*, 2017, 46, 4895–4950.

71 V. V. Rostovtsev, L. G. Green, V. V. Fokin and K. B. Sharpless, *Angew. Chemie - Int. Ed.*, 2002, **41**, 2596–2599.

72 C. W. Tornøe, C. Christensen and M. Meldal, *J. Org. Chem.*, 2002, **67**, 3057–3064.

73 J. Dommerholt, S. Schmidt, R. Temming, L. J. A. Hendriks, F. P. J. T. Rutjes, J. C. M. Van Hest, D. J. Lefeber, P. Friedl and F. L. Van Delft, *Angew. Chemie Int. Ed.*, 2010, **49**, 9422–9425.

74 R. E. Bird, S. A. Lemmel, X. Yu and Q. A. Zhou, *Bioconjug. Chem.*, 2021, **32**, 2457–2479.

75 E. M. Sletten and C. R. Bertozzi, *Acc. Chem. Res.*, 2011, **44**, 666–676.

76 K. Kettenbach and T. L. Ross, *Medchemcomm*, 2016, **7**, 654–657.

77 R. García-Vázquez, J. T. Jørgensen, K. E. Bratteby, V. Shalgunov, L. Hvass, M. M. Herth, A. Kjær and U. M. Battisti, *Pharmaceuticals*, 2022, **15**, 245.

78 R. García-Vázquez, U. M. Battisti, J. T. Jørgensen, V. Shalgunov, L. Hvass, D. L. Stares, I. N. Petersen, F. Crestey, A. Löffler, D. Svatunek, J. L. Kristensen, H. Mikula, A. Kjaer and M. M. Herth, *Chem. Sci.*, 2021, **12**, 11668–11675.

79 C. A. Maitz, S. Delaney, B. E. Cook, A. R. Genady, R. Hoerres, M. Kuchuk, G. Makris, J. F. Valliant, S. Sadeghi, J. S. Lewis, H. M. Hennkens, J. N. Bryan and B. M. Zeglis, *Mol. Pharm.*, 2022, **19**, 3153–3162.

80 J.-P. Meyer, J. L. Houghton, P. Kozlowski, D. Abdel-Atti, T. Reiner, N. V. K. Pillarsetty, W. W. Scholz, B. M. Zeglis and J. S. Lewis, *Bioconjug. Chem.*, 2016, **27**, 298–301.

81 W. Levason, F. M. Monzittu and G. Reid, *Coord. Chem. Rev.*, 2019, **391**, 90–130.

82 R. Ting, C. Harwig, U. Auf Dem Keller, S. McCormick, P. Austin, C. M. Overall, M. J. Adam, T. J. Ruth and D. M. Perrin, *J. Am. Chem. Soc.*, 2008, **130**, 12045–12055.

83 K. Chansaenpak, M. Wang, Z. Wu, R. Zaman, Z. Li and F. P. Gabbaï, *Chem. Commun.*, 2015, **51**, 12439–12442.

84 K. Chansaenpak, B. Vabre and F. P. Gabbaï, *Chem. Soc. Rev.*, 2016, 45, 954–971.

85 Y. Li, Z. Liu, J. Lozada, M. Q. Wong, K. S. Lin, D. Yapp and D. M. Perrin, *Nucl. Med. Biol.*, 2013, **40**, 959–966.

86 Z. Li, K. Chansaenpak, S. Liu, C. R. Wade, P. S. Conti and F. P. Gabbaï, *Medchemcomm*, 2012, **3**, 1305–1308.

87 P. J. Kocieński, *Protecting Groups*, Thieme Verlag, 2015.

88 R. Schirrmacher, G. Bradtmöller, E. Schirrmacher, O. Thews, J. Tillmanns, T. Siessmeier, H. G. Buchholz, P. Bartenstein, B. Wängler, C. M. Niemeyer and K. Jurkschat, *Angew. Chemie Int. Ed.*, 2006, **45**, 6047–6050.

89 P. Rosa-Neto, B. Wängler, L. Iovkova, G. Boening, A. Reader, K. Jurkschat and E. Schirrmacher, *ChemBioChem*, 2009, **10**, 1321–1324.

90 R. Schirrmacher, V. Bernard-Gauthier, E. Schirrmacher, J. J. Bailey, K. Jurkschat, C. Wängler and B. Wängler, *Fluor. Life Sci. Pharm. Med. Diagnostics, Agrochem. Prog. Fluor. Sci. Ser.*, 2019, 551–574.

91 A. P. Kostikov, J. Chin, K. Orchowski, S. Niedermoser, M. M. Kovacevic, A. Aliaga, K. Jurkschat, B. Wängler, C. Wängler, H. J. Wester and R. Schirrmacher, *Bioconjug.*

Chem., 2012, **23**, 106–114.

92 Q. Zheng, H. Xu, H. Wang, W. G. H. Du, N. Wang, H. Xiong, Y. Gu, L. Noodleman, K. B. Sharpless, G. Yang and P. Wu, *J. Am. Chem. Soc.*, 2021, **143**, 3753.

93 K. R. Scroggie, M. V. Perkins and J. M. Chalker, *Front. Chem.*, 2021, 9, Article 687678.

94 H. Hong, L. Zhang, F. Xie, R. Zhuang, D. Jiang, H. Liu, J. Li, H. Yang, X. Zhang, L. Nie and Z. Li, *Nat. Commun.*, 2019, **10**, Article number 989.

95 R. Bhalla, C. Darby, W. Levason, S. K. Luthra, G. McRobbie, G. Reid, G. Sanderson and W. Zhang, *Chem. Sci.*, 2014, **5**, 381–391.

96 W. Levason, S. K. Luthra, G. McRobbie, F. M. Monzittu and G. Reid, *Dalton Trans.*, 2017, **46**, 14519–14522.

97 F. M. Monzittu, I. Khan, W. Levason, S. K. Luthra, G. McRobbie and G. Reid, *Angew. Chem. Int. Ed.*, 2018, **57**, 6658–6661.

98 J. N. Whetter, B. A. Vaughn, A. J. Koller and E. Boros, *Angew. Chemie Int. Ed.*, 2022, **61**, e202114203.

99 L. Deilami-nezhad, L. Moghaddam-Banaem, M. Sadeghi and M. Asgari, *Appl. Radiat. Isot.*, 2016, **118**, 124–130.

100 J. Maffey-Steffan, L. Scarpa, A. Svirydenka, B. Nilica, C. Mair, S. Buxbaum, J. Bektic, E. von Guggenberg, C. Uprimny, W. Horninger and I. Virgolini, *Eur. J. Nucl. Med. Mol. Imaging*, 2020, **47**, 695–712.

101 S. Schmitt and E. Moreau, *Coord. Chem. Rev.*, 2023, **480**, 215028-215062.

102 W. J. McBride, R. M. Sharkey, H. Karacay, C. A. D'Souza, E. A. Rossi, P. Laverman, C. H. Chang, O. C. Boerman and D. M. Goldenberg, *J. Nucl. Med.*, 2009, **50**, 991–998.

103 S. J. Archibald and L. Allott, *EJNMMI Radiopharm. Chem.*, 2021, **6**, 1–28.

104 C. Fersing, A. Bouhlel, C. Cantelli, P. Garrigue, V. Lisowski and B. Guillet, *Molecules*, 2019, **24**, 2866.

105 S. Ahenkorah, C. Cawthorne, E. Murce, C. M. Deroose, T. Cardinaels, Y. Seimbille, G. Bormans, M. Ooms and F. Cleeren, *Nucl. Med. Biol.*, 2023, 108338.

106 P. Laverman, C. A. D'Souza, A. Eek, W. J. McBride, R. M. Sharkey, W. J. G. Oyen, D. M. Goldenberg and O. C. Boerman, *Tumor Biol.*, 2012, **33**, 427–434.

107 D. Kang, U. Simon, F. M. Mottaghy and A. T. J. Vogg, *Pharmaceuticals*, 2021, **14**, 818.

108 L. Li, W. Zhao, X. Sun, N. Liu, Y. Zhou, X. Luan, S. Gao, S. Zhao, J. Yu and S. Yuan, *Transl. Lung Cancer Res.*, 2020, **9**, 1324–1332.

109 W. Wan, N. Guo, D. Pan, C. Yu, Y. Weng, S. Luo, H. Ding, Y. Xu, L. Wang, L. Lang, Q. Xie, M. Yang and X. Chen, *J. Nucl. Med.*, 2013, **54**, 691–698.

110 W. Cheng, Z. Wu, S. Liang, H. Fu, S. Wu, Y. Tang, Z. Ye and H. Wang, *PLoS One*, 2014, **9**, e100521.

111 T. Long, N. Yang, M. Zhou, D. Chen, Y. Li, J. Li, Y. Tang, Z. Liu, Z. Li and S. Hu, *Clin. Nucl. Med.*, 2019, **44**, 452–458.

112 E. Pauwels, F. Cleeren, T. Tshibangu, M. Koole, K. Serdons, L. Boeckxstaens, J. Dekervel, T. Vandamme, W. Lybaert, B. Van den Broeck, A. Laenen, P. M. Clement, K. Geboes, E. Van Cutsem, S. Stroobants, C. Verslype, G. Bormans and C. M. Deroose, *J. Nucl. Med.*, 2023, **64**, 632–638.

113 E. Pauwels, F. Cleeren, T. Tshibangu, M. Koole, K. Serdons, J. Dekervel, E. Van Cutsem, C. Verslype, K. Van Laere, G. Bormans and C. M. Deroose, *Eur. J. Nucl. Med. Mol. Imaging*, 2020, **47**, 3033–3046.

114 T. Liu, C. Liu, X. Xu, F. Liu, X. Guo, N. Li, X. Wang, J. Yang, X. Yang, H. Zhu and Z. Yang, *J. Nucl. Med.*, 2019, **60**, 1284–1292.

115 X. Jiang, X. Wang, T. Shen, Y. Yao, M. Chen, Z. Li, X. Li, J. Shen, Y. Kou, S. Chen, X. Zhou, Z. Luo and Z. Cheng, *Front. Oncol.*, 2021, **11**, 649148.

116 C. Da Pieve, L. Allott, C. D. Martins, A. Vardon, D. M. Ciobota, G. Kramer-Marek and G. Smith, *Bioconjug. Chem.*, 2016, **27**, 1839–1849.

117 L. Allott, C. Da Pieve, D. R. Turton and G. Smith, *React. Chem. Eng.*, 2017, **2**, 68–74.

118 U. M. Battisti, K. Bratteby, J. T. Jørgensen, L. Hvass, V. Shalgunov, H. Mikula, A. Kjær and M. M. Herth, *J. Med. Chem.*, 2021, **64**, 15297–15312.

119 D. Svatunek, M. Wilkovitsch, L. Hartmann, K. N. Houk and H. Mikula, *J. Am. Chem. Soc.*, 2022, **144**, 8171–8177.

120 F. Cleeren, J. Lecina, M. Ahamed, G. Raes, N. Devoogdt, V. Caveliers, P. McQuade, D. J. Rubins, W. Li, A. Verbruggen, C. Xavier and G. Bormans, *Theranostics*, 2017, **7**, 2924–2939.

121 L. Russelli, J. Martinelli, F. De Rose, S. Reder, M. Herz, M. Schwaiger, W. Weber, L. Tei and C. D'Alessandria, *ChemMedChem*, 2019, cmdc.201900652.

122 R. Gramiak and P. Shah, *Invest. Radiol.*, 1968, **3**, 356–366.

123 S. Sirsi and M. Borden, *Bubble Sci. Eng. Technol.*, 2009, **1**, 3–17.

124 A. Ignee, N. S. S. Atkinson, G. Schuessler and C. F. Dietrich, *Endosc. Ultrasound*, 2016, 5, 355–362.

125 A. Upadhyay and S. V. Dalvi, *Ultrasound Med. Biol.*, 2019, **45**, 301–343.

126 E. Talu, M. M. Lozano, R. L. Powell, P. A. Dayton and M. L. Longo, *Langmuir*, 2006, **22**, 9487-9490.

127 R. E. Pattle, *Nature*, 1955, 175, 1125–1126.

128 M. W. Keller, S. B. Feinstein and D. D. Watson, *Am. Heart J.*, 1987, **114**, 570–575.

129 V. Paefgen, D. Doleschel and F. Kiessling, *Front. Pharmacol.*, 2015, 6.

130 F. Cavalieri, M. Ashokkumar, F. Grieser and F. Caruso, *Langmuir*, 2008, **24**, 10078–10083.

131 A. H. Myrset, H. Nicolaysen, K. Toft, C. Christiansen and T. Skotland, *Biotechnol. Appl. Biochem.*, 1996, **24**, 145–53.

132 M. W. Grinstaff and K. S. Suslick, *Proteinaceous Microspheres,* 1992, pp. 218–226.

133 M. A. Wheatley, B. Schrope and P. Shen, *Biomaterials*, 1990, **11**, 713–717.

134 E. G. Schutt, D. H. Klein, R. M. Mattrey and J. G. Riess, *Angew. Chem. Int. Ed.*, 2003, 42, 3218–3235.

135 T. A. Fritz, E. C. Unger, G. Sutherland and D. Sahn, *Invest. Radiol.*, 1997, **32**, 735–740.

136 F. Cavalieri, A. El Hamassi, E. Chiessi, G. Paradossi, R. Villa and N. Zaffaroni, *Macromol. Symp.*, 2006, **234**, 94–101.

137 F. Cavalieri, A. El Hamassi, E. Chiessi and G. Paradossi, *Langmuir*, 2005, **21**, 8758–8764.

138 R. H. Abou-Saleh, S. A. Peyman, B. R. G. Johnson, G. Marston, N. Ingram, R. Bushby, P. L. Coletta, A. F. Markham and S. D. Evans, *Soft Matter*, 2016, **12**, 7223–7230.

139 K. W. Ferrara, M. A. Borden and H. Zhang, *Acc. Chem. Res.*, 2009, **42**, 881–892.

140 A. Upadhyay, S. V. Dalvi, G. Gupta and N. Khanna, *Mater. Sci. Eng. C*, 2017, **71**, 425–430.

141 I. Lentacker, B. G. De Geest, R. E. Vandenbroucke, L. Peeters, J. Demeester, S. C. De

Smedt and N. N. Sanders, *Langmuir*, 2006, **22**, 7273–8.

142 S. M. Demos, H. Önyüksel, J. Gilbert, S. I. Roth, B. Kane, P. Jungblut, J. V. Pinto, D. D. Mcpherson and M. E. Klegerman, *J. Pharm. Sci.*, 1997, **86**, 167–171.

143 W. H. Wright, T. P. McCreery, E. A. Krupinski, P. J. Lund, S. H. Smyth, M. R. Baker, R. L. Hulett and E. C. Unger, *Acad. Radiol.*, 1998, **5**, Supplement 1, S240-242.

144 A. L. Klibanov, *Adv. Drug Deliv. Rev.*, 1999, 37, 139–157.

145 A. S. Wadajkar, S. Santimano, M. Rahimi, B. Yuan, S. Banerjee and K. T. Nguyen, *Biotechnol. Adv.*, 2013, 31, 504–513.

146 A. L. Klibanov, *J. Cardiovasc. Transl. Res.*, 2013, **6**, 729–739.

147 F. Moccetti, C. C. Weinkauf, B. P. Davidson, J. T. Belcik, E. R. Marinelli, E. Unger and J. R. Lindner, *Ultrasound Med. Biol.*, 2018, **44**, 1155–1163.

148 D. B. Ellegala, H. Leong-Poi, J. E. Carpenter, A. L. Klibanov, S. Kaul, M. E. Shaffrey, J. Sklenar and J. R. Lindner, *Circulation*, 2003, **108**, 336–341.

149 H. Leong-Poi, J. Christiansen, A. L. Klibanov, S. Kaul and J. R. Lindner, *Circulation*, 2003, **107**, 455–460.

150 S. Pochon, I. Tardy, P. Bussat, T. Bettinger, J. Brochot, M. von Wronski, L. Passantino and M. Schneider, *Invest. Radiol.*, 2010, **45**, 89–95.

151 M. Smeenge, F. Tranquart, C. K. Mannaerts, T. M. De Reijke, M. J. Van De Vijver, M. P. Laguna, S. Pochon, J. J. M. C. H. De La Rosette and H. Wijkstra, *Invest. Radiol.*, 2017, **52**, 419–427.

152 J. K. Willmann, L. Bonomo, A. C. Testa, P. Rinaldi, G. Rindi, K. S. Valluru, G. Petrone, M. Martini, A. M. Lutz and S. S. Gambhir, *J. Clin. Oncol.*, 2017, **35**, 2133–2140.

153 M. Ukai, K. Shimizu, K. Uno, M. Mayama, S. Tano, M. Yoshihara, T. Takeda, T. Harata, Y. Kishigami, H. Oguchi, F. Moro, I. De Blasis, B. Virgilio, A. Di Legge, G. Rindi, L. Bonomo, M. Storto and A. C. Testa, *Ultrasound Obstet. Gynecol.*, 2016, **48**, 255–255.

154 P. A. Dijkmans, L. J. M. Juffermans, R. J. P. Musters, A. van Wamel, F. J. ten Cate, W. van Gilst, C. A. Visser, N. de Jong and O. Kamp, *Eur. J. Echocardiogr.*, 2004, 5, 245–256.

155 S. Ibsen, C. E. Schutt and S. Esener, *Drug Des. Devel. Ther.*, 2013, 7, 375–388.

Chapter 2: Development of facile methods to access ^{18}F-labelled microbubbles for cancer imaging

Part of the work in this chapter has been published in:

J. H. Teh, M. Braga, L. Allott, C. Barnes, J. Hernández-Gil, M. X. Tang, E. O. Aboagye and N. J. Long, *Chem. Commun,* 2021, **57**, 11677-11680.

2.1 Introduction to radiolabelled microbubbles

Given the advancement and applications of microbubbles in molecular imaging and drug delivery, the ability to evaluate their whole-body distribution and/or pharmacokinetics could facilitate the development of new microbubble formulations with improved properties.[1] Although the localised nature of ultrasound imaging does not allow this objective to be easily achieved, concurrent use of other imaging modalities could overcome this issue.

In this regard, selection of a complementary imaging modality should account for the short lifetime of microbubbles and low microbubble dose,[2] where the high sensitivity of contrast-enhanced ultrasound allows the detection of individual microbubbles.[3] Since MRI typically requires high contrast agent concentrations (millimolar range for MRI, picomolar range for PET),[4–7] it is not the ideal modality for this purpose. Apart from MRI, CT imaging requires long imaging durations, whereas optical imaging is not suited for *in vivo* imaging due to its limited penetration depth.[5] In comparison, nuclear imaging techniques, such as PET and SPECT offer unlimited depth penetration and high sensitivity for *in vivo* imaging,[8] making them ideal for monitoring the whole body distribution of microbubbles. This is also advantageous compared to traditional biodistribution studies requiring direct tissue sampling, where animals are sacrificed to obtain a distribution at each time point. In comparison, nuclear imaging techniques minimises animal numbers, and allows analysis at a wider range of time points, since animals need only be sacrificed at the end of the entire imaging procedure.

2.1.1 Current radiolabelled microbubble formulations and their biodistribution

Several groups have developed dual modal PET/US or SPECT/US microbubble formulations to quantitatively assess whole-body pharmacokinetics and distribution of microbubbles.[2,9–16] Apart from binding specificity, these studies also provided insight on the elimination pathways of microbubbles. A summary of the key properties of published radiolabelled microbubble studies is given in **Table 2.1**.

Pioneering work in this area was conducted by Walday *et al.* on Albunex microbubbles, where air-filled, human serum albumin- (HSA-) shelled microbubbles were radiolabelled with ^{125}I.[9] Reaction of [^{125}I]NaI and sodium hypochlorite generates [^{125}I]I_2, which reacts with the aromatic residues on albumin. Centrifugation was carried out to separate the ^{125}I-labelled microbubbles (^{125}I-Albunex) from unincorporated radioactivity. *Ex vivo* biodistribution studies showed that less than 20 % of the injected radioactivity remained in circulation after 3 min, and this remained constant for at least 30 min. Notably, the biodistribution of ^{125}I-MBs were significantly different in pigs and rats. At 3 mins, 90 % of the injected dose (%ID) accumulated in the lung in pigs. In comparison, 60 %ID accumulated in the lung in rats. This was attributed mainly to

the presence of pulmonary intravascular macrophages in pigs, which are absent in humans and rats. In the liver, accumulation of radioactivity was primarily attributed to Kupffer cells (liver macrophages). Through precipitation studies with trichloroacetic acid and ^{125}I-labelled native human serum albumin, the authors concluded that the ^{125}I-MBs were cleared mainly as intact microbubbles or microbubble shells, rather than native albumin.

Table 2.1: Key properties of radiolabelled microbubble formulations to-date

Microbubble	Isotope	Radiolabelling strategy	Targeting	*Ex vivo* distribution
^{125}I-Albunex[9] 1994 HSA Air	^{125}I	S_EAr Iodination of aromatic residues [^{125}I]NaI, NaOCl	x	**Rat 3 min** (%ID) Liver – 60 Spleen – 7 Lung – 3
^{123}I-Quantison[10] 1997 HSA Air	^{123}I	S_EAr Iodination of aromatic residues	x	**60 min** (%ID) Liver – 41.8 Spleen – 11 Lung – 4
^{18}F-MBs[11] 2008 Lipid C_4F_{10}	^{18}F	Nucleophilic substitution of lipid with tosylate group	x	**Rat 90 min** (%ID) Liver – 14.3 Spleen – 7.11
^{18}F-tMB[2] 2008 Lipid Perfluorocarbon	^{18}F	[^{18}F]SFB conjugated to biotinylated antibodies. Attachment of antibodies onto streptavidin-bearing MBs	VEGFR2	**Mice 60 min** (% ID/g) Liver – 37.4 Spleen – 19.1 Kidneys – 6.3
^{111}In-MB[17] 2008 Cyanoacrylate Air	^{111}In	Biotin-DTPA conjugate attached onto streptavidin-bearing MBs. Labelling of DTPA-MBs with ^{111}In-oxine	x	**Mice 2 h** (%ID/g) Liver – 16.0 Spleen – 7.8 Lung – 10.6 Kidneys – 7.0
^{99m}Tc-MB[12] 2011 Lipid Perfluorocarbon	^{99m}Tc	^{99m}Tc-labelled biotin conjugate was attached onto streptavidin-bearing MBs	x	**Mice 60 min** (%ID/g) Liver – 93.3 Spleen – 213.4

^{18}F-SFB-tMB[13] 2013 HSA C_3F_8	^{18}F	[^{18}F]SFB conjugated directly onto MBs	VEGFR2	**Mice 60 min** (%ID/g) Liver – 24.1 Lung – 18.6
P-selectin-MB[14] 2014 Lipid C_3F_8	^{99m}Tc	^{99m}Tc-labelled antibodies were attached to streptavidin-bearing MBs	P-selectin	**Mice 60 min** (%ID/g) Liver – 9.2 Lung – 42.4 Spleen – 23.4 Kidneys – 9.1
^{68}Ga-A2B1-MB[15] 2014 Lipid SF_6	^{68}Ga	^{68}Ga-labelled peptide incorporated directly into microbubble shell	Integrin α2β1 (glioma)	**Mice 15 min*** (%ID/g) Liver – 2.37 Kidney – 16.56
^{68}Ga-MBs[16] 2019 Lipid C_4F_{10}	^{68}Ga	^{68}Ga-labelled tetrazine reacted with TCO-functionalised lipid, then incorporated into MBs	x	**Mice 20 min** (%ID/g) Liver – 47 Lung – ca 20 Spleen – 40

*with focused ultrasound

Subsequently, Perkins *et al.* examined the distribution of ^{123}I-labelled Quantison™ microbubbles, which have a similar composition to Albunex with a HSA shell and air core.[10] Expectedly, a similar *ex vivo* distribution was observed for ^{123}I-Quantison compared to ^{125}I-Albunex, where the majority of the radioactive dose accumulated in the liver (41.8 %ID). Notably, high accumulation was also observed in the spleen (11 %ID) compared to other organs (<5 %ID).

The first *in vivo* biodistribution study of microbubbles was reported by Tartis *et al*. in 2008.[11] An ^{18}F-labelled lipid (**[^{18}F]FDP**, **Figure 2.1**) was synthesised by nucleophilic substitution of a tosylated phospholipid. This was then incorporated into the microbubble shell to produce ^{18}F-labelled microbubbles (^{18}F-MBs). The authors noted a systematic difference between the *in vivo* and *ex vivo* values obtained, attributed mainly to fluid loss and attenuation corrections during the acquisition of PET data. Nevertheless, both values concurred that the liver was the organ with the highest radioactive accumulation. One limitation of this study was that **[^{18}F]FDP** was eluted with hexane and dried under a stream of nitrogen. The toxicity of this solvent would necessitate strict quality control measures to ensure its absence in the final

radiopharmaceutical formulation, which presents an obstacle for this method to be implemented for producing clinical-grade ^{18}F-MBs.

In the same year, Willmann *et al*. evaluated the whole-body distribution of ^{18}F-labelled, VEGFR2-targeted microbubbles (^{18}F-tMB).[2] Radiofluorination was achieved by reaction of *N*-succinimidyl-4-[^{18}F]fluorobenzoate (**[^{18}F]SFB**) with lysine residues on anti-VEGFR antibodies. The antibodies were then attached onto microbubbles by streptavidin-biotin interaction. It is worth noting that preliminary studies to directly radiolabel the microbubbles resulted in their degradation. In terms of biodistribution, ^{18}F-tMBs showed highest accumulation in the liver *in vivo* (33.4 %ID/g at 60 min) and fast blood clearance, with 50 % cleared after 3.5 mins. In contrast, radiolabelled anti-VEGFR2 antibodies cleared much slower, with 80 % remaining in the blood after 60 min. The radiolabelled antibodies accumulated mainly in the kidneys (25.4 %ID/g at 60 min), where ^{18}F-tMBs showed low accumulation (7.8 %ID/g at 60 min). Significantly, accumulation of ^{18}F-tMBs in the tumour was higher than adjacent skeletal muscles. However, there were several limitations with this study: (i) radioactive accumulation in the tumour was not compared to non-targeted microbubbles, (ii) a low tumour-to-muscle ratio of 1.6 was obtained, which complicates tumour delineation, and (iii) the use of immunogenic streptavidin-bearing microbubbles precludes translation for human use.

The only study to directly radiolabel microbubbles was reported by Palmowski *et al*.[17] DTPA-bis-biotin was conjugated onto streptavidin-bearing microbubbles. Incorporation of ^{111}In was achieved by incubating the microbubbles with commercially available [^{111}In]In-oxine. Notably, the labelling reaction required incubation over several hours, which meant that it would only be applicable to radioisotopes with long half-lives; and hard, polymer-shelled microbubbles, which are more stable than lipid- or protein-shelled microbubbles. When examined *in vivo*, the ^{111}In-MBs showed fast blood pool clearance, with radioactive blood signal decreasing rapidly to less than 2 % of the maximum level after 1 min. The ^{111}In-MBs also showed early pooling in the lung (12.2 %ID), liver (10.3 %ID) and spleen (5.7 %ID), where radioactivity in the lungs reached a maximum after 5 min, then decreased continually. The authors noted a spike in radioactive blood signal at 60 min, which was attributed to activity being released from the lungs. At 2 h, the highest concentration of radioactivity was found in the liver (16.0 %ID) and spleen (7.8 %ID), which was similar to the distribution of lipid- and protein-shelled microbubbles.

Apart from this, Lazarova *et al.* reported a convenient procedure to radiolabel microbubbles using ^{99m}Tc.[12] To achieve this, $[^{99m}Tc(CO)_3]^+$ was bound using a tridentate dipicolylamine chelator with a biotin arm (**[^{99m}Tc]TcL1**, **Figure 2.1**). This was then attached to streptavidin-bearing microbubbles. The authors reported a facile purification strategy to remove

[^{99m}Tc]TcL1 by using streptavidin-bearing magnetic beads, which could be advantageous compared to centrifugation in terms of reducing radioactive dose during the radiosynthesis. Similar to previous studies, the ^{99m}Tc-MBs showed high accumulation in the liver and spleen (93.3 %ID/g and 213.4 %ID/g respectively at 60 min), and was rapidly cleared from blood stream, with 15.6 %ID/g remaining after 4 min.

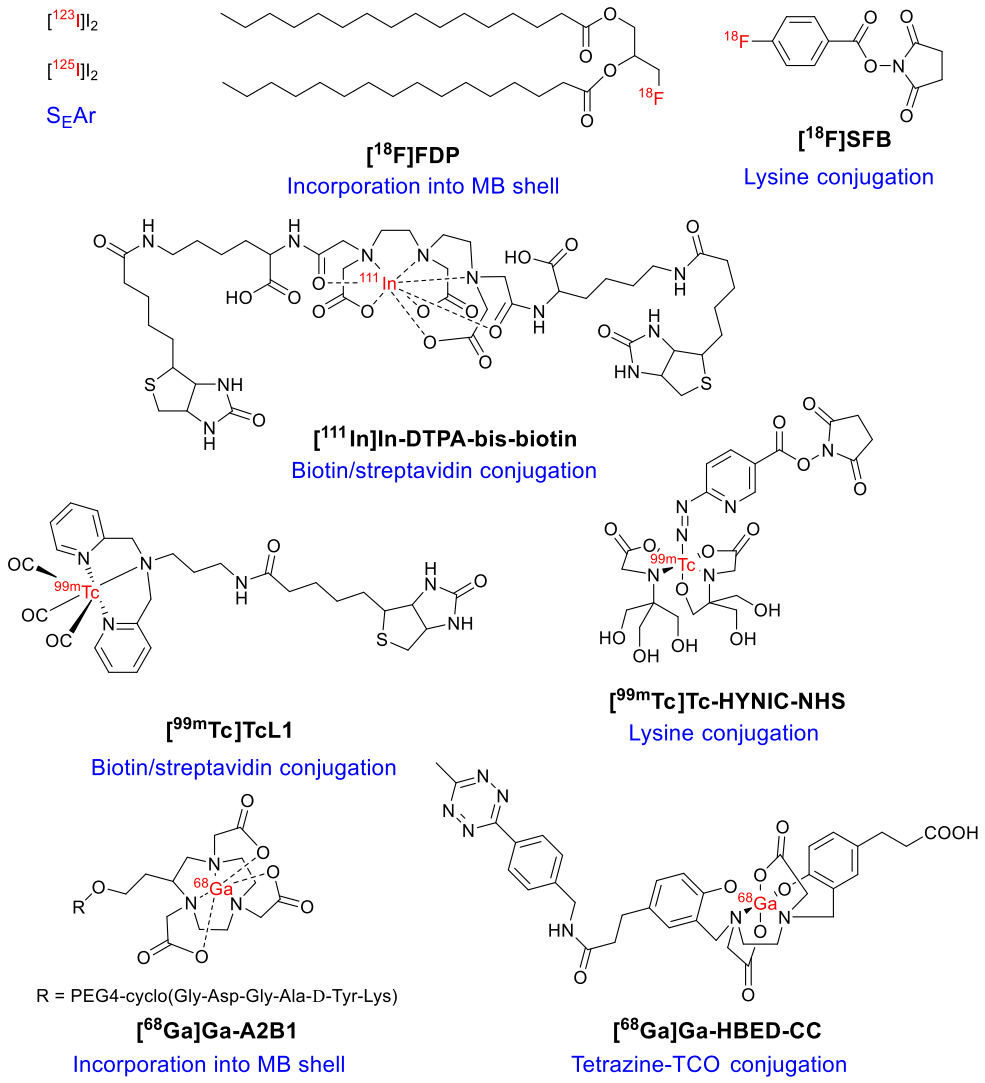

Figure 2.1: Structures of molecules used in microbubble radiolabelling. Radioisotope highlighted in red, conjugation strategy to microbubbles highlighted in blue.

To expand on Willmann *et al.*'s work on radiolabelled, VEGFR2-targeted lipid microbubbles, Liao *et al.* conducted a similar study on albumin-shelled microbubbles.[13] [^{18}F]SFB was conjugated directly onto the microbubble shell to produce non-targeted microbubbles (^{18}F-SFB-MBs) and VEGFR2-targeted microbubbles (^{18}F-SFB-tMBs). A decay-corrected radiochemical yield (RCY) of 35-40 % based on [^{18}F]SFB radioactivity was obtained. Targeting was achieved by attaching anti-VEGFR2 antibodies onto avidin-containing microbubbles. The VEGFR2-targeted ^{18}F-SFB-tMBs showed higher radioactive accumulation in the tumour

(1.01 %ID/g at 60 min) compared to non-targeted ^{18}F-SFB-MBs (0.31 %ID/g), and provided clear delineation of the tumour in the PET image. Blocking studies for ^{18}F-SFB-tMBs by pre-administering the antibody gave a similar accumulation to the non-targeted microbubbles, with 0.23% ID/g recorded in the tumour after 60 min. Notably, ^{18}F-SFB-tMBs and ^{18}F-SFB-MBs had longer blood pool retention than previously reported microbubbles, with a lifetime of 30 min. The authors also reported a higher surface ligand density (15000/μm^2) compared to lipid-shelled microbubbles (6000/μm^2), potentially accounting for the higher tumour-to-muscle ratio of 2.7 compared to 1.6 obtained by Willmann *et al*.

A year later, Warram *et al*. reported P-selectin-targeted microbubbles radiolabelled with ^{99m}Tc.[14] ^{99m}Tc was incorporated using the HYNIC method, and conjugated onto the antibodies by reaction of lysine residues with *N*-hydroxysuccinimide. The radiolabelled antibodies were then attached onto streptavidin-bearing lipid microbubbles. As with previous lipid formulations, P-selectin-MBs showed fast blood pool clearance, with only 3.6 %ID/g remaining at 60 min, and high accumulation in the liver (42.7 %ID/g), lung (42.4 %ID/g) and spleen (23.4 %ID/g). Compared to IgG-control-microbubbles, P-selectin-MBs showed significantly higher accumulation in the tumour (1.3 %ID/g at 5 min, IgG-MB: 0.4 %ID/g). At 60 min, the difference was not significant. However, P-selectin-MBs showed significantly higher tumour uptake compared to adjacent skeletal muscles.

In the same year, Chung *et al*. incorporated a ^{68}Ga-labelled peptide (**^{68}Ga-A2B1**) into SonoVue microbubbles for imaging integrin α2β1.[15] Validation of **^{68}Ga-A2B1** incorporation was done by PD-10 purification, with 80 % activity incorporated. Since the peptide remains buried in the microbubble shell and is unavailable for targeting, secondary targeting was achieved by focused ultrasound (FUS) sonication, where the ^{68}Ga-A2B1-MBs were destructed in the tumour to release the **^{68}Ga-A2B1** peptide. Tumour uptake between three groups were compared at 15 min: **^{68}Ga-A2B1** (1.45 %ID/g), **^{68}Ga-A2B1** + MB + FUS (2.25 %ID/g), and ^{68}Ga-A2B1-MB + FUS (2.6 %ID/g). From these studies, radioactive uptake was highest when the peptide was incorporated into microbubbles and release by insonation, which was attributed to sonoporation and the shorter distance between released **^{68}Ga-A2B1** and integrin receptors, as compared to **^{68}Ga-A2B1** in systemic circulation. The lower uptake of ^{68}Ga-A2B1 was attributed to peptide metabolism, which potentially show that its incorporation into microbubbles might be advantageous. The ^{68}Ga-A2B1-MBs showed low uptake in the liver (2.37 %ID/g), but high uptake in the kidney (16.56 %ID/g), which resembled the distribution of small molecule peptide tracers more than lipid-shelled microbubbles.

More recently, Hernández-Gil *et al.* reported a fast and efficient method to radiolabel microbubbles with ^{68}Ga,[16] based on the inverse-electron-demand Diels-Alder (IEDDA)

reaction between a tetrazine-functionalised chelator and a *trans*-cyclooctene (TCO) functionalised phospholipid. Two chelator-tetrazine conjugates, HBED-CC-tetrazine and DOTA-tetrazine, were evaluated (**Figure 2.1**), with HBED-CC-tetrazine selected due to its ability to label ^{68}Ga at room temperature. This allowed the formation of ^{68}Ga-MBs with 40-50 % RCY in 40-50 min. Direct labelling of chelator-functionalised phospholipids was also attempted. However, purification of the resulting product was non-facile due to phospholipid retention on a range of different solid-phase purification cartridges. *In vivo* imaging of the ^{68}Ga-MBs showed long circulation times, with high accumulation in the liver (47 %ID/g), spleen (40 %ID/g), lung (20 %ID/g) and urine (57 %ID/g) at 20 min post-injection.

Based on the studies reported to-date, several trends could be identified. (i) Incorporation of radioisotopes onto microbubbles have largely been carried out using prosthetic group chemistry, with only one study reporting the direct radiolabelling of microbubbles. This is mainly due to the instability of the microbubbles, which precludes the use of high temperatures, extreme pH, or organic solvents. (ii) Microbubbles accumulate mainly in the liver and spleen. Accumulation in the liver has been attributed to Kupffer cells, whereas accumulation in spleen could be due to the small spleen channel sizes (200-500 nm diameter, *c.f.* microbubbles 1-5 μm diameter) or uptake by splenic macrophages. (iii) Microbubbles usually have a short circulation time *in vivo*, often cleared within 20 min.[18–20] (iv) The incorporation of targeting ligands can increase the radioactive accumulation of microbubbles at tumours, relative to non-targeted microbubbles.

Although these studies have significantly improved our understanding on the pharmacokinetics and biodistribution of microbubbles, two main limitations remain. (i) Radioisotope incorporation often involves the use of streptavidin/biotin conjugation. Whilst this method is useful in preclinical studies, the immunogenicity of streptavidin limits translation for human use. (ii) Published radiolabelling procedures are often multi-step, and require expertise in radiochemical synthesis, which present an obstacle for their routine use to study new microbubble formulations. Thus, the development of a convenient method to access radiolabelled microbubbles without the use of streptavidin/biotin interactions could facilitate the study of new microbubble formulations in humans. This forms the basis of the aims of this chapter, which are outlined in the next section.

2.1.2 Aims and objectives

The primary aim of this chapter is to develop a facile method to access ^{18}F-labelled microbubbles that is amenable to clinical translation. We envisioned that this could be achieved using the aluminium-[^{18}F]fluoride ([^{18}F]AlF) radiolabelling method and the highly efficient IEDDA reaction. A schematic representation is given in **Figure 2.2**.

To achieve this, the following objectives were identified:

A. Production and characterisation of TCO-functionalised microbubbles (TCO-MB)
B. Synthesis of an [^{18}F]AlF-labelled tetrazine ([^{18}F]AlF-Tz)
C. Production of [^{18}F]AlF-labelled microbubbles ([^{18}F]AlF-MB) through IEDDA reaction

To demonstrate the advantages of the [^{18}F]AlF methodology, comparison to an alternative ^{18}F-labelled tetrazine, [^{18}F]FBox-Tz, was also undertaken. Such a study provides a complementary method to access ^{18}F-labelled microbubbles and proves that TCO-MB could be conjugated to tetrazines bearing other functionalities.

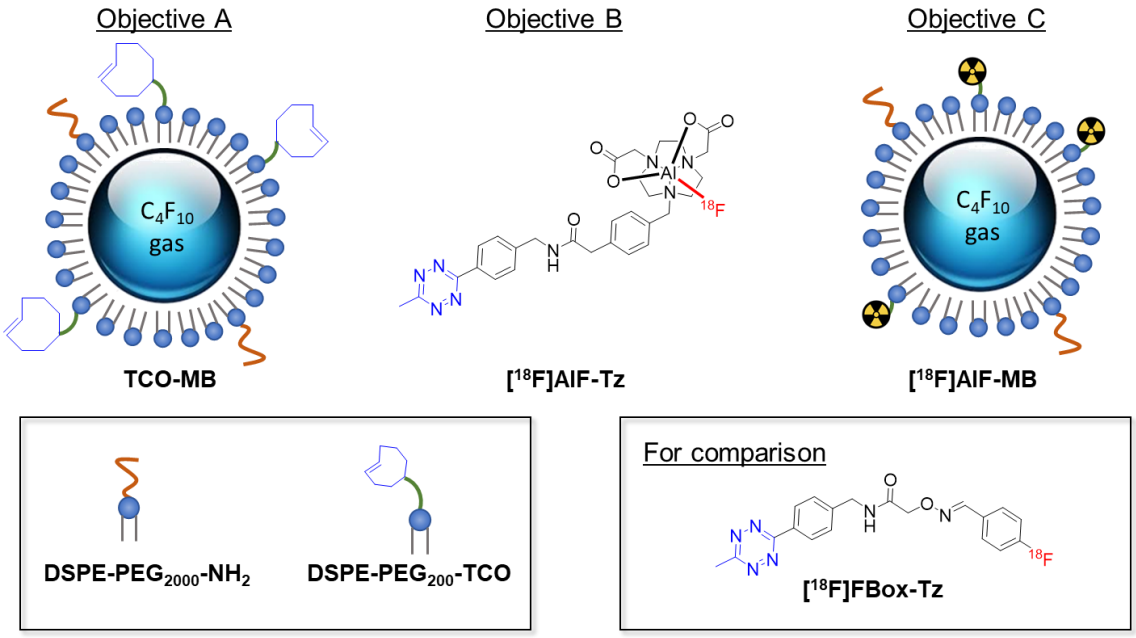

Figure 2.2: Schematic representation of ^{18}F-labelling of microbubbles based on the objectives identified.

Once the microbubbles were radiolabelled, incorporation of a targeting vector was examined to determine if the [^{18}F]AlF-labelled microbubbles could be used for molecular imaging. Specifically, the feasibility of incorporating a T140 peptide into the microbubbles to enable CXCR4 targeting was examined. Subsequently, the binding capability of the T140-functionalised microbubbles *in vitro* was evaluated.

2.2 Production and characterisation of TCO-MB

In this project, lipid-shelled microbubbles were evaluated because their high versatility and widespread use.[16,21,22] A modified formulation based on those reported by Hernández-Gil *et al*.[16] and Braga *et al.*[23] was developed, in which the positively charged dipalmitoyl phosphatidylcholine (DPPC) forms the majority of the microbubble shell. A small amount of negatively charged dipalmitoyl phosphate (DPPA) was also added, since this has been shown to form stable CXCR4-targeting microbubbles by Braga *et al*.[23] Both DPPC and DPPA are biocompatible surfactants which are widely used in liposomes for drug delivery.[24] A small amount of DSPE-PEG_{2000}-NH_2 was also added to increase the stability of the microbubbles, since the inclusion of long polyethylene glycol (PEG) brush layers reduce microbubble coalescence and increases circulation time.[25] A *trans*-cyclooctene-functionalised lipid (DSPE-PEG_{200}-TCO) was synthesised as reported previously,[16] and incorporated into the microbubble shell.

With a lipid composition of 75:10:10:5 mol% DPPC:DPPA:DSPE-PEG_{200}-TCO:DSPE-PEG_{2000}-NH_2, TCO-MB was produced with a concentration of (4.32 ± 0.90) × 10^8 microbubbles per mL (MB/mL) and a mean diameter of 1.98 ± 1.55 µm. The zeta potential of the microbubbles was determined to be (+8.0 ± 0.5) mV, slightly lower than that reported by Hernández-Gil *et al.* (+12.4 ± 1.1 mV).[16] This was reasonable, since their formulation did not include the negatively charged DPPA. The size distribution and summarised characterisation data of TCO-MB are shown in **Figure 2.3**.

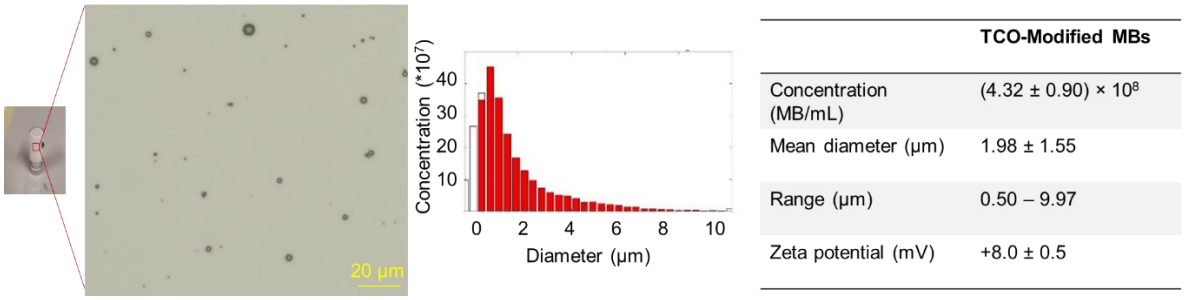

	TCO-Modified MBs
Concentration (MB/mL)	(4.32 ± 0.90) × 10^8
Mean diameter (µm)	1.98 ± 1.55
Range (µm)	0.50 – 9.97
Zeta potential (mV)	+8.0 ± 0.5

Figure 2.3: Left: optical microscopy image of TCO-MBs. Middle: size distribution of microbubbles. Right: characterisation data of TCO-MBs.

With the successful production of TCO-MB, the next objective was the synthesis of an [^{18}F]AlF-labelled tetrazine for conjugation.

2.3 Synthesis of [^{18}F]AlF-Tz

Since the pentadentate 1,4,7-triazacyclononane-1,4-diacetate (NODA) chelator enables high labelling efficiency and forms stable [^{18}F]AlF complexes,[26,27] a tetrazine-NODA conjugate (NODA-MPAA-Tz) was designed based on the bifunctional chelator reported by McBride *et al.*[27] NODA was chosen instead of 1,4,7-triazacyclononane-1,4,7-triacetate (NOTA) because the additional carbonyl arm on NOTA could interfere with $^{18}F^-$ binding to aluminium,[26] since the Al^{3+} ion will be saturated by a coordination number of 6.

2.3.1 Chemical synthesis of NODA-MPAA-Tz

The synthesis of NODA-MPAA-Tz is outlined in **Scheme 2.1**. NODA^{t}Bu-MPAA was synthesised using a modified procedure from that reported by McBride *et al.*[27] In their synthesis, NODA^{t}Bu was added dropwise to a solution of 4-(bromomethyl)phenylacetic acid. Attempted purification by reverse-phase flash chromatography proved challenging, where analysis by liquid chromatography-mass spectrometry (LC-MS) indicated the presence of an over-alkylated product (**Figure 2.4**, t_R = 10.69 min), presumably formed due to the addition of NODA^{t}Bu to an excess of 4-(bromomethyl)phenyl acetic acid. Changing the order of addition of reagents circumvented this problem, resulting in the formation of NODA^{t}Bu-MPAA in 39% yield following purification.

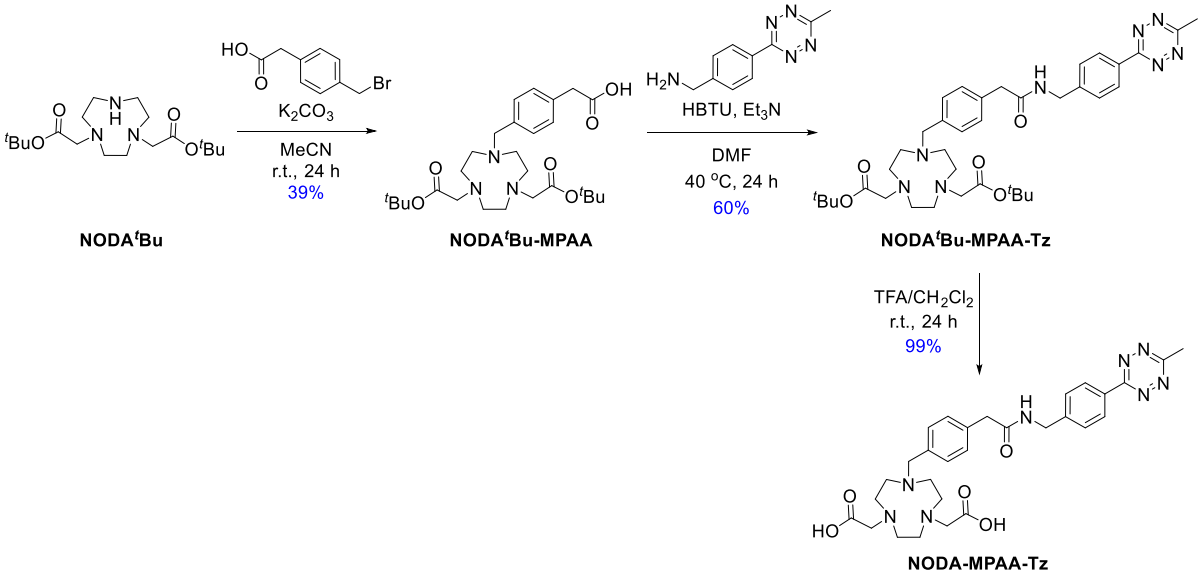

Scheme 2.1: Synthetic route for NODA-MPAA-Tz.

With HBTU as a coupling agent, amide coupling was then carried out to form NODA^{t}Bu-MPAA-Tz in 60 % yield. Deprotection by trifluoroacetic acid then revealed the carboxylate arms to give NODA-MPAA-Tz in quantitative yield, which was subsequently radiolabelled with [^{18}F]AlF.

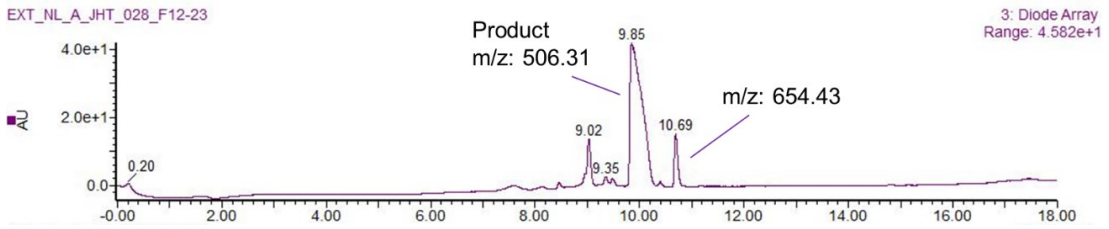

Figure 2.4: UV absorbance chromatogram from LC-MS analysis of purified NODA^{t}Bu-MPAA, showing the presence of an over-alkylated product (m/z: 654.43, t_R =10.69 min).

To reduce the tetrazine-TCO conjugation time, synthesis of a more reactive tetrazine **2.4** was attempted, where the 6-Me group is replaced with a hydrogen atom (**Scheme 2.2**). Monosubstituted tetrazines have been shown to be more reactive than disubstituted tetrazines due to additional distortion energies of the substituents.[28] Compared to Me-tetrazines, H-tetrazines are also more reactive due to electronic effects.[28,29]

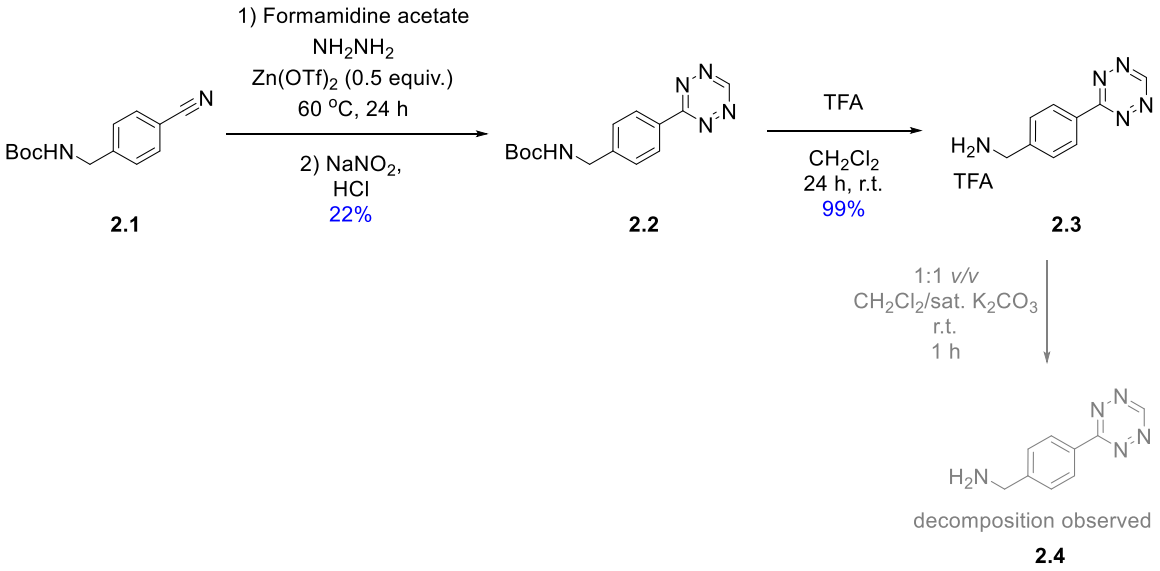

Scheme 2.2: Attempted synthesis of monosubstituted tetrazine **2.4**.

During the synthesis,[30] it was found that **2.3** decomposes upon desalting with saturated K_2CO_3. Visibly, the reaction turned from pink to black within minutes, and analysis by ^{1}H NMR spectroscopy also revealed the presence of multiple additional peaks (**Figure 2.5**:, bottom). This decomposition is likely due to the nucleophilic attack of a hydroxide ion on the tetrazine ring,[31] where mass fragments of the possible decomposition products are shown in **Figure 2.5**.

Since tetrazines have been shown to be susceptible to nucleophilic attack,[32] and have limited stability in basic or aqueous media,[33,34] further attempts to synthesise the monosubstituted tetrazine were not made, since labelling by [^{18}F]AlF involves relatively harsh conditions (>100 °C heating under aqueous conditions).

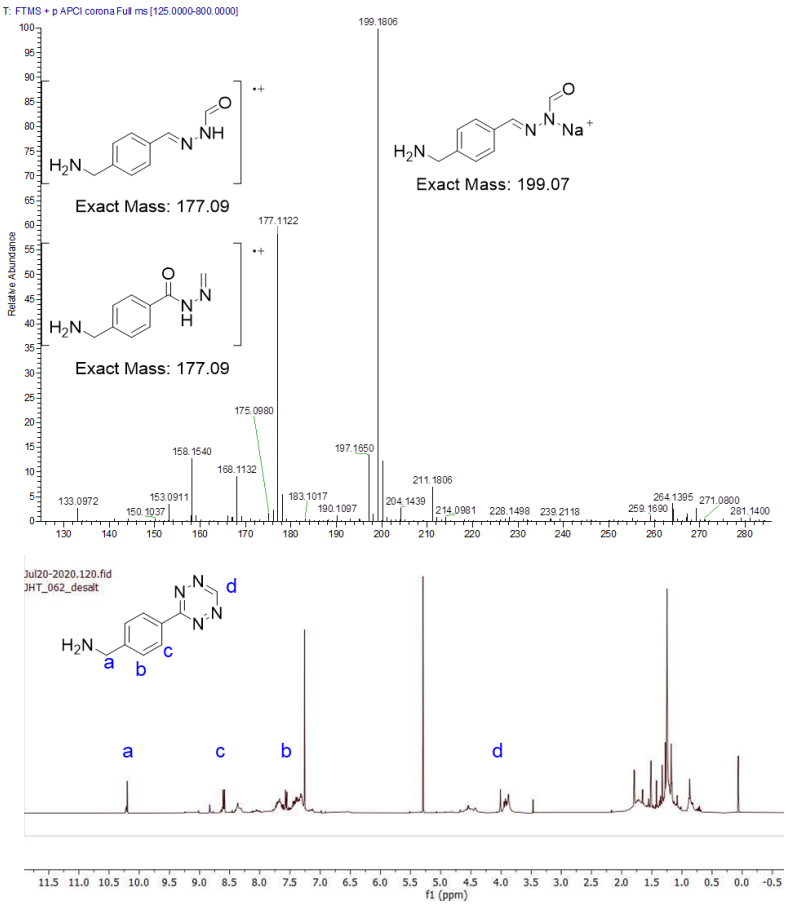

Figure 2.5: Top: Mass spectrum of **2.3** upon desalting with K_2CO_3, showing possible decomposition products. Bottom: ^{1}H NMR spectrum of **2.3** after desalting in $CDCl_3$ at r.t.

Additionally, reaction of the disubstituted tetrazine with TCO has been shown to have fast reaction kinetics,[29] with 80-85 % conversion observed after 15 min.[16] Thus, NODA-MPAA-Tz was carried forward for [^{18}F]AlF-labelling.

2.3.2 Optimisation of [^{18}F]AlF-Tz radiosynthesis

[^{18}F]AlF-labelling of NODA-MPAA-Tz was initially attempted using conditions shown in **Scheme 2.3**, similar to that used by Da Pieve *et al*. to radiolabel a NODA-tetrazine conjugate.[35] Since 100 nmol of DSPE-PEG$_{200}$-TCO was used to form the TCO-MBs, the same amount of NODA-MPAA-Tz was used in the radiosynthesis of [^{18}F]AlF-Tz. This was slightly more than the amount of chelator Da Pieve *et al*. used (28 nmol), which should ideally result in a higher radiochemical conversion (RCC).

Under these conditions, a 62 % RCC was obtained (estimated by radio-HPLC, **Figure 2.6A**). This was slightly lower than that obtained by Da Pieve *et al*. (70-95 %) and could likely be attributed to the difference in purity of the [^{18}F]NaF solutions used. Since non-purified [^{18}F]NaF from cyclotrons was used in both cases, presence of trace metal impurities could affect the

reaction yields,[27,36,37] which possibly explains the somewhat large variation in RCC (70-95 %) obtained by Da Pieve *et al*. Thus, [^{18}F]NaF was purified using a quaternary methyl ammonium (QMA) solid-phase extraction (SPE) cartridge in all experiments to remove unwanted metal impurities and ensure that the final reaction mixture will have a pH range within 4.0-5.0, which improved RCC to 75 %.[37–39] Subsequent purification [^{18}F]AlF-Tz was facile, which only required trapping and elution with an Oasis® HLB cartridge, since $^{18}F^-$ and/or [^{18}F]AlF^{2+} was the only major impurity.

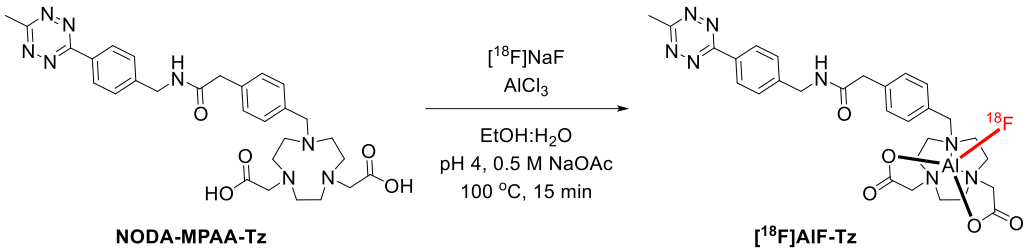

Scheme 2.3: [^{18}F]AlF-labelling of NODA-MPAA-Tz.

Notably, in the radio-HPLC chromatograms, the presence of a small peak is detected before the peak corresponding to [^{18}F]AlF-Tz. When [^{18}F]AlF-Tz was left to stand in EtOH after purification, it was found that this peak increases at a rate of 3-5 % per hour, and thus could be attributed to the decomposition of [^{18}F]AlF-Tz. This has been observed for similar [^{18}F]AlF-labelled tetrazine conjugates,[35,36] where the decomposed product has been shown to not react with TCO. Therefore, it is likely that the tetrazine moiety is degrading. Nevertheless, the effect of this decomposition can be minimised if the tetrazine-TCO conjugation is carried out immediately after isolation of [^{18}F]AlF-Tz.

Since [^{18}F]AlF-labelling with NODA chelators has been shown to give radiochemical yields (RCYs) of >90 %,[27,35] optimisation of the radiosynthesis of [^{18}F]AlF-Tz was conducted. Varying the organic co-solvent and reaction time was first attempted (**Table 2.2**). It was found that a polar aprotic organic co-solvent offered improved yields, as shown by MeCN, DMSO and DMF (Entries 3-5) giving higher yields than MeOH and EtOH (Entries 1-2). Of these, MeCN was used in further reactions since it afforded the best yield. Using MeCN as a co-solvent also slightly reduced the decomposition of [^{18}F]AlF-Tz when compared to EtOH (**Figure 2.6D**). Optimisation of reaction time (Entries 6-9) showed that the reaction was completed in 20 min. An alternative method used by Cleeren *et al*.,[38] where the formation of an [^{18}F]AlF^{2+} complex was carried out prior to addition of the chelator, was attempted, but no further improvement in RCC was observed.

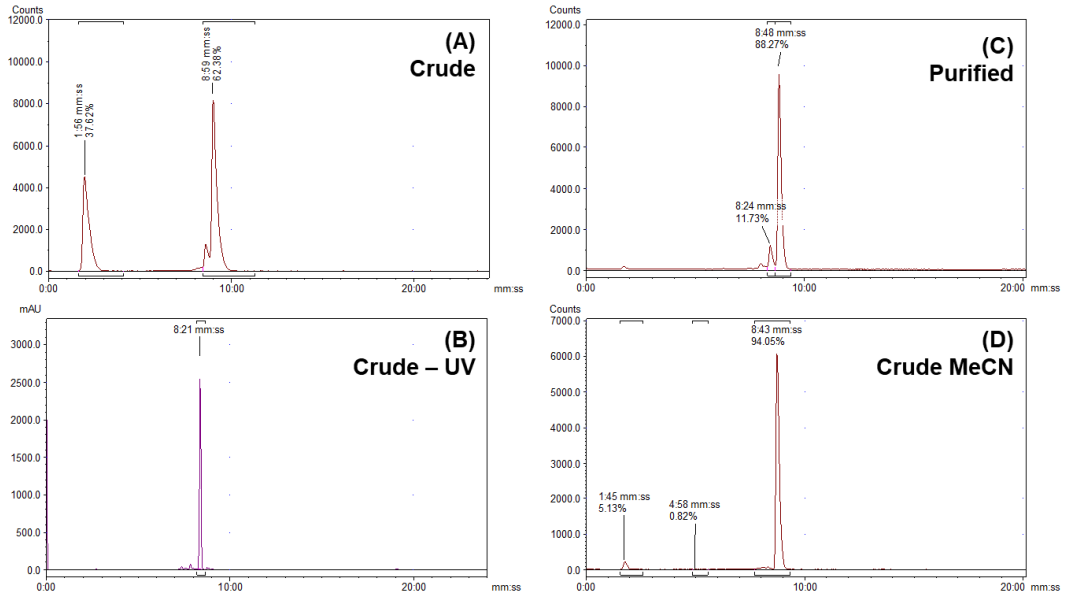

Figure 2.6: (A) radio-HPLC chromatogram of crude [^{18}F]AlF-Tz. (B) UV-HPLC chromatogram of NODA-MPAA-Tz as reference. (C) radio-HPLC chromatogram of purified [^{18}F]AlF-Tz. (D) radio-HPLC chromatogram of crude reaction with MeCN as co-solvent instead of EtOH. UV peak is expected at a slightly earlier retention time than the radio peak due to detector set-up.

Table 2.2: Optimisation of radiolabelling conditions for [^{18}F]AlF-Tz. [a] Determined by radio-HPLC. Reactions were carried out with an Aq:Org ratio of 1:1 at 100 °C.

Entry	Organic co-solvent	Reaction time (min)	RCC (%)[a]
1	EtOH	15	75
2	MeOH	15	73
3	MeCN	15	90
4	DMSO	15	88
5	DMF	15	88
6	MeCN	10	80
7	MeCN	15	93
8	MeCN	20	>95
9	MeCN	25	>95
10	MeCN ([AlF]$^{2+}$ method)	15	90

Next, the ratio of the aqueous to organic solvents was optimised (**Table 2.3**). Increasing the amount of organic co-solvent resulted in an increased RCC, in agreement with the results obtained by McBride *et al*.[27] This was attributed to the increased solubility of the reactants in the presence of the organic co-solvent.

Table 2.3: Optimisation of ratio of aqueous to organic solvent. [a] Determined by radio-HPLC

Entry	Aq:Org ratio	Reaction time (min)	RCC (%)[a]
1	3:2	15	81
2	1:1	15	82
3	2:3	15	87
4	2:3	20	>95

With the optimised conditions, the efficiency of radiolabelling at different precursor amounts was investigated (**Table 2.4**). As expected, RCC decreases with decreasing precursor amount, which is commonly observed in radiometal-based labelling.[40,41] The RCCs obtained were in agreement to reported RCYs conducted at similar reaction concentrations (20-50 μM).[27,35]

Table 2.4: Investigation of radiolabelling efficiency at different precursor amounts. Figure plots the increase in RCC with increasing precursor amounts. [a] Determined by radio-HPLC

Precursor amount (nmol)	RCC (%)[a]
20	69
50	86
75	92
100	95

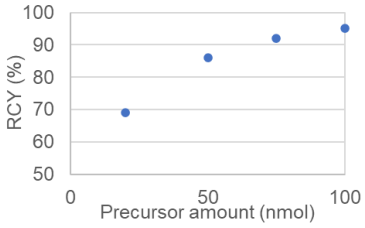

With the optimised conditions (**Scheme 2.4**), [^{18}F]AlF-Tz could be isolated with a radiochemical yield of 91 ± 2 % in 30-35 min, with an apparent molar activity (A_m) of 2.4 ± 2 MBq/nmol. Although this is slightly lower than that of reported [^{18}F]AlF-labelled molecules (7.4-28.5 MBq/nmol),[35,36,42] optimisation of A_m of [^{18}F]AlF-Tz was not essential since it is not conjugated to a receptor-targeted biomolecule.

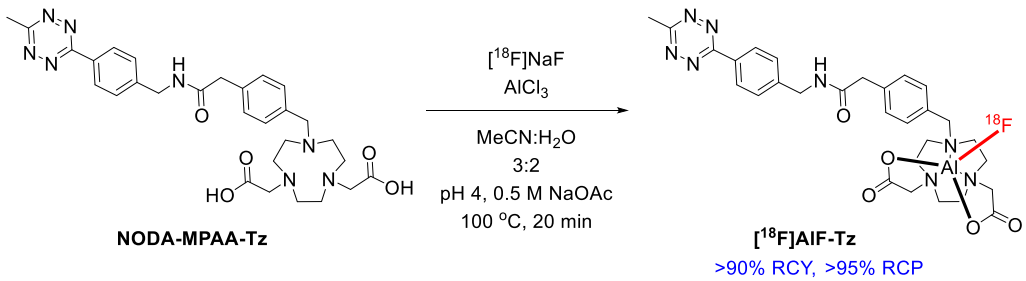

Scheme 2.4: Optimised conditions for [^{18}F]AlF-labelling of NODA-MPAA-Tz

2.4 Development of a kit-based approach to aluminium-[^{18}F]fluoride-labelled microbubbles

2.4.1 Manual approach

The initial approach to produce [^{18}F]AlF-MBs was based on the Hernandez *et al.*'s previous method to produce ^{68}Ga-MBs.[16] In brief, three steps were involved (**Figure 2.7**): (A) synthesis of [^{18}F]AlF-Tz, (B) conjugation of [^{18}F]AlF-Tz to DSPE-PEG$_{200}$-TCO to obtained a ^{18}F-labelled lipid ([^{18}F]AlF-lipid), and (C) incorporation of [^{18}F]AlF-lipid to form microbubbles.

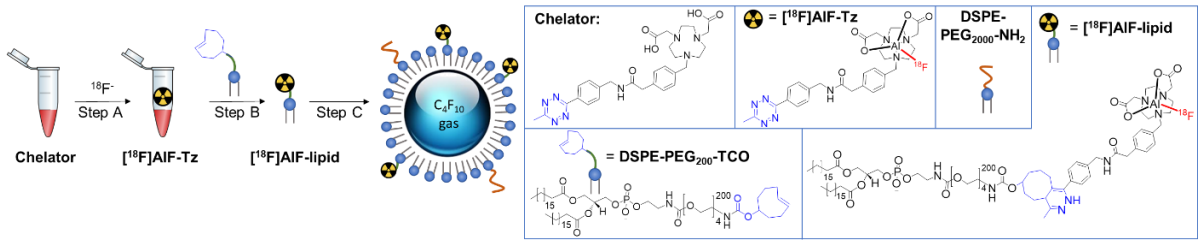

Figure 2.7: Graphical representation of manual approach used to obtain [^{18}F]AlF-MBs. Step A: Radiosynthesis of [^{18}F]AlF-Tz (>90 % RCY, RCP); step B: IEDDA reaction of [^{18}F]AlF-Tz with DSPE-PEG$_{200}$-TCO (40-50 % RCC); step C: Formation of [^{18}F]AlF-MBs (40-50 % RCY). Image reproduced from *Chem. Commun.,* **2021**, 57, 11677 with permission from the Royal Society of Chemistry.

To obtain [^{18}F]AlF-lipid, direct [^{18}F]AlF-labelling of lipids functionalised by a NOTA-chelator was not attempted, since phospholipids have been shown to undergo hydrolysis under acidic conditions.[43] Schnorenberg *et al.* showed that this occurs at 60 °C, which was significantly lower than the 100-105 °C required for [^{18}F]AlF-labelling of NOTA-derived chelators. Furthermore, Hernandez *et al*. showed that ^{68}Ga-labelled lipids were irreversibly retained on a range of different solid-phase extraction cartridges, which makes their purification challenging.[16]

Radio-HPLC and radio-TLC were used to analyse the efficiency of conversion of [^{18}F]AlF-Tz to [^{18}F]AlF-lipid *via* the IEDDA reaction (**Figure 2.8**). Chromatograms of pure [^{18}F]AlF-Tz were first recorded as controls. For analysis by radio-TLC, with the eluent tested (1:1 *v:v* MeOH: 2 M NH_4OAc), [^{18}F]AlF-Tz travels to the solvent front, whereas [^{18}F]AlF-lipid remains on the baseline. Different HPLC column and eluents were required compared to those used when characterising [^{18}F]AlF-Tz, because the hydrophobic [^{18}F]AlF-lipid was being retained on the C18 column. To address this, an Aeris C4 200 Å column was used in combination with a mobile phase containing a higher ratio of organic solvent. To further assist with the elution of [^{18}F]AlF-lipid, sodium dodecyl sulfate (SDS) was also added to the mobile phase.[44] SDS is the most commonly used surfactant in micellar liquid chromatography (MLC),[44] and possibly

improves the elution of [^{18}F]AlF-lipid by two mechanisms: (i) SDS adsorbs onto the alkyl chain of the C4 stationary phase, reducing the hydrophobic interaction of [^{18}F]AlF-lipid with the stationary phase; or (ii) SDS forms micelles with [^{18}F]AlF-lipid, encapsulating the C18 alkyl chain of [^{18}F]AlF-lipid. Using these conditions, it was possible to confirm the formation of [^{18}F]AlF-lipid, which eluted with longer retention time (t_R = 7:35 min:s) compared to [^{18}F]AlF-Tz (t_R = 1:29).

Reaction of [^{18}F]AlF-Tz with an equimolar amount of DSPE-PEG$_{200}$-TCO resulted in a 40-50% conversion after 20 min at 60 °C. This was lower than that obtained by Hernandez *et al*., where 80-85% conversion was achieved when a ^{68}Ga-labelled tetrazine was reacted with DSPE-PEG$_{200}$-TCO.[16] One possible reason is the degradation of the TCO functional group in DSPE-PEG$_{200}$-TCO, or its isomerisation to *cis*-cyclooctene (CCO), due to exposure to light during the handling of the compound.[45,46] This was confirmed when reaction with a freshly prepared batch of DSPE-PEG$_{200}$-TCO resulted in a 75-80 % conversion when analysed by radio-TLC. To maximise radioactive concentration, the reaction mixture was heated at 60 °C unsealed to allow evaporation of ethanol.

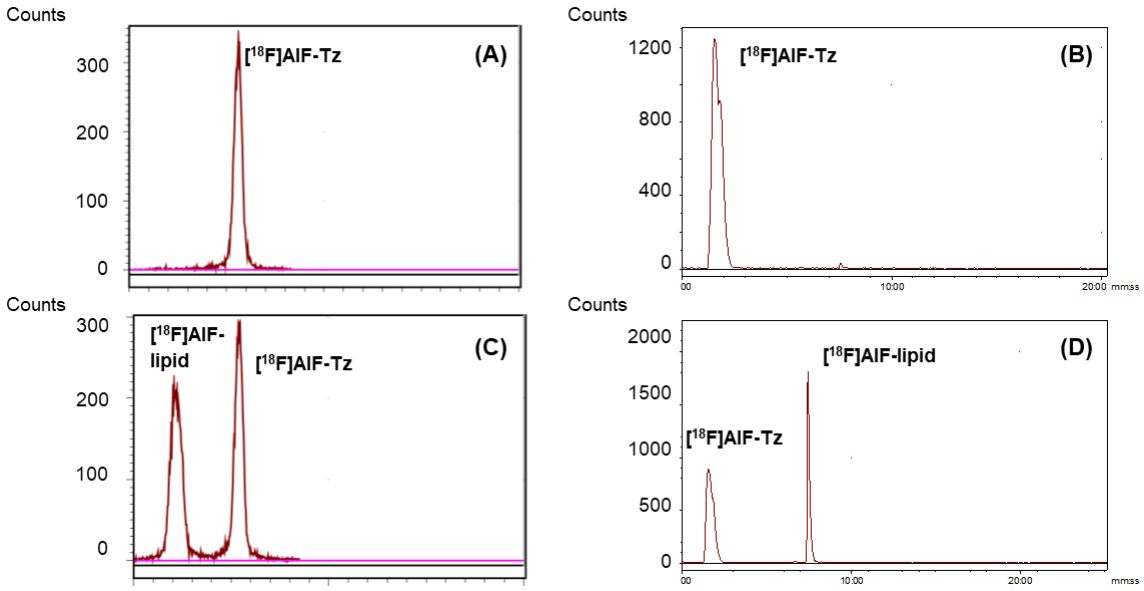

Figure 2.8: Radio-TLC and radio-HPLC chromatograms of reaction between [^{18}F]AlF-Tz and DSPE-PEG$_{200}$-TCO to form [^{18}F]AlF-lipid. (A) radio-TLC chromatogram of pure [^{18}F]AlF-Tz. (B) radio-HPLC chromatogram of pure [^{18}F]AlF-Tz (t_R = 1:29 min:s). (C) radio-TLC chromatogram of reaction showing formation of [^{18}F]AlF-lipid at baseline. (D) radio-HPLC chromatogram of reaction showing formation of [^{18}F]AlF-lipid (t_R = 7:35 min:s).

Upon synthesis of [^{18}F]AlF-lipid, its incorporation into microbubbles was evaluated. An aliquot of [^{18}F]AlF-lipid (70-100 MBq, 100 µL) in ethanol was mixed with DPPC, DPPA and DSPE-PEG$_{2000}$-NH$_2$, and activated to form microbubbles. Successful microbubble production was

indicated by the formation of a homogeneous white suspension (**Figure 2.9A**). Since the gas-filled microbubbles are less dense than water, unreacted [^{18}F]AlF-Tz and unincorporated [^{18}F]AlF-lipid could be removed by centrifugation. After centrifuging, microbubbles were collected near the top of the vial as a concentrated layer of white foam, whereas unincorporated [^{18}F]AlF-Tz, [^{18}F]AlF-lipid, and non-radioactive lipids remained in the infranatant. Incorporation of [^{18}F]AlF-lipid into microbubbles could be inferred from radio-HPLC and radio-TLC analysis of the infranatant (**Figure 2.9C** and **D**), which showed a decreased amount of [^{18}F]AlF-lipid compared to [^{18}F]AlF-Tz, when compared to before microbubble formation. Further confirmation of successful ^{18}F-labelling of microbubbles was obtained during the centrifugal purification process. This was done by comparing the activity of the microbubble foam layer to that of the infranatant from each successive centrifugal wash (**Figure 2.9B**). After the third wash, the microbubbles accounted for almost all (>95%) of the remaining activity in the vial, showing incorporation of the ^{18}F isotope onto the microbubbles.

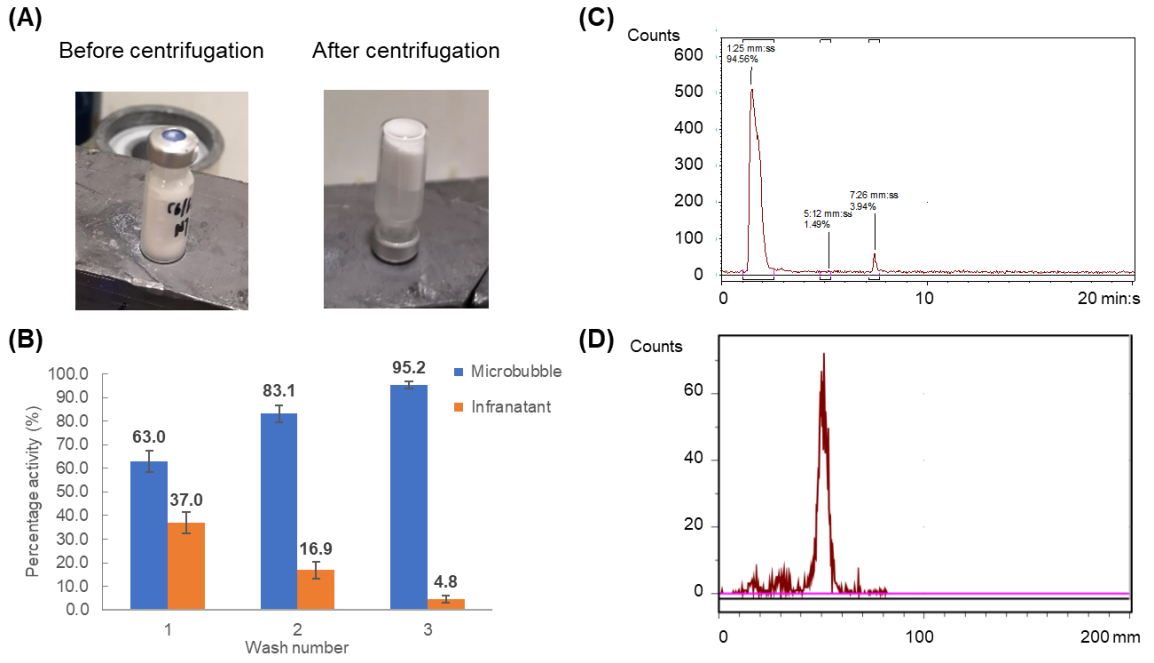

Figure 2.9: Analysis of [^{18}F]AlF-MBs after purification. (A) Image of microbubbles before and after centrifugation, where microbubbles are collected as a layer of foam at the top of the vial after centrifugation. (B) Comparison of percentage activities of microbubble foam layer against infranatant after each successive centrifuge wash. (C) radio-HPLC and (D) radio-TLC chromatograms of infranatant after 1st centrifuge wash, both showing decreased amount of [^{18}F]AlF-lipid upon its incorporation into microbubbles. Values presented as mean ± SD.

Finally, to prove that the radioactivity of [^{18}F]AlF-MBs was due to the incorporation of [^{18}F]AlF-lipid instead of [^{18}F]AlF-Tz, the microbubbles were dissolved in methanol and analysed by radio-HPLC. Gratifyingly, only [^{18}F]AlF-lipid was detected in the resulting chromatogram

(**Figure 2.10**). Using this production method, [^{18}F]AlF-MBs were generated in good RCY (31 ± 5 %, decay-corrected to the start of synthesis), and concentrations of (4.32 ± 0.9) × 10^8 microbubbles per mL (MB/mL). The production process required 60-70 min, resulting in 48 ± 12 MBq of [^{18}F]AlF-MBs.

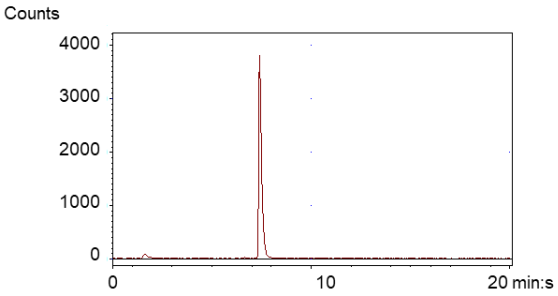

Figure 2.10: Radio-HPLC chromatogram of [^{18}F]AlF-MBs dissolved in MeOH, showing only [^{18}F]AlF-lipid.

2.4.2 Semi-automated approach

To facilitate the safe production of larger radioactive doses of [^{18}F]AlF-Tz and reduce unnecessary exposure to radioactivity, the synthesis of [^{18}F]AlF-Tz was automated using the GE FASTLab™ platform.[36] In addition, automated radiochemistry also enables higher batch reproducibility and compliance to good manufacturing practices (GMP) production. The automated sequence for producing [^{18}F]AlF-Tz is outlined in **Figure 2.11**.

High RCYs for [^{18}F]AlF-labelling are typically achieved with low reaction volumes to maximise chelator concentration.[35] However, the GE-FASTlab™ platform is a cassette-based platform assembled around a fixed reactor vessel, where components are fixed at pre-defined locations, making it less suitable for small volume manipulations.[36] To address this, the reaction components (NODA-MPAA-Tz, $AlCl_3$ and MeCN) were pre-mixed in the reactor vessel prior to the radiosynthesis. A larger amount of NODA-MPAA-Tz was also used to account for the larger reaction volume.

Initially, the elution of [^{18}F]fluoride from the QMA cartridge into the reactor vessel was carried out using 3 M NaOAc. However, this resulted in low RCYs (34 ± 4 %) and RCPs (75 ± 3 %). Since it has been reported that low acetate ion concentration increases radiolabelling yields,[47] the eluent for [^{18}F]fluoride was replaced with 0.9 % NaCl. To facilitate better mixing, nitrogen was also bubbled through the reaction solution after addition [^{18}F]fluoride into the reactor vessel. These resulted in improved automated radiosynthesis, generating 507 ± 40 MBq of [^{18}F]AlF-Tz in 63 ± 3 % RCY within 45-50 min. The results obtained were consistent with the automated synthesis of a reported [^{18}F]AlF-tetrazine conjugate.[36]

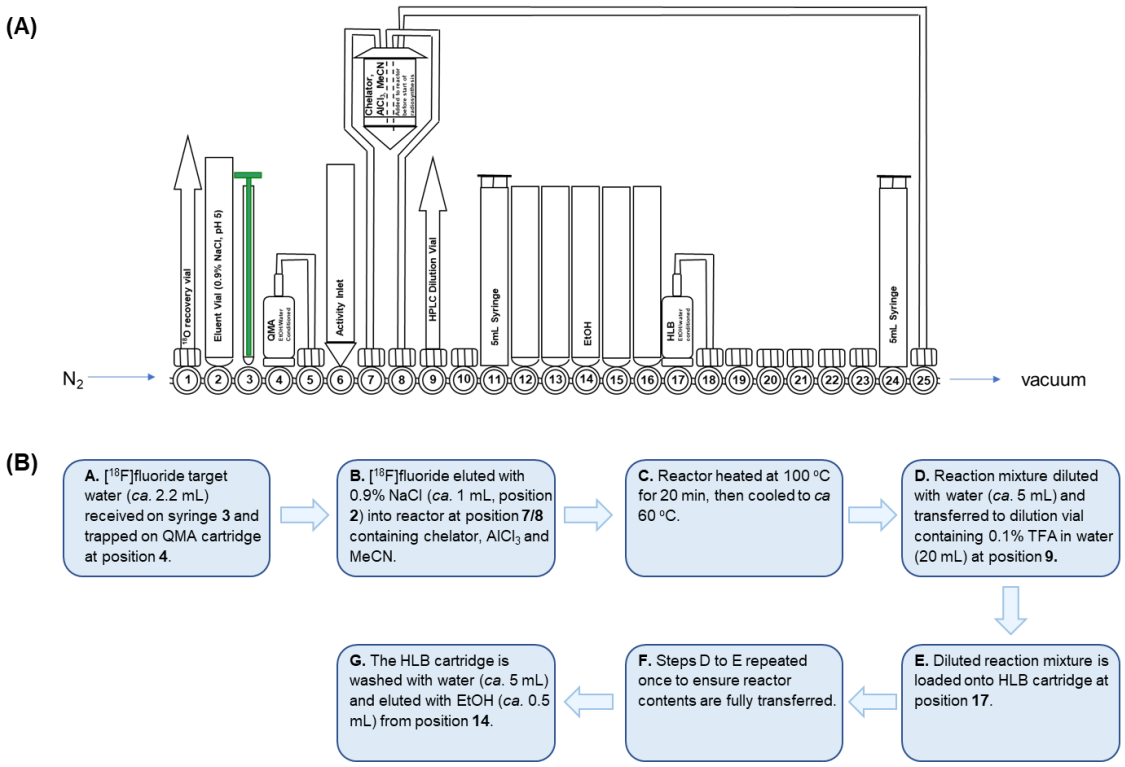

Figure 2.11: (A) Schematic representation of GE FASTlab™ cassette set up for the synthesis of [^{18}F]AlF-Tz. (B) Brief overview of the automated radiosynthesis process.

The automated radiosynthesis of [^{18}F]AlF-Tz was also investigated at higher starting activities (**Figure 2.12**). It was found that [^{18}F]AlF-Tz could only be isolated with high radiochemical purities (>95 %) when the radiosynthesis was carried out with less than 1.1 GBq of activity. Above this, decomposition of [^{18}F]AlF-Tz, presumably by radiolysis, was observed. This is demonstrated by the elution of two additional peaks with a slightly shorter retention time than [^{18}F]AlF-Tz in the radio-HPLC chromatogram (**Figure 2.12**, left). When an isolated mixture from the 11.7 GBq reaction was analysed, only a 39 % RCP was obtained. Correspondingly, incubating this with an equimolar amount of DSPE-PEG$_{200}$-TCO resulted in only a 20 % conversion to [^{18}F]AlF-lipid, showing that decomposition of [^{18}F]AlF-Tz is likely at the tetrazine moiety.

Given these results, starting activities of 1067 ± 58 MBq were used in the automated synthesis of [^{18}F]AlF-Tz. Upon reaction with DSPE-PEG$_{200}$-TCO to form [^{18}F]AlF-lipid, an aliquot of the reaction mixture was mixed with DPPC, DPPA and DSPE-PEG$_{2000}$-NH$_2$ to form [^{18}F]AlF-MBs, identical to that used in the manual approach. These resulted in the production of microbubbles with higher activities (136 ± 6 MBq), but slightly lower RCY (22 ± 1 %) compared to the manual approach. The production process was also slightly longer, requiring 85-90 min. Nevertheless, the semi-automated approach allows the production of [^{18}F]AlF-MBs with higher radioactive concentrations, which could be beneficial for investigating their distribution in

larger animals. This is because optimal PET images are typically obtained when radiotracer injection doses are adjusted based on body weight.[48,49]

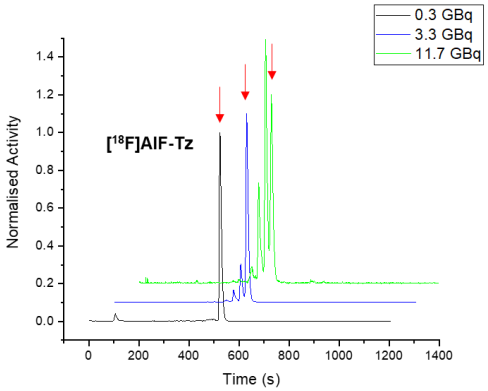

Starting activity (GBq)	RCP (%)	Isolated yield (GBq)	A_m (MBq/nmol)
0.3	>95	0.23	2.3
1.1	>95	0.51	2.1
2.5	81	1.35	6.8
3.3	79	1.90	8.0
11.7	39	3.99	n/a

Figure 2.12: Left: radio-HPLC chromatograms showing increasing decomposition of [^{18}F]AlF-Tz with increasing starting activities. The peak corresponding to [^{18}F]AlF-Tz is shown by the red arrow. Right: Table showing RCPs, isolated yields and molar activities of [^{18}F]AlF-Tz synthesised.

2.4.3 Kit-based approach

To improve the applicability of this method for clinical translation, the production of [^{18}F]AlF-MBs was further simplified. With the rapid and efficient tetrazine-TCO conjugation, it was hypothesised that a kit-based approach to producing [^{18}F]AlF-MBs could be possible, where a TCO-MB formulation is labelled directly with [^{18}F]AlF-Tz (**Figure 2.13**). To test this hypothesis, DSPE-PEG$_{200}$-TCO was mixed with DPPC, DPPA, and DSPE-PEG$_{2000}$-TCO, and lyophilised in the same vial. Upon resuspension of the lipids in PBS : propylene glycol : glycerol (80 : 15 : 5, *v:v:v),* a purified aliquot of [^{18}F]AlF-Tz in ethanol (*ca.* 80 µL) was added. Next, the vial was sealed and purged with C_4F_{10}, then activated to form microbubbles by mechanical agitation. Before centrifuging, the microbubble suspension with [^{18}F]AlF-Tz was left to stand for 5 min to allow adequate time for the tetrazine-TCO reaction,

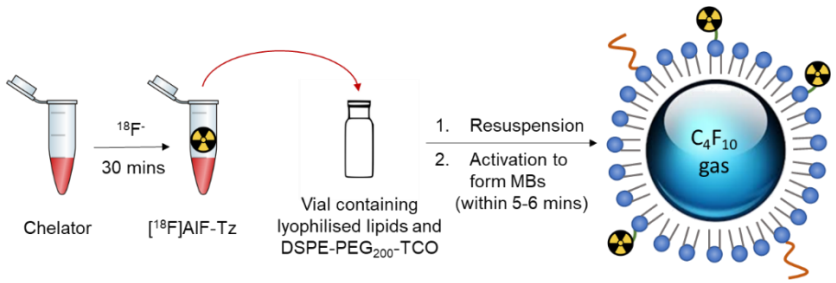

Figure 2.13: Graphical representation of the development of a kit-based approach to produce ^{18}F-labelled microbubbles.

After centrifugal purification, [^{18}F]AlF-MBs were produced with 40-50 % incorporation of radioactivity, in agreement with the radiochemical conversion obtained when [^{18}F]AlF-Tz was reacted with DSPE-PEG$_{200}$-TCO. Further analysis of the [^{18}F]AlF-MBs and infranatant from the centrifuge washes showed identical profiles to those obtained in **Figure 2.9**, demonstrating the feasibility of a kit-based approach to obtain ^{18}F-labelled microbubbles using a formulation with DSPE-PEG$_{200}$-TCO.

Since a kit-based approach entails simple, rapid and reproducible radiolabelling,[50,51] the radiosynthesis of [^{18}F]AlF-Tz was further simplified by eliminating its purification step. To enable this, the reaction co-solvent was changed from the toxic MeCN to EtOH, which is a more GMP compatible solvent. However, using ethanol as a co-solvent resulted in a decreased reaction yield (80 %) compared to MeCN (>95 %), consistent with the results obtained in **Table 2.2**. Nonetheless, increasing the reaction time to 30 min resulted in full incorporation, which removes the need for purification by a SPE cartridge.

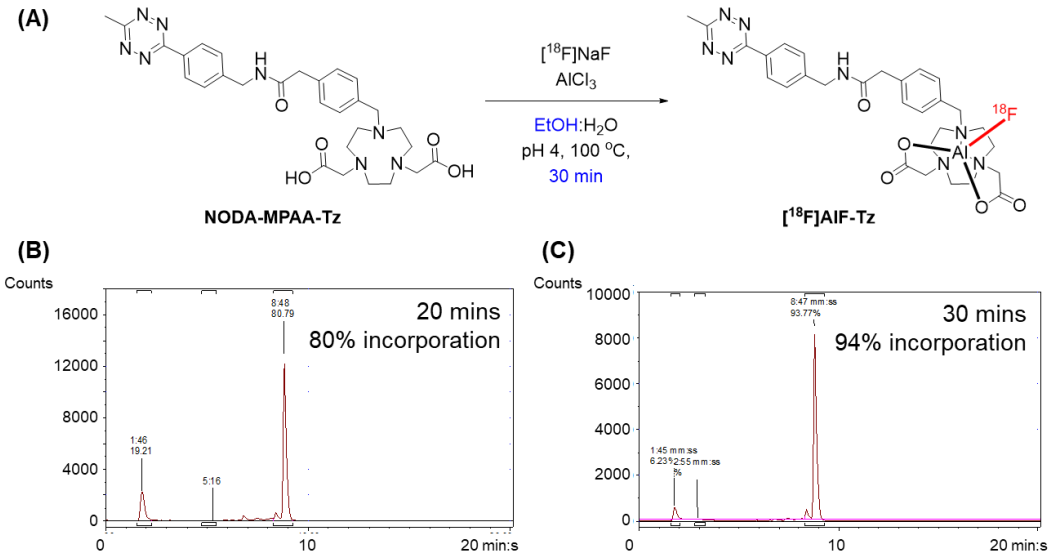

Figure 2.14: Kit-based synthesis of [^{18}F]AlF-Tz. (A) Reaction scheme showing modified conditions. (B) radio-HPLC chromatogram of reaction after 20 min. (C) radio-HPLC chromatogram of reaction after 30 min.

Upon simplifying the radiosynthesis of [^{18}F]AlF-Tz, a kit-based production of [^{18}F]AlF-MBs was developed with [^{18}F]NaF as the starting point. Each kit requires two separate vials, one containing the chelator, and one containing the lyophilised lipid mixture with DSPE-PEG$_{200}$-TCO. Together with the necessary buffer solutions, [^{18}F]AlF-MBs can be easily prepared in three steps from commercially available [^{18}F]NaF: heating, mechanical shaking and centrifuge purification. In addition, the use of disposable vials with pre-dispensed reagents improves reliability by minimising errors relating to reagent transfer, facilitating clinical translation.[52,53]

This optimised kit-based production protocol produces [^{18}F]AlF MBs with activities of 13 ± 2 MBq, in 30 ± 2 % RCY, within 50-60 min. Although [^{18}F]AlF-MBs were produced with lower activities, this is sufficient for pre-clinical biodistribution studies in multiple animals, since current studies require only 0.37-7.4 MBq per mouse.[2,11,13,16]

A comparison of the three different methods used to produce [^{18}F]AlF-MBs is summarised in **Table 2.5**. Although the semi-automated approach produces [^{18}F]AlF-MBs with lower RCYs and requires a longer synthesis duration, higher starting activities can be used, resulting in the production of [^{18}F]AlF-MBs with higher isolated activities.

Table 2.5: Comparison of [^{18}F]AlF-MBs produced using the manual, semi-automated and kit-based approach. Data are presented as mean ± SD (*n* = 3). [a]decay-corrected to the start of synthesis.

Method	Starting activity (MBq)	Isolated activity (MBq)	RCY (%)[a]	Synthesis time (min)
Manual	227 ± 25	48 ± 12	31 ± 5	60-70
Semi-automated	1067 ± 58	136 ± 6	22 ± 1	85-90
Kit-based	65 ± 5	13 ± 2	30 ± 2	50-60

For all three approaches, the [^{18}F]AlF-MBs can be used for both ultrasound and PET in the same pre-clinical imaging study. This is because the instrument detection limits for both modalities would be met: >0.37 MBq for PET, >1×10^7 microbubbles/mL for ultrasound.[23] The three approaches described generate microbubbles with a concentration of 0.3-3.2 MBq/10^7 microbubbles, thus enabling them to be used for both modalities concurrently.

2.5 Development of ^{18}F-labelled microbubbles with a [^{18}F]fluorobenzaldehyde prosthetic group

To demonstrate the advantage of the [^{18}F]AlF methodology, as well as to provide a complementary method to produce ^{18}F-labelled microbubbles, comparison with an organic ^{18}F-labelling method was conducted.

2.5.1 Radiosynthesis of [^{18}F]FBox-Tz

[^{18}F]FBox-Tz was synthesised fully automated on a GE FASTLab™ platform using a previously developed procedure (**Scheme 2.5**).[54] In brief, 4-formyl-*N,N,N*-trimethylanilinium triflate **(2.5)** was reacted with azeotropically dried [^{18}F]fluoride to form [^{18}F]FBA, which was

then reacted with aminoxy-tetrazine **(2.5)** to form [^{18}F]FBox-Tz by oxime ligation. Starting with 3.1 ± 0.9 GBq of activity, [^{18}F]FBox-Tz was synthesised with 977 ± 47 MBq of activity, in 32 ± 3 % RCY within 85 min.

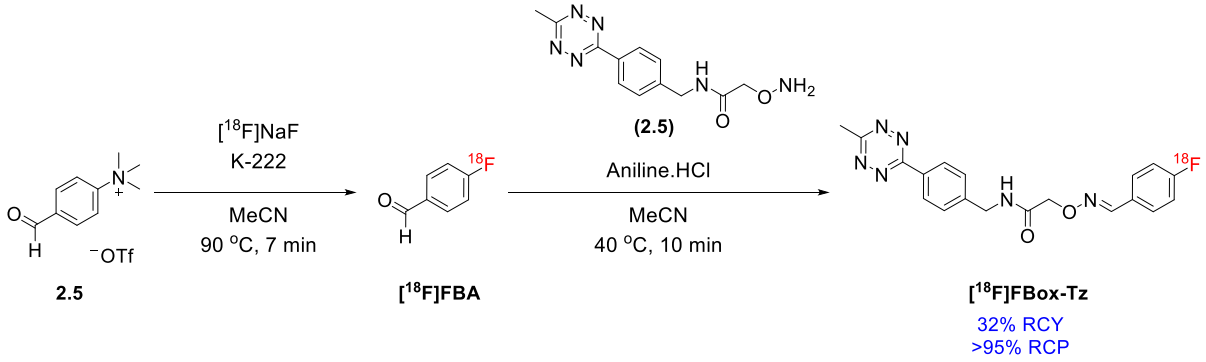

Scheme 2.5: Radiosynthetic route to [^{18}F]FBox-Tz

Compared to [^{18}F]AlF-Tz, which was synthesised with *ca.* 80 % RCP when a starting activity of 3.3 GBq was used, [^{18}F]FBox-Tz was synthesised with a higher RCP of >95 % (**Figure 2.15**). However, the synthesis duration of [^{18}F]FBox-Tz was approximately twice as long, and the isolated activity of [^{18}F]FBox-Tz was half of that of [^{18}F]AlF-Tz. These are presumably due to S_NAr and oxime ligation steps not achieving full radiochemical conversions.[54] Nevertheless, the isolated activity of [^{18}F]FBox-Tz was sufficient for producing multiple batches of ^{18}F-labelled microbubbles.

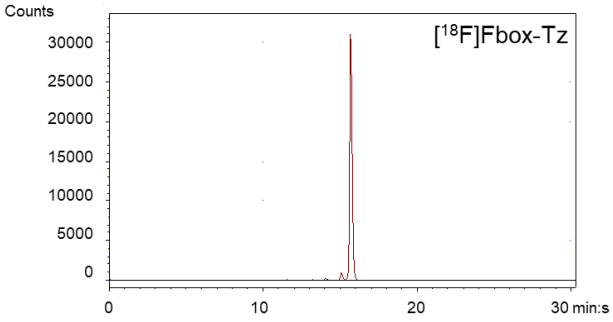

Figure 2.15: Radio-HPLC chromatogram of [^{18}F]FBox-Tz

2.5.2 Microbubble production

Similar to the production of [^{18}F]AlF-MBs, [^{18}F]FBox-MBs were produced using two approaches: (i) a step-wise method by first producing [^{18}F]FBox-lipid, and (ii) a kit-based method by adding [^{18}F]FBox-Tz directly into a vial containing DSPE-PEG$_{200}$-TCO and the other lipid components (**Figure 2.16**).

Using the stepwise approach (i), reaction of [^{18}F]FBox-Tz with DSPE-PEG$_{200}$-TCO resulted in a 50-60 % radiochemical conversion to [^{18}F]FBox-lipid, determined by radio-TLC and radio-

HPLC (**Figure 2.17**). The radiochemical conversion observed was similar to that obtained by [^{18}F]AlF-Tz, where the moderate RCC could be attributed to the quality of the DSPE-PEG$_{200}$-TCO used. Upon activation of the lipid mixture to form [^{18}F]FBox-MBs, a decreased proportion of [^{18}F]FBox-lipid compared to [^{18}F]FBox-Tz was observed by both radio-TLC and radio-HPLC for the microbubble infranatant, signifying incorporation of [^{18}F]FBox-Tz into the microbubble shells.

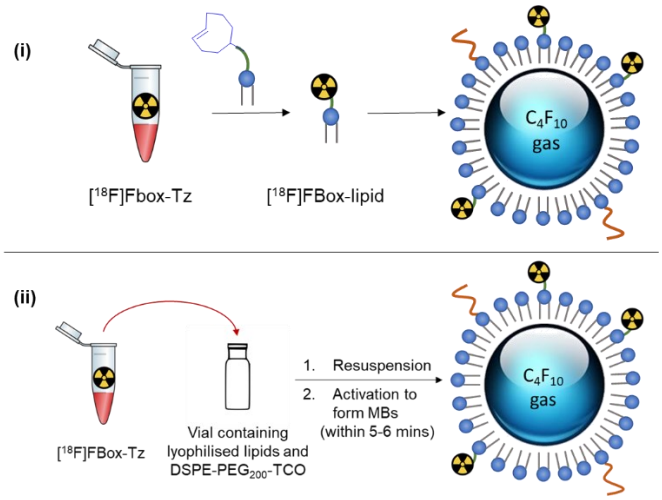

Figure 2.16: Two approaches used to produce [^{18}F]FBox-MBs. (i) Step-wise method by first producing [^{18}F]FBox-lipid, then activating to form MBs. (ii) Kit-based approach by adding [^{18}F]FBox-Tz directly to vial containing DSPE-PEG$_{200}$-TCO.

With the stepwise approach, [^{18}F]FBox-MBs could be generated with a similar amount of activity (93 ± 30 MBq) compared to the semi-automated approach of the [^{18}F]AlF-MBs (136 ± 6 MBq). However, [^{18}F]FBox-MBs were generated with lower RCYs (6.2 ± 0.5 %) compared to [^{18}F]AlF-MBs (22 ± 1 %). This could be attributed mainly to the lower RCY of [^{18}F]FBox-Tz (32 ± 3%) radiosynthesis, compared to [^{18}F]AlF-Tz (63 ± 3%). A similar RCY was obtained for the [^{18}F]FBox-MBs using the kit-based approach, highlighting the consistency of this method for generating ^{18}F-labelled microbubbles. A comparison of the two approaches to generate [^{18}F]FBox-MBs is summarised in **Table 2.6**.

Table 2.6: Comparison of [^{18}F]FBox-MBs produced using the stepwise and kit-based approaches. Data are presented as mean ± SD (*n* = 3). [a] decay-corrected to the start of synthesis.

Method	Starting activity (MBq)	Isolated activity (MBq)	RCY (%)[a]	Synthesis time (min)
Stepwise	3133 ± 901	93 ± 30	6.2 ± 0.5	115-120
Kit-based	1017 ± 76	30 ± 3	5.8 ± 1.0	100-105

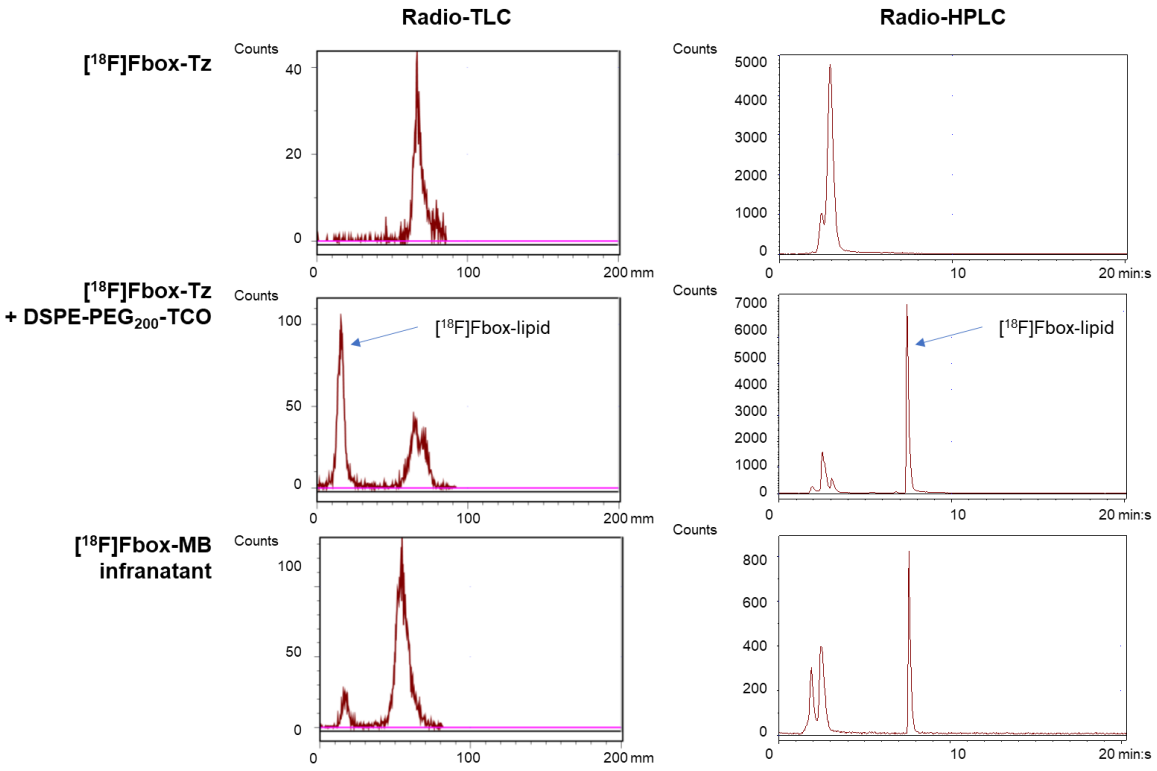

Figure 2.17: Radio-TLC and radio-HPLC traces of [^{18}F]FBox-Tz (Top row); [^{18}F]FBox-Tz after reaction with DSPE-PEG$_{200}$-TCO (Middle row), showing additional peaks corresponding to [^{18}F]FBox-lipid; and [^{18}F]FBox-MB infranatant (Bottom row), showing decreased proportion of [^{18}F]FBox-lipid after MB incorporation.

Comparison of [^{18}F]AlF-MBs to [^{18}F]FBox-MBs

The main difference between the two approaches used to generate the ^{18}F-labelled microbubbles was the radiosynthesis of the ^{18}F-labelled tetrazine prosthetic group. In essence, the production of [^{18}F]AlF-Tz offers the convenience of a radiometal-based synthesis.[37] Partially aqueous conditions can be used during the ^{18}F-fluorination step, eliminating the need for azeotropic drying of the [^{18}F]fluoride. Furthermore, [^{18}F]AlF-Tz only requires one radiosynthesis step with facile solid-phase extraction cartridge-based purification. In comparison, [^{18}F]FBox-Tz requires a 2-step radiosynthesis due to the instability of tetrazines towards the harsh basic conditions required to facilitate nucleophilic substitution,[33,54,55] and purification by preparative-HPLC. Due to these, the radiosynthesis of [^{18}F]FBox-Tz requires a longer duration (85-90 min), compared to [^{18}F]AlF-Tz (35-50 min). In addition, the lower RCY of [^{18}F]FBox-Tz also requires larger amounts of starting activity, which potentially increases radiation exposure.

Nevertheless, in summary, upon isolation of an ^{18}F-labelled tetrazine, ^{18}F-labelled microbubbles could be produced within 25-30 min. Both approaches gave similar

radiochemical conversions when reacted with DSPE-PEG_{200}-TCO, highlighting the reliability and consistency of the IEDDA approach to generate radiolabelled microbubbles.

2.5.3 Comparison of [^{18}F]AlF-MBs to reported methods for radiolabelling microbubbles

Given that only a few methods to radiolabel microbubbles have been reported, this section discusses the advantages and limitations of the design and radiosynthesis of [^{18}F]AlF-MB in comparison to currently available methods.

^{68}Ga-MBs:[16] Previously, the Long group reported a similar method to radiolabel microbubbles by using the inverse-electron-demand Diels-Alder reaction and radiometal chelation. This produced ^{68}Ga-MBs with 30-35 MBq of activity, in 40-50% RCY, and microbubble concentrations of (1.28 ± 0.68) x 10^9 MB/mL, within 40-50 minutes. Compared to this, the RCY of the [^{18}F]AlF-MBs produced using the same method was slightly lower (31 ± 5%), due to the lower tetrazine-TCO conjugation yield. However, with the larger dose of cyclotron-produced ^{18}F compared to ^{68}Ga, [^{18}F]AlF-MBs could be produced with higher activities (48 ± 12 MBq) compared to ^{68}Ga-MBs. In addition, the semi-automated approach offers the ability to produce [^{18}F]AlF-MBs with higher activities (136 ± 6 MBq) to allow imaging of larger animals. Given the relatively onerous microbubble radiosynthesis process, the longer half-life of ^{18}F compared to ^{68}Ga reduces the time pressure for microbubble radiolabelling and increases the possibility for further functionalisation of the radiolabelled microbubbles with targeting moieties. Nevertheless, the [^{18}F]AlF-MBs were developed as an alternative, rather than a replacement, to the ^{68}Ga-MBs. With the availability of ^{68}Ge/^{68}Ga generators,^{68}Ga-MBs could be produced on-site in areas without access to cyclotron-produced ^{18}F.

^{18}F-MBs, ^{18}F-tMBs, and ^{18}F-SFB-tMBs:[2,11,13] The main advantage of the [^{18}F]AlF method in comparison to reported methods to produce ^{18}F-labelled microbubbles is the ease of synthesis of the ^{18}F-labelled prosthetic group. Current methods to produce ^{18}F-labelled microbubbles involve the formation of C-^{18}F bonds *via* S_NAr or S_N2 reactions, which require anhydrous radiolabelling conditions, thus necessitating the ^{18}F to be azeotropically dried. In contrast, the [^{18}F]AlF method enables the radiolabelling step to be conducted under partially aqueous conditions, which simplifies the radiosynthesis. In addition, the [^{18}F]AlF-MBs were generated without the need for streptavidin-biotin conjugations, making them amenable for clinical translation.

^{68}Ga-A2B1-MBs:[15] Apart from ^{68}Ga-A2B1-MBs, all other methods to radiolabel microbubbles involve covalent modification of the microbubble shell (e.g. conjugation of radiolabelled prosthetic group onto pre-formed microbubble shells) or microbubble shell components (e.g.

producing a radiolabelled lipid). The ^{68}Ga-A2B1-MBs are unique because a radiolabelled peptide is incorporated directly into the microbubble shell by non-covalent interactions. Whilst this method offers good incorporation of radioactivity (80%), it might not be directly translatable to more hydrophilic peptides. In addition, the biological distribution of microbubbles radiolabelled by this method is expected to be different than microbubbles radiolabelled by covalent attachment of radioisotopes to the microbubble shell. This is because the biodistribution of ^{68}Ga-A2B1-MBs mirror the biodistribution of the ^{68}Ga-A2B1 peptide, rather than the lipid shell components of the microbubbles. This is shown when the ^{68}Ga-A2B1-MBs had the highest uptake in the kidneys, rather than the liver and spleen. Thus, this method would be more suited to investigate the targeted delivery of specific drugs that are incorporated into microbubble shells, rather than to investigate the distribution of new microbubble formulations.

^{125}I-Albunex and ^{123}I-Quantison:[9,10] Apart from radioisotopes for PET imaging, microbubbles have also been labelled with isotopes for SPECT imaging. These have been conducted using [^{125}I]I_2 and [^{123}I]I_2, which reacts with aromatic residues on albumin. Thus, radiolabelling microbubbles with this method is mostly limited to protein-shelled microbubbles. In addition, the long half-life of ^{125}I (59.5 days) renders it less preferable for imaging microbubbles, with ^{123}I ($t_{1/2}$ = 13 h) being preferable.

^{111}In-MBs: Although this remains the only method to radiolabel pre-formed microbubbles, the several hours required for ^{111}In chelation by DTPA limits the use of this procedure to microbubbles with long half-lives. This precludes the application of this method for radiolabelling the more commonly used lipid-shelled microbubbles, due to their tendency to aggregate over time.[56] Also, the use of biotin-streptavidin interactions prevents the clinical translation of this method.

^{99m}Tc-MBs and P-selectin MBs:[12,14] The use of ^{99m}Tc offers the advantages of a generator-produced radioisotope. In addition, given that streptavidin-bearing, lipid-shelled microbubble formulations are available commercially, using these formulations for the preliminary evaluation of the whole-body biodistribution and molecular imaging capability of new microbubble formulations appear attractive. However, it could be argued that such an approach is limited to determining whether a biomarker could be potentially imaged using microbubbles. This is because studies have shown that changing the composition of lipid-shelled vehicles (such as changing the fluorescent dye incorporated in liposomes) changes their biodistribution.[57–59] Since the streptavidin-bearing microbubble formulations are ultimately not viable for clinical translation, re-evaluation of the biodistribution and

pharmacokinetics of targeted microbubbles without streptavidin is required. This could potentially delay the clinical translation of the new microbubble formulations developed.

[^{18}F]AlF-MBs (this study): The use of the [^{18}F]AlF method and tetrazine-TCO conjugation to radiolabel microbubbles also has several minor disadvantages. Firstly, *trans*-cyclooctene can undergo isomerism to the less reactive *cis*-cyclooctene, resulting in decreased reactivity over time.[45,46] Secondly, the requirement of an organic co-solvent, such as ethanol, to enable efficient [^{18}F]AlF-labelling (>95 % RCY) results in the presence of an additional surfactant, which could interfere with microbubble formation. Nevertheless, these can be easily addressed by appropriate handling and storage of the TCO-lipid and TCO-MBs. Minimising the volume of ethanol used in the [^{18}F]AlF-labelling step will also enable the [^{18}F]AlF-MBs to be formed with the required concentration and size profile.

Finally, the kit-based method to radiolabel microbubbles by [^{18}F]AlF developed in this study also offers the following advantages:

i) Facile and convenient radiolabelling – minimal expertise is required to generate the [^{18}F]AlF-MBs. Starting from [^{18}F]NaF, the production process only requires heating, centrifuging and standard microbubble preparation techniques.

ii) Widespread applicability – the DSPE-PEG$_{200}$-TCO synthesised could be lyophilised with other lipid components. Thus, this method could be easily applied to study the distribution and pharmacokinetics of new phospholipid-based microbubble formulations, with or without targeting functionalities, which facilitates their clinical translation.

iii) Easy route to commercialisation – components required to produce the [^{18}F]AlF-MBs could be pre-dispensed and lyophilised in separate vials. This allows them to be stored safely and activated upon use. Additional functionalities such as targeting moieties could be introduced as biomolecule-lipid conjugates to the vial prior to activation.

2.6 CXCR4-targeted microbubbles for cancer imaging

With the successful synthesis of [^{18}F]AlF-MBs, the methodology was applied to produce cancer-targeted microbubbles. C-X-C chemokine receptor 4 (CXCR4) was chosen as the target due to its overexpression in more than 20 tumour types,[60,61] including leukemia,[62,63] breast cancer,[64] prostate cancer,[65] and ovarian cancer.[66] CXCR4 is a transmembrane protein that is usually absent or has low expression in healthy tissues.[67] Upon binding to its natural ligand (CXCL12), multiple signalling pathways are activated, leading to cell proliferation, survival and migration.[68] However, these pathways can be exploited by cancer cells to promote tumour growth, angiogenesis, metathesis, and therapy resistance.[60,69] Due to its role in cancer biology, several CXCR4-targeted PET tracers have been developed to probe its role as a prognosis biomarker.[70–72] These are mainly based on CXCR4 antagonists, with the most successful being peptide-based compounds such as T140 and Pentixafor (**Figure 2.18**),[73–75]; or CXCR4 agonists, which are macrocyclic compounds such as AMD3100 and AMD3465.[76,77]

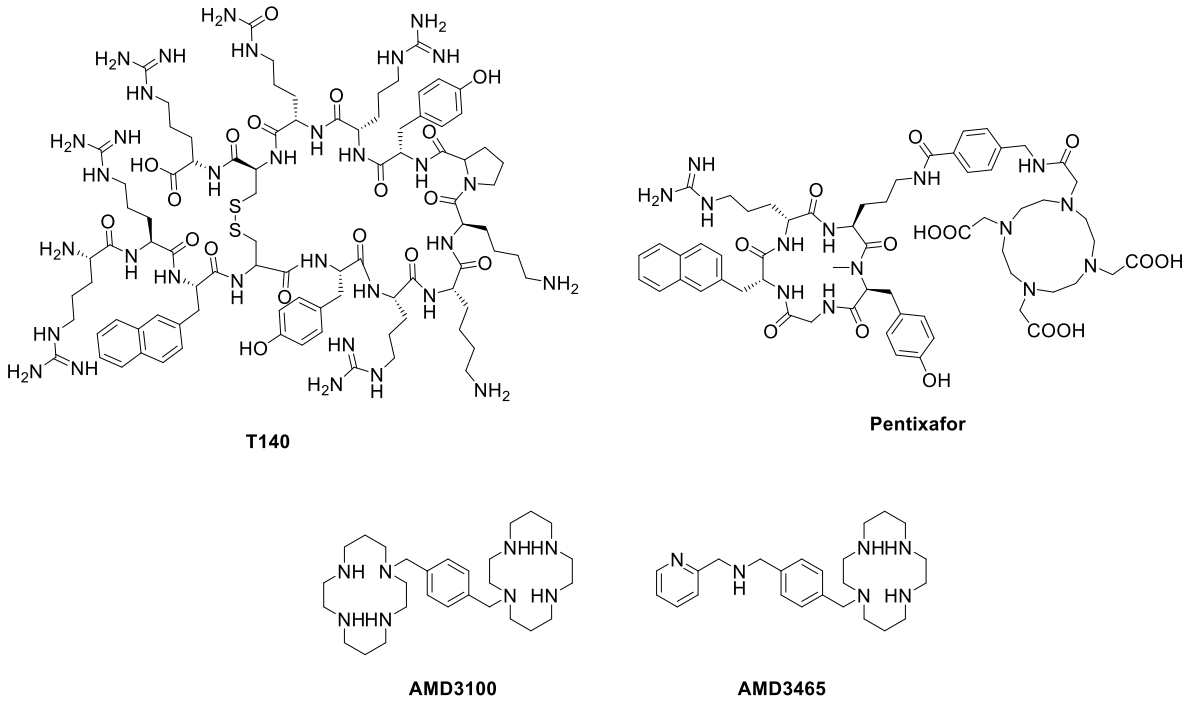

Figure 2.18: Examples of CXCR4-targeted PET probes.

Although the use of these tracers have been relatively successful, with [^{68}Ga]Ga-Pentixafor being evaluated in multiple clinical trials,[23,78] the repeated use of these radiotracers for cancer evaluation and therapy monitoring is not ideal due to the high cost and exposure of patients and staff to ionising radiation. Hence, the development of CXCR4-targeted probes for alternative imaging modalities could be beneficial. Given that CXCR4 expression has been detected in the vasculature,[79,80] and that contrast-enhanced ultrasound offers high senstivity,[81] molecular imaging of CXCR4 expression by ultrasound could overcome the above drawbacks

of PET imaging. In addition to being affordable and widely available, ultrasound imaging does not involve the use of ionising radiation and has excellent safety record.[21,82]

2.6.1 Synthesis of T140-lipid conjugate

Synthesis of a CXCR4-targeted peptide-lipid conjugate (**2.6**) was attempted based on the procedure reported by Braga *et al*. (**Figure 2.19**),[23] where amide coupling was used to couple the T140 peptide to DSPE-PEG$_{2000}$-NH$_2$. A long polyethylene glycol (PEG) linker was used to separate the lipid from the T140 peptide to provide sufficient distance from the microbubble surface for binding to CXCR4. Initial attempts at synthesising **2.6** were carried out using HATU as the coupling reagent. However, despite several attempts, only the guanidino side product was observed after purification of the reaction mixture by dialysis (**Figure 2.20**). Since this has been reported to be a problem when activation of the carboxyl group is slow,[83] the coupling was attempted using a phosphonium coupling reagent, PyBOP.

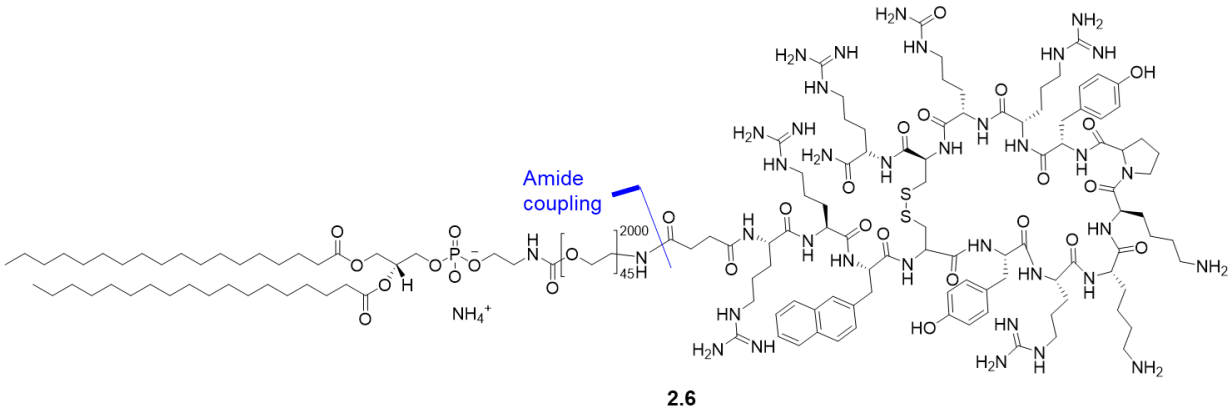

2.6

Figure 2.19: T140-lipid conjugate **2.6** reported by Braga *et al*., M_w = 4926.7. **2.6** was synthesised by amide coupling.

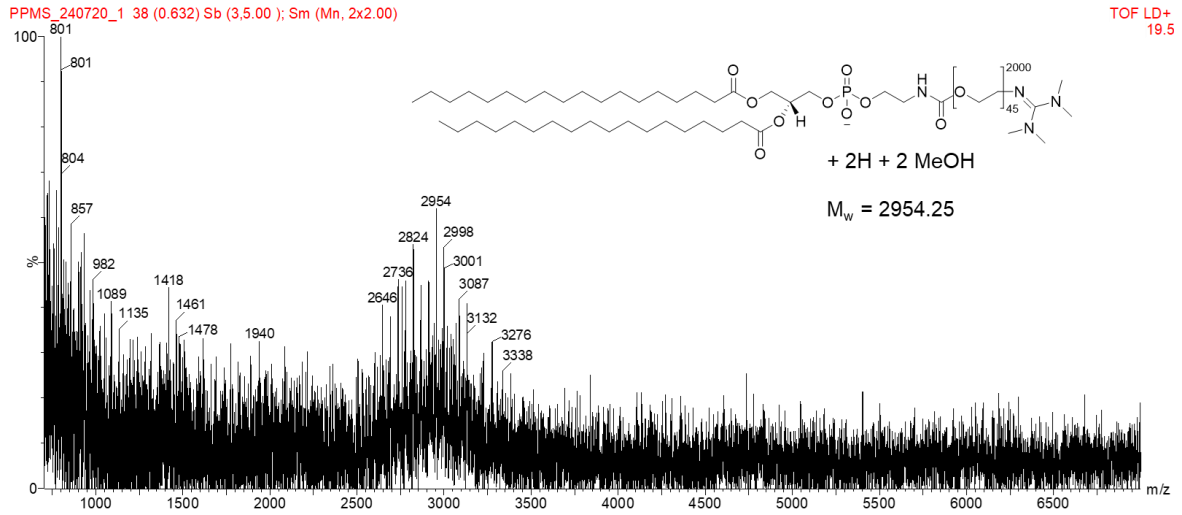

Figure 2.20: MALDI-TOF spectrum of reaction mixture of **2.6** after dialysis, only showing the guanidino side product.

With PyBOP, only the dimerised T140 peptide was observed (**Figure 2.21**), which was not unexpected given the presence of two unprotected lysine residues. The fact that the peak at *m/z* 4159.0 lacks a broad distribution pattern corresponding to a PEG chain also further indicates unsuccessful coupling to DSPE-PEG$_{2000}$-NH$_2$. Due to this, it was decided that amide coupling was not the ideal strategy for the synthesis of a T140-lipid conjugate.

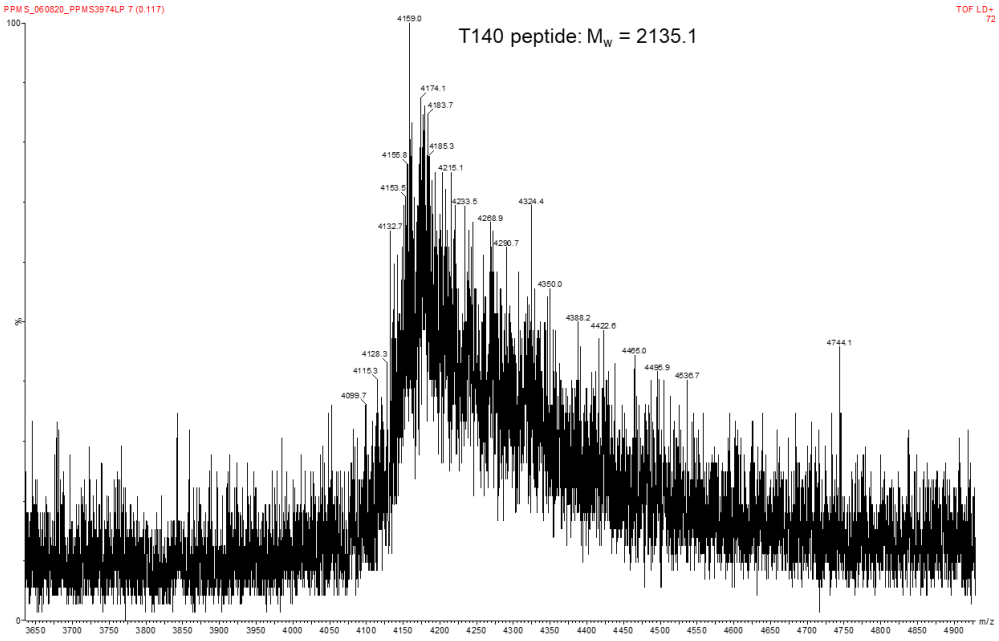

Figure 2.21: MALDI-TOF spectrum of PyBOP reaction mixture, showing only T140 peptide dimer.

To address this, 1,4-phenylene-diisothiocyanate was used to conjugate DSPE-PEG$_{2000}$-NH$_2$ to the lysine residues of T140 (**Figure 2.22**). This was possible since both lysine residues are not critical for the binding of T140 to CXCR4, with Arg^2, Nal^3, Tyr^5, and Arg^{14} identified as critical residues for binding by computational docking studies.[84]

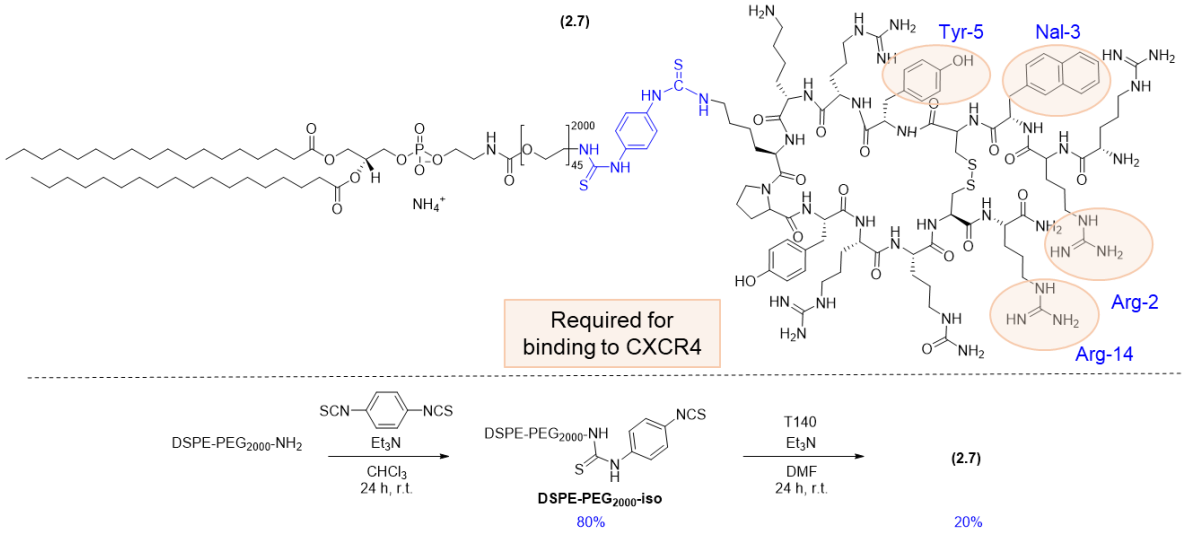

Figure 2.22: Strategy for synthesis of T140-lipid conjugate **2.7** using a diisothiocyanate linker.

Using an excess of 1,4-phenylene-diisothiocyanate during the reaction, DSPE-PEG$_{2000}$-iso was synthesised in 80 % yield. Subsequent conjugation to the T140 peptide afforded **2.7** in 20 % yield, which was characterised by MALDI-TOF mass spectrometry (**Figure 2.23**). In the mass spectrum, a peak was also detected around *m/z* = 2207.8, which is likely due to fragmentation of **2.7** at the diisothiocyanate linker and at the end of the PEG chain. The purity of **2.7** was confirmed by analytical HPLC, showing only a single peak with >99 % purity (**Figure 2.23**, insert). Notably, the starting T140 peptide was also isolated during purification, with a retention time of 2 mins. A di-lipid-peptide conjugate (*m/z* = 8031) was also isolated, arising from the reaction of the second lysine residue on the T140 peptide with DSPE-PEG$_{2000}$-iso.

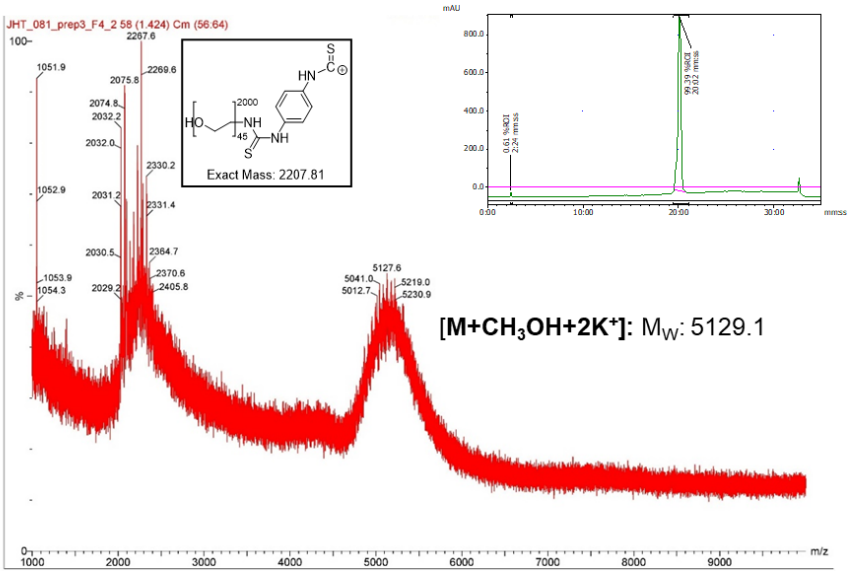

Figure 2.23: MALDI-TOF mass spectrum of **2.7**, showing the desired mass adduct peak around m/z = 5127.6. Inserts: possible mass fragment generated around *m/z* = 2207.8, and HPLC chromatogram indicating the purity of **2.7**.

2.6.2 Production of T140-MBs and *in vitro* evaluation

Upon successful synthesis of T140-lipid conjugate **2.7**, T140-functionalised microbubbles (T140-MBs) were produced using the same composition as that reported by Braga *et al*. (**Table 2.7**).[23] To enable clearer visualisation of the microbubbles during *in vitro* uptake experiments a small amount of a lipophilic membrane stain (DiI) was added to the microbubble formulation.

The T140-MBs were then characterised by optical microscopy (**Figure 2.24**). Although the T140-MBs had a similar concentration (4.09 ± 0.90 MB/mL) and size distribution (diameter = 2.39 ± 1.42 μm) to the TCO-MBs (concentration = 4.32 ± 0.90 MB/mL, diameter = 1.98 ± 1.55 μm), it was observed that the T140-MBs tend to aggregate. This was supported by the lower magnitude of the zeta potential of the T140-MBs (+3.6 ± 0.6 mV) compared to the TCO-MBs (+8.0 ± 0.5 mV), signifying that they are less stable.[85]

Table 2.7: Constituents of T140-MB

Reagent	**Amount (nmol)**	**Mole fraction (%)**	**Volume (μL)**
DPPC	753	81.7	
DPPA	79.2	8.6	
DSPE-PEG$_{2000}$-NH$_2$	43.8	4.8	
T140-lipid (**2.7**)	43.8	4.8	
Dil (fluorescent dye)[a]	2.1	0.2	1
Propylene glycol			160
PBS			800
Glycerol			50

[a] A solution of Dil in DMSO (2 mg/mL) was used

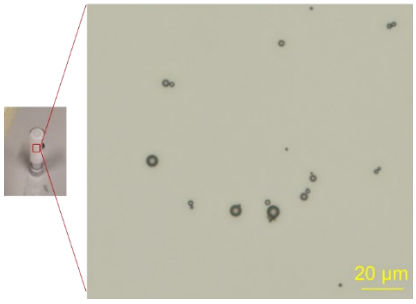

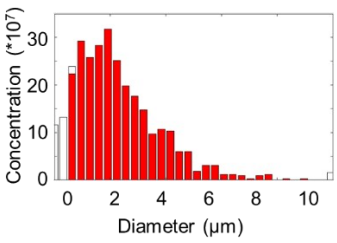

	T140-MB
Concentration (MB/mL)	(4.09 ± 0.90) × 10^8
Mean diameter (μm)	2.39 ± 1.42
Range (μm)	0.50 – 9.97
Zeta potential (mV)	+3.6 ± 0.6

Figure 2.24: Left: optical microscopy image of T140-MBs, showing signs of aggregation. Middle: size distribution. Right: characterisation data of T140-MBs

Nevertheless, upon production of the T140-MBs, their binding to CXCR4-expressing cells (MDA-MB-231) were evaluated. Non-targeted microbubbles (NT-MBs) with the same composition, replacing T140-lipid **2.7** with DSPE-PEG$_{2000}$-NH$_2$, were used as the control (**Figure 2.25**). It was observed that only the T140-MBs bound to the cells, with microbubbles appearing as dark round spots. This showed that functionalisation of the microbubbles with T140 enables binding of the microbubbles to CXCR4-expressing cells.

Next, the specificity of the T140-MBs were evaluated by incubation with CXCR4-negative cells. An isogenic cell model developed by Braga *et al.* was used, where MDA-MB-231 cells were transfected with a doxycycline-inducible lentiviral vector shRNA encoding for CXCR4 knockdown.[23] The results for incubation of fluorescent T140-MBs with the doxycycline-treated cells (CXCR4 negative) and non-treated cells (CXCR4 positive) are shown in **Figure 2.26**, where binding of the T140-MBs was sensitive to CXCR4 expression, with a significant decrease in fluorescent intensity for CXCR4 negative cells (30 % decrease, p<0.01). Notably, the decrease in fluorescence intensity was lower than that obtained by Braga *et al*. (60 %

decrease), which could be due to the different conjugation methodologies used to produce the T140-lipid conjugates **2.6** and **2.7**.

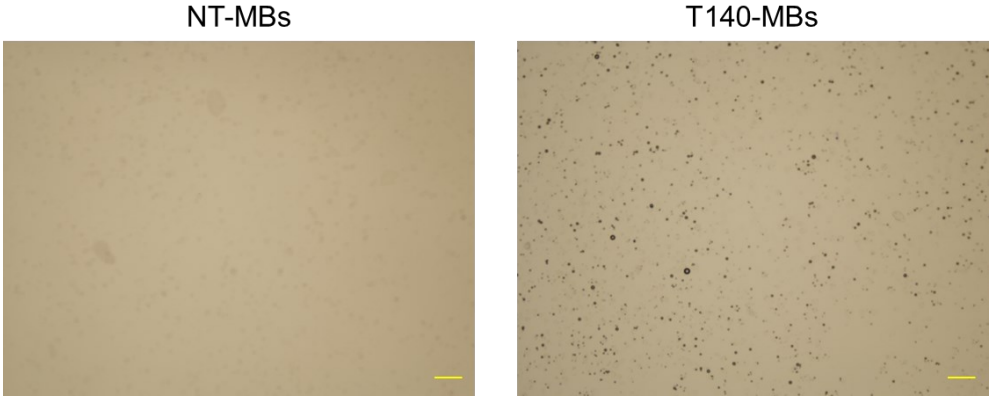

Figure 2.25: Brightfield images of MDA-MB-231 cells after incubation with NT-MBs and T140-MBs, where binding was only observed for T140-MBs. Images were obtained under 10x magnification and scale bar represents 50 µm.

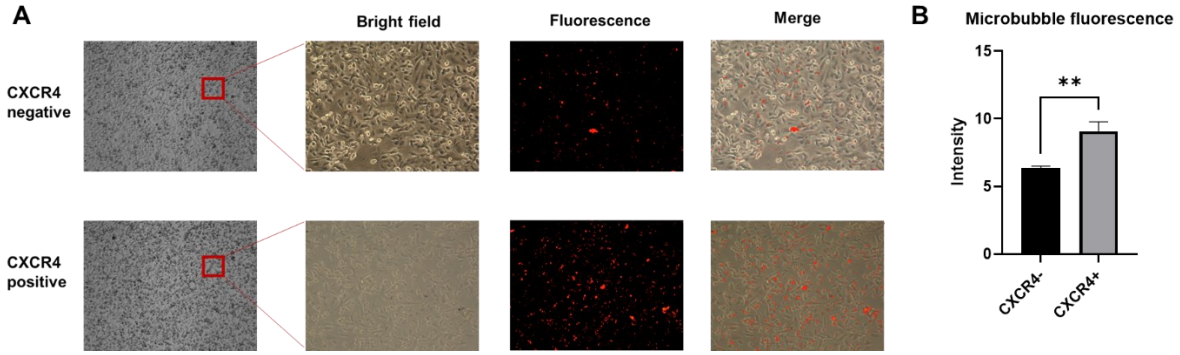

Figure 2.26: A: Brightfield, fluorescent, and merged images of CXCR4-positive and CXCR4-negative cells after incubation with DiI-modified T140-MBs. B: Intensity of microbubble fluorescence normalised to cell area. Images were acquired under 4x and 10x magnification. Data presented as mean ± SD.

Nevertheless, upon confirmation that the NT-MBs do not bind to CXCR4-expressing cells, and that the binding of T140-MBs was sensitive to CXCR4 expression, generation of [^{18}F]AlF-labelled, CXCR4-targeting microbubbles was attempted.

2.6.3 Production of [^{18}F]AlF-T140-MBs and *in vitro* evaluation

Initial attempts to produce [^{18}F]AlF-T140-MBs were carried out using the manual approach used to produce the [^{18}F]AlF-MBs. In this approach, [^{18}F]AlF-lipid in 100 µL of ethanol was added to the microbubble formulation. However, this resulted in [^{18}F]AlF-T140-MBs being formed with low concentration and stability (**Figure 2.27**).

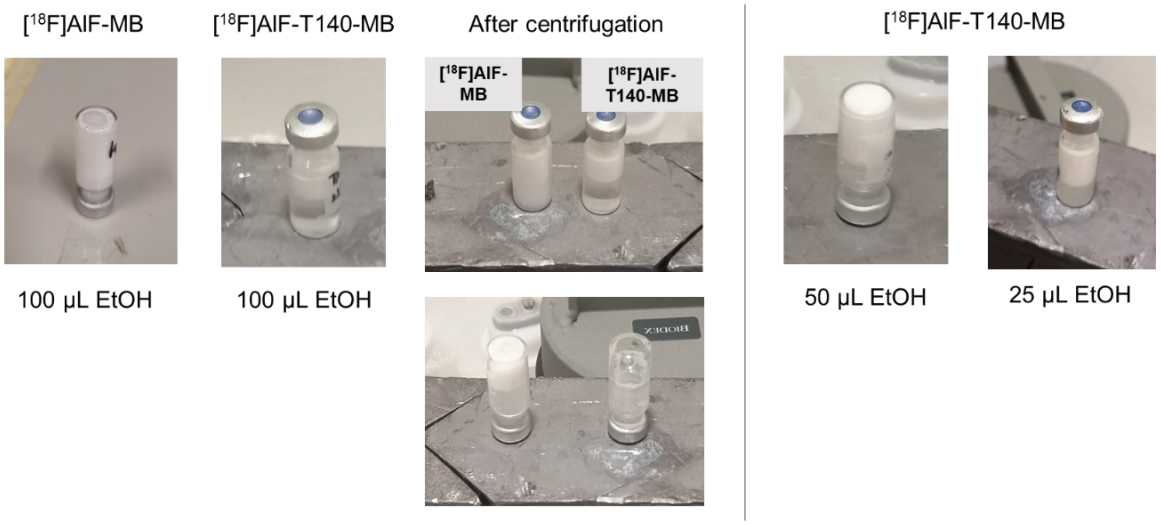

Figure 2.27: Production of [^{18}F]AlF-T140-MBs with varying levels of ethanol used to dissolve [^{18}F]AlF-lipid. [^{18}F]AlF-T140-MBs were produced with sufficiently high concentration and stability when the amount of ethanol used was reduced to 25 µL.

Upon mechanical agitation, a homogeneous white suspension was not obtained for the [^{18}F]AlF-T140-MBs, which then dissolved after centrifugation. It is hypothesized that ethanol, being a surfactant, could disrupt the formation of the [^{18}F]AlF-T140-MBs, since the T140-MBs formed well when ethanol was not added to the microbubble formulation. To address this, the formation of [^{18}F]AlF-T140-MBs was investigated with varying amounts of ethanol. With 50 µL of ethanol, a homogeneous white suspension was not obtained. However, microbubbles could be generated with a concentration of 2.16 × 10^7 MBs/mL, which was about 50-fold less than the concentration of [^{18}F]AlF-MBs (4.32 ± 0.90 × 10^8 MBs/mL).

When the amount of ethanol was reduced to 25 µL, a homogeneous white suspension was still not obtained. However, microbubbles were produced with a similar concentration (2.07 × 10^8 MBs/mL) to the [^{18}F]AlF-MBs. Since further reducing the amount of ethanol would result in insufficient radioactivity of the [^{18}F]AlF-T140-MBs for *in vitro* uptake experiments, 25 µL of ethanol was used in subsequent experiments.

Following the successful generation of [^{18}F]AlF-T140-MBs, *in vitro* uptake experiments were conducted to test the binding capability and specificity of the microbubbles to CXCR4 (**Figure 2.28**). To prove that the [^{18}F]AlF-T140-MBs exhibit increased binding to CXCR4-expressing cells, negative control experiments were conducted using [^{18}F]AlF-MBs, [^{18}F]AlF-lipid and [^{18}F]AlF-Tz. To prove the specificity of the [^{18}F]AlF-T140-MBs for CXCR4, CXCR4-negative cells (**Figure 2.28**, column 2) and a blocking study with excess T140 (**Figure 2.28**, column 3) were also carried out.

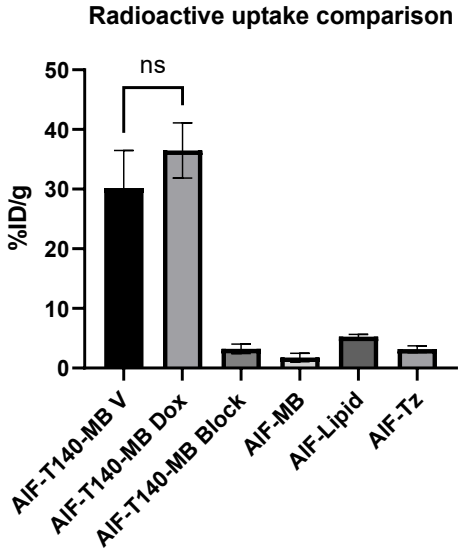

Figure 2.28: Comparison of radioactive *in vitro* uptake of [^{18}F]AlF-T140-MBs in CXCR4 positive cells (V), CXCR4 negative cells (Dox) and CXCR4 positive cells blocked with excess T140 peptide (Block). Uptake of [^{18}F]AlF-MB, [^{18}F]AlF-lipid and [^{18}F]AlF-Tz in CXCR4 positive cells were also compared.

The [^{18}F]AlF-T140-MBs showed increased binding to CXCR4-expressing cells compared to the non-targeted [^{18}F]AlF-MBs, [^{18}F]AlF-lipid and [^{18}F]AlF-Tz. Furthermore, the specificity of the [^{18}F]AlF-T140-MBs were confirmed using a blocking study with excess T140 peptide, where a significant decrease in radioactive uptake was observed (**Figure 2.28**, columns 1 and 3). However, it appeared that the sensitivity of the [^{18}F]AlF-T140-MBs was low, since high uptake was observed for the CXCR4-negative cell line (**Figure 2.28**, columns 1 and 2).

It was initially suspected that the knockdown of CXCR4 was not successfully achieved following treatment of the cells with doxycycline. Hence, western blot was used to determine the expression of CXCR4 in the cells (**Figure 2.29**). Through this, successful knockdown of CXCR4 following treatment of Dox was indicated by the absence of bands corresponding to the receptor.

The next hypothesis was that the incorporation of the T140 peptide into [^{18}F]AlF-MBs could potentially affect its binding to CXCR4. To investigate this, a peptide-based probe (**T140-NODA**, **Scheme 2.6**) was synthesised using the same isothiocyanate conjugation method to produce T140-lipid **2.7**.

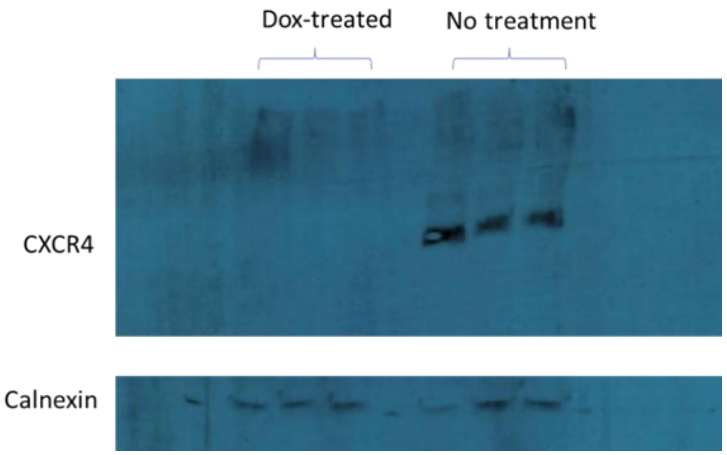

Figure 2.29: Western blot analysis of CXCR4 expression in MDA-MB-231 cells upon treatment with and without doxycycline (Dox) treatment. Calnexin was used as a loading control.

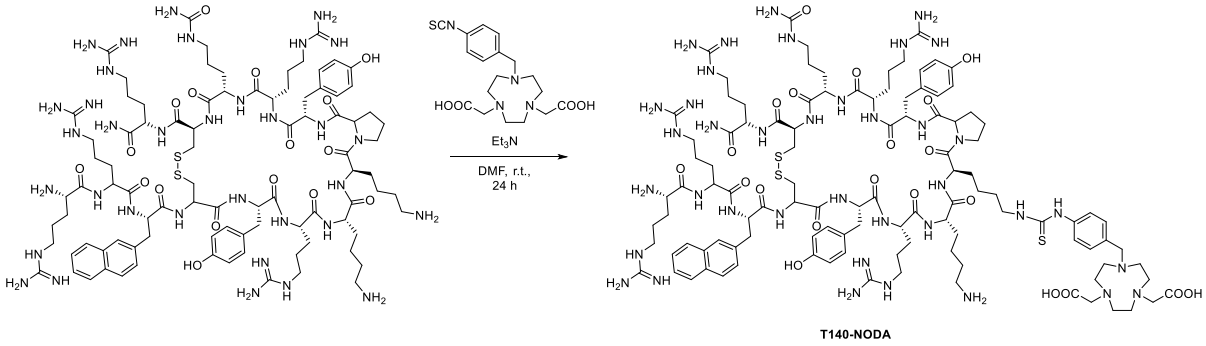

Scheme 2.6: Synthesis of T140-NODA.

T140-NODA was then radiolabelled using the [^{18}F]AlF method in 80% RCC within 20 min. Upon purification, [^{18}F]AlF-T140 was isolated with 50 % RCY and >95% RCP (**Figure 2.30**). Following this, *in vitro* evaluation of [^{18}F]AlF-T140 was conducted (**Figure 2.31**). Surprisingly, no difference in uptake of [^{18}F]AlF-T140 was observed for both CXCR4 positive and negative cells. This was unexpected, since ^{18}F-labelled T140 radiotracers have demonstrated success for imaging CXCR4 *in vitro* and *in vivo*.[86,87]

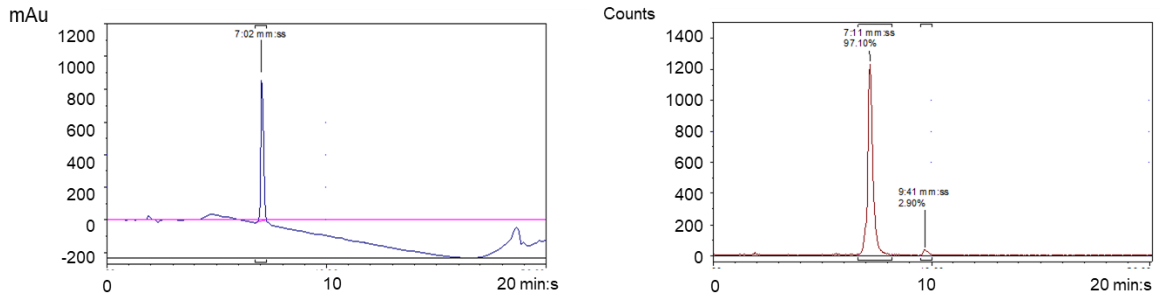

Figure 2.30: Left: UV-HPLC chromatogram of T140-NODA as reference. Right: radio-HPLC chromatogram of purified [^{18}F]AlF-T140.

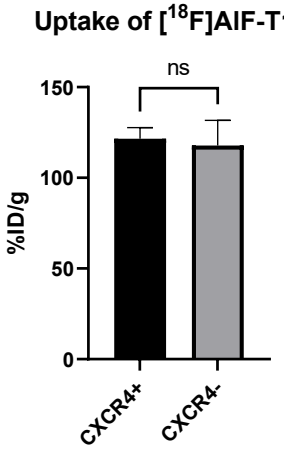

Figure 2.31: *In vitro* uptake of [^{18}F]AlF-T140, where high radioactive accumulation was observed in both CXCR4 positive and negative cells.

It is thus suspected that the non-specific binding of [^{18}F]AlF-T140-MBs and [^{18}F]AlF-T140 could be due to the conjugation at the lysine resides. This was because Braga *et al*. demonstrated that T140-MBs modified at the N-terminus of the T140 peptide could bind specifically to CXCR4-expressing cells *in vitro*.[23] However, this hypothesis was rejected when Jacobsen *et al*. showed that conjugation at the lysine residues improved specificity of a ^{64}Cu-labelled T140 tracer.[71]

One potential explanation for the low sensitivity and specificity of [^{18}F]AlF-T140-MBs and [^{18}F]AlF-T140 was the low apparent molar activities of these tracers generated in this study (A_m of [^{18}F]AlF-T140-MBs = 2.0-4.1 MBq/nmol, A_m of [^{18}F]AlF-T140 = 0.8-1.1 MBq/nmol). In comparison, the molar activities of reported ^{18}F-labelled T140 tracers are generally 5-fold to 10-fold higher (13.6-18.9 MBq/nmol).[86,87] The lower A_m of the radiotracers used in this study could result in reduced specificity and sensitivity due to self-blocking. Hence, one potential improvement would be to use a higher starting activity during the synthesis of these tracers.

However, further studies on CXCR4-targeting with microbubbles were not pursued because there was no significant difference in perfusion parameters between non-targeted microbubbles and T140-modified microbubbles in an ultrasound imaging study.[23] Although the T140-modified MBs showed slower wash-in and wash-out rates from the tumour compared to non-targeted microbubbles, this was not statistically significant. In comparison, studies on a vascular endothelial growth factor receptor 2 (VEGFR2)-targeted microbubble formulation undergoing clinical trials, BR55, showed significant increases in retention and longer wash-out rates compared to non-targeted microbubbles.[88]

To conclude, although T140 peptide analogues have been shown to be exhibit high specificity and sensitivity to CXCR4 for imaging by PET,[71,86,89,90] these might not be directly translatable

for incorporation onto microbubbles for imaging by ultrasound. For PET imaging of CXCR4, radiotracers selectively accumulate and internalise at the tumour over time, generating a contrast to surrounding tissues.[86] In comparison, contrast-enhanced ultrasound imaging does not involve internalisation of microbubbles, which are restricted to the vascular component. Hence, for molecular imaging of CXCR4 by contrast enhanced ultrasound, identification of a targeting vector capable of stronger binding under shear flow conditions would likely be necessary, such as Pentixafor, where its affinity to CXCR4 is compared to T140 in **Table 2.8** below.

Table 2.8: Comparison of dissociation constants (K_D) and half-maximal inhibitory constants of T140 and Pentixafor to Jurkat cells.[72,90,91]

Targeting Vector	**K_D (nM)**	**IC_{50} (nM)**
T140	124-187	65.8
Pentixafor	0.4	17.8-24.6

2.7 [^{18}F]AlF-labelling of nanobubbles

2.7.1 Introduction

Whilst microbubbles are excellent ultrasound contrast agents and have been widely used in clinics, these micron-sized particles (1-8 μm in diameter) have two main limitations:[92] (i) Microbubbles are confined to the vasculature due to their size, which only allows them to image vascular biomarkers; and (ii) they have a relatively short circulation time (half-life of *ca.* 3 min). To address these, nanobubbles (100-500 nm in diameter) have been proposed as a potential alternative.[92–94] Nanobubbles (NBs) have been suggested to be able to extravasate from blood vessels and accumulate in cancer cells through the enhanced permeability and retention (EPR) effect. In addition, they have a longer circulation time (half-life of *ca*. 10 min) compared to microbubbles,[95,96] providing a longer window for accumulation at the target site. As such, there has been a rapid growth in research using nanobubbles for molecular imaging of cancer biomarkers and delivery of targeted payloads.[92]

Given the potential advantages of nanobubbles in diagnostic and therapeutic applications, the ability to monitor their whole-body pharmacokinetics and biodistribution could be beneficial. Thus, the aim of this section is to investigate if the [^{18}F]AlF-labelling approach for microbubbles could be applied to radiolabel nanobubbles.

2.7.2 Nanobubble production

The nanobubbles were produced according to the mechanical agitation protocol used by Claire *et al*.,[95] with slight modifications. Perfluorobutane was used instead of perfluoropropane, since both gases can be used to form microbubbles. DSPE-PEG_{200}-TCO was also included to enable radiolabelling by [^{18}F]AlF-Tz. Compared to microbubbles, the production of each batch of nanobubbles by mechanical agitation requires about 10 times more phospholipids (10 mg/mL, compared to 0.8 mg/mL for microbubbles), presumably to improve nanobubble yield and decrease coalescence.[92,97] Following agitation of the mixture (**Table 2.9**), a homogenous white suspension was formed, identical to that of microbubble production. Upon purification by centrifuging, microbubbles were collected at the top of the vial as a white foam, whereas nanobubbles were obtained as a white suspension in the infranatant. This was consistent with the fact that bubbles of both size profiles have been shown to be present in Definity® microbubble formulations.[98]

Table 2.9: Formulation of TCO-functionalised nanobubbles (TCO-NBs)

Reagent	**Amount (mg)**	**Volume (µL)**
DBPC	6	
DPPA	1	
DPPE	2	
DSPE-PEG_{2000}-OMe	1	
DSPE-PEG_{200}-TCO	0.13	
Propylene glycol		100
PBS		800
Glycerol		100

Next, to verify that the production of TCO-NBs was successful, and to determine their size profile, dynamic light scattering (DLS) was used for characterisation.[99] In parallel, microbubbles were produced and used as controls (**Figure 2.32**). From the intensity-size distribution graph, it appeared that nanobubbles were produced with the desired size profile, with diameters of 100-200 nm.

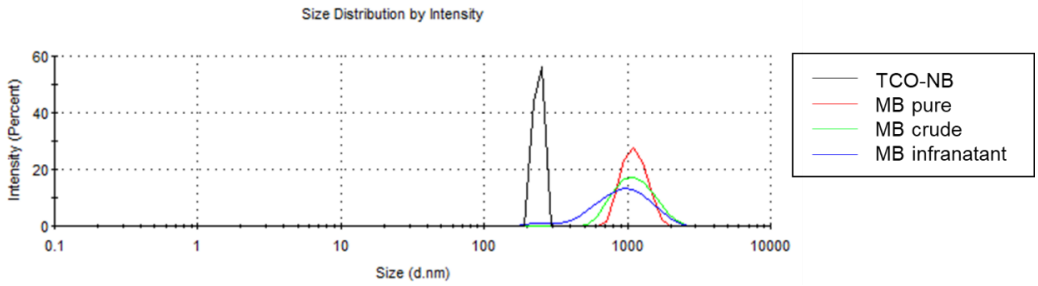

Figure 2.32: Size distribution of TCO-NBs compared to microbubbles.

However, closer analysis of the data revealed that the z-average diameter of the TCO-NBs were approximately 722 nm (**Table 2.10**). The mismatch in size profile from the intensity-size graph and the z-average diameter is likely a result of the high sample concentration, where an intensity of about 50% was recorded. This could have resulted in particle-particle interactions and multiple scattering of photons during the DLS measurement,[100] which could also result in the high polydispersity index (PDI) recorded.

Hence, the TCO-NBs were further diluted for measurement. Gratifyingly, the intensity-size distribution recorded matched the corresponding z-average diameters (**Figure 2.33**), and nanobubbles of the desired size (400-500 nm in diameter) were produced. However, it was observed that the TCO-NBs were aggregating during each subsequent measurement. This could be rationalised from the low zeta-potential of the nanobubbles (+1.28 ± 0.05 mV), since liposomes with near-neutral charges have been reported to be prone to aggregation.[85]

Table 2.10: z-average diameter and PDI of TCO-NBs compared to microbubbles.

Entry	z-average diameter (nm)	PDI
TCO-NB	722	0.731
MB pure	1113	0.107
MB crude	1051	0.128
MB infranatant	814	0.171

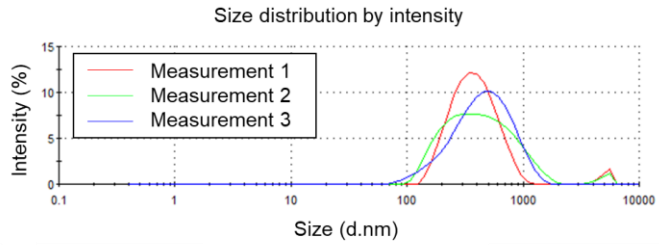

Measurement	z-average diameter (nm)	PDI
1	401	0.245
2	491	0.297
3	504	0.240

Figure 2.33: Size distribution of nanobubbles after dilution.

Nevertheless, the TCO-NBs were assumed to be stable for use, since the same formulation, without DSPE-PEG$_{200}$-TCO, has been tested for contrast enhanced ultrasound imaging *in vivo*.[95] To further purify the TCO-NBs, they were passed through a size-exclusion column (SEC). The results for the purification are summarized in **Table 2.11**. Almost no bubbles were collected in Fraction 1, with the signal being too dilute for proper analysis. Expectedly, the size of the nanobubbles decreased from Fraction 2 to 3, although these seemed to have a similar PDI as the sample before purification. Subsequent fractions appeared too dilute for measurement, and had a transparent appearance, indicating the absence of bubbles.

With the successful production, purification and characterisation of the TCO-functionalised nanobubbles, their radiolabelling was then investigated.

Table 2.11: z-average diameter and PDI of TCO-NBs after purification

Fraction	z-average diameter (nm)	PDI	Comments
1	-	-	Poor signal, too dilute
2	345 ± 5	0.256 ± 0.049	
3	307 ± 5	0.256 ± 0.015	
4	-	-	Poor signal

2.7.3 Nanobubble radiolabelling

The nanobubbles were radiolabelled using the manual approach, similar to that used to radiolabel the microbubbles (**Figure 2.34**). After the addition of [^{18}F]AlF-lipid in approximately 35 µL of ethanol, and mechanical agitation to form the nanobubbles, a white suspension with a cloudy infranatant was obtained. This was not observed in the formation of the TCO-NBs in the absence of ethanol, once again showing that ethanol could disrupt the formation of lipid-shelled bubbles.

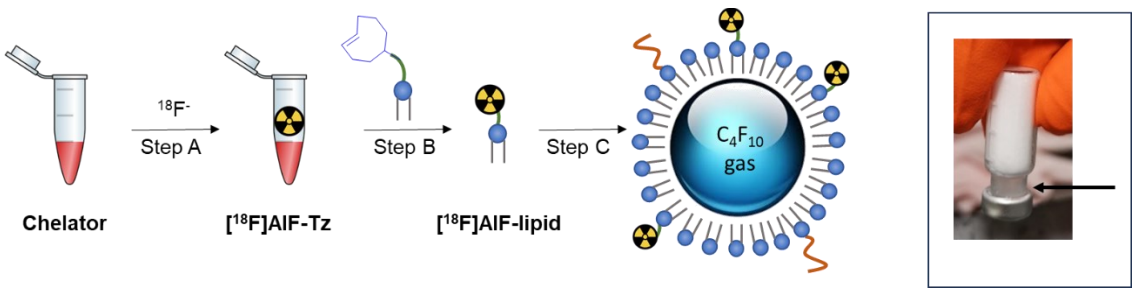

Figure 2.34: Nanobubble labelling approach. Insert: picture of nanobubble suspension after radiolabelling; black arrow shows a cloudy infranatant, obtained immediately after mechanical agitation.

Upon centrifugation, the [^{18}F]AlF-labelled nanobubbles ([^{18}F]AlF-NBs) were isolated as a cloudy suspension (**Figure 2.35**). To ensure that the nanobubbles were free of unreacted tetrazines and unincorporated lipids, purification by SEC was carried out. The amount of radioactivity in each fraction was then compared (**Figure 2.35**). The fraction with the largest amount of radioactivity was determined to be fraction 3, which corresponded to nanobubbles with diameters of 307 ± 5 nm. This was generated with 8.8 MBq of activity after 80 min, in 5 % RCY (decay corrected to start of synthesis). Interestingly, no [^{18}F]AlF-Tz was detected in all fractions, suggesting complete consumption of the tetrazine.

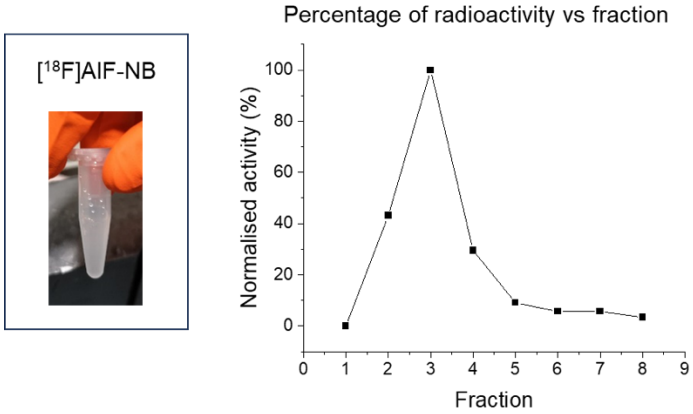

Figure 2.35: Appearance of [^{18}F]AlF-NBs as a cloudy suspension, and comparison of activity in each fraction following purification by SEC.

Although not conducted due to time constraints, one further verification would be to elute [^{18}F]AlF-Tz and [^{18}F]AlF-lipid through the same size-exclusion column. This would allow the identification of their expected elution profiles to be compared to the that of the [^{18}F]AlF-NBs. In addition, formation and characterisation of the TCO-NBs in the presence of ethanol would likely be more representative of the characteristics of the [^{18}F]AlF-NBs produced.

2.8 Conclusions

A facile method to produce ^{18}F-labelled microbubbles was successfully developed, which makes use of the convenient [^{18}F]AlF labelling approach and the efficient inverse-electron-demand Diels-Alder reaction. Compared to previous ^{18}F-labelled microbubble formulations, this method eliminates the need for expertise in ^{18}F-fluorination chemistry and immunogenic streptavidin/biotin interactions. In addition, [^{18}F]AlF-Tz can be replaced with any tetrazine-bearing functionality (targeting vector, different radioisotope, drug etc.), making this a versatile microbubble formulation for functionalisation.

Reliable validation checkpoints were also identified throughout the microbubble production process, which enabled the development of a kit-based approach to producing the [^{18}F]AlF-MBs. With this approach, heating was the only step required for the incorporation of radioactivity, and centrifugation subsequently afforded pure [^{18}F]AlF-MBs with 13 ± 2 MBq of activity in 30 ± 2% RCY. With the convenience of this radiolabelling approach, it is envisioned that ^{18}F-labelled microbubble formulations will be more accessible. This could facilitate the development of new phospholipid-based microbubble formulations with targeting vectors by allowing early *in vivo* evaluation of their whole-body biodistribution and pharmacokinetics.

The development of CXCR4-targeted, [^{18}F]AlF-labelled microbubbles was subsequently attempted. Although the T140-MBs produced were sensitive and specific to CXCR4-expressing cells; upon radiolabelling, the [^{18}F]AlF-T140-MBs showed poor specificity, where binding to CXCR4-negative cells was observed. Thus, evaluation of a different targeting peptide, such as the cyclic pentapeptide, cyclo(Tyr-Lys-Arg-Nal-Gly), used in PentixaFor could be attempted to improve specificity. Alternatively, evaluation of the [^{18}F]AlF-MBs with a targeting vector for a different vascular biomarker could be attempted to demonstrate the applicability of this microbubble formulation for molecular imaging.

Lastly, preliminary attempts to radiolabel nanobubbles using the [^{18}F]AlF approach seemed promising, where the highest activity isolated during SEC purification corresponded to nanobubbles with diameters of 307 ± 5 nm. Further validation of the [^{18}F]AlF-NBs could potentially be carried out by allowing them to decay before carrying out size measurements, although aggregation would likely affect the accuracy of the size profiles obtained. Alternatively, upon characterisation of TCO-NBs produced in the presence of ethanol, comparison of the elution profiles of [^{18}F]AlF-Tz, [^{18}F]AlF-lipid and [^{18}F]AlF-NB by SEC could be undertaken to qualitatively verify the production of [^{18}F]AlF-NB.

2.9 References

1 J. K. Willmann, N. van Bruggen, L. M. Dinkelborg and S. S. Gambhir, *Nat. Rev. Drug Discov.*, 2008, 7, 591–607.

2 J. K. Willmann, Z. Cheng, C. Davis, A. M. Lutz, M. L. Schipper, C. H. Nielsen and S. S. Gambhir, *Radiology*, 2008, **249**, 212–219.

3 A. L. Klibanov, P. T. Rasche, M. S. Hughes, J. K. Wojdyla, K. P. Galen, J. H. Wible and G. H. Brandenburger, *Invest. Radiol.*, 2004, **39**, 187–95.

4 J. O' Doherty and P. Schleyer, *EJNMMI Phys.*, 2017, **4**, 1–10.

5 N. J. Long and W. T. Wong, *The Chemistry of Molecular Imaging*, John Wiley & Sons, Inc, Hoboken, NJ, 2014.

6 A. Kiani, A. Esquevin, N. Lepareur, P. Bourguet, F. Le Jeune and J. Gauvrit, *Contrast Media Mol. Imaging*, 2016, **11**, 92–98.

7 L. E. Jennings and N. J. Long, *Chem. Commun.*, 2009, 3511-3524.

8 S. S. Gambhir, *Nat. Rev. Cancer*, 2002, 2, 683–693.

9 P. Walday, H. Tolleshaug, T. Gjoen, G. M. Kindberg, T. Berg, T. Skotland and E. Holtz, *Biochem. J.*, 1994, **299**, 437–443.

10 A. C. Perkins, M. Frier, A. J. Hindle, P. E. Blackshaw, S. E. Bailey, J. M. Hebden, S. M. Middleton and M. L. Wastie, 2014, **70**, 603–611.

11 M. S. Tartis, D. E. Kruse, H. Zheng, H. Zhang, A. Kheirolomoom, J. Marik and K. W. Ferrara, *J. Control. Release*, 2008, **131**, 160–166.

12 N. Lazarova, P. W. Causey, J. A. Lemon, S. K. Czorny, J. R. Forbes, A. Zlitni, A. Genady, F. S. Foster and J. F. Valliant, *Nucl. Med. Biol.*, 2011, **38**, 1111–1118.

13 A. H. Liao, S. Y. Wu, H. E. Wang, C. H. Weng, M. F. Wu and P. C. Li, *Ultrasonics*, 2013, **53**, 320–327.

14 J. M. Warram, A. G. Sorace, M. Mahoney, S. Samuel, B. Harbin, M. Joshi, A. Martin, L. Whitworth, K. Hoyt and K. R. Zinn, *J. Drug Target.*, 2014, **22**, 387–394.

15 Y. H. Chung, P. H. Hsu, C. W. Huang, W. C. Hsieh, F. T. Huang, W. C. Chang, H. Chiu, S. T. Hsu and T. C. Yen, *Mol. Pharm.*, 2014, **11**, 3904–3914.

16 J. Hernández-Gil, M. Braga, B. I. Harriss, L. S. Carroll, C. H. Leow, M.-X. Tang, E. O. Aboagye and N. J. Long, *Chem. Sci.*, 2019, **10**, 5603–5615.

17 M. Palmowski, B. Morgenstern, P. Hauff, M. Reinhardt, J. Huppert, M. Maurer, E. C. Woenne, S. Doerk, G. Ladewig, J. W. Jenne, S. Delorme, L. Grenacher, P. Hallscheidt, G. W. Kauffmann, W. Semmler and F. Kiessling, *Invest. Radiol.*, 2008, **43**, 162–169.

18 S. Sirsi and M. Borden, *Bubble Sci. Eng. Technol.*, 2009, **1**, 3–17.

19 A. Upadhyay and S. V. Dalvi, *Ultrasound Med. Biol.*, 2019, **45**, 301–343.

20 R. H. Abou-Saleh, S. A. Peyman, B. R. G. Johnson, G. Marston, N. Ingram, R. Bushby, P. L. Coletta, A. F. Markham and S. D. Evans, *Soft Matter*, 2016, **12**, 7223–7230.

21 L. Abou-Elkacem, S. V. Bachawal and J. K. Willmann, *Eur. J. Radiol.*, 2015, **84**, 1685–1693.

22 B. A. Kaufmann, J. M. Sanders, C. Davis, A. Xie, P. Aldred, I. J. Sarembock and J. R. Lindner, *Circulation*, 2007, **116**, 276–284.

23 M. Braga, C. H. Leow, J. H. Gil, J. H. Teh, L. Carroll, N. J. Long, M. X. Tang and E. O. Aboagye, *PLoS One*, 2021, **16**, e0260186.

24 M. Khvedelidze, T. Mdzinarashvili, E. Shekiladze, M. Schneider, D. Moersdorf and I. Bernhardt, *J. Liposome Res.*, 2015, **25**, 20–31.

25 C. C. Chen and M. A. Borden, *Langmuir*, 2010, **26**, 13183–13194.

26 D. Shetty, S. Y. Choi, J. M. Jeong, J. Y. Lee, L. Hoigebazar, Y. S. Lee, D. S. Lee, J. K. Chung, M. C. Lee and Y. K. Chung, *Chem. Commun.*, 2011, **47**, 9732–9734.

27 C. A. D'Souza, W. J. McBride, R. M. Sharkey, L. J. Todaro and D. M. Goldenberg, *Bioconjug. Chem.*, 2011, **22**, 1793–1803.

28 J. A. Wagner, D. Mercadante, I. Nikic, E. A. Lemke and F. Gräter, *Chem. Eur. J.*, 2015, **21**, 12431–12435.

29 B. L. Oliveira, Z. Guo and G. J. L. Bernardes, *Chem. Soc. Rev.*, 2017, 46, 4895–4950.

30 J. Yang, M. R. Karver, W. Li, S. Sahu and N. K. Devaraj, *Angew. Chem. Int. Ed.*, 2012, **51**, 5222–5225.

31 J. C. Oxley, J. L. Smith and J. Zhang, *J. Phys. Chem. A*, 2000, **104**, 6764–6777.

32 S. G. Tolshchina, G. L. Rusinov and V. N. Charushin, *Chem. Heterocycl. Compd.*, 2013, **49**, 66–91.

33 Z. Li, H. Cai, M. Hassink, M. L. Blackman, R. C. D. D. Brown, P. S. Conti and J. M. Fox, *Chem. Commun.*, 2010, **46**, 8043–8045.

34 M. R. Karver, R. Weissleder and S. A. Hilderbrand, *Bioconjug. Chem.*, 2011, **22**, 2263–2270.

35 C. Da Pieve, L. Allott, C. D. Martins, A. Vardon, D. M. Ciobota, G. Kramer-Marek and G. Smith, *Bioconjug. Chem.*, 2016, **27**, 1839–1849.

36 L. Allott, C. Da Pieve, D. R. Turton and G. Smith, *React. Chem. Eng.*, 2017, **2**, 68–74.

37 S. J. Archibald and L. Allott, *EJNMMI Radiopharm. Chem.*, 2021, **6**, 1–28.

38 F. Cleeren, J. Lecina, J. Bridoux, N. Devoogdt, T. Tshibangu, C. Xavier and G. Bormans, *Nat. Protoc.*, 2018, **13**, 2330–2347.

39 W. J. McBride, C. A. D'souza, R. M. Sharkey, H. Karacay, E. A. Rossi, C. H. Chang and D. M. Goldenberg, *Bioconjug. Chem.*, 2010, **21**, 1331–1340.

40 B. J. B. Nelson, J. D. Andersson, F. Wuest and S. Spreckelmeyer, *EJNMMI Radiopharm. Chem.*, 2022, **7**, 1–26.

41 I. Velikyan, *Mol. 2015, Vol. 20, Pages 12913-12943*, 2015, **20**, 12913–12943.

42 J.-P. Meyer, J. L. Houghton, P. Kozlowski, D. Abdel-Atti, T. Reiner, N. V. K. Pillarsetty, W. W. Scholz, B. M. Zeglis and J. S. Lewis, *Bioconjug. Chem.*, 2016, **27**, 298–301.

43 M. R. Schnorenberg, S. P. Yoo, M. V. Tirrell and J. L. Labelle, *ACS Omega*, 2018, **3**, 14144–14150.

44 M. J. Ruiz-Angel, E. Peris-García and M. C. García-Alvarez-Coque, *Green Chem.*, 2015, **17**, 3561–3570.

45 Y. Fang, J. C. Judkins, S. J. Boyd, C. W. am Ende, K. Rohlfing, Z. Huang, Y. Xie, D. S. Johnson and J. M. Fox, *Tetrahedron*, 2019, **75**, 4307–4317.

46 H. E. Murrey, J. C. Judkins, C. W. Am Ende, T. E. Ballard, Y. Fang, K. Riccardi, L. Di, E. R. Guilmette, J. W. Schwartz, J. M. Fox and D. S. Johnson, *J. Am. Chem. Soc.*, 2015, **137**, 11461–11475.

47 P. Laverman, W. J. McBride, R. M. Sharkey, A. Eek, L. Joosten, W. J. G. Oyen, D. M. Goldenberg and O. C. Boerman, *J. Nucl. Med.*, 2010, **51**, 454–461.

48 H. Sagara, K. Inoue, H. Yaku, A. Ohsawa, T. Someya, K. Yanagisawa, S. Ohashi, R. Ishigaki, M. Wakabayashi, Y. Muramatsu and H. Fujii, *Ann. Nucl. Med.*, 2021, **35**, 1177.

49 C. P. W. Cox, D. M. E. van Assema, F. A. Verburg, T. Brabander, M. Konijnenberg and M. Segbers, *EJNMMI Res.*, 2021, **11**, 1–10.

50 J. D. Young, V. Abbate, C. Imberti, L. K. Meszaros, M. T. Ma, S. Y. A. Terry, R. C. Hider, G. E. Mullen and P. J. Blower, *J. Nucl. Med.*, 2017, **58**, 1270–1277.

51 W. J. McBride, C. A. D'Souza, H. Karacay, R. M. Sharkey and D. M. Goldenberg, *Bioconjug. Chem.*, 2012, **23**, 538–547.

52 S. Thompson, M. R. Kilbourn and P. J. H. Scott, *ACS Cent. Sci.*, 2016, **2**, 497–505.

53 L. Allott and E. O. Aboagye, *Mol. Pharm.*, 2020, **17**, 2245–2259.

54 L. Allott, A. Amgheib, C. Barnes, M. Braga, D. Brickute, N. Wang, R. Fu, S. Ghaem-Maghami and E. O. Aboagye, *React. Chem. Eng.*, 2021, **6**, 1070–1078.

55 E. M. F. Billaud, S. Belderbos, F. Cleeren, W. Maes, M. Van De Wouwer, M. Koole, A. Verbruggen, U. Himmelreich, N. Geukens and G. Bormans, *Bioconjug. Chem.*, 2017, **28**, 2915–2920.

56 N. Deshpande, A. Needles and J. K. Willmann, *Clin. Radiol.*, 2010, **65**, 567–581.

57 G. Wang, M. Zannikou, L. Lofchy, Y. Li, H. Gaikwad, I. V. Balyasnikova and D. Simberg, *ACS Nano*, 2021, **15**, 11880–11890.

58 J. Cauzzo, M. Nystad, A. M. Holsæter, P. Basnet and N. Škalko-Basnet, *Int. J. Mol. Sci. 2020, Vol. 21, Page 4847*, 2020, **21**, 4847.

59 R. Münter, K. Kristensen, D. Pedersbæk, J. B. Larsen, J. B. Simonsen and T. L. Andresen, *Nanoscale*, 2018, **10**, 22720–22724.

60 S. Chatterjee, B. Behnam Azad and S. Nimmagadda, in *Advances in Cancer Research*, Academic Press Inc., 2014, vol. 124, pp. 31–82.

61 A. M. E. Walenkamp, C. Lapa, K. Herrmann and H.-J. Wester, *J. Nucl. Med.*, 2017, **58**, 77S-82S.

62 J. Barretina, J. Juncà, A. Llano, A. Gutiérrez, A. Flores, J. Blanco, B. Clotet and J. A. Esté, *Ann. Hematol.*, 2003, **82**, 500–505.

63 S. Konoplev, J. L. Jorgensen, D. A. Thomas, E. Lin, J. Burger, H. M. Kantarjian, M. Andreeff, L. J. Medeiros and M. Konopleva, *Cancer*, 2011, **117**, 4689–4695.

64 O. Salvucci, A. Bouchard, A. Baccarelli, J. Deschenes, G. Sauter, R. Simon, R. Bianchi and M. Basik, *Breast Cancer Res. Treat.*, 2006, **97**, 275–283.

65 T. Akashi, K. Koizumi, K. Tsuneyama, I. Saiki, Y. Takano and H. Fuse, *Cancer Sci.*, 2008, **99**, 539–542.

66 M. V. Barbolina, M. Kim, Y. Liu, J. Shepard, A. Belmadani, R. J. Miller, L. D. Shea and M. S. Stack, *Mol. Cancer Res.*, 2010, **8**, 653–664.

67 H. Zhao, L. Guo, H. Zhao, J. Zhao, H. Weng and B. Zhao, *Oncotarget*, 2015, **6**, 5022–5040.

68 M. E. Bianchi and R. Mezzapelle, *Front. Immunol.*, 2020, **11**, Article no. 2109.

69 A. Orimo, P. B. Gupta, D. C. Sgroi, F. Arenzana-Seisdedos, T. Delaunay, R. Naeem, V. J. Carey, A. L. Richardson and R. A. Weinberg, *Cell*, 2005, **121**, 335–348.

70 T. Vag, K. Steiger, A. Rossmann, U. Keller, A. Noske, P. Herhaus, J. Ettl, M. Niemeyer, H. J. Wester and M. Schwaiger, *EJNMMI Res.*, , DOI:10.1186/s13550-018-0442-0.

71 O. Jacobson, I. D. Weiss, L. P. Szajek, G. Niu, Y. Ma, D. O. Kiesewetter, A. Peled, H. S. Eden, J. M. Farber and X. Chen, *J. Control. Release*, 2012, **157**, 216–223.

72 J. Kuil, T. Buckle and F. W. B. van Leeuwen, *Chem. Soc. Rev.*, 2012, **41**, 5239–5261.

73 B. Debnath, S. Xu, F. Grande, A. Garofalo and N. Neamati, *Theranostics*, 2013, **3**, 47–75.

74 H. Tamamura, A. Hori, N. Kanzaki, K. Hiramatsu, M. Mizumoto, H. Nakashima, N. Yamamoto, A. Otaka and N. Fujii, *FEBS Lett.*, 2003, **550**, 79–83.

75 P. Linde, C. Baues, S. Wegen, M. Trommer, A. Quaas, J. Rosenbrock, E. Celik, S. Marnitz, C. J. Bruns, T. Fischer, K. Schomaecker, H. J. Wester, A. Drzezga, L. van Heek and C. Kobe, *Cancer Imaging*, 2021, **21**, 1–11.

76 E. De Clercq, *Nat. Rev. Drug Discov. 2003 27*, 2003, **2**, 581–587.

77 Z. Zeng, Y. X. Shi, I. J. Samudio, R. Y. Wang, X. Ling, O. Frolova, M. Levis, J. B. Rubin, R. R. Negrin, E. H. Estey, S. Konoplev, M. Andreeff and M. Konopleva, *Blood*, 2009, **113**, 6215–6224.

78 S. Spreckelmeyer, O. Schulze and W. Brenner, *EJNMMI Radiopharm. Chem.*, 2020, **5**, 1–9.

79 R. Salcedo, K. Wasserman, H. A. Young, M. C. Grimm, O. M. Z. Howard, M. R. Anver, H. K. Kleinman, W. J. Murphy and J. J. Oppenheim, *Am. J. Pathol.*, 1999, **154**, 1125–1135.

80 C. Feil and H. G. Augustin, *Biochem. Biophys. Res. Commun.*, 1998, **247**, 38–45.

81 S. Unnikrishnan and A. L. Klibanov, *Am. J. Roentgenol.*, 2012, **199**, 292–299.

82 A. Ignee, N. S. S. Atkinson, G. Schuessler and C. F. Dietrich, *Endosc. Ultrasound*, 2016, **5**, 355–362.

83 E. I. Vrettos, N. Sayyad, E. M. Mavrogiannaki, E. Stylos, A. D. Kostagianni, S. Papas, T. Mavromoustakos, V. Theodorou and A. G. Tzakos, *RSC Adv.*, 2017, **7**, 50519–50526.

84 J. O. Trent, Z. X. Wang, J. L. Murray, W. Shao, H. Tamamura, N. Fujii and S. C. Peiper, *J. Biol. Chem.*, 2003, **278**, 47136–47144.

85 L. M. Kranz, M. Diken, H. Haas, S. Kreiter, C. Loquai, K. C. Reuter, M. Meng, D. Fritz, F. Vascotto, H. Hefesha, C. Grunwitz, M. Vormehr, Y. Hüsemann, A. Selmi, A. N. Kuhn, J. Buck, E. Derhovanessian, R. Rae, S. Attig, J. Diekmann, R. A. Jabulowsky, S. Heesch, J. Hassel, P. Langguth, S. Grabbe, C. Huber, Ö. Türeci and U. Sahin, *Nature*, 2016, **534**, 396–401.

86 X. Yan, G. Niu, Z. Wang, X. Yang, D. O. Kiesewetter, O. Jacobson, B. Shen and X. Chen, *Mol. Imaging Biol.*, 2016, **18**, 135–142.

87 X. X. Zhang, Z. Sun, J. Guo, Z. Wang, C. Wu, G. Niu, Y. Ma, D. O. Kiesewetter and X. Chen, *Mol. Imaging Biol.*, 2013, **15**, 758–767.

88 K. Sugimoto, F. Moriyasu, Y. Negishi, N. Hamano, H. Oshiro, N. G. Rognin, T. Yoshida, N. Kamiyama, Y. Aramaki and Y. Imai, *J. Ultrasound Med.*, 2012, **31**, 1909–1916.

89 O. Jacobson, I. D. Weiss, D. O. Kiesewetter, J. M. Farber and X. Chen, *J. Nucl. Med.*, 2010, **51**, 1796–1804.

90 G. P. C. George, E. Stevens, O. Åberg, Q. D. Nguyen, F. Pisaneschi, A. C. Spivey and E. O. Aboagye, *Bioorg. Med. Chem.*, 2014, **22**, 796–803.

91 A. Poschenrieder, M. Schottelius, M. Schwaiger, H. Kessler and H. J. Wester, *EJNMMI Res.*, 2016, **6**, 1–8.

92 A. A. Exner and M. C. Kolios, *Curr. Opin. Colloid Interface Sci.*, 2021, **54**, 101463.

93 H. Wu, N. G. Rognin, T. M. Krupka, L. Solorio, H. Yoshiara, G. Guenette, C. Sanders, N. Kamiyama and A. A. Exner, *Ultrasound Med. Biol.*, 2013, **39**, 2137–2146.

94 R. H. Perera, E. Abenojar, P. Nittayacharn, X. Wang, G. Ramamurthy, P. Peiris, I. Bederman, J. P. Basilion and A. A. Exner, *Nanotheranostics*, 2022, **6**, 270–285.

95 C. Counil, E. Abenojar, R. Perera, A. A. Exner, C. Counil, E. Abenojar, R. Perera and A. A. Exner, *Small*, 2022, **18**, 2200810.

96 R. H. Perera, C. Hernandez, H. Zhou, P. Kota, A. Burke and A. A. Exner, *Wiley*

Interdiscip. Rev. Nanomedicine Nanobiotechnology, 2015, **7**, 593–608.

97 T. Segers, D. Lohse, M. Versluis and P. Frinking, *Langmuir*, 2017, **33**, 10329–10339.

98 E. C. Unger, T. Porter, W. Culp, R. Labell, T. Matsunaga and R. Zutshi, *Adv. Drug Deliv. Rev.*, 2004, **56**, 1291–1314.

99 Q. Wang, H. Zhao, N. Qi, Y. Qin, X. Zhang and Y. Li, *Sci. Reports 2019 91*, 2019, **9**, 1–9.

100 J. Stetefeld, S. A. McKenna and T. R. Patel, *Biophys. Rev.*, 2016, **8**, 409.

Chapter 3: Delivery of [^{18}F]AlF-MBs to tumours by ultrasound-mediated microbubble destruction

Ultrasound imaging and microbubble destruction were done in collaboration with:

Dr. Kai Riemer, Laura Taylor, Ala Amgheib, Chris Barnes, Joel Abrahams, Dr. Ruisi Fu

3.1 Ultrasound-mediated microbubble destruction in drug delivery

The use of microbubbles in combination with therapeutic ultrasound pulses has been shown to increase blood vessel and cell membrane permeability through sonoporation.[1,2] Upon exposure to ultrasound (US), microbubbles undergo cavitation, where they expand and contract in response to the rarefaction and compression phases of the ultrasound waves. Under an ultrasound field of low acoustic pressure (<50 kPa), microbubbles behave linearly, where their oscillation cycles are symmetric (**Figure 3.1**, left). When focused ultrasound is applied, microbubbles are subjected to high acoustic pressures (**Figure 3.1**, right), resulting in non-linear behaviour due to asymmetry in their expansion and compression factors.[3] Expansion to more than twice their original size leads to a subsequent collapse and destruction of the microbubbles (inertial cavitation),[3] generating shockwaves and microjets. The impact of these mechanical forces results in the formation of transient pores on the surrounding membranes, which enhances drug delivery.

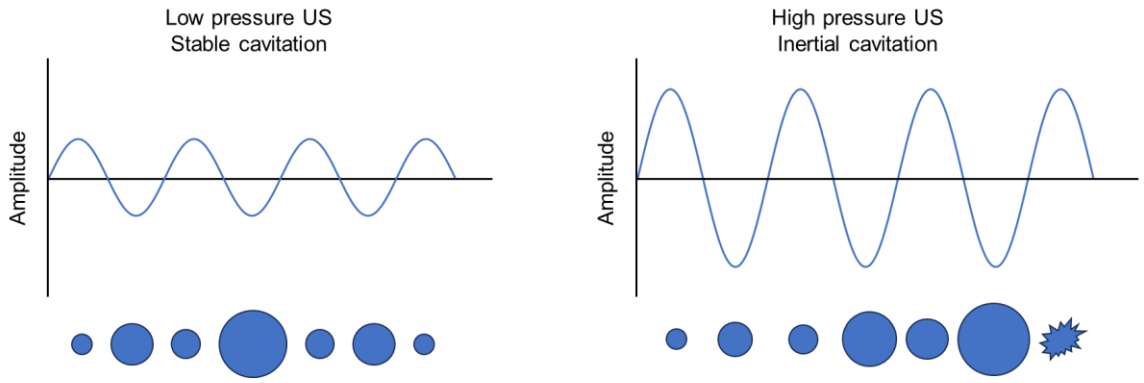

Figure 3.1: Schematic representation of microbubble responses in the presence of ultrasound waves of low and high acoustic pressures. Image adapted from *Colloids Surf. B,* 2018, 83-93.[4]

The technique in **Figure 3.1**, termed ultrasound-mediated microbubble destruction (UMMD) or ultrasound-targeted microbubble destruction (UTMD) has been widely studied to facilitate drug delivery and increase treatment efficiency.[5,6] With UMMD, drugs can either be co-administered with microbubbles, or incorporated into the microbubbles (**Figure 3.2**),[6–10] both having their respective advantage and drawbacks (**Table 3.1**). Of note, although the incorporation of drugs into microbubbles results in a reduced delivery dose due to the low drug loading capabilities of microbubbles, increased treatment efficiencies were still observed compared to using the free drug alone. This is likely due to the increased drug delivery to the target site, since drug metabolism during systemic circulation can be reduced. Nevertheless, both methods of drug administration in combination with UMMD have shown improved treatment efficacies when compared to control studies without ultrasound sonication.[1,6,9,11]

Table 3.1: Advantages and drawbacks of the two drug administration methods for UMMD.

	Co-injection of drugs with microbubbles	**Drug incorporation into microbubbles**
Advantages	Higher drug injection dose Longer drug circulation time could increase drug delivery	Drug and microbubbles reach target site simultaneously Reduced drug metabolism before reaching target Possibility for image-guided delivery
Drawbacks	Drug could be prone to metabolism Systemic side effects of drug	Low drug loading capability of MBs

3.1.1 Drug-loaded lipid microbubbles with UMMD

Several methods have been explored to incorporate drugs into microbubbles (**Figure 3.2**), these include (i) encapsulation of drugs into liposomes and forming liposome-microbubble complexes (LMCs); (ii) incorporation of drugs into microbubble shells through hydrophobic interactions; (iii) attachment of drugs onto microbubble shells by electrostatic interactions; and (iv) dissolution of drugs into an oil layer within the microbubble shell.[12] Since the [^{18}F]AlF-MBs produced in this study are lipid-shelled, a brief analysis of the efficacy of drug delivery and treatment using drug-loaded lipid-shelled microbubbles is carried out in **Table 3.2**.

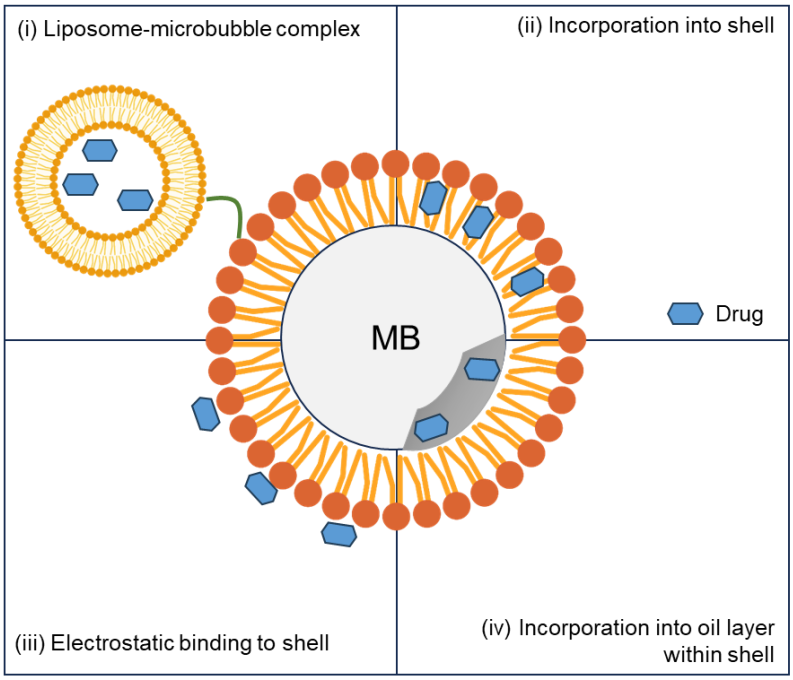

Figure 3.2: Graphical representation of possible approaches for drug-loading onto or into microbubbles.

Table 3.2: Drug-loaded, lipid-shelled microbubbles used in ultrasound-mediated microbubble destruction studies.

Drug	**Application**	**Encapsulation capacity**	**Treatment efficacy**	**Ref.**
Irinotecan	VEGFR2-targeted, irinotecan-loaded liposome-microbubble complex for treatment of colorectal cancer	0.26 mg/mL	50% inhibition of tumour growth, compared to 38% by free irinotecan.	9
Doxorubicin (Dox)	Dox-loaded liposome-microbubble complex for treatment of glioblastoma cells	Not reported	4-fold decrease in cell viability compared to free doxorubicin and Dox-MB without US	13
Doxorubicin (Dox)	Dox-liposome-microbubble complexes for breast cancer treatment	73%	Increased Dox delivery, retention and treatment efficacy *in vitro*	14
Paclitaxel (PTX)	PTX-liposome-microbubble complexes for breast cancer treatment	0.138 mg/10^8 MBs	Increased inhibition of tumour growth compared to controls	15
Carmustine	Carmustine-loaded MBs for treatment of glioblastoma across BBB	68% 1.67 mg/mL	Decreased tumour progression and increased survival compared to drug alone	16
Doxorubicin (Dox)	SPION-conjugated, dox-loaded MBs for enhanced drug delivery into brain tumours	0.707 mg/mL	2.05-fold increase in dox deposition compared to without US	17
Hydroxycamptothecin (HCPT)	HCPT-loaded MBs for cancer treatment	85.2% *ca.* 2.55 mg/mL	Tumour inhibition rate increased to 70.6% compared to HCPT alone (49.4%)	18
Docetaxel (Doc)	Doc-loaded MBs for tumour treatment with low-intensity focused-US treatment	46.3% *ca.* 0.15 mg/mL	Approximately 60% inhibition rate compared to control and doc (20%) *in vitro*	19
Docetaxel (Doc)	Doc-loaded MBs for treatment of liver carcinoma	50%	Improved *in vivo* inhibition of tumour growth	20
Doxorubicin (Dox)	Dox-loaded microbubbles for tumour therapy	0.306 mg/mL	12-fold increase in Dox to tumour with ultrasound, significantly lower tumour growth	21,22
Paclitaxel (PTX)	PTX-loaded, LRHa-targeted MBs for ovarian cancer treatment	96.5%	Increased inhibition of cell proliferation, increased apoptosis *in vitro*	23

Recently in 2020, Ingram *et al*. described the use of VEGFR2-targeted, irinotecan-loaded liposome-microbubble complexes for enhancing the therapeutic efficacy of cytotoxic drugs.[9] Irinotecan was investigated (FDA-approved drug for colorectal cancer treatment) since its therapeutic dose is limited due to severe side effects.[24] In this study, a VEGFR2-targeting antibody was first attached onto biotin-bearing, irinotecan-loaded liposomes by thiol maleimide conjugation. The liposomes were then attached onto streptavidin-bearing microbubbles. The liposome-microbubble complexes (thMBs) and VEGFR-targeted microbubbles demonstrated similar binding efficiencies *in vitro*, showing that targeting ability was not diminished by the liposome payload. More importantly, the tumour growth inhibition rate for the thMBs with ultrasound (50 %) was significantly higher than that of free irinotecan treatment (38 %). Without the application of ultrasound, the thMBs showed no significant tumour growth inhibition. In addition, the authors showed that free irinotecan was subjected to rapid metabolism, with high levels of the metabolised (by glucuronidation) drug detected in the kidney, spleen and liver at 1 and 72 h, whereas no drug was detected in the tumour. In comparison, the thMBs showed a different distribution, with no metabolised drug detected in kidney and spleen at 72 h, but a significant dose was detected in the tumour. With these, it was concluded that encapsulating drugs in a liposome-microbubble complex for ultrasound-mediated treatment could increase therapeutic efficiency and limit side effects.

Escoffre *et al*. also reported a doxorubicin-loaded, liposome-microbubble complex (Dox-LMC) to reduce the systemic side effects of free doxorubicin.[13] In this study, it was shown that treatment of glioblastoma cells with free doxorubicin (Dox) resulted in a 33 % decrease in cell viability. In comparison, treatment of cells with Dox-LMCs in the presence of ultrasound resulted in a 79 % decrease in cell viability, which further highlights the advantages of drug-loaded MBs in combination with UMMD compared to using free drugs.

Using a similar Dox-LMC, Deng *et al*. studied the efficacy of UMMD and Dox-LMCs for reversing multidrug resistance in breast cancer cells.[14] The authors compared the treatment efficiency of Dox-LMC + US to two control groups: Dox-LMC without ultrasound (Dox-LMC – US) and Dox-liposome + verapamil + US (DL + V+ US), where verapamil is a drug reported to reverse multidrug resistance.[25] Treatment of cells with Dox-LMC + US gave significantly higher intracellular drug concentration and drug retention compared to both control groups. Upon treatment, cell viability of the Dox-LMC + US was 52.1 %, significantly lower than the 69.5 % observed for DL + V + US, and 80.1 % for Dox-LMC – US, demonstrating increased cytotoxicity using liposome-microbubble complexes in combination with UMMD, compared to multidrug therapy.

Following on, Yan *et al*. investigated the efficiency of paclitaxel-loaded LMCs (PTX-LMCs) for treatment of breast cancer *in vitro* and *in vivo*.[15] The authors found that *in vitro* treatment with PTX-LMCs + US resulted in a 58 % decrease in cell viability, compared to a 30 % decrease with PTX-liposomes + US. A significant decrease in tumour growth was also observed *in vivo* with this treatment (PTX-LMC + US) compared to controls with PBS, PTX-LMC – US, and PTX-liposome + US. After 22 days, tumour sizes were *ca*. 1233 mm^3 (PBS), 872 mm^3 (PTX-LMC – US), 837 mm^3 (PTX-liposome + US) and 360 mm^3 (PTX-LMC + US). These showed that ultrasound sonication in the absence of microbubbles does not significantly improve treatment efficacy. Subsequent biodistribution studies showed that PTX-LMC + US increased PTX accumulation in tumours by 4.31-fold when compared to PTX-LMC – US and 3.54-fold when compared to PTX-liposome + US. Histological assays further revealed that tumour growth was inhibited by increased apoptosis and reduced angiogenesis.

To facilitate the treatment of brain tumours, Ting *et al*. designed carmustine (BCNU)-loaded microbubbles (BCNU-MBs) for ultrasound-mediated drug delivery across the blood-brain barrier.[16] Compared to free BCNU, which hydrolyses rapidly, incorporation of BCNU into BCNU-MBs gave a 5-fold increase in BCNU circulation time, and 5-fold reduction in liver accumulation, reducing liver toxicity. Without ultrasound, 4.22 μg of free BCNU accumulated in the brain. With ultrasound-mediated microbubble destruction (UMMD), this increased to 24.00 μg, whereas BNCU-MBs gave a comparable level of 17.87 μg. With the increase in BCNU delivery across the BBB, the treatment of glioblastoma was compared between free BCNU and BCNU-MB + US. Although free BCNU reduced tumour growth by 4.8-fold, tumour progression continued and the animals had a maximal survival of 43 days (39 days without treatment). With BCNU-MB + US, tumour progression was successfully controlled, with a 0.5-fold decrease in tumour size, and significant extension of maximal survival time to 59 days, showing the impact of UMMD for treatment of brain tumours.

Fan *et al*. then investigated the delivery of superparamagnetic iron-oxide (SPIO) nanoparticles conjugated to Dox-loaded microbubbles (SPIO-Dox-MBs) into the brain for concurrent MRI imaging.[17] The authors also examined the ability to use magnetic targeting (MT) to further increase the deposition of SPIO particles in the brain. The delivery of Dox to brain tissues was increased by 2.05-fold with Dox-MBs + US, whereas there was no increase in delivery for Dox + US, compared to free Dox. For SPIO nanoparticle delivery, compared to SPIO-Dox-MB alone, SPIO-Dox-MB + US gave a 2.67-fold increase, whereas SPIO-Dox-MB + MT gave a 2.28-fold increase. Combining both MT and US led to a more significant increase in SPIO particles by 4.04-fold, showing the synergistic effect of both targeting methods. This showed the theranostic potential of the SPIO-Dox-MBs for image-guided drug delivery across the BBB when UMMD is applied.

To overcome the low aqueous solubility of HCPT for systemic injection, Li *et al*. developed HCPT-loaded microbubbles (HCPT-MBs) for the treatment of liver cancer.[18] Upon treatment with US and HCPT-MBs, a 5-fold increase in HCPT concentration was observed in tumours, compared to HCPT-MBs - US, HCPT - US and HCPT + US. This also led to a more significant tumour growth rate inhibition, where HCPT-MB + US demonstrated a 70.9 % decrease in tumour growth, compared to 49.4 % for HCPT, and 47.8 % for HCPT-MB - US, showing the benefits of ultrasound-mediated treatment with drug loaded-microbubbles.

Similarly, docetaxel (Doc) has poor water solubility, and is dissolved with tween-80 for tumour therapy, which potentially causes allergic reactions. To address this, Ren *et al*. developed Doc-loaded microbubbles (Doc-MBs), and investigated their antitumour effect in combination with low-frequency ultrasound (LFUS) treatment.[19] LFUS was used because it has better tissue penetration and results in lower tissue damage. With the Doc-MBs, ultrasound enhancement in the liver was similar to commercially available SonoVue microbubbles, showing that drug incorporation does not affect the acoustic properties of microbubbles. Although only investigated *in vitro,* the Doc-MBs + LFUS showed significantly higher cell growth inhibition (*ca*. 60 %) compared to Doc + LFUS (*ca*. 20 %). Interestingly, unloaded MBs + LFUS also showed a higher inhibition (*ca.* 45 %), attributed to sonodynamic effects.

Kang *et al*. also investigated the efficiency of Doc-MBs for the treatment of liver tumours *in vivo*.[20] In this study, Doc-MBs + US gave the highest tumour growth rate inhibition (30 %), compared to Doc (11 %), Doc + US (12 %), Doc-MBs - US (9 %) and MB + US (6 %). Although all groups showed metastasis in the abdominal cavity, extensive metastasis was not observed for the Doc-MB + US group, which also showed the longest survival time.

In 2010, Tinkov *et al*. reported Dox-loaded microbubbles for targeted tumour therapy.[21,22] When kidney carcinoma cells were treated *in vitro*, Dox-MBs + US gave 5.71-fold reduction of cell proliferation. In comparison, Dox-MBs - US only resulted in a 1.62-fold decrease, similar to free dox (1.77-fold). When investigated *in vivo* for treatment of pancreatic cancer, Dox-MBs + US resulted in a 12-fold increase in tumour concentration of Dox compared to Dox-MBs - US. Tumour growth was also significantly decreased by 70 %, whereas Dox-MB - US resulted in a smaller decrease of 27 %, highlighting the role of ultrasound in enhancing drug release and membrane permeability for treatment with drug-loaded microbubbles.

To improve the targeting efficiency of paclitaxel-loaded MBs, Liu *et al*. incorporated a luteinizing hormone-releasing hormone analogue (LHRHa) for targeting ovarian cancer.[23] Upon incorporation of LHRHa through biotin-streptavidin interactions, LHRHa-PTX-MBs showed increased binding to ovarian cancer cells *in vitro*, whereas no detectable binding was observed for non-targeted PTX-MBs. When cell proliferation inhibition rate was assessed after

72 h, LHRHa-PTX-MBs + US gave the highest inhibition (75.93 %), whereas PTX-MBs + US gave a 57.47 % inhibition. This demonstrated the benefits of incorporating targeting functionalities to improve localisation of the microbubbles at the disease site.

In summary, the results of these studies showed that incorporation of drugs into microbubbles, either as liposome-microbubble complexes, or directly into the microbubble shells, enhances treatment efficacy when ultrasound is applied. These could be attributed to three main reasons: (i) improved solubility of hydrophobic drugs, (ii) reduction in systemic side effects of free drugs, and (iii) increased delivery of drugs at the cancer site. To further increase drug delivery at the target site, targeting functionalities could also be incorporated to improve microbubble accumulation.

3.1.2 Radiolabelled microbubbles with UMMD

Although several studies have been reported on UMMD with small molecule radiotracers for PET imaging, these have largely been in the field brain imaging.[26,27] In these studies, UMMD was used to temporarily open the blood-brain barrier (BBB), and subsequent injection of a radiotracer allowed imaging of brain tumours. Whilst the use of UMMD enabled improved tracer delivery and PET imaging of the brain, these studies are not discussed further since they do not involve the use of radiolabelled microbubbles. In comparison, only a handful of studies on UMMD using radiolabelled microbubbles have been reported (**Figure 3.3**).

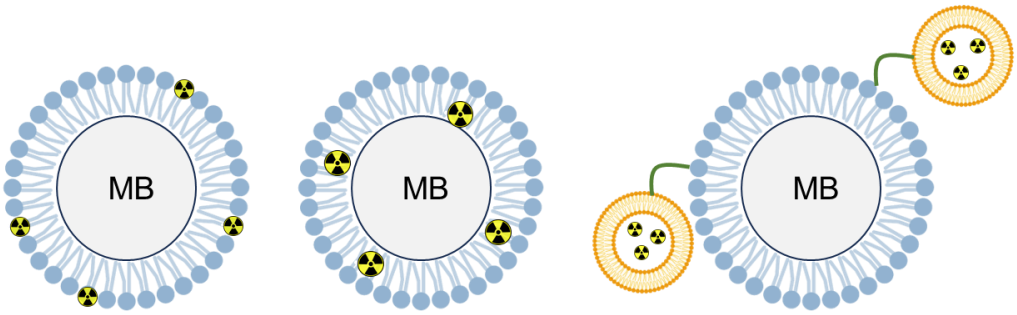

Figure 3.3: Graphical representation of radiolabelled microbubbles used with UMMD.

The first example was reported by Tartis *et al*. in 2008, where ^{18}F-labelled microbubbles were delivered to healthy mice for biodistribution studies.[28] For UMMD, one kidney was treated with therapeutic ultrasound pulses for over 20 min, and the other kidney was used as a control. Between the treated and untreated kidneys, only a small difference in radioactive accumulation was noted (less than 0.1 %ID/cm^3). However, the treated kidneys typically showed 15-20 % higher accumulation of radioactivity, demonstrating that sonoporation can increase the amount of lipids being delivered to the treatment region.

Later in 2014, Chung *et al*. reported the use of ^{68}Ga-labelled MBs in combination with UMMD for the detection of glioblastoma.[29] In this study, an integrin *α2β*1-targeted cyclic peptide was labelled with ^{68}Ga (^{68}Ga-A2B1), and incorporated into microbubble shells by hydrophobic interactions. The tumour uptake of ^{68}Ga-A2B1-MBs + US (2.62 %ID/g) was then compared to ^{68}Ga-A2B1 alone (1.48 %ID/g), and ^{68}Ga-A2B1 co-injected with MBs + US (2.25 %ID/g). In comparison to the ^{68}Ga-A2B1 group, ^{68}Ga-A2B1 + MB + US group gave a 1.51-fold increase in tumour uptake, and the ^{68}Ga-A2B1-MBs + US group gave a 1.76-fold increase. The slightly higher uptake of the ^{68}Ga-A2B1-MBs + US group compared to ^{68}Ga-A2B1 + MB + US group was attributed to the closer distance of the radiotracer to the microbubble cavitation events, which facilitated their extravasation to the target site.

More recently in 2020, Ingram *et al*. reported the use of VEGFR-targeted, ^{89}Zr-labelled liposome-microbubble complexes (^{89}Zr-VEGFR-LMC) as a proxy to investigate the delivery of cytotoxic drugs to tumours.[9] Apart from showing improved treatment efficacy using irinotecan-loaded liposome-microbubble complexes (Section 3.1.1), PET imaging was used to obtain a direct comparison of the delivery dose between ^{89}Zr-VEGFR-liposomes and ^{89}Zr-VEGFR-LMC + US. In the tumour, radioactive accumulation of the ^{89}Zr-VEGFR-LMC + US group was approximately twice that of the ^{89}Zr-VEGFR-liposome group. In addition, pharmacokinetic and distribution studies revealed that the liver to tumour ratio of ^{89}Zr-VEGFR-LMC + US was 3-fold less than ^{89}Zr-VEGFR-liposomes. Taken together with studies using irinotecan, the use of ultrasound and VEGFR-targeted LMC resulted in lower systemic circulation of the free drug and increased delivery to tumours. A lower dose of irinotecan was also sufficient for the LMC + US group (2 mg/kg) compared to liposomal irinotecan (3.75 mg/kg), which highlights the benefits of ultrasound-mediated microbubble destruction treatments with drug-loaded microbubbles compared to the systemic injection of free drugs.

In summary, these three studies showed that the use of radiolabelled microbubbles in combination with UMMD can increase the amount of radioactive accumulation at the target site. This provides a basis for the study conducted in this chapter, which aims to quantify the increase in deposition of radioactivity in tumours using the [^{18}F]AlF-MBs.

3.1.3 Aims and objectives

Using the [^{18}F]AlF-MBs produced in the Chapter 2, the primary aim of this chapter was to determine if there would be an increase in radioactive accumulation in tumours when a focused ultrasound pulse is applied (**Figure 3.4**), compared to control experiments without application of focused ultrasound.

In addition, the following objectives were identified:

A. Ultrasound imaging of the tumour to confirm microbubble perfusion and evaluate tumour vasculature.
B. Evaluation of the biodistribution of the [^{18}F]AlF-MBs.
C. Quantification if a sufficiently high amount of radioactivity is deposited in the tumour.

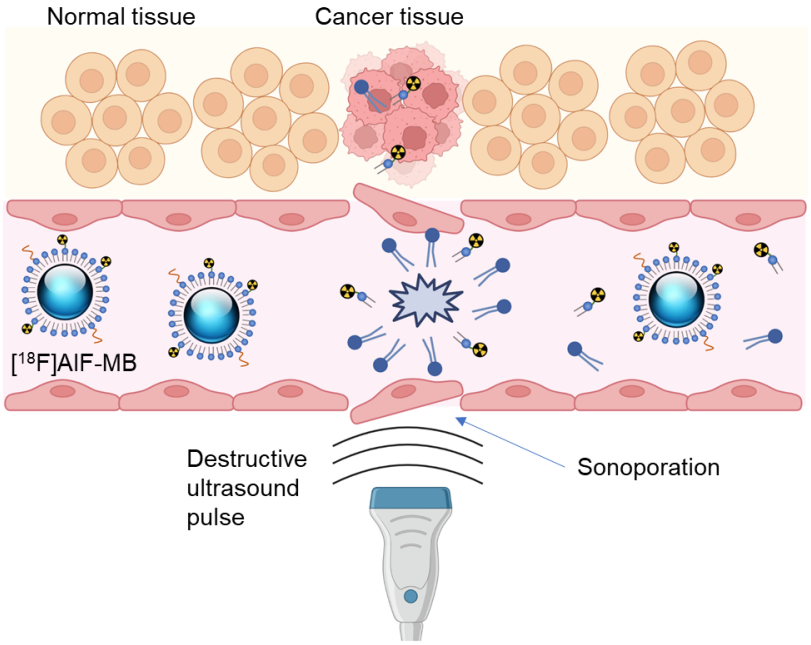

Figure 3.4: Schematic representation of sonoporation for increased radioactive deposition in tumours upon ultrasound-mediated microbubble destruction of [^{18}F]AlF-MBs.

For objective B, since a similar microbubble formulation and production method was used in the previously developed ^{68}Ga-MBs,[30] it is expected that [^{18}F]AlF-MBs would show a similar biodistribution to ^{68}Ga-MBs. For objective C, if a relatively high level of radioactivity is deposited in the tumour compared to other organs, incorporation of a therapeutic radioisotope (such as ^{177}Lu or ^{90}Y) onto the microbubbles could be explored.

3.2 Experimental set up

A graphical representation of the experimental set up is shown in **Figure 3.5**. U-2932 tumours (diffuse B-cell lymphoma) were implanted in the upper flank of the mice to allow unbiased visualisation by PET, away from organs receiving larger doses such as the liver, spleen and kidney. This also facilitates ultrasound imaging and treatment since the ultrasound transducer can be placed directly above the tumour (**Figure 3.5A**).

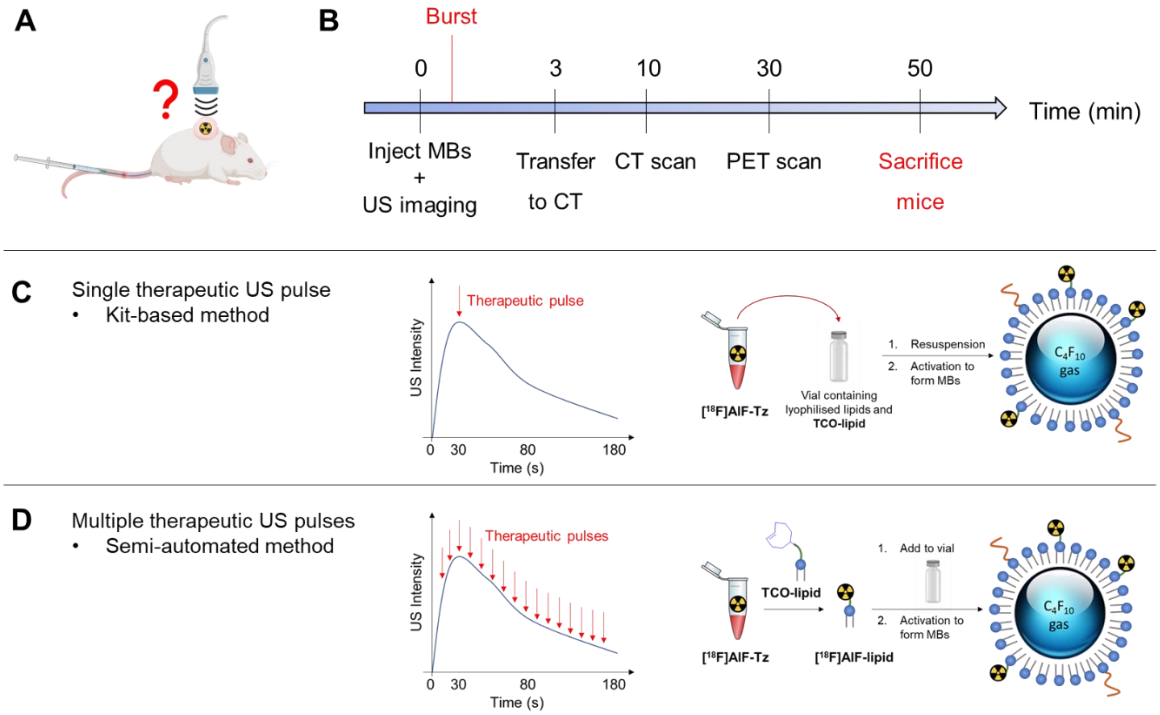

Figure 3.5: (A) Graphical representation of experimental set-up. (B) Experimental timeline, where bursting was carried out 30 s post-injection. (C) UMMD treatment with a single focused ultrasound pulse, carried out using microbubbles produced by the kit-based method. (D) UMMD treatment with multiple focused ultrasound pulses, carried out using microbubbles produced by the semi-automated method.

To minimise animal numbers, each mouse served as its own control. The control experiment without UMMD was carried out one day before the UMMD experiment to allow sufficient time for ^{18}F decay. Upon completion of the UMMD experiment, the mice were then sacrificed for *ex vivo* biodistribution analysis. The experimental timeline is shown in **Figure 3.5B**. Microbubble destruction (bursting) was carried out 30 s post injection because this was the time at which peak ultrasound enhancement is expected, with the expected intensity-time curve shown in **Figure 3.5C**.[31]

Two different sets of experiments were conducted: (i) treatment with a single focused ultrasound pulse, using [^{18}F]AlF-MBs produced by the kit-based method; and (ii) treatment

with multiple focused ultrasound pulses, using [^{18}F]AlF-MBs produced by the semi-automated approach (**Figure 3.5C** and **D**). The microbubble production approach was changed in the second experiment to minimise radioactive exposure, since [^{18}F]AlF-MBs had to be produced fresh prior to each injection.

3.3 Ultrasound imaging of [^{18}F]AlF-MBs in U2932 tumours

Three objectives were identified for ultrasound imaging and therapy: (a) microbubble destruction, (b) ultrasound imaging to verify microbubble perfusion in the tumour, and (c) super-resolution imaging to visualise tumour microvasculature. To determine if all three objectives could be achieved, three different ultrasound transducers were tested, (i) L11-4v, (ii) L22-14vx, and (iii) L12-3v. The results obtained are discussed in the subsequent sections.

3.3.1 Ultrasound imaging for single focused destruction pulse

Microbubble destruction and ultrasound imaging of microbubble perfusion was initially carried out using transducer (i), L11-4v. Focused ultrasound was performed with a transmit frequency of 4 MHz and a mechanical index (MI) of 1.5, below the FDA-approved limit of 1.9 to minimise tissue damage.[32] Concurrently, ultrasound imaging was performed at a transmit frequency of 8 MHz, at MI = 0.1. However, processing of the ultrasound images revealed poor signal to noise ratio (**Figure 3.6**), where microbubble perfusion in the tumour could not be accurately quantified.

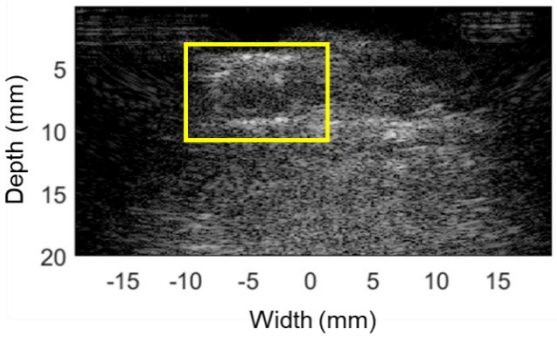

Figure 3.6: Representative ultrasound image following microbubble injection using transducer (i), L11-4v, showing poor signal to noise ratio. Tumour is delineated by the yellow box.

To address this, transducer (ii), L22-14vx, was used, which allows ultrasound imaging at higher frequency of 15 MHz, at a similar mechanical index (MI = 0.08). Transducer (ii) enabled clear visualisation of the tumour with minimal background noise (**Figure 3.7A**). Upon injection of microbubbles, increased intensity was observed in the maximum intensity projection image along the edge of the tumour (**Figure 3.7B**), which represents microbubble perfusion. To enable differentiation between ultrasound signals arising from the tissue and microbubbles, clutter-filtering was applied (**Figure 3.7C**), which revealed microbubble perfusion within the

tumour. However, super-resolution imaging for visualisation of the tumour microvasculature could not be achieved from the same dataset, due to differences in ultrasound parameters used in perfusion imaging and super-resolution imaging.[31,33,34]

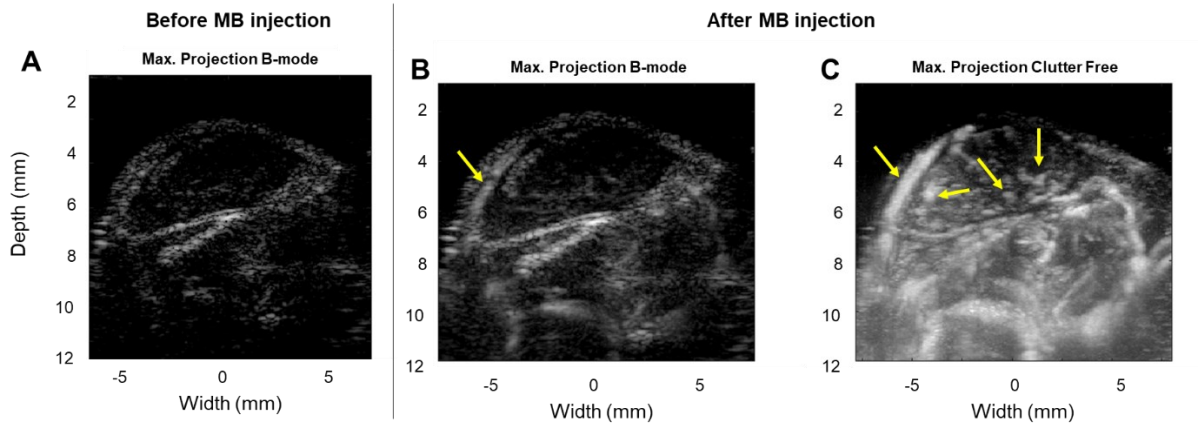

Figure 3.7: Representative ultrasound images using transducer (ii), L22-44vx, showing clear delineation of the tumour. Microbubbles denoted by yellow arrows.

Nevertheless, these experiments revealed several key results and learning points. Firstly, transducer (i) was not ideal for imaging tumours approximately 100 mm^3 in size due to its large field of view. Next, microbubble perfusion in the tumour was confirmed with transducer (ii), but concurrent perfusion imaging and super-resolution imaging was not achieved. Lastly, although transducer (ii) allows excellent imaging of the tumour, it is unsuitable for microbubble destruction studies, which requires focusing ultrasound waves of higher pressures. Thus, a different transducer was required.

3.3.2 Ultrasound imaging for multiple focused destruction pulses

To enable simultaneous perfusion imaging and microbubble destruction, transducer (iii), L12-3v, was used. With a transmission frequency of 11 MHz and MI = 0.1, clear visualisation of the tumour was obtained (**Figure 3.8A**). However, upon processing the ultrasound data, no bubbles were observed in the ultrasound images. The corresponding intensity-time curves (**Figure 3.8B** and **C**) also did not show the expected microbubble wash-in and wash out trends observed in the same tumour.[31]

Two potential reasons were identified. Firstly, necrosis could prevent perfusion of the [18F]AlF-MBs into the tumour. This could be analysed by histological staining of the tumour sections (Section 3.5.3). Secondly, the [18F]AlF-MBs produced using the semi-automated approach could have a different size and charge profile compared to the kit-based approach. Although precise characterisation and comparison of the [18F]AlF-MBs produced using the two approaches were not possible due to practical limitations (microscope/zetasizer for radioactive

samples not available), comparison of the biodistribution of the [^{18}F]AlF-MBs would provide information on whether they have identical characteristics.

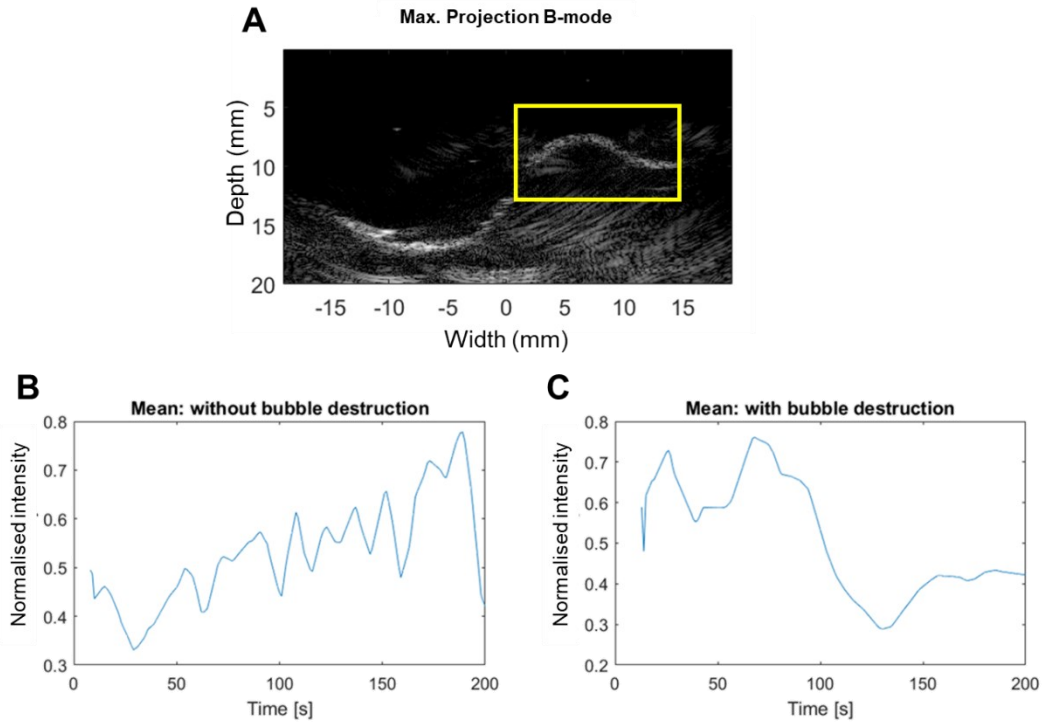

Figure 3.8: (A) Representative ultrasound image using transducer (iii), where tumour is delineated by the yellow box. Normalised intensity-time curves (B) without microbubble destruction and (C) with microbubble destruction, both not showing the expected trends (*n* = 4).

3.4 *In vivo* and e*x vivo* biodistribution of [^{18}F]AlF-MBs after UMMD

3.4.1 *Ex vivo* biodistribution of [^{18}F]AlF-MBs after UMMD

The *ex vivo* biodistribution of the [^{18}F]AlF-MBs are shown in **Figure 3.9**. Although the differences in radioactive accumulation in the respective tissues/organs were not statistically significant, several key differences could be identified. For [^{18}F]AlF-MBs produced using the kit-based approach, radioactive accumulation were highest in the urine, spleen, liver and lungs (38.4 ± 25.7, 34.2 ± 21.0, 20.5 ± 6.4, and 16.6 ± 11.7 %ID/g respectively). The relatively high radioactive accumulation in the urine and lung could be explained by the fact that microbubbles are eliminated through the renal and respiratory pathways,[28,35] whereas accumulation in the spleen and liver can be attributed to uptake by splenic macrophages and hepatic Kupffer cells.[35–37]

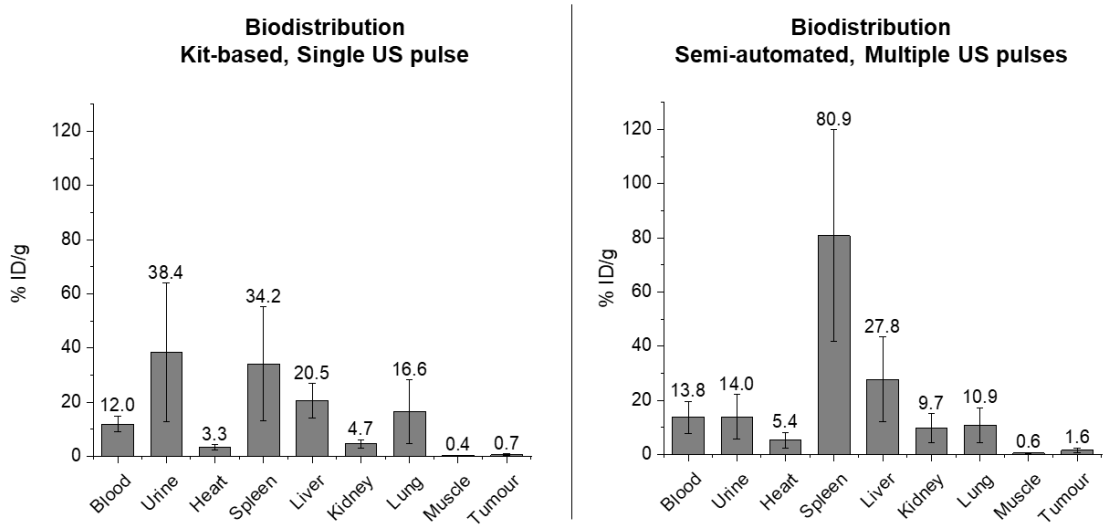

Figure 3.9: *Ex vivo* biodistribution of the [18F]AlF-MBs in the two experiments. Data presented as mean ± SD, where *n* = 4.

In comparison, [18F]AlF-MBs produced using the semi-automated approach showed significantly higher radioactive accumulation in the spleen (80.9 ± 39.1 %ID/g), followed by the liver (27.8 ± 15.7 %ID/g), compared to the other tissues. One possible explanation for the difference in biodistributions for the two approaches is the increased tetrazine-TCO conjugation time in the semi-automated approach, where the [18F]AlF-lipid was synthesised prior to the generation of [18F]AlF-MBs. Since [18F]AlF-lipid or TCO-lipid forms up to 10 mol% of the microbubble shell, this could potentially affect the zeta potential and/or size distribution of the [18F]AlF-MBs generated. Despite the large size of these lipid-shelled vehicles, it has been shown that a slight variation of their shell composition could affect their distributions.[38,39]

Nevertheless, the biodistribution of the [18F]AlF-MBs produced using the kit-based approach showed similar trends to that of the 68Ga-MBs produced by Hernandez *et al.*, where radioactive accumulation was also highest in the urine (57 ± 11 %ID/g), liver (47 ± 4 %ID/g), spleen (40 ± 2 %ID/g) and lung (*ca*. 20 %ID/g).[30] Notably, in the 68Ga-MB formulation, the negatively-charged DPPA was not used. In contrast, the high splenic uptake observed for the [18F]AlF-MBs produced using the semi-automated approached was similar to that observed for the 18F-MBs produced by Tartis *et al.*, which includes DPPA in their formulation.[28] This was in agreement with the findings obtained by Kranz *et al*., where a more negative zeta potential has been shown to increase splenic uptake of lipid-based vehicles.[40]

For both approaches, radioactive accumulation in the tumour was low after UMMD (kit-based: 0.7 ± 0.4 %ID/g, semi-automated: 1.6 ± 1.0 %ID/g). This translated to low tumour-to-muscle ratios (kit-based: 1.8 ± 0.5, semi-automated: 2.7 ± 0.6). Since no [18F]AlF-MBs were observed in the tumour using the semi-automated approach, it is difficult to ascertain whether the

increase in radioactive accumulation was due to the increase in number of focused ultrasound pulses. Also, red blood cell extravasation was observed in the tumours treated by the multiple ultrasound pulses, which could potentially explain the higher radioactive dose obtained.

Three potential reasons were identified for the low radioactive dose delivered to the tumours: (i) a large fraction of the microbubbles injected do not reach the target site, as they mainly accumulate in the liver and other excretion pathways; (ii) microbubbles have a short circulation time, and hence do not have sufficient time to accumulate in the target site; and (iii) only a 2-dimensional region of the tumour was insonified. This was an inherent limitation that resulted from the experimental design, because one of the objectives of this study was to use diagnostic ultrasound imaging to characterise microbubble perfusion and tumour vasculature. Thus, one potential improvement would be to use an ultrasound transducer that allows 3-dimensional insonation across the whole tumour volume to increase ultrasound-mediated microbubble destruction and sonoporation.

3.4.2 Comparison of healthy organ uptakes between control and UMMD experiment

Representative *in vivo* PET images are shown in **Figure 3.10**. The high radioactive accumulation observed in the liver and spleen concur with the *ex vivo* distribution studies. Expectedly, no contrast was observed in the tumours due to the relatively low radioactive dose delivered.

Upon recovery from the control experiment, the mice experienced a slight loss in weight (6.8 ± 2.6 %). Hence, radioactive accumulation in three healthy organs (lungs, heart and liver) was first examined to determine if there was a change in physiological behaviour of the mice between the control and UMMD experiments. The heart was chosen because it was located distally from the tumour and ultrasound transducer, where radioactive accumulation could potentially be affected by ultrasound waves. The lungs and liver were chosen since these are the main excretion pathways for microbubbles.[28,41]

To compare between the control and UMMD experiments, the accumulated radioactivity in each organ was normalised to that of the leg muscle. From the time-activity curves (TACs), the radioactive uptake in each organ remained constant across the 20-min scan period for all cases (**Figure 3.11**). This was expected, since the PET scans were carried out 30 min after microbubble injection, and microbubbles have been shown to be cleared from the circulation within 10-20 mins.[28,36,42] As a consequence of ultrasound and CT imaging being conducted prior to PET imaging, evaluation of the initial pharmacokinetic profiles of the [^{18}F]AlF-MBs was not possible.

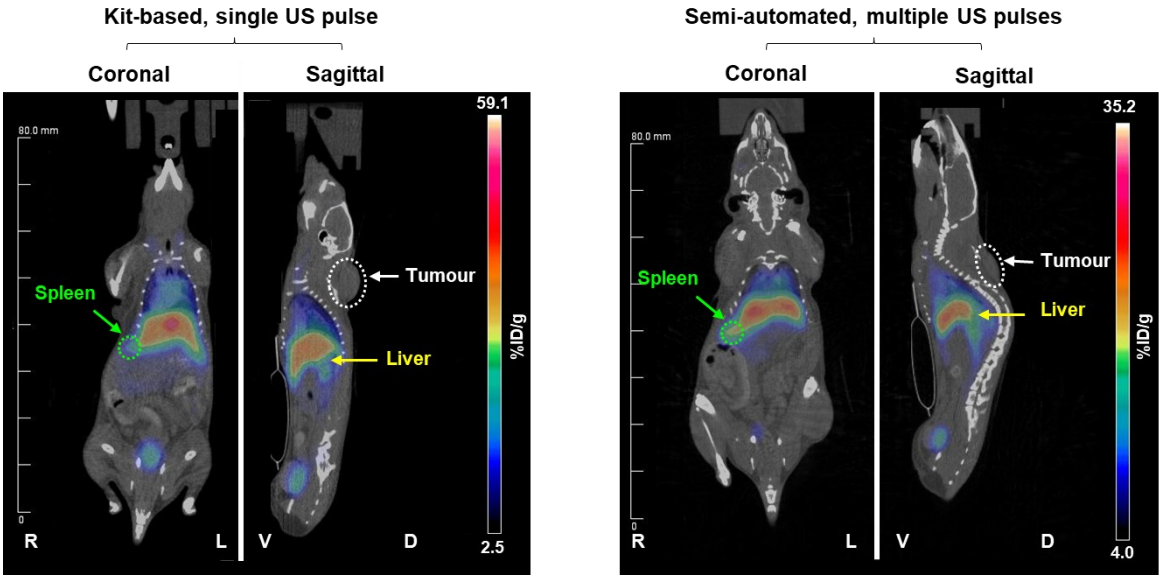

Figure 3.10: Representative maximum intensity projection PET images of [^{18}F]AlF-MB for the two experiments, showing high uptake in the liver and spleen. Data are representative of 4 mice.

Since the time-activity curves of each organ remained constant over time, the organ uptake values for each mouse were time-averaged and compared (**Figure 3.12**). Gratifyingly, between the control and UMMD experiment, the differences in organ-to-muscle ratio were not significant in all cases. Such a result indicated that the application of destructive ultrasound pulses did not significantly affect the uptake of [^{18}F]AlF-MB in non-insonated tissues. Notably, the similar uptake values in the heart suggest that focused ultrasound pulses were delivery specifically to the tumour, minimising off-target effects. This was a necessary consideration since UMMD has been shown to induce thermal and mechanical effects in tissues.[13,43] For the semi-automated approach, the high interquartile range obtained for the liver-to-muscle ratio in the control experiment (**Figure 3.12**, far right) was skewed by the value of one mouse, though this did not affect the conclusion obtained.

Nevertheless, comparison of the radioactive dose delivered to the healthy organs suggest that despite experiencing a loss in weight after the control experiment, the uptake of [^{18}F]AlF-MBs remains unaffected. Hence, a difference in tumour uptake of [^{18}F]AlF-MBs between the control and UMMD experiments would likely be due to the effect of ultrasound treatment and sonoporation, rather than a change in mouse physiology.

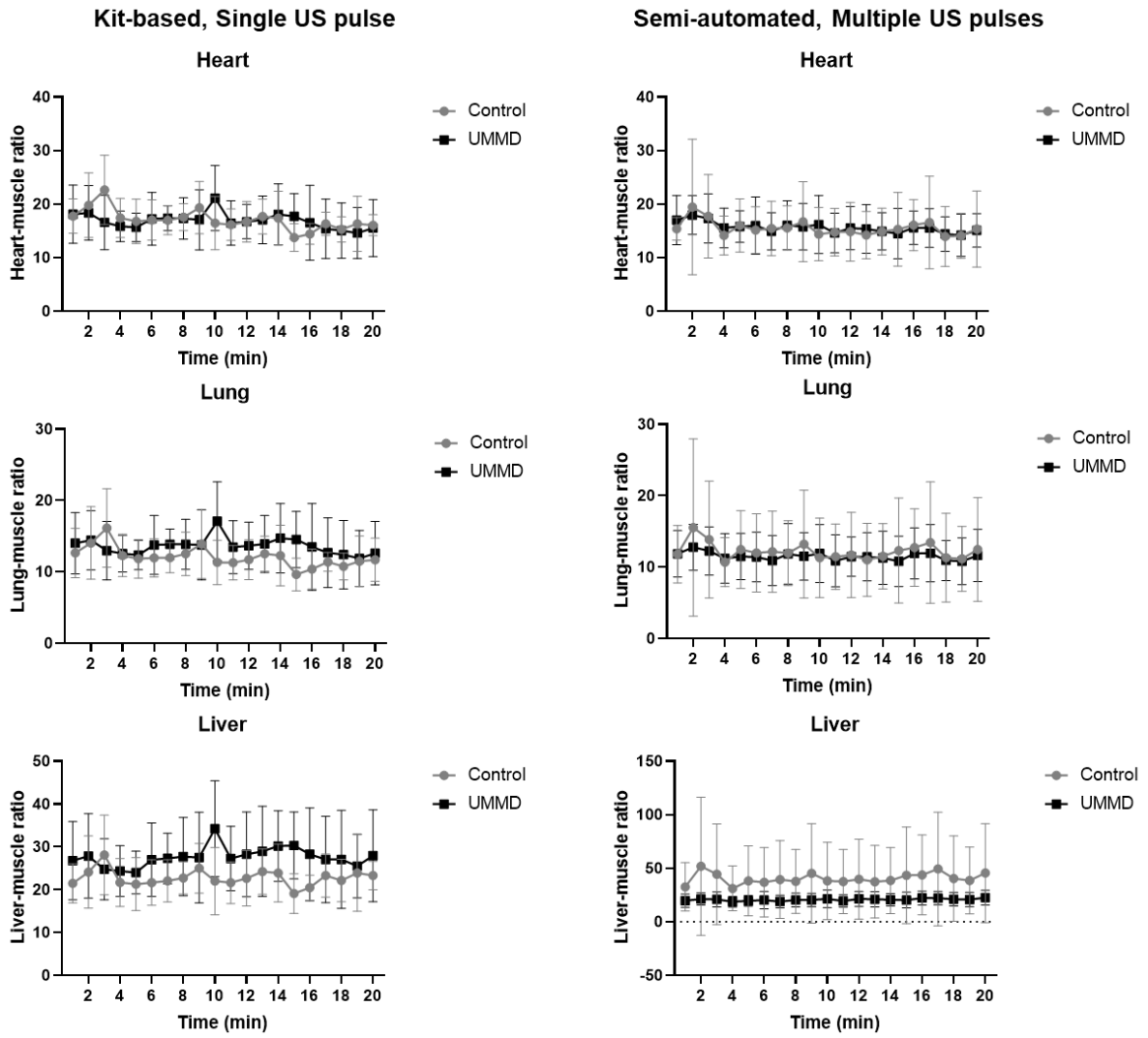

Figure 3.11: Time-activity curves of healthy organs after normalisation to muscle uptake, showing constant radioactive uptake across the 20-min imaging period. Data presented as mean ± SD, n = 4.

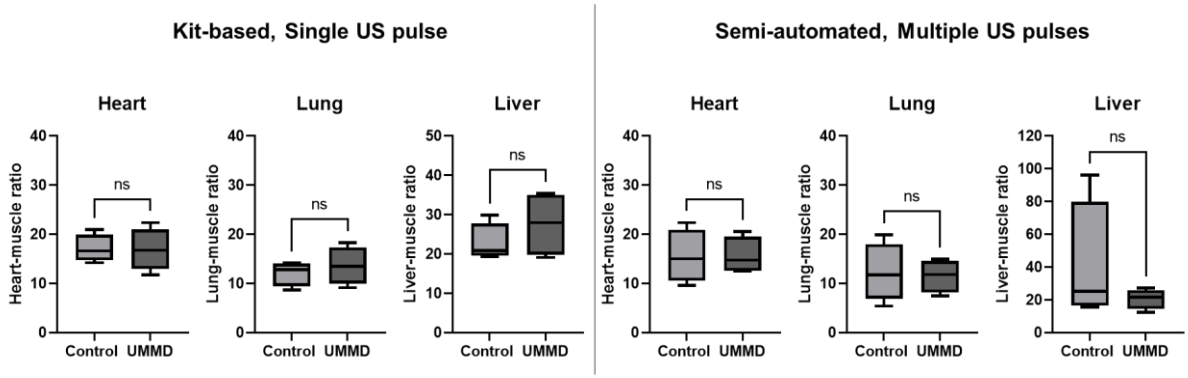

Figure 3.12: Comparison of organ-to-muscle ratio between control and UMMD experiments, where all cases showed a non-significant difference. Box plots were generated using time-averaged values for each mouse (n = 4). Statistical analyses were conducted using paired t-tests.

3.5 Radioactive accumulation in tumours following UMMD

3.5.1 Delivery of [^{18}F]AlF-MBs to tumour following single ultrasound destructive pulse

As observed in other organs, radioactive accumulation in the tumour remained constant over time (**Figure 3.13A**). Thus, the tumour uptake values for each mouse were time-averaged and compared (**Figure 3.13B**). Importantly, a statistically significant increase (p < 0.05) was observed in the tumour following UMMD when compared to the control experiment. In addition, when analysed individually, a significant increase in radioactive accumulation was observed in each mouse (**Figure 3.13C**), showing that UMMD is effective in increasing the amount of [^{18}F]AlF-MBs delivered to tumours.

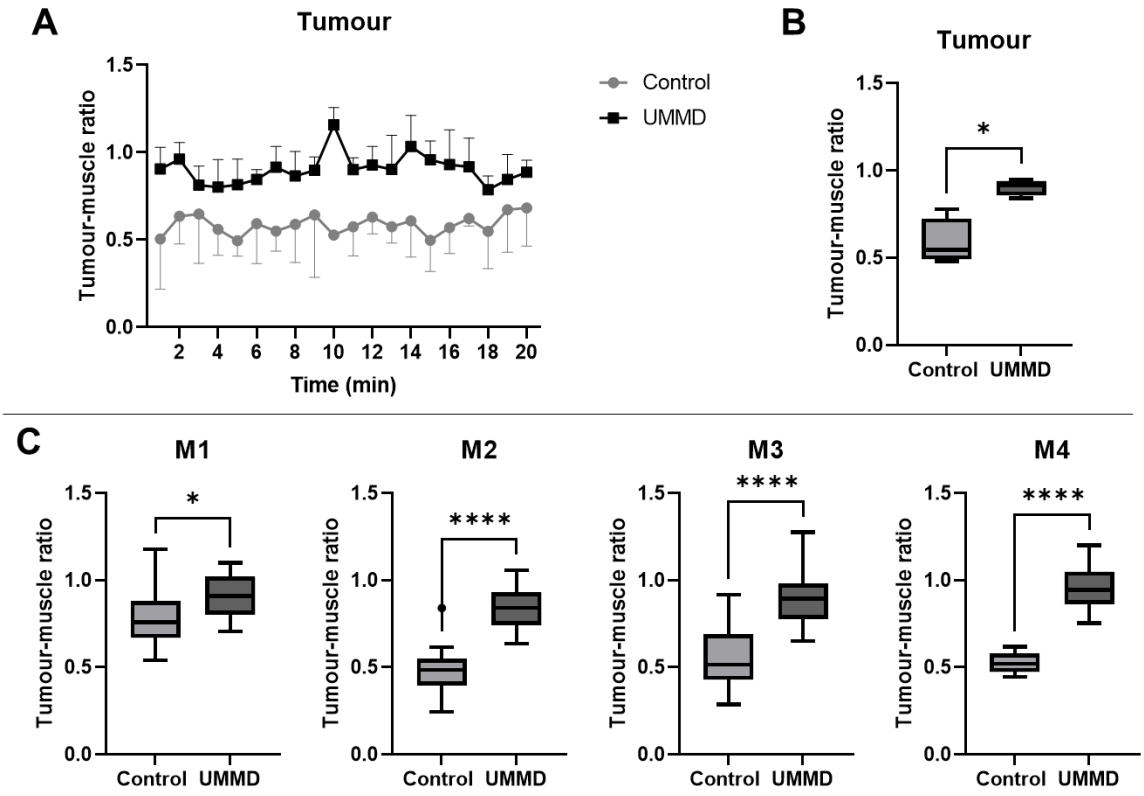

Figure 3.13: Comparison of radioactive accumulation of [^{18}F]AlF-MBs in tumours after a single ultrasound destruction pulse to control experiment without microbubble destruction. (A) Time-activity curve normalised by muscle uptake. Data presented as mean ± SD, n = 4. (B) Box plot comparing radioactive accumulation in tumours for all 4 mice. (C) Box plots comparing radioactive accumulation in individual mice, generated using 20 data points collected over a duration of 20 min. Statistical analyses were conducted using paired t-tests.

On average, radioactive accumulation increased by 58.7 ± 28.4 %, which was higher than the 15-20 % increase observed by Tartis *et al*. when UMMD was carried out in the kidneys. Although Chung *et al*. observed an almost 2-fold increase in tumour accumulation, this was

done using a 3-D ultrasound transducer, and microbubbles loaded with a targeted peptide tracer (^{68}Ga-A2B1),[29] which offers additional active targeting to receptors. In comparison, the [^{18}F]AlF-lipid released does not offer receptor targeting capabilities.

However, the tumour-to-muscle ratios obtained were low (Control: 0.58 ± 0.13, UMMD: 0.90 ± 0.04), which was expected given the low contrast observed in the PET images. Although this was slightly different to the value obtained from the *ex vivo* biodistribution study after UMMD (UMMD: 1.8 ± 0.5, control not available since the mice were allowed to recover), the difference between *in vivo* and *ex vivo* values could be attributed to fluid loss when the organs were harvested.[28] Nonetheless, both values indicated that the amount of radioactivity deposited in the tumour was low. As mentioned previously (Section 3.4.1), one possible reason is that only a 2-dimensional region of the tumour was insonified. Furthermore, only a single focused ultrasound pulse was delivered to induce microbubble destruction in this study. In comparison, Tartis *et al*. and Chung *et al*. reported sonication durations lasting 20 min and 120 s respectively,[28,29] significantly longer than that used in this study. Thus, to improve the accumulation of radioactivity in the tumours, the next section explores a longer ultrasound treatment duration.

3.5.2 Delivery of [^{18}F]AlF-MBs to tumour following multiple ultrasound destructive pulses

An identical analysis was carried out to that in the previous section. Expectedly, radioactive accumulation in the tumour remained constant with time (**Figure 3.14A**), which enabled subsequent statistical comparisons. Surprisingly, it was found that the difference in radioactive uptake between the control and UMMD experiment was not significant (**Figure 3.14B**). In fact, when data for each individual mice was examined, three out of the four mice showed a significant decrease in uptake (**Figure 3.14C**). On average, an 8.2 % decrease in radioactivity was observed upon UMMD compared to the control. This seemingly contradicts the experiment hypothesis, where increasing the duration of the focused ultrasound treatment was expected to increase the number of microbubble inertial cavitation events, and hence the amount of radioactivity deposited.

However, the overall difference between the control and UMMD experiments was not significant. Taken together with the fact that no microbubbles were observed in the tumours by ultrasound imaging (Section 3.3.2), it is likely that ultrasound-mediated microbubble destruction did not occur. Without the presence of microbubbles to induce sonoporation, it has been shown that treatment efficacy remains the same, with or without focused ultrasound treatment.[9,15,20] Furthermore, histological analysis of the tumour (next section, section 3.5.3) revealed that tumour morphology was not the cause of the difference in radioactive uptake.

Therefore, to enable a more definitive conclusion to be drawn, this study could be repeated with the following changes:

(i) Production of microbubbles carried out using the kit-based approach.

(ii) Use of ultrasound transducer (i), L11-4v, for focused ultrasound treatment – consistent with the study on UMMD with a single focused ultrasound pulse.

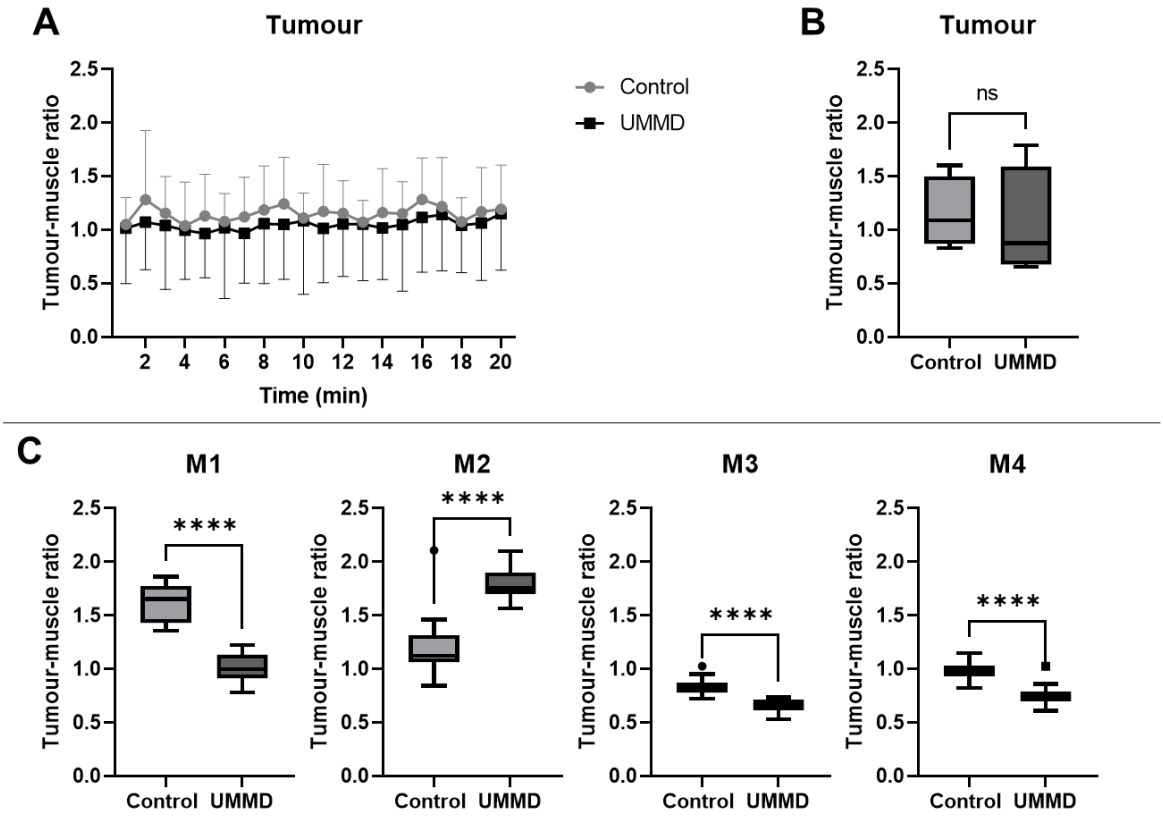

Figure 3.14: Comparison of radioactive accumulation of [^{18}F]AlF-MBs in tumours after a multiple ultrasound destruction pulses to control experiment without microbubble destruction. (A) Time-activity curve normalised by muscle uptake. Data presented as mean ± SD, *n* = 4. (B) Box plot comparing radioactive accumulation in tumours for all 4 mice. (C) Box plots comparing radioactive accumulation in individual mice, generated using 20 data points collected over a duration of 20 min. Statistical analyses were conducted using paired *t*-tests.

3.5.3 Tumour morphology

Finally, to confirm that variations in tumour morphology was not the cause of the different results obtained in the two studies, histological analysis was carried out. The excised tumours were stained with haematoxylin & eosin (H&E), which revealed the key characteristics of diffuse large B cell lymphoma, where vesicular chromatin and membrane-bound nucleoli were identified in whole the field of view (**Figure 3.15**).[44] Notably, necrosis was not observed,

suggesting that this was not the reason for the low radioactive dose delivered to the tumours in both studies.

Importantly, the tumour morphologies observed were consistent between the two studies. Combined with the fact that radioactive accumulation in the healthy organs (liver, lung and heart) were not significantly different, it is likely that the difference in results obtained was due to the change in microbubble production method and ultrasound transducer used.

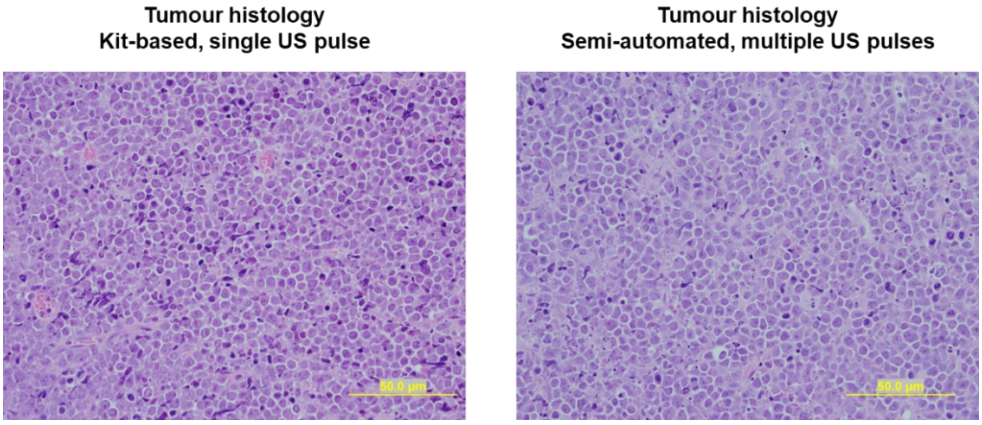

Figure 3.15: Representative images of the excised tumours after haematoxylin & eosin staining, showing the expected characteristics of a diffuse large B cell lymphoma. Scale bar represents 50 µm.

3.6 Conclusions

The evaluation of three different ultrasound transducers and imaging parameters allowed the identification of a diagnostic ultrasound transducer that enables concurrent focused ultrasound treatment and perfusion imaging. With the confirmation of microbubble perfusion in the tumours by ultrasound imaging, ultrasound-mediated microbubble destruction was used to increase radioactive uptake of the [^{18}F]AlF-MBs. Following focused ultrasound treatment using a single focused ultrasound pulse, a significant increase (58.7 ± 28.4 %) in radioactive uptake in the tumour was achieved when compared to control experiments without ultrasound treatment.

In addition, biodistribution studies were carried out on the [^{18}F]AlF-MBs produced using the kit-based approach and semi-automated approach. [^{18}F]AlF-MBs produced using the kit-based approach showed high uptakes in the urine, spleen, liver and lungs, consistent with microbubble elimination pathways. Although the [^{18}F]AlF-MBs produced using the semi-automated approach showed a slightly different biodistribution, with significantly higher uptakes in the spleen, this was consistent with previous observations that microbubbles are eliminated by splenic macrophages. Presumably, the different distributions observed for the [^{18}F]AlF-MBs produced using both approaches could be due to the final composition of the [^{18}F]AlF-MBs. A higher fraction of [^{18}F]AlF-lipid is expected to be present in the microbubbles produced using the semi-automated approach, since additional reaction time was allowed for the TCO-tetrazine conjugation. To elucidate this, non-radioactive AlF-Tz could be synthesised to enable more accurate characterisation of the [^{18}F]AlF-MBs generated using both approaches. More significantly, no microbubbles were observed in the tumours for [^{18}F]AlF-MBs produced using the semi-automated approach, which undermines the conclusions that could be drawn from this experiment.

Nevertheless, comparison of radioactive uptakes in healthy organs showed that the application of UMMD does not significantly affect the distribution of [^{18}F]AlF-MBs. The similar uptakes in the heart, located distally from the ultrasound transducer, showed that focused ultrasound was delivered specifically to the tumour.

Finally, three of the four chapter aims were achieved: (i) increasing radioactive uptake in the tumour by UMMD, (ii) evaluation of microbubble perfusion by ultrasound imaging, and (iii) analysis [^{18}F]AlF-MB biodistribution. Although the final aim of delivering a sufficiently high radioactive dose to the tumours was not achieved, further work could be carried out to improve this, which are outlined in the next section.

3.7 Future work

A major practical limitation was identified for the experiments conducted in this study – focused ultrasound pulses were applied in a 2D plane. This was to allow concurrent ultrasound imaging and destruction of the microbubbles. Since the perfusion of [^{18}F]AlF-MBs in the tumours has been confirmed in this experiment, future studies could first explore the use of a 3-D ultrasound transducer designed for focused ultrasound treatment.[29]

Next, an active targeting group for VEGFR2 could be included in the [^{18}F]AlF-MBs to improve localisation of radioactivity in the tumour. This was because Fan *et al*. showed that active targeting further increases the amount of drug delivered to tumours when compared to using UMMD alone.[17] To increase circulation time, and enable enhanced extravasation using the enhanced permeability and retention (EPR) effect, the [^{18}F]AlF-labelled nanobubbles produced in the previous chapter could also be investigated for this purpose.

Finally, once a sufficient radioactive dose could be delivered to the tumours, incorporation of a therapeutic radioisotope in place of the [^{18}F]AlF complex could be explored. Since radiolabelling of the [^{18}F]AlF-MBs takes place via a chelator-based approach followed by tetrazine-TCO conjugation, incorporation of radiometals such as ^{177}Lu or ^{90}Y will likely be feasible using a DOTA-functionalised tetrazine.

3.8 References

1 J. Wischhusen and F. Padilla, *IRBM*, 2019, 40, 10–15.

2 C. F. Caskey, X. Hu and K. W. Ferrara, *J. Control. Release*, 2011, 156, 297–306.

3 V. Uhlendorf, *Encycl. Diagnostic Imaging*, 2008, 1361–1362.

4 G. Peruzzi, G. Sinibaldi, G. Silvani, G. Ruocco and C. M. Casciola, *Colloids Surfaces B Biointerfaces*, 2018, **168**, 83–93.

5 S. Al-Jawadi and S. S. Thakur, *Int. J. Pharm.*, 2020, **585**, 119559.

6 T.-Y. Wang, K. E. Wilson, S. Machtaler and J. K. Willmann, *Curr. Pharm. Biotechnol.*, 2014, **14**, 743-752.

7 D. L. Miller and J. Quddus, *Ultrasound Med. Biol.*, 2000, **26**, 661–667.

8 H. Chen and J. H. Hwang, *J. Ther. Ultrasound*, 2013, **1**, Article no. 10.

9 N. Ingram, L. E. Mcveigh, R. H. Abou-Saleh, J. Maynard, S. A. Peyman, J. R. Mclaughlan, M. Fairclough, G. Marston, E. M. A. Valleley, J. L. Jimenez-Macias, A. Charalambous, W. Townley, M. Haddrick, A. Wierzbicki, A. Wright, M. Volpato, P. B. Simpson, D. E. Treanor, N. H. Thomson, P. M. Loadman, R. J. Bushby, B. R. G. Johnson, P. F. Jones, J. A. Evans, S. Freear, A. F. Markham, S. D. Evans and P. Louise Coletta, *Theranostics*, 2020, **10**, 10973–10992.

10 G. Dimcevski, S. Kotopoulis, T. Bjånes, D. Hoem, J. Schjøt, B. T. Gjertsen, M. Biermann, A. Molven, H. Sorbye, E. McCormack, M. Postema and O. H. Gilja, *J. Control. Release*, 2016, **243**, 172–181.

11 X. Liang, Y. Xu, C. Gao, Y. Zhou, N. Zhang and Z. Dai, *NPG Asia Mater.*, 2018, **10**, 761–774.

12 I. Lentacker, S. C. De Smedt and N. N. Sanders, *Soft Matter*, 2009, **5**, 2161–2170.

13 J. M. Escoffre, C. Mannaris, B. Geers, A. Novell, I. Lentacker, M. Averkiou and A. Bouakaz, *IEEE Trans. Ultrason. Ferroelectr. Freq. Control*, 2013, **60**, 78–87.

14 Z. Deng, F. Yan, Q. Jin, F. Li, J. Wu, X. Liu and H. Zheng, *J. Control. Release*, 2014, **174**, 109–116.

15 F. Yan, L. Li, Z. Deng, Q. Jin, J. Chen, W. Yang, C. K. Yeh, J. Wu, R. Shandas, X. Liu and H. Zheng, *J. Control. Release*, 2013, **166**, 246–255.

16 C. Y. Ting, C. H. Fan, H. L. Liu, C. Y. Huang, H. Y. Hsieh, T. C. Yen, K. C. Wei and C.

K. Yeh, *Biomaterials*, 2012, **33**, 704–712.

17 C. H. Fan, C. Y. Ting, H. J. Lin, C. H. Wang, H. L. Liu, T. C. Yen and C. K. Yeh, *Biomaterials*, 2013, **34**, 3706–3715.

18 P. Li, Y. Zheng, H. Ran, J. Tan, Y. Lin, Q. Zhang, J. Ren and Z. Wang, *J. Control. Release*, 2012, **162**, 349–354.

19 S. T. Ren, Y. R. Liao, X. N. Kang, Y. P. Li, H. Zhang, H. Ai, Q. Sun, J. Jing, X. H. Zhao, L. F. Tan, X. L. Shen and B. Wang, *Pharm. Res.*, 2013, **30**, 1574–1585.

20 J. Kang, X. Wu, Z. Wang, H. Ran, C. Xu, J. Wu, Z. Wang and Y. Zhang, *J. Ultrasound Med.*, 2010, **29**, 61–70.

21 S. Tinkov, G. Winter, C. Coester and R. Bekeredjian, *J. Control. Release*, 2010, **143**, 143–150.

22 S. Tinkov, C. Coester, S. Serba, N. A. Geis, H. A. Katus, G. Winter and R. Bekeredjian, *J. Control. Release*, 2010, **148**, 368–372.

23 H. Liu, S. Chang, J. Sun, S. Zhu, C. Pu, Y. Zhu, Z. Wang and R. X. Xu, *Mol. Pharm.*, 2014, **11**, 40–48.

24 M. J. Ratain, *J. Clin. Oncol.*, 2002, **20**, 7–8.

25 T. Tsuruo, H. Iida, S. Tsukagoshi and Y. Sakurai, *Cancer Res.*, 1981, **41**, 1967–1972.

26 J. Blesa, J. A. Pineda-Pardo, K. I. Inoue, C. Gasca-Salas, T. Balzano, N. L. G. Del Rey, A. Reinares-Sebastián, N. Esteban-García, R. Rodríguez-Rojas, R. Márquez, M. Ciorraga, M. Del Álamo, L. García-Cañamaque, S. Ruiz de Aguiar, I. Rachmilevitch, I. Trigo-Damas, M. Takada and J. A. Obeso, *Sci. Adv.*, 2023, **9**, eadf4888.

27 R. Rodriguez-Rojas, J. A. Pineda-Pardo, R. Martinez-Fernandez, R. V. Kogan, C. A. Sanchez-Catasus, M. del Alamo, F. Hernández, L. García-Cañamaque, K. L. Leenders and J. A. Obeso, *Eur. J. Nucl. Med. Mol. Imaging*, 2020, **47**, 425–436.

28 M. S. Tartis, D. E. Kruse, H. Zheng, H. Zhang, A. Kheirolomoom, J. Marik and K. W. Ferrara, *J. Control. Release*, 2008, **131**, 160–166.

29 Y. H. Chung, P. H. Hsu, C. W. Huang, W. C. Hsieh, F. T. Huang, W. C. Chang, H. Chiu, S. T. Hsu and T. C. Yen, *Mol. Pharm.*, 2014, **11**, 3904–3914.

30 J. Hernández-Gil, M. Braga, B. I. Harriss, L. S. Carroll, C. H. Leow, M.-X. Tang, E. O. Aboagye and N. J. Long, *Chem. Sci.*, 2019, **10**, 5603–5615.

31 M. Braga, C. H. Leow, J. H. Gil, J. H. Teh, L. Carroll, N. J. Long, M. X. Tang and E. O. Aboagye, *PLoS One*, 2021, **16**, e0260186.

32 S. B. Barnett, G. R. Ter Haar, M. C. Ziskin, H. D. Rott, F. A. Duck and K. Maeda, *Ultrasound Med. Biol.*, 2000, **26**, 355–366.

33 K. Riemer, M. Toulemonde, J. Yan, M. Lerendegui, E. Stride, P. D. Weinberg, C. Dunsby and M. X. Tang, *IEEE Trans. Med. Imaging*, 2023, **42**, 1056-1067.

34 K. Christensen-Jeffries, O. Couture, P. A. Dayton, Y. C. Eldar, K. Hynynen, F. Kiessling, M. O'Reilly, G. F. Pinton, G. Schmitz, M. X. Tang, M. Tanter and R. J. G. van Sloun, *Ultrasound Med. Biol.*, 2020, **46**, 865–891.

35 S. Sirsi, J. Feshitan, J. Kwan, S. Homma and M. Borden, *Ultrasound Med. Biol.*, 2010, **36**, 935-948.

36 J. K. Willmann, Z. Cheng, C. Davis, A. M. Lutz, M. L. Schipper, C. H. Nielsen and S. S. Gambhir, *Radiology*, 2008, **249**, 212–219.

37 S. Ibsen, C. E. Schutt and S. Esener, *Drug Des. Devel. Ther.*, 2013, 7, 375–388.

38 G. Wang, M. Zannikou, L. Lofchy, Y. Li, H. Gaikwad, I. V. Balyasnikova and D. Simberg, *ACS Nano*, 2021, **15**, 11880-11890.

39 R. Münter, K. Kristensen, D. Pedersbæk, J. B. Larsen, J. B. Simonsen and T. L. Andresen, *Nanoscale*, 2018, **10**, 22720–22724.

40 L. M. Kranz, M. Diken, H. Haas, S. Kreiter, C. Loquai, K. C. Reuter, M. Meng, D. Fritz, F. Vascotto, H. Hefesha, C. Grunwitz, M. Vormehr, Y. Hüsemann, A. Selmi, A. N. Kuhn, J. Buck, E. Derhovanessian, R. Rae, S. Attig, J. Diekmann, R. A. Jabulowsky, S. Heesch, J. Hassel, P. Langguth, S. Grabbe, C. Huber, Ö. Türeci and U. Sahin, *Nature*, 2016, **534**, 396–401.

41 V. Paefgen, D. Doleschel and F. Kiessling, *Front. Pharmacol.*, 2015, 6.

42 A. H. Liao, S. Y. Wu, H. E. Wang, C. H. Weng, M. F. Wu and P. C. Li, *Ultrasonics*, 2013, **53**, 320–327.

43 S. B. Keller and M. A. Averkiou, *Bioconjug. Chem.*, 2022, **33**, 1049–1056.

44 Y. Xie, S. Pittaluga and E. S. Jaffe, *Semin. Hematol.*, 2015, **52**, 57–66.

Chapter 4: Development of new chelators for $[^{18}F]AlF^{2+}$ complexation

Apart from utilising the [^{18}F]AlF method to radiolabel biomolecules by the tetrazine-TCO ligation, this thesis also explored the possibility of improving on the currently available methods for [^{18}F]AlF-labelling by investigating the use of new chelators.

4.1 Current chelators for [^{18}F]AlF^{2+} complexation

The Al^{3+} ion has a small ionic radius of 50-54 pm and can be classified as a hard metal ion.[1,2] Based on the Hard and Soft Acids and Bases (HSAB) theory, hard donor atoms are favoured for coordination to Al^{3+}.[3,4] It is thus unsurprising that all chelators reported for [^{18}F]AlF^{2+} complexation only feature N- and O-atoms as donors.[5] These chelators can be broadly divided into two groups: cyclic chelators and acyclic chelators (**Figure 4.1**). Even though a wide range of studies spanning different chelators have been conducted over the past decade, there still seems to be a lack of consensus on the chelator of choice for radiolabelling by the [^{18}F]AlF method, with a range of chelators reported in the literature.

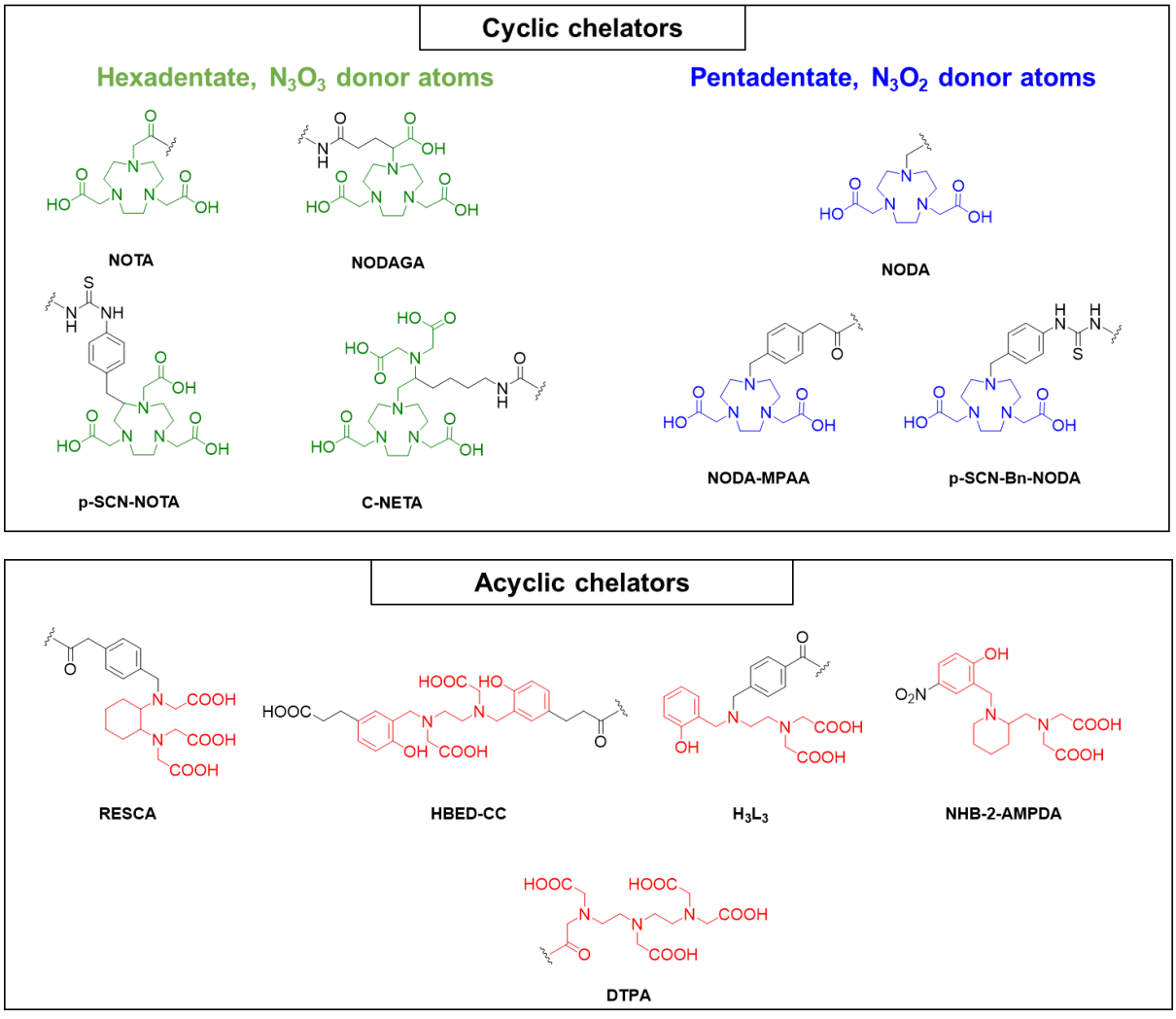

Figure 4.1: Reported chelators for [^{18}F]AlF^{2+} radiolabelling, where coloured part of the molecule represents chelator.

In 2009, when McBride *et al*. first reported the [^{18}F]AlF method for radiolabelling, **DTPA** and **NOTA** were examined.[6] Although excellent incorporation could be obtained with **DTPA** (up to 98 % RCY), the resulting complex was found to be unstable in water and human serum, which precluded the use of **DTPA** in further studies. In comparison, although **NOTA** only resulted in low RCYs of 5-20 %, the resulting [^{18}F]AlF complexes were stable in serum for up to 4 h. Subsequent *in vivo* PET imaging also showed excellent stability, where low bone uptake was observed (<1 %ID/g). Should the resulting [^{18}F]AlF complex be unstable, high bone uptake is expected, since PET imaging using free $^{18}F^-$ and [^{18}F]AlF^{2+} gave high uptakes in the scapula ($^{18}F^-$: 6.13 %ID/g, [^{18}F]AlF^{2+}: 9.83 %ID/g) and spine ($^{18}F^-$: 19.88 %ID/g, [^{18}F]AlF^{2+}: 19.03 %ID/g).

Upon successful identification of a stable [^{18}F]AlF complex for *in vivo* PET imaging, subsequent studies focused on improving radiochemical yields by assessing different NOTA-derivatives and radiolabelling conditions.[7] Though some form of reaction optimisation is usually conducted for [^{18}F]AlF-labelling, several key parameters can be identified to enable high-yielding reactions for these macrocyclic chelators:[5]

i) Preparation of $^{18}F^-$ solution by trapping on a QMA cartridge and elution with NaCl.
ii) Reaction should be carried out at pH 4-5 with NaOAc as a buffer.
iii) Heating at 90 – 110 °C for more than 10 min is necessary.
iv) An organic co-solvent of 50 % by volume is required for small molecules.

Due to these relatively harsh conditions, several acyclic chelators (**Figure 4.1**) have been developed to enable radiolabelling of heat-sensitive biomolecules, such as affibodies or proteins.[8,9] It is notable that whilst the macrocyclic chelators usually feature an N_3O_2 donor set, acyclic chelators typically feature an N_2O_3 donor set. In the subsequent section, an in-depth analysis of each class of chelator is carried out in terms of their:

i) Development and rationale for use
ii) Labelling conditions – temperature, pH, time
iii) Yield – RCY, RCP, A_m
iv) Stability – *in vitro* and *in vivo*

4.1.1 Macrocyclic chelators

In 2010, Laverman and McBride *et al*. first investigated the effect of buffer type, peptide concentration and $AlCl_3$ concentration for the labelling of **NOTA-octreotide** (**Figure 4.2**).[10] It was found that MES, HEPES and acetate buffers all resulted in similar RCYs of 46 – 49 %. However, no radiolabelling was obtained with a citrate buffer, since citrate has been known to complex aluminium.[11] Increasing the peptide concentration improved RCYs, where a peptide-to-$AlCl_3$ ratio of 26 : 1 was found to result in optimal radiolabelling yields.

In the same year, McBride *et al*. compared the radiolabelling efficiencies of four NOTA-derivatives, **p-SCN-NOTA**, **NODAGA**, **NOTA** and **C-NETA** (**Figure 4.1**). Under identical conditions, **C-NETA** gave the highest RCY of 87 %, followed by **p-SCN-NOTA** (44 %), **NOTA** (31 %) and **NODAGA** (5.8 %). The effect of reaction pH was also assessed, where the optimal pH was determined to be between 4.3 and 5.5. However, no labelling was achieved when the reaction temperature was decreased from 100 to 50 °C. At 5 min, incorporation of [^{18}F]AlF^{2+} was nearly complete (68 %), which only increased slightly when left for 15 min (71 %) and 30 min (75 %).

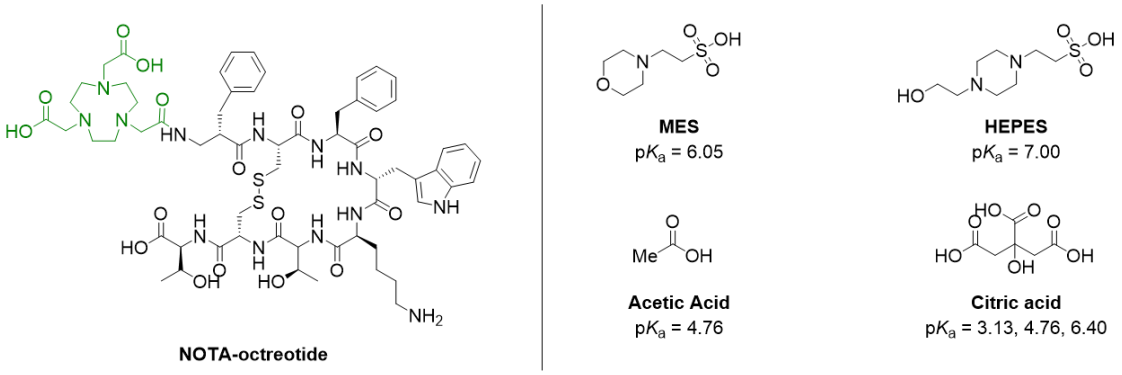

Figure 4.2: Structure of **NOTA-octreotide** and buffers used in initial optimisation of radiosynthesis. pK_a values at 37 °C shown.[12]

The subsequent year both McBride *et al*. and Shetty *et al*. reported the pentadentate **NODA** chelator for high-yielding [^{18}F]AlF reactions.[13,14] Both studies reported the successful isolation of AlF-NODA complexes for X-ray crystallography studies, where **AlF-NODA-MPAA** and **AlF-NODA** had comparable Al-F bond lengths of 1.714 Å and 1.709 Å respectively (**Figure 4.3**, left). It was revealed that the coordination geometry around the Al^{3+} ion was a slightly distorted octahedron, with three nitrogen atoms binding facially. The coordination sphere was completed by the two oxygen atoms from each carboxylate arm and the fluoride ion binding to the opposite face. In terms of radiolabelling, McBride *et al*. reported that the use of an organic co-solvent improved the RCY to 91 %, significantly higher than the moderate yields (43.5 %) obtained using fully aqueous conditions. When Shetty *et al*. studied the effect of varying the final substituent on the NODA macrocycle (**Figure 4.3**, right), it was found that having an intramolecular donor atom capable of forming a 5- or 6-membered ring with the aluminium centre significantly reduces radiolabelling efficiency.

Even though these preliminary studies indicated that a pentadentate chelator appears ideal for [^{18}F]AlF^{2+} complexation, NOTA remains the most widely used chelator.[5] **Table 4.1** provides a summary of the optimised radiolabelling conditions, yield and stability of reported macrocyclic chelators to date. In general, labelling conditions (pH, temperature and time) are relatively consistent, and thus will not be discussed in detail. However, large variations in RCY

and molar activity (A_m) have been observed even within each class of chelator, which could presumably be attributed to the different labelling conditions and objectives of each study.

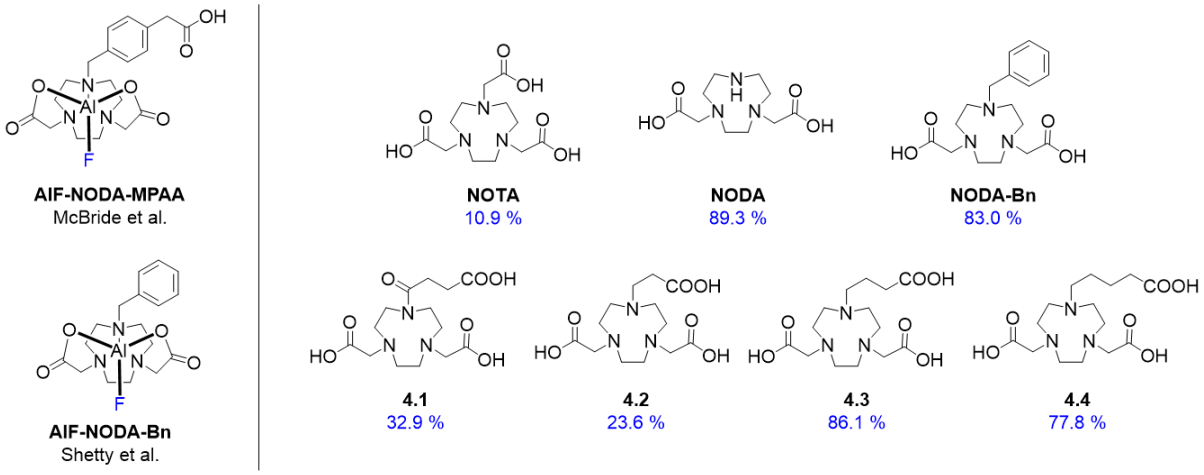

Figure 4.3: Left: Structures of isolated AlF-NODA complexes characterized by X-ray crystallography. Right: Structures of NOTA and NODA derivatives investigated by Shetty *et al*. for [^{18}F]AlF-labelling, numbers in blue represent radiochemical conversions determined by radio-TLC.[14]

Table 4.1: Reported radiolabelling conditions and results for macrocyclic chelators.[5] RCY: radiochemical yield; RCP: radiochemical purity; A_m: molar activity; *nr:* not reported.

Chelator	**Labelling conditions**	**Yield**	**Stability**
NOTA	pH 4 – 4.6 95 – 105 °C 5 – 20 min	RCY: 10 – 97 % RCP: 92 – 99 % A_m : 0.6 – 158 MBq/nmol	Stable *in vitro* and *in vivo*
NODAGA	pH 4 100 °C 15 min	RCY: 5 – 33 % RCP: 95 – 98 % A_m : 1.85 – 1.95 MBq/nmol	Degrades in mouse serum after 2 h Stable *in vivo*
p-SCN-NOTA	pH 4 90 – 110 °C 10 – 20 min	RCY: 5 – 92 % RCP: 95 – 98 % A_m : 1.25 – 90 MBq/nmol	Stable *in vitro* High bone uptake *in vivo*
C-NETA	pH 4 100 – 105 °C 15 min	RCY: 85 % RCP: *nr* A_m : *nr*	Stable *in vitro* and *in vivo*
NODA, NODA-MPAA, p-SCN-Bn-NODA	pH 4 – 4.5 100 – 110 °C 10 – 15 min	RCY: 36 – 95% RCP: 95 – 99 % A_m : 4 – 261 MBq/nmol	Stable *in vitro* and *in vivo*

NOTA: The wide range of yields obtained (10-97 % RCY) can largely be attributed to the radiosynthesis methods and conditions. Typically, radiosynthesis on automated platforms result in lower RCYs of (13-66 %) compared to manual synthesis (up to 99 %),[15–17] which could be due to the larger volumes required and less efficient transfer of reagents for automated set-ups.[18,19] In addition, the lack of standardization for radiolabelling conditions also impacts the yields obtained. For example, even though the use of a sub-stoichiometric amount of $AlCl_3$ has been shown to give optimal reaction yields,[7,18] the use of excess $AlCl_3$ has also been reported.[20,21] The large range of A_m reported is also a result of the different radiosynthesis methods, where starting activity, precursor amount and purification method could significantly impact the A_m obtained. Nevertheless, the ability to obtain high RCYs and RCPs for NOTA-functionalised compounds, and the high stability of the [^{18}F]AlF complexes have resulted in the widespread use of this chelator for radiolabelling by [^{18}F]AlF, with several compounds already entering clinical trials.[22–26]

NODAGA: Apart from the initial screening of NOTA-derived chelators by McBride *et al*.,[7] only three studies have reported the use of NODAGA for [^{18}F]AlF complexation.[27–29] Although the authors reported promising results for imaging integrin $\alpha_v\beta_3$,[27] asiaglycoprotein,[28] and gastrin-releasing peptide (GPR) receptors,[29] the low radiochemical yields obtained and low stability of [^{18}F]AlF-NODAGA complexes in serum precluded their use in further experiments. It is notable that all three studies were published between 2012 and 2013, which was relatively early considering that the [^{18}F]AlF method was only reported in 2009.[6] Potentially, given the similar size and radiolabelling methodology of [^{18}F]AlF and ^{68}Ga, the limited stability data available resulted in the use of NODAGA for the early [^{18}F]AlF studies, since NODAGA is widely used for ^{68}Ga-labelling.

p-SCN-NOTA: Despite having the same coordination sphere as NODAGA, with three free carboxylate arms, good to excellent RCYs (65-92 %) can be obtained.[30,31] Nevertheless, a majority the studies reported moderate RCYs (30-45 %).[31–33] Although high bone uptake (4.47 %ID/g) has been observed in one study, this was due to the expression of the targeted receptor in the bone marrow, where PET imaging with a ^{68}Ga analogue also showed relatively high bone uptake (5.75 %ID/g). The *in vivo* stability of the [^{18}F]AlF complexes formed using **p-SCN-NOTA** was confirmed by the low bone uptake (<1-2 %ID/g) observed in other studies.[30,31,34]

C-NETA: Although good radiochemical yields (85 %) and *in vivo* stability was reported by McBride *et al*. in 2010,[7] only one other study was published using **C-NETA** as a chelator for [^{18}F]AlF.[35] However, no data regarding the RCY or RCP of the resulting [^{18}F]AlF-labelled

compound was reported in this study. Therefore, due to the lack of data regarding this chelator, a definite conclusion could not be drawn regarding its suitability for [^{18}F]AlF complexation.

NODA: Following reports by McBride *et al*. and Shetty *et al*. on the suitability of pentadentate chelators for [^{18}F]AlF complexation,[13,14] there has been an increase in use of **NODA** as a chelator for [^{18}F]AlF-labelling. In general, moderate to excellent radiochemical yields (36-95 %) can be obtained, with the resulting [^{18}F]AlF complex being stable both *in vitro* and *in vivo*.[36–44] In addition, three studies have also reported the use of pre-complexed AlOH-NODA precursors for [^{18}F]AlF-labelling,[13,45,46] which offer two potential advantages: (i) reducing the potential for metal contamination during radiolabelling, and (ii) higher A_m since an excess of precursor to $AlCl_3$ is not required. Nevertheless, similar RCYs can be obtained using both pre-complexed AlOH-NODA and NODA as precursors.

In summary, although the pentadentate **NODA** has been identified to be ideal for [^{18}F]AlF complexation, **NOTA** remains the most widely used chelator, presumably due to its widespread commercial availability. The similar radiolabelling efficiencies and stabilities afforded by **NOTA** compared to **NODA** also justify its use, with almost all clinical trials for [^{18}F]AlF-labelled compounds reporting the use of **NOTA** as a chelator. **HBED-CC** (**Figure 4.1**, acyclic chelator) is the only other chelator being evaluated for [^{18}F]AlF-labelled compounds undergoing clinical trials, despite it not being an ideal chelator. Nevertheless, the excellent radiolabelling efficiencies and stabilities afforded by both **NOTA** and **NODA** will likely result in their continued use for small molecule and peptide radiolabelling.

4.1.2 Acyclic chelators

Due to the harsh conditions required for radiolabelling macrocyclic chelators, heat-sensitive biomolecules such as proteins or antibodies cannot be radiolabelled directly. Instead, a two-step labelling approach using prosthetic groups has been used to circumvent this issue.[39,47] Thus, several acyclic chelators have been developed to enable direct [^{18}F]AlF-labelling at ambient temperatures (**Table 4.2**).

H_3L_3: In 2016, Cleeren *et al*. reported a study of eight acyclic ligands for [^{18}F]AlF-labelling (**Figure 4.4**). It was found that only chelators with the ethylenediamine-*N,N'*-diacetic acid (EDDA) fragment (**H_3L1-4**) resulted in [^{18}F]AlF^{2+} complexation, whereas **H_3L5-8** gave <10 % RCY. At room temperature, **H_3L1** gave the highest radiolabelling efficiency (>90 % RCC), whereas **H_3L2-4** resulted in <50 % RCC. This increased significantly to >75 % RCC when the reaction was carried out at 40 °C, and stayed constant even when the temperature was increased to 60, 80 and 110 °C. When incubated in rat serum, [^{18}F]AlF-**H_3L3** had a stability of >90 % after 1 h, but decreased to 66 % after 4 h. In comparison, <40 % of [^{18}F]AlF-**H_3L1,**

[^{18}F]AlF-**H_3L2** and [^{18}F]AlF-**H_3L4** were intact after 1 h in rat serum due to demetallation and/or defluorination, making them unsuitable for further use. When studied *in vivo*, [^{18}F]AlF-**H_3L3** showed low bone uptake (0.74 %ID/g), demonstrating its promise as a potential chelator for [^{18}F]AlF^{2+} complexation.

Table 4.2: Reported radiolabelling conditions and results for acyclic chelators.[5] RCY: radiochemical yield; RCP: radiochemical purity; A_m: molar activity; *nr:* not reported.

Chelator	**Labelling conditions**	**Yield**	**Stability**
H_3L_3	pH 4.5 r.t. to 40 °C 12 min	RCY: 89 – 96 % RCP: >98 % A_m : 27 MBq/nmol	66 % intact after 4 h in rat serum No bone uptake *in vivo*
RESCA	pH 4.5 r.t. to 37 °C 12 – 15 min	RCY: 20 – 85 % RCP: >98 % A_m : 23.2 – 85 MBq/nmol	Stable *in vitro* and *in vivo*
2-Aminimethylpiperidine (2-AMP)	pH 4 – 5 r.t. to 37 °C 12 min	RCY: 69 – 86 % RCP: *nr* A_m : 32 MBq/nmol	87% intact after 4 h in human serum No bone uptake *in vivo*
HBED-CC	pH 4 – 5 r.t. to 50 °C 5 – 15 min	RCY: 15 – 90 % RCP: 92 – 100 % A_m : 28 – 544 MBq/nmol	65 % intact after 2 h in human serum 3.3 %ID/g bone uptake after 1 h

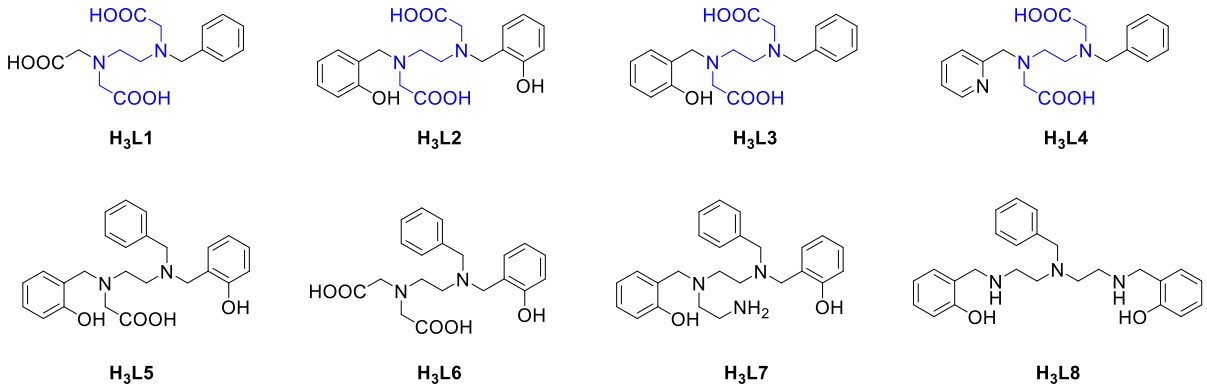

Figure 4.4: Structures of acyclic ligands investigated by Cleeren *et al.*, where **H_3L1-4** have a common ethylenediamine-*N,N'*-diacetic acid (EDDA) fragment (highlighted in blue).

RESCA: A year later, Cleeren *et al*. designed a new **RES**trained **C**omplexing **A**gent (**RESCA**) for [^{18}F]AlF labelling at room temperature (**Figure 4.5**).[9] With this chelator, low to good RCYs of 20-85 % could be obtained within 15 min at room temperature. The increased stability of **RESCA** compared to the chelators in **Figure 4.4** was attributed to the rigidity of the *trans*-cyclohexyl backbone, where the resulting [^{18}F]AlF complex was shown to be stable *in vitro* for at least 4 h.[48] Low bone uptake was also observed *in vivo*, demonstrating the applicability of this chelator for labelling heat-sensitive biomolecules.[9,49]

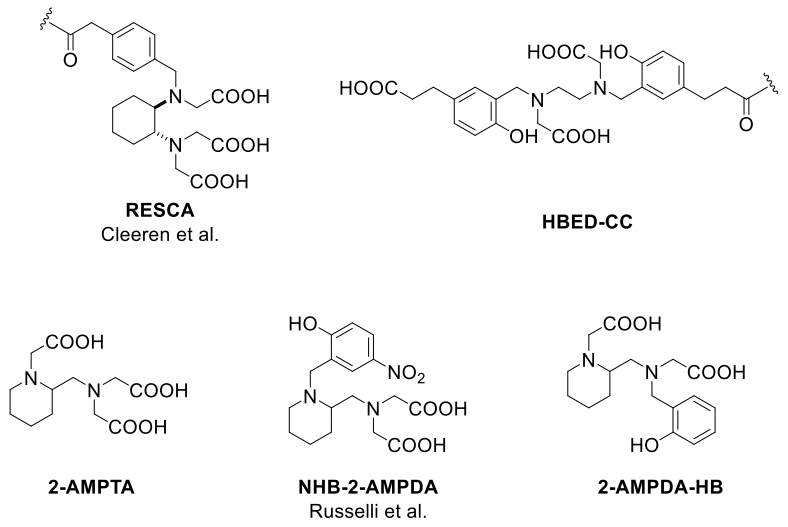

Figure 4.5: Structures of acyclic chelators evaluated for [^{18}F]AlF labelling.

AMP: More recently, in 2021, Russelli *et al*. reported the development of a new class of 2-aminomethylpiperidine (**2-AMP**) chelators (**Figure 4.5**).[50] At pH 4, only **2-AMPTA** demonstrated good RCYs of >80 %. However, at pH 5, all three chelators investigated resulted in moderate to good RCYs of 55-80 %, with **2-AMPTA** giving the best RCY of 81%. Surprisingly, all three chelators were capable of complexing [^{18}F]AlF^{2+} at pH 6.5 (approximately 50 % RCY), demonstrating the potential of these compounds to be used for radiolabelling acid-sensitive molecules. [^{18}F]AlF complexes of **2-AMPTA** and **NHB-2-AMPDA** were found be unstable in human serum, with 72 and 51 % remaining after 60 min. In comparison, 90 % of [^{18}F]AlF-**2-AMPDA-HB** remained intact after 120 min. When investigated *in vivo*, low bone uptake (1.63 %ID/g) was observed for [^{18}F]AlF-**2-AMPDA-HB**, showing the potential of this chelator for functionalising biomolecules for PET imaging.

HBED: The use of HBED as a chelator for [^{18}F]AlF was first reported by Malik *et al*. in 2015.[51] Notably, all reports on the use of HBED involved the use of a clinically-approved precursor for PSMA imaging by ^{68}Ga (**Figure 4.6**).[51–56] Although excellent labelling (up to 90 % RCY) could be obtained, the resulting tracer was only stable in human serum for up to 1 h (91 % remaining after 1 h, 65 % after 2 h). When investigated *in vivo*, high bone uptake was also observed

(3.3 %ID/g, ^{68}Ga analogue: 0.1 %ID/g), showing that the [^{18}F]AlF-HBED complex is relatively unstable.[51,53]

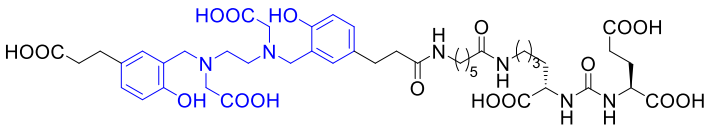

PSMA-HBED

Figure 4.6: Structure of PSMA-HBED used in ^{68}Ga- and [^{18}F]AlF-labelling.

Nevertheless, high tumour uptakes were still observed using [^{18}F]AlF-PSMA-HBED when an imaging period of 1 h was used. However, one limitation is that the detection of bone metastasis of prostate cancer could be hampered when using this radiotracer. Taken together, the use of HBED poses an interesting conundrum: HBED is a poor chelator for [^{18}F]AlF given the instability of the resulting complex, yet [^{18}F]AlF-PSMA-HBED has been taken forward to clinical trials due to the high demand for PSMA-targeted radiotracers.[24,57,58] With this, it could be argued that the current set of chelators might already be sufficient for labelling by the [^{18}F]AlF method. However, a different perspective could also be taken – the commercial availability of a clinically-approved precursor can facilitate the clinical evaluation and translation of analogous radiotracers produced using a different radionuclide. This is mainly due to the high demand for imaging PSMA by PET. Therefore, it could be argued that the implementation of [^{18}F]AlF-PSMA-HBED does not detract from efforts to pursue optimal chelators for [^{18}F]AlF, but rather provides the opportunity for clinically relevant compounds to be translated quickly in cases where demand is high.[58]

In summary, the development of acyclic chelators has enabled [^{18}F]AlF-labelling at lower temperatures (25-50 °C). Whilst the macrocyclic chelators usually feature an N_3O_2 donor set, acyclic chelators usually feature an N_2O_3 donor set, where chelators with an EDDA moiety have been shown to give the best chelation efficiency. Of these, **HBED** seems to be the most advanced in terms of clinical translation, despite it not being the best chelator for [^{18}F]AlF^{2+}. This can be attributed to the high demand for PSMA-targeted radiotracers. In comparison, **RESCA** and **2-AMPDA-HB** result in the formation of more stable [^{18}F]AlF complexes, showing their potential to be conjugated onto different clinically relevant targeting vectors.

4.1.3 Bisphosphonate chelators for Al complexation

The design of potential chelators for [^{18}F]AlF was initially based on chelates for treating aluminium overload, where Al^{3+} has been shown to bind strongly to phosphate groups and phosphorylated amino acids.[1,59] The strong affinity between aluminium and phosphates, coupled with the strong metal binding ability of bisphosphonate (BP) ligands, has inspired the

use of bisphosphonates to sequester Al^{3+}.[60–62] It is hypothesized that if these chelates are able to form stable complexes with aluminium under physiological conditions (pH 7.4, 37 °C), they could potentially be translated for [^{18}F]AlF radiolabelling.

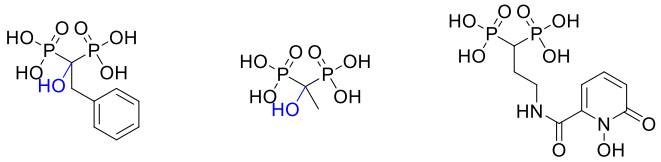

BP-L1 **BP-L2** **BP-L3**

Figure 4.7: Structures of bisphosphonate ligands investigated for Al^{3+} chelation, where 1-hydroxy groups are highlighted in blue.

In their investigation of Al^{3+} complexation, Gumienna-Kontecka *et al*. reported formation constants of 18.7 and 19.1 for Al-**BP-L1** and Al-**BP-L2** respectively (**Figure 4.7**), determined by potentiometric titrations.[60] Interestingly, this was higher than the formation constant reported for Al-**NOTA** (log *K* = 17.9).[63] However, the different buffer salts used for potentiometric titrations could potentially influence the values obtained in both studies. Upon the addition of a hydroxypyridinone group for increased binding affinity, the formation constant for Al-**BP-L3** was found to be slightly lower at 17.2.[62] This could suggest that the 1-hydroxy groups are involved in Al^{3+} binding, since the presence of additional donor atoms on the hydroxypyridinone group did not increase binding affinity through the chelate effect.

In brief, the high formation constants reported for the Al-BP complexes, comparable to that of Al-**NOTA**, suggest that the Al-BP complexes might be stable *in vivo*. Although the binding of fluoride could affect the formation constants of the Al-BP complexes, radiolabelling efficiency and *in vitro* stability tests can reveal the suitability of bisphosphonate ligands for [^{18}F]AlF complexation.

4.1.4 Salen-derived chelators for Al complexation

Apart from bisphosphonates, salen-derived ligands were also identified as potential chelators for [^{18}F]AlF. This is mainly due to the wide range of literature available on the use of salen-Al and salan-Al complexes for catalysis and biomedical applications,[64–70] which demonstrates the strong ability of these ligands to bind Al^{3+}. More promisingly, two salen aluminium fluoride complexes have been reported (**Figure 4.8**),[71,72] providing further evidence that these ligands can be suitable for complexing [^{18}F]AlF.

In 2017, Brodbeck *et al*. reported the use of **AlF-salen** as a catalyst for asymmetric carboxycyanation.[72] When **AlF-salen** was isolated and characterised by X-ray crystallography, monomeric or dimeric aggregates could be obtained, depending on the counterion of the

ligand (BF_4: dimer, PF_6: monomer). The fact that a dimer could be obtained suggests that a stable chelate for [^{18}F]AlF should at least have five donor atoms. In the monomeric structure, the Al-F bond length was determined to be 1.688 Å, shorter than that of the dimeric structure (1.870 Å for bridging Al-F-Al, 1.776 Å for terminal Al-F). More significantly, the **AlF-salen** complex showed excellent stability in the presence of oxygen and water, and up to temperatures of >220 °C. These indicated that the AlF-salen complexes could have sufficient stability *in vitro* and *in vivo*.

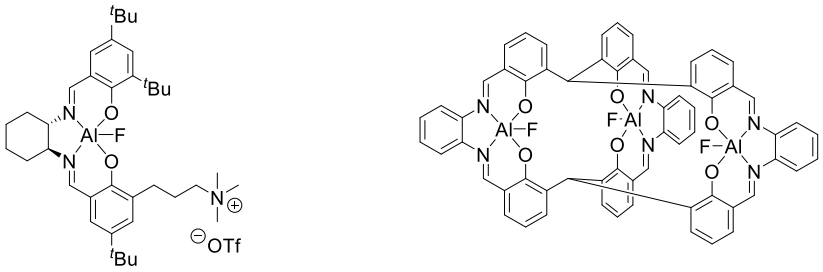

Figure 4.8: Structures of reported AlF-salen complexes.[71,72]

Following that, Yin *et al*. reported the synthesis and characterisation of **AlF-salphen-cryptand** for cell imaging. Although the authors used the Al-Cl analogue in their cell internalisation studies, **AlF-salphen-cryptand** was isolated and characterised by X-ray crystallography. The coordination geometry around each Al^{3+} was a distorted octahedron, which was completed by a methoxide ion (N_2O_3 donor set). The Al-F bond was found to have an average length of 1.755 Å, slightly longer than the 1.709-1.714 Å reported for AlF-NOTA (N_3O_2 donor set), which could indicate that the AlF complexes formed with salen ligands might be less stable than that formed with NOTA ligands due to the weaker Al-F bond.

Nevertheless, the isolation of the two AlF-salen complexes in **Figure 4.8**, which were stable in air and moisture, indicates that salen-derivatives could be suitable chelators for [^{18}F]AlF^{2+}. Therefore, this chapter will explore the synthesis of Al-salen complexes. Following that, fluorination under aqueous conditions will be investigated to determine if these can perform better than currently available [^{18}F]AlF^{2+} chelators.

4.1.5 Aims and objectives

The main aim of this chapter is to identify and synthesize a range of ligands that have the potential to form stable [^{18}F]AlF complexes at physiological conditions (pH 7.4, 37 °C). To achieve this, the following objectives were identified:

A. Synthesis and characterisation of a set of bisphosphonate and salen ligands
B. Evaluation of their feasibility for [^{18}F]AlF-labelling
C. Evaluation of the stability of the resulting [^{18}F]AlF complexes

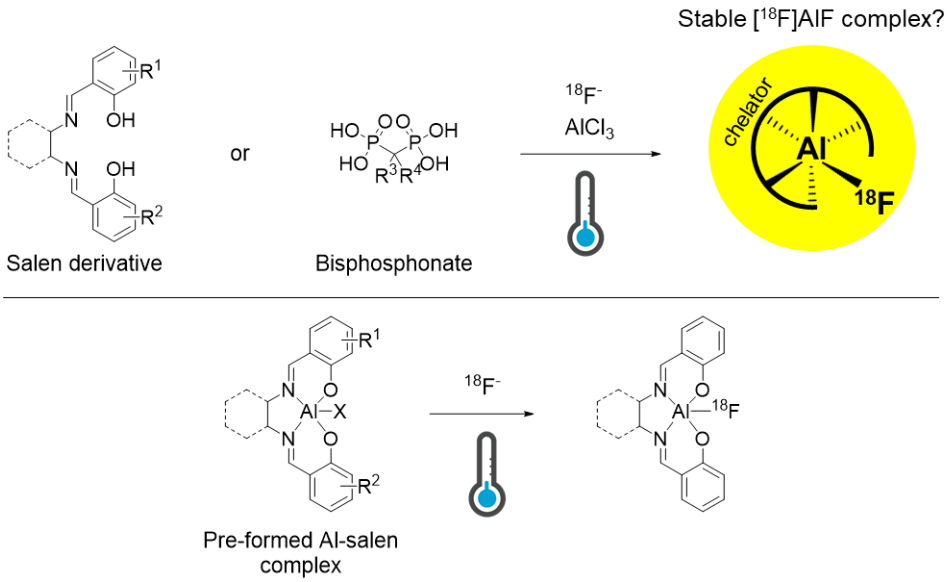

Figure 4.9: Schematic representation of the aims in this chapter. Top: Investigation on the feasibility of radiolabelling salen and bisphosphonate chelators by the [^{18}F]AlF method. Bottom: feasibility of radiolabelling pre-formed Al-salen complexes.

Upon synthesis of the ligands, [^{18}F]AlF-labelling at a range of temperatures and pH will be examined. If successful radiolabelling is achieved, the stability of the complex in PBS and human serum will be evaluated. As an extension, evaluation of pre-formed Al-salen complexes for ^{18}F-labelling will also be conducted, since this can reduce trace metal contamination during radiolabelling and result in radiotracers with higher molar activities.[13,45]

4.2 Bisphosphonate chelators

4.2.1 Preliminary radiolabelling reactions

To obtain an insight into the feasibility of forming [^{18}F]AlF complexes with bisphosphonates, three commercially-available ligands were tested (**Figure 4.10**, left). When alendronic acid was used, a new species was observed on the baseline of the radio-TLC chromatogram (R_f = 0) after 20 min at 37 °C (**Figure 4.10**). In comparison, [^{18}F]AlF^{2+} travels slightly (R_f = 0.05), and could be distinguished from the newly formed [^{18}F]AlF-alendronate. It is possible that [^{18}F]AlF-alendronate remains on the baseline due to the poor solubility of alendronic acid in the presence of organic solvents. When analysed by reverse-phase high-performance liquid chromatography (RP-HPLC), radioactivity remained trapped on the column, which could also be attributed to the poor solubility of alendronic acid. To verify that an [^{18}F]AlF complex was formed with alendronic acid, the reaction was carried out in the absence of $AlCl_3$. Under these conditions, only free [^{18}F]fluoride was observed on the radio-TLC, signifying that Al^{3+} was essential for the reaction.

In comparison, no reaction was observed when etidronic acid was used, where the amine chain on alendronic acid was swapped with a methyl group. Changing the methyl group for an imidazole in zoledronic acid also did not result in any reaction, potentially signifying that the amine group on alendronic acid is involved in binding [^{18}F]AlF^{2+}. Unfortunately, further attempts to isolate and characterise the [^{18}F]AlF-alendronate species were unsuccessful due to it being retained on the on the different sorbents tested (silica, C2, C4 and C18).

4.2.2 Design and synthesis of pentadentate bisphosphonate chelators

Given that initial tests using alendronic acid showed promising results, the synthesis of pentadentate chelators capable of forming stable [^{18}F]AlF complexes was attempted. With reference to alendronic acid, bisphosphonate **4.5** was designed, where two additional carboxylate arms were attached onto the primary amine (**Scheme 4.1**). Due to the synthetic route starting from **4.1**, the 1-hydroxy group on alendronic acid is absent in the final chelator. **4.1** was synthesised according to a reported protocol,[73] and subsequent amide coupling with **4.2** produced **4.3** in 45 % yield. Notably, the ^{31}P NMR of **4.3** showed a single peak at 15.8 ppm, similar to that of **4.1** (16.4 ppm).

Deprotection of the bisphosphonate esters and *tert*-butyl groups of **4.3** was carried out using the McKenna reaction, where bromotrimethylsilane (TMSBr) was used for silyldealkylation, followed by hydrolysis of the silyl esters using a mixture of MeOH/H_2O.[74,75] Based on analysis by ^{1}H NMR, the ethyl and *tert*-butyl protecting groups were successfully removed (**Figure 4.11**). The expected proton peaks were present, where an indicative triplet was observed at

4.82 ppm with a large $^{2}J_{HP}$ coupling constant (22.3 Hz). Although several impurities can be observed around 3.8 ppm, these only amounted to approximately 10 % of the mixture. Only one peak at 14.0 ppm was observed in the ^{31}P NMR, consistent with the 10-25 ppm range obtained by Matthew *et al* for bisphosphonic acids.[76]

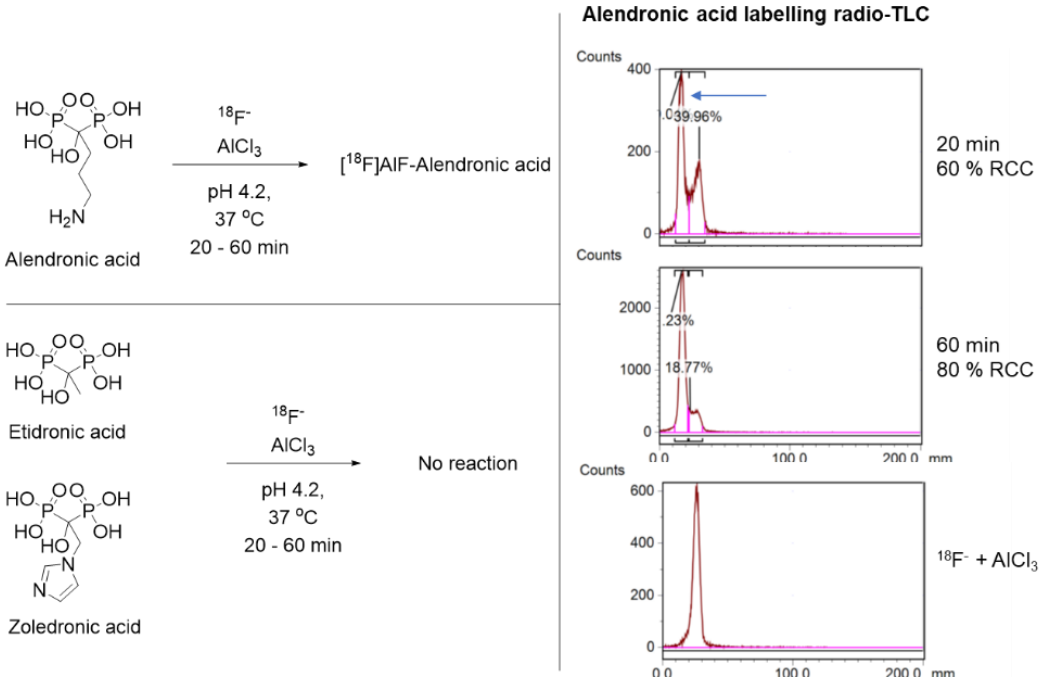

Figure 4.10: Left: [^{18}F]AlF-labelling of alendronic acid, etidronic acid and zoledronic acid. Right: radio-TLC chromatograms of alendronic acid reaction showing reaction after 20 min, 60 min and free [^{18}F]AlF^{2+} for comparison. Blue arrow indicates the possible [^{18}F]AlF-alendronic acid species. Radio-TLC eluted with 1:1 *v:v* MeOH:2 M NH_4OAc.

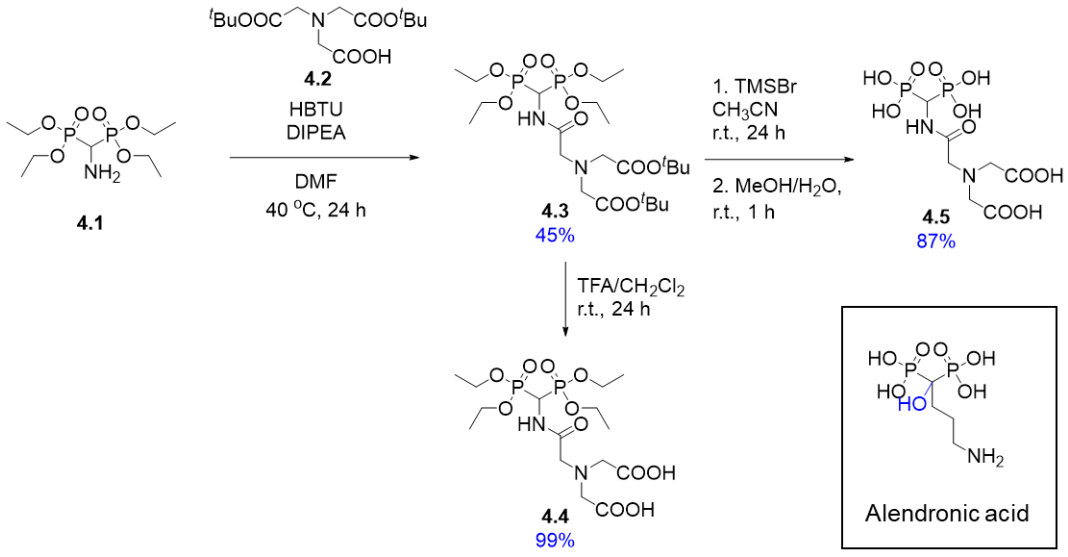

Scheme 4.1: Synthesis of pentadentate bisphosphonate chelator **4.5**. Insert: structure of alendronic acid for comparison, with 1-hydroxy group highlighted in blue.

To prove that the bisphosphonic acid groups in **4.5** are required for [^{18}F]AlF complexation, partial deprotection of **4.3** was carried out using TFA to give **4.4**. Expectedly, a single peak at 16.0 ppm was observed in the ^{31}P NMR spectrum, and removal of the ^{t}Bu group was indicated by the absence of peaks around 1.5 ppm in the ^{1}H NMR spectrum.

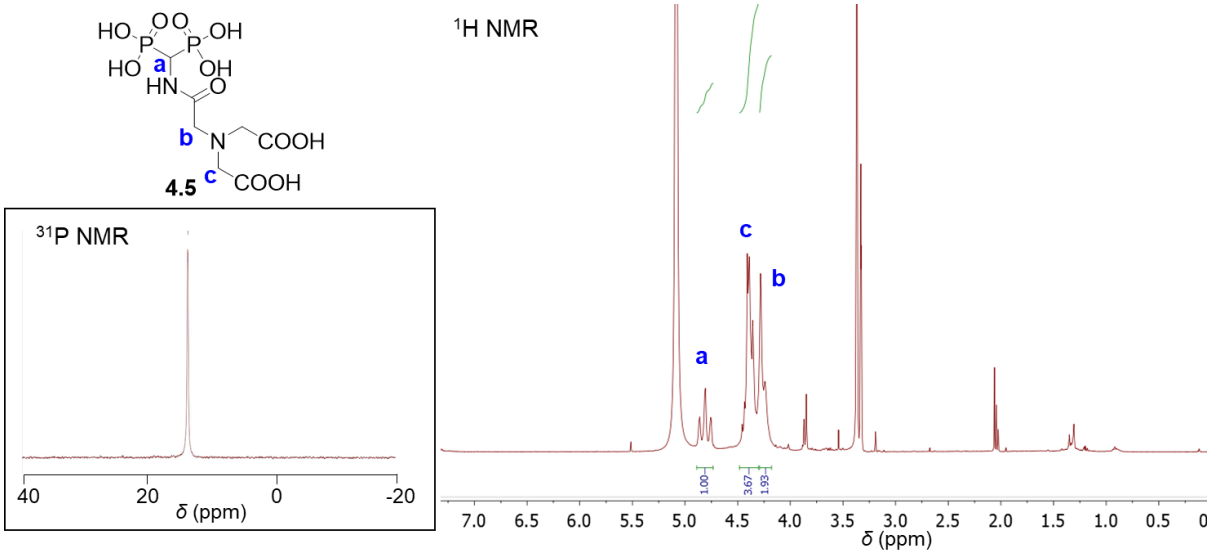

Figure 4.11: Assigned ^{31}P and ^{1}H NMR spectrum of **4.5** in MeOD at room temperature.

To increase the scope of pentadentate bisphosphonate chelators, Michael addition of different amine nucleophiles to bisphosphonate ester **4.6** was envisioned (**Scheme 4.2**). The feasibility of this reaction was first investigated using **4.7**, where the benzyl group could be deprotected to reveal a carboxylate arm for coordination.

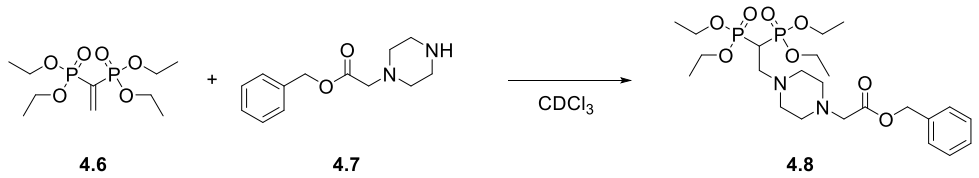

Scheme 4.2: Synthesis of additional bisphosphonate chelators by Michael addition to **4.6**.

Upon analysis of the reaction mixture in **Scheme 4.2** by ^{1}H NMR, complete consumption of **4.6** was indicated by the disappearance of the alkene CH_2 peaks at 7.00 ppm (**Figure 4.12**). The successful formation of **4.8** can also be inferred by the appearance of a peak corresponding to -C$\underline{H}_2$CHP$_2$- as a set of triplet of doublets ($^{3}J_{PH}$ = 14.8 Hz, $^{3}J_{HH}$ = 6.2 Hz). However, purification of the reaction mixture to remove trace amounts of the starting material was unsuccessful, with **4.6** being recovered quantitatively instead. This observation was supported by the results reported by Hutchinson *et al.*, where the addition of amine nucleophiles to **4.6** was found to be reversible.[77] Due to the instability of the resulting compound, further synthesis of bisphosphonates by this route was not pursued.

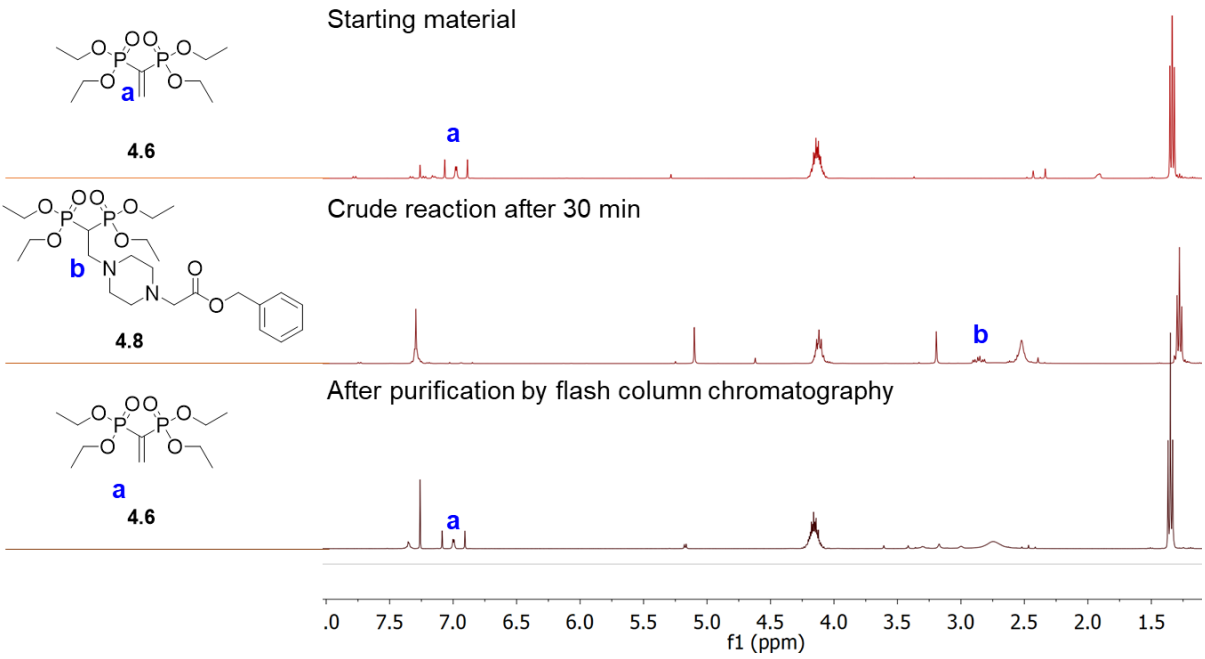

Figure 4.12: Stacked ^{1}H NMR spectra in $CDCl_3$ of: (Top) compound **4.6**; (Middle) crude reaction of **Scheme 4.2** after 30 min; and (Bottom) isolated product after purification, showing that **4.8** undergoes retro-Michael addition.

Next, the feasibility of [^{18}F]AlF^{2+} complexation was investigated using compounds **4.4** and **4.5**. However, under the conditions tested for alendronic acid (pH 4.5, 37 °C), no complexation of [^{18}F]AlF^{2+} could be detected by radio-TLC (**Figure 4.13**), even when the temperature was increased to 100 °C. The reaction was then carried out at pH 7.4, since phosphonates have been reported to bind aluminium at this pH.[62] Unfortunately, no labelling was observed at both 37 and 100 °C, showing that **4.5** is likely a poor chelator for [^{18}F]AlF-labelling.

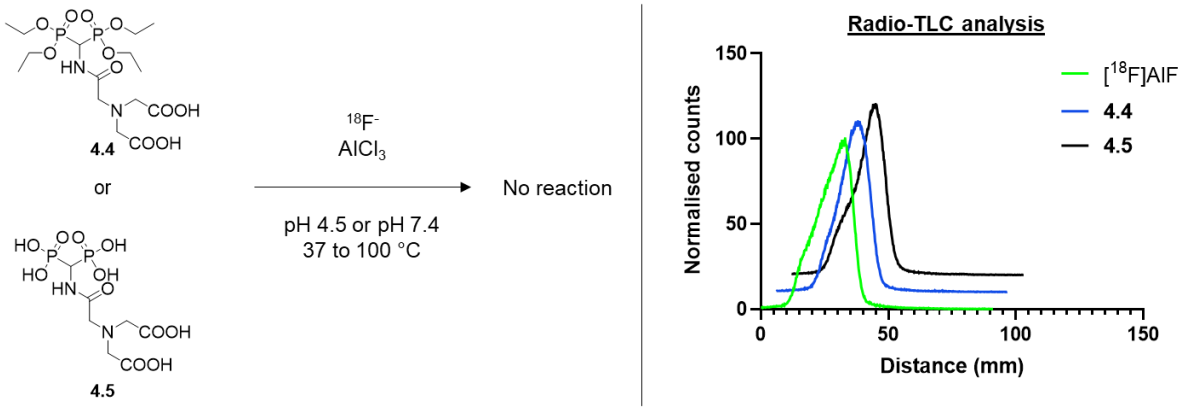

Figure 4.13: Left: [^{18}F]AlF-labelling conditions investigated for compounds **4.4** and **4.5**. Right: radio-TLC chromatograms showing no reaction has occurred.

Although further functionalisation of alendronic acid to a pentadentate chelator is possible using the amine chain, this was not carried out due to the poor solubility of alendronic acid in

organic solvents. In addition, the strong binding affinity of bisphosphonates with calcium, and their widespread use in osteoporosis treatment,[78] could potentially result in transchelation of the [^{18}F]AlF complex *in vivo*. More importantly, since **4.5** gave no indication of [^{18}F]AlF complexation, and that an efficient route for producing a library of chelators was not identified, the investigation of bisphosphonates for [^{18}F]AlF-labelling was not pursued further.

4.3 Salen chelators

4.3.1 Design and synthesis of Al-Salen complexes

Based on the AlF-salen complexes isolated in **Figure 4.8** (**AlF-salen-cryptand** and **AlF-salen**), the following ligands were designed and synthesised (**Figure 4.14**). Salphen **4.9** was synthesised to obtain a monomeric form of **AlF-salen-cryptand**, and salcyen **4.10** would give an analogue of **AlF-salen** without the presence of additional aromatic functionalities. The *tert*-butyl groups on **AlF-salen** were omitted in **4.10** to improve hydrophilicity. Salcyan **4.11** was investigated as a salan derivative to **4.10**, since the imine groups could be prone to hydrolysis,[64] and saldien **4.12** was investigated as a pentadentate chelator for [^{18}F]AlF^{2+}.

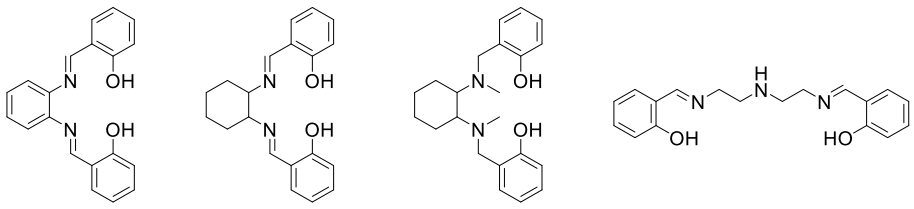

Figure 4.14: Structures of salen-derivatives investigated in this chapter.

Salphen **4.9** was synthesised by the condensation of 1,2-diaminobenzene and salicylaldehyde in 60 % yield. Although **4.9** was sufficiently stable for immediate analysis in $CDCl_3$, analysis in d_6-DMSO revealed that the imine groups were prone to hydrolysis (**Figure 4.15**). The amount of hydrolysed ligand increased with time, showing the instability of **4.9** in the presence of water.

Despite the poor hydrolytic stability of **4.9**, complexation of **4.9** was carried out using $AlCl_3$, since **AlF-salen-cryptand** was formed using the same method (**Scheme 4.3**).[71] Compared to **4.9**, the resulting complex was insoluble in $CDCl_3$. Hence, analysis was carried out in d_6-DMSO. Successful complexation was shown by the downfield shift of the imine protons in **Salphen-AlCl** (**Figure 4.16**) compared to **4.9**. When analysed by high-resolution mass spectrometry (HRMS), masses corresponding to [Salphen-Al(MeCN)]$^+$ and [Salphen-Al(MeCN)(H_2O)]$^+$ were found, showing successful aluminium complexation and the lability of the Al-Cl bond.

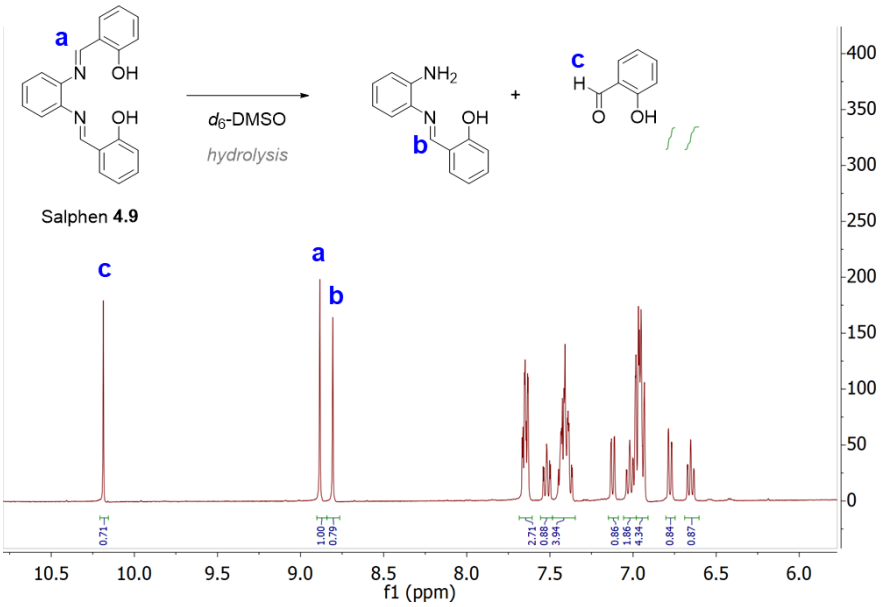

Figure 4.15: ^{1}H NMR spectrum of **4.9** when analysed in d_6-DMSO at room temperature.

Interestingly, no hydrolysis of the imine bonds was observed for **Salphen-AlCl** in DMSO for up to 24 h, potentially indicating that the imine bonds are stabilised upon complexation to aluminium. Since labelling by [^{18}F]AlF is usually carried out under acidic aqueous conditions, it is likely beneficial that [^{18}F]AlF-labelling of the salen ligands are carried out using pre-formed Al-salen complexes to minimise hydrolysis.

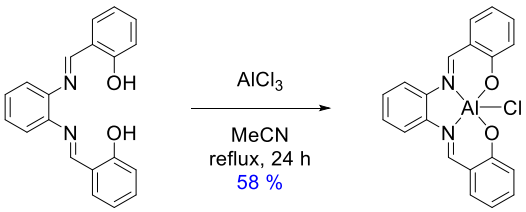

Scheme 4.3: Synthesis of **Salphen-AlCl.**

Upon isolation of **Salphen-AlCl**, formation of an aluminium-fluoride complex was attempted using the conditions reported by Yin *et al.,* where NH_4F was used as the fluoride source (**Scheme 4.4**).[71] Due to the poor solubility of the resulting solid in a variety of solvents (DMSO, H_2O, CH_3CN, THF, acetone, toluene, MeOH and EtOH), analysis by NMR spectroscopy proved challenging.

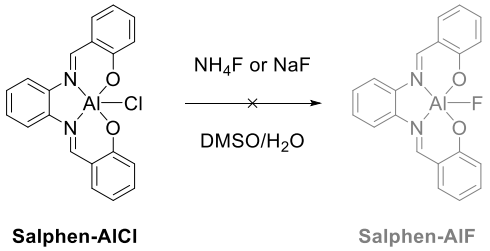

Scheme 4.4: Attempted synthesis of **Salphen-AlF** using NH_4F and NaF as fluoride sources.

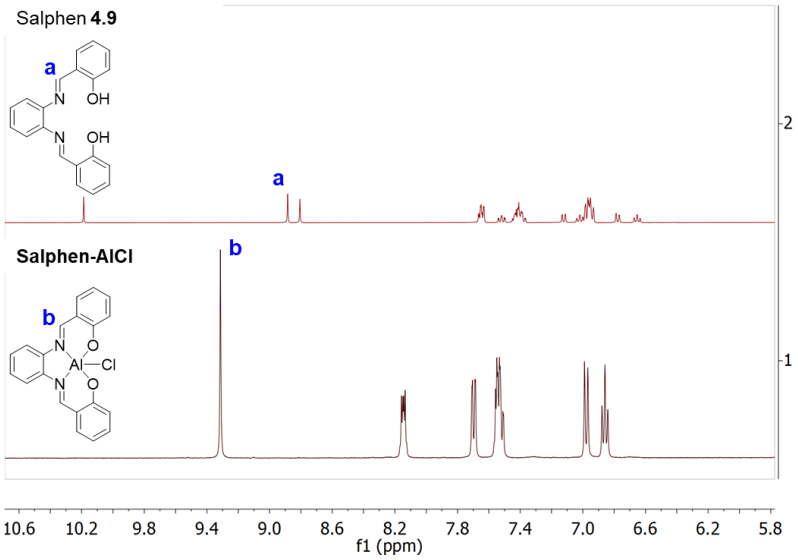

Figure 4.16: Comparison of ^{1}H NMR spectra of salphen **4.9** and **Salphen-Al-Cl**, where the imine proton was found to shift downfield upon complexation.

However, analysis by HRMS only showed the coordination of DMSO to the Al centre (**Figure 4.17**). The same results were obtained when NaF was used as a fluoride source, potentially suggesting that the formation of an AlF complex was unsuccessful, or the Al-F bond was cleaved when analysed by mass spectrometry. In comparison, AlF-NOTA complexes reported by McBride *et al*. and Shetty *et al*. were stable when analysed by mass spectrometry.[13,14] It is possible that the Al-F bond in **Salphen-AlF** is kinetically less stable because it can undergo both associative or dissociative substitution, whereas only dissociative substitution is possible for AlF-NOTA complexes due to the saturation of the Al coordination sphere.

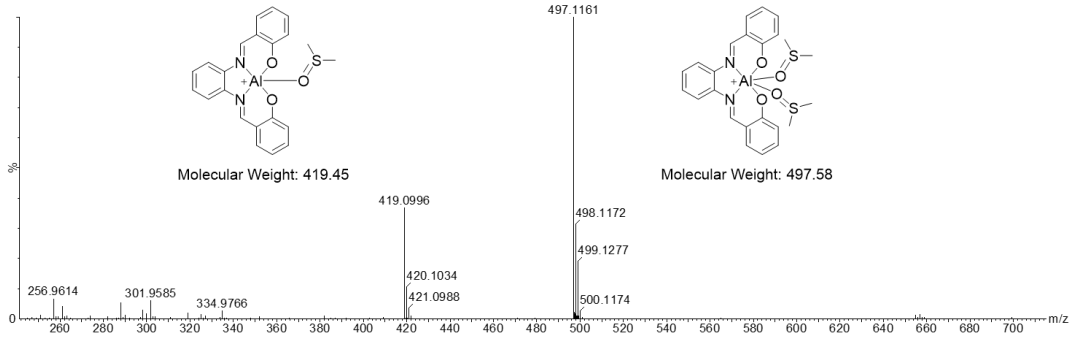

Figure 4.17: HRMS spectrum showing the coordination of DMSO instead of the fluoride ion to [Salphen-Al]$^{+}$.

To probe the formation of an AlF complex using **salphen-AlCl**, ^{18}F-labelling was attempted (**Figure 4.18A**). However, no indication of fluorination was obtained at 37 °C, with only unreacted ^{18}F^{-} eluting at the solvent front in the radio-HPLC chromatogram (**Figure 4.18B**). When analysed by radio-TLC, a similar elution profile was obtained when compared to ^{18}F^{-}, suggesting that no reaction has occurred.

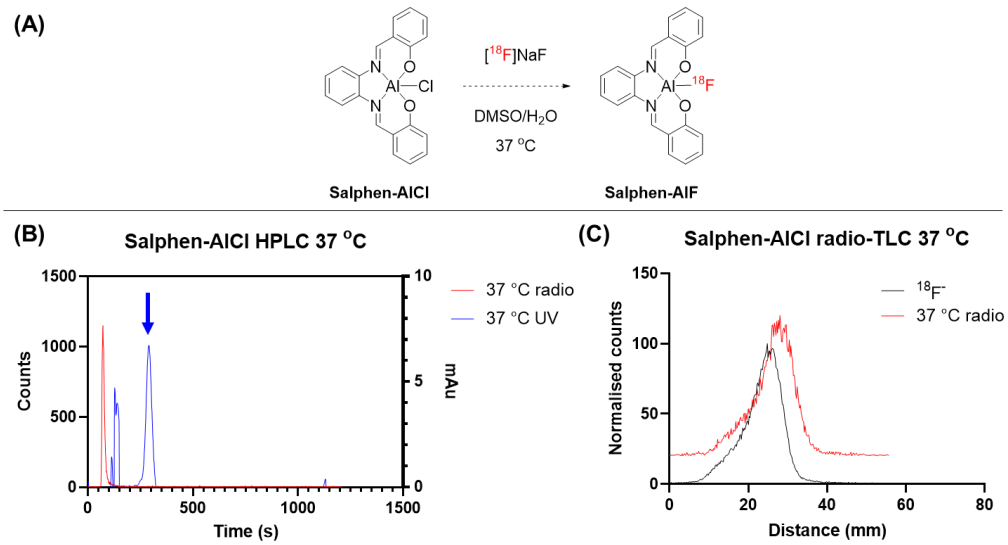

Figure 4.18: (A) ^{18}F-labelling of **Salphen-AlCl**; (B) Superimposed radio-HPLC and UV-HPLC chromatograms, where blue arrow indicates **Salphen-AlCl** at t_R = 290 s. Only free ^{18}F$^-$ was observed at the solvent front by radio-HPLC; (C) Stacked radio-TLC chromatograms of the reaction compared to free ^{18}F$^-$.

When the reaction was heated to 60 °C. two peaks were observed at the solvent front in the radio-HPLC (**Figure 4.19A**). A large amount of activity was also retained on the columns (both C4 and C18), indicating that a new hydrophobic species could be formed. When analysed by radio-TLC, a slight change in the shape of the radioactive peak was observed (**Figure 4.19B**). However, this does not provide conclusive evidence of successful [^{18}F]AlF complexation, since the newly formed peak was not separable from the ^{18}F$^-$ peak. In addition, a new species was observed in the UV-HPLC at t_R = 500 s. Since a corresponding peak was not observed in the radio-HPLC chromatogram, this suggests that degradation of the **salphen-AlCl** precursor occurs at 60 °C. Due to the inability to conclusively prove that an [^{18}F]AlF-salphen complex was obtained, further efforts were focused on alternative salen derivatives.

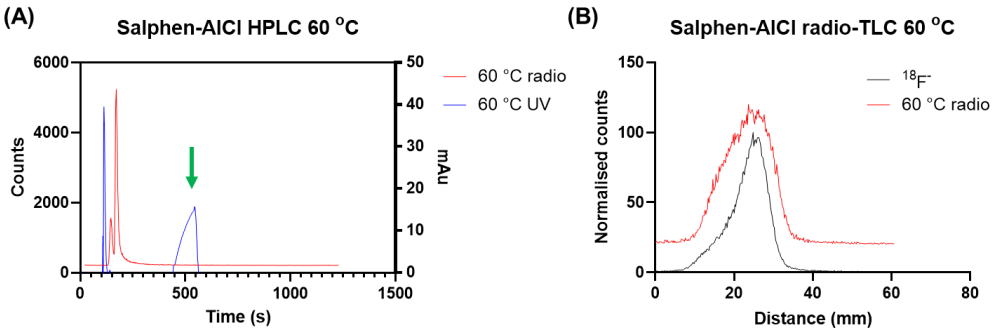

Figure 4.19: (A) Stacked radio-HPLC and UV-HPLC chromatograms when the reaction in **Figure 4.18A** was carried out at 60 °C, green arrow shows the formation of a new species at t_R = 500 s. (B) Radio-TLC of the reaction when compared to free ^{18}F$^-$, showing a slight change in peak shape.

Next, Al-complexation of salcyen **4.10** was carried out under the same conditions using $AlCl_3$. Interestingly, a slight upfield shift was observed for the imine proton (**Figure 4.20**), which was opposite to that observed for salphen **4.9**. Nevertheless, evidence of Al-complexation was obtained by HRMS, which showed ions corresponding to [Salcyen-Al(MeCN)]$^+$ and [Salcyen-Al(MeCN)(H_2O)]$^+$, identical to that observed for the complexation of salphen **4.9**.

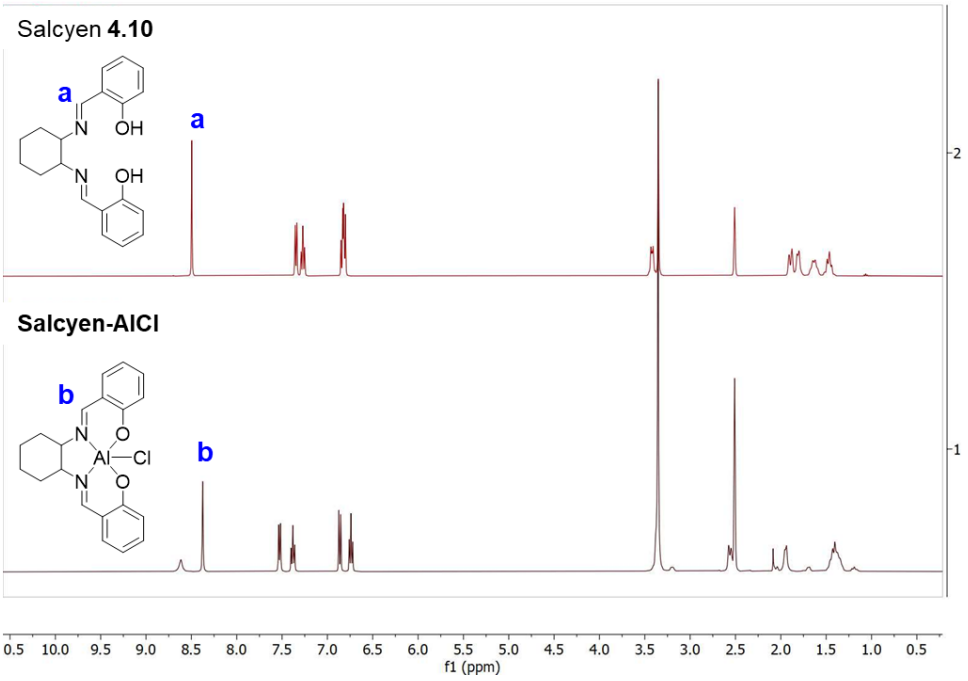

Figure 4.20: Comparison of ^{1}H NMR spectra of salcyen **4.10** and **Salcyen-Al-Cl**, where the imine proton was found to shift upfield upon complexation.

Upon isolation of **salphen-AlCl**, fluorination was carried out with NaF (**Scheme 4.5**). Similar to the salphen analogue, the resulting solid was poorly soluble in a range of solvents. However, it was found to be soluble in an acidic mixture of MeCN/H_2O, which enabled analysis by LC-MS. Comparison of the resulting LC-MS tracers, however, did not reveal a change in retention time, absorption spectrum and mass spectrum (**Figure 4.21**: UV absorbance chromatograms from LC-MS analysis of **Salcyen-AlCl** (top) and its reaction **Figure 4.21**), suggesting that formation of an Al-F bond was unsuccessful, or the Al-F bond is susceptible to hydrolysis under the acidic aqueous conditions.

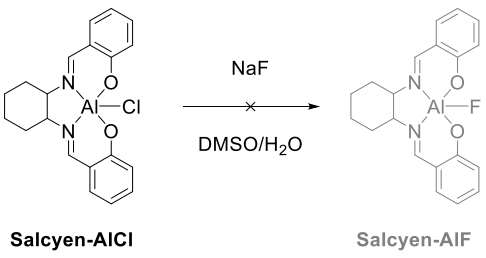

Scheme 4.5: Attempted synthesis of **salcyen-AlF**.

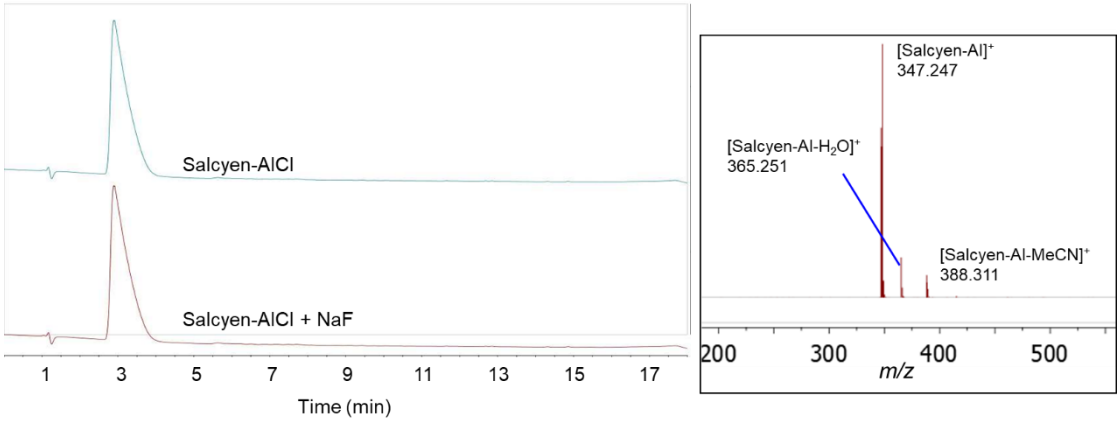

Figure 4.21: UV absorbance chromatograms from LC-MS analysis of **Salcyen-AlCl** (top) and its reaction with NaF (bottom). The mass spectra from both analysis are shown in the insert, where only [Salcyen-Al]$^+$, [Salcyen-Al-H_2O]$^+$ and [Salcyen-Al-MeCN]$^+$ were observed.

Since the formation of an Al-F bond was not successfully detected using salen derivatives, and degradation of **salphen-AlCl** was observed at 60 °C under aqueous ^{18}F fluorination conditions, a salan derivative, **4.11**, was investigated (**Figure 4.22**). It was hypothesised that degradation could be avoided for salcyan **4.11**, since the absence of imine bonds precludes hydrolysis. In addition, the use of tertiary amines as donors in acyclic ligands enabled successful [^{18}F]AlF-labelling for **RESCA** and **HBED**, though the absence of carboxylate arms could affect the ability of salcyan **4.11** to form an AlF complex.[9,51] However, using $AlCl_3$, formation of an aluminium complex was unsuccessful, where analysis by LC-MS only showed salcyan **4.11** (**Figure 4.22B** and **C**), in contrast to the Al-complexes observed for **salphen-AlCl** and **salcyen-AlCl**. This possibly shows that carboxylate arms are required for efficient aluminium complexation when salan derivatives.

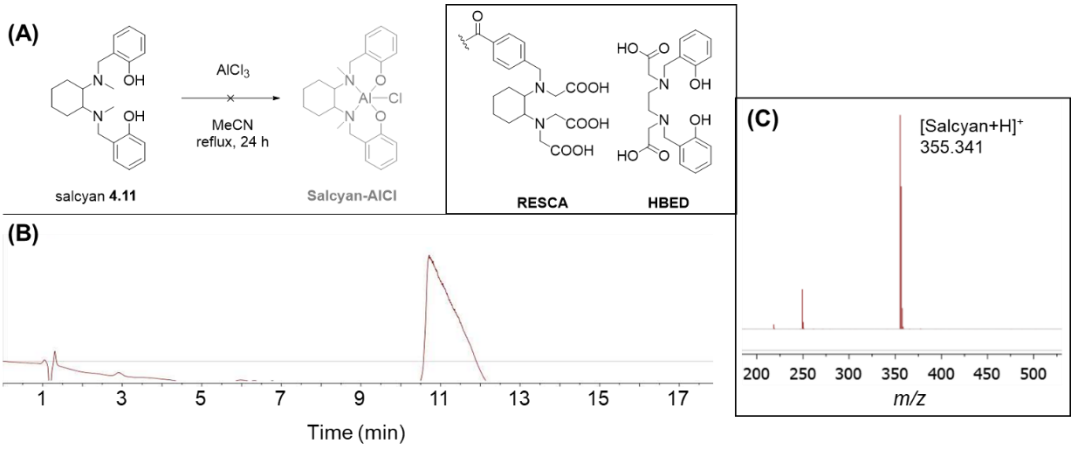

Figure 4.22: (A) Unsuccessful formation of **salcyan-AlCl** using $AlCl_3$. Insert: structures of RESCA and HBED for comparison. (B) UV absorbance chromatograms from LC-MS analysis of the reaction, showing only one species. (C) Mass spectrum of peak at t_R = 11 min, showing only [salcyan+H]$^+$.

To investigate the use of a pentadentate salen chelator for AlF complexation, saldien **4.12** was then synthesised. However, during its reaction with $AlCl_3$ instead of the formation of an aluminium complex, hydrolysis of the imine bonds was observed (**Figure 4.23**). Compared to salcyen **4.10**, which did not undergo hydrolysis under the same reaction conditions, this observation suggests that the steric rigidity offered by the cyclohexyl backbone increases the stability of the imine bonds to hydrolysis.

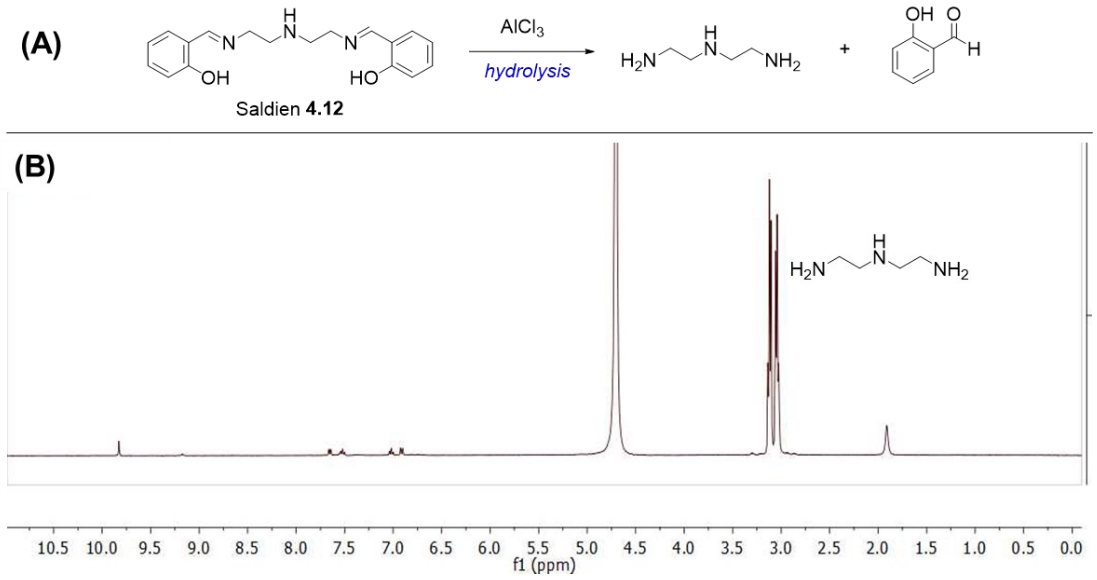

Figure 4.23: (A) Hydrolysis of saldien **4.12** when heated with $AlCl_3$. (B) ^{1}H NMR spectrum of the reaction in D_2O at room temperature, showing only diethylene triamine.

Apart from this, two salalen ligands were also synthesised to investigate their efficiency at AlF complexation (**Scheme 4.6**). Salalen **4.14** was isolated in a lower yield due to its higher solubility in MeOH, which was used to recrystallise the ligands during purification. Single crystals suitable for X-ray diffraction studies were isolated for salalen **4.14**, which showed intramolecular hydrogen bonding between the phenolic OH groups and nitrogen atoms, consistent with that observed for salcyen **4.10**.[79]

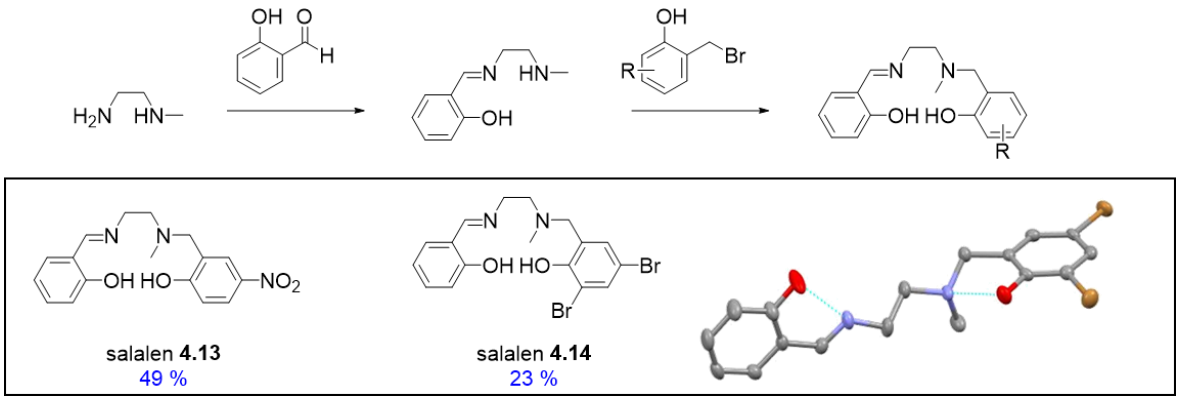

Scheme 4.6: Synthetic scheme for salalens **4.13** and **4.14**. Crystal structure of **4.14** is shown with thermal ellipsoids at 50% level, hydrogens omitted for clarity.

When reacted with $AlCl_3$, hydrolysis of the imine bond in **4.13** was observed by the disappearance of the imine proton in the ^{1}H NMR (**Figure 4.24**). The same observation was also recorded for salalen **4.14**, further confirming the hypothesis that the imine bonds are prone to hydrolysis without the rigid cyclohexyl backbone.

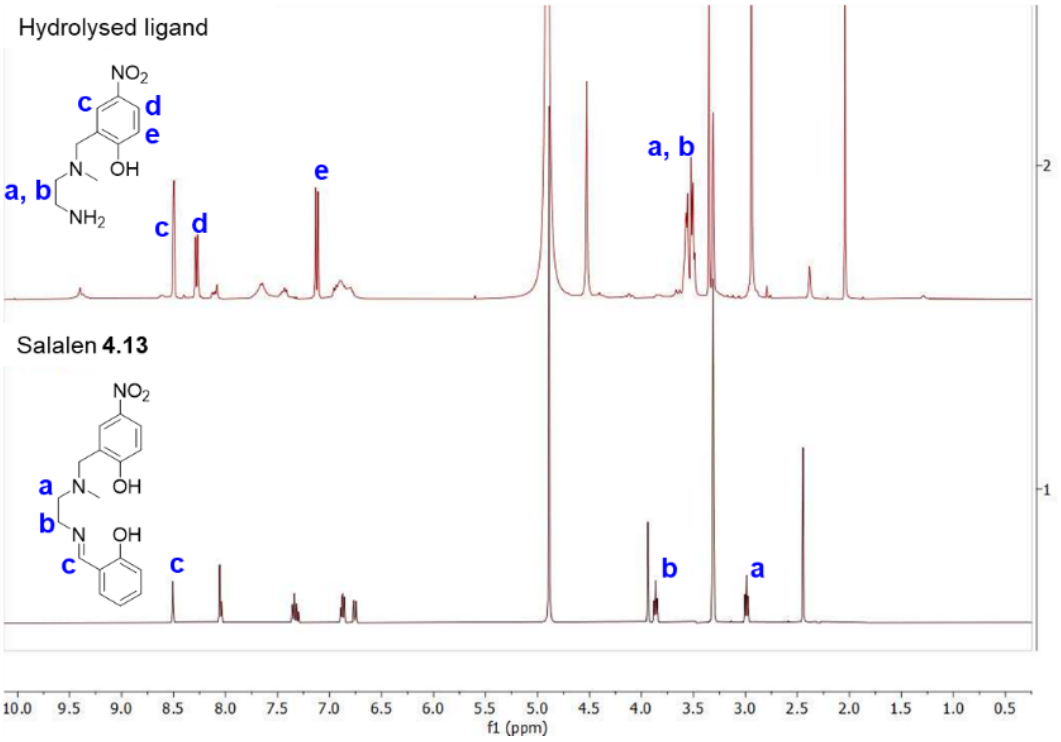

Figure 4.24: Comparison of ^{1}H NMR spectrum of salalen **4.13** before (bottom) and after (top) heating with $AlCl_3$, showing hydrolysis of the imine bond.

To avoid hydrolysis, the formation of an aluminium complex of **4.13** was attempted under anhydrous conditions using Et_2AlCl. When analysed by ^{1}H NMR, the formation of **salalen-AlCl** was indicated by a slight downfield shift of the imine proton (**Figure 4.25**). In addition, each diastereotopic proton in the ethylene backbone and benzylic position appear as a distinct signal, showing the formation of a chiral aluminium centre.

However, purification of **salalen-AlCl** by recrystallisation and trituration proved challenging due to its poor solubility in non-polar solvents such as hexane and toluene, which are typically used in the purification of salalen aluminium complexes.[69,70] The poor solubility of **salalen-AlCl** could be due to the absence of ^{t}Bu groups, which reduces its hydrophobicity and increases the possibility of aggregation to form 6-coordinate aluminium centres. When dissolution of the complex in a coordinating solvent such as THF and MeCN was attempted,[66] heating the suspension to increase solubility resulted in the degradation of the complex.

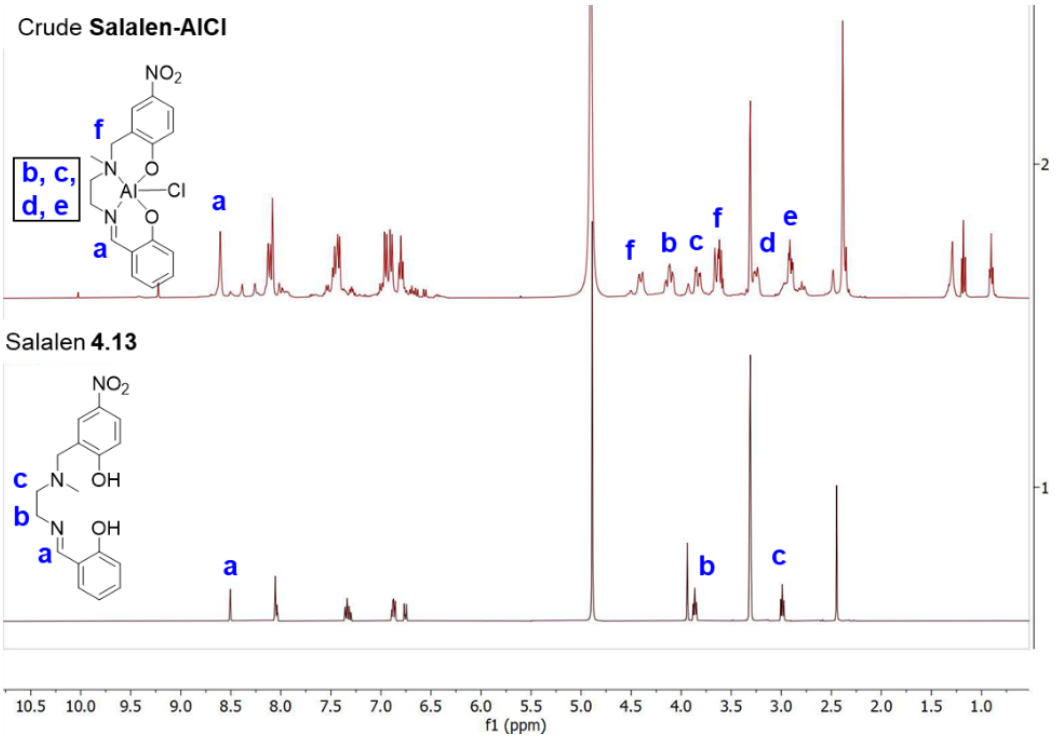

Figure 4.25: Comparison of ^{1}H NMR of salalen **4.13** before (bottom) and after (top) reaction with Et_2AlCl.

Unfortunately, further purification and synthesis of Al-salen and AlF-salen complexes were not explored due to time constraints. However, the result from this investigation shows that Et_2AlCl can be used as an alternative precursor to $AlCl_3$ for generating Al-salen complexes for ligands that are prone to hydrolysis. In comparison, complexation reactions using $AlCl_3$ were conducted in non-anhydrous MeCN, where the presence of water could potentially result in the production of HCl, contributing to the hydrolysis of the imine bonds. Although the stability of the resulting Al-salen complexes are yet to be evaluated due to the presence of impurities, the fact that **salphen-AlCl** was more stable towards hydrolysis compared to salphen **4.9** shows that this could be a viable route to synthesise pre-formed Al-complexes for ^{18}F-labelling.

4.4 Conclusions

Preliminary ^{18}F-labelling reactions using alendronic acid demonstrated that bisphosphonates could be used as potential ligands for [^{18}F]AlF-complexation, since the formation of a new radiolabelled species was observed. However, the retention of this compound on a range of analytical sorbents (silica, C4 and C18) precluded further characterisation.

To improve the stability of the resulting [^{18}F]AlF complex, a pentadentate chelator **4.5** was synthesised. However, the synthesis of a library of pentadentate chelators by Michael addition to bisphosphonate **4.6** was found to be unfeasible due to the susceptibility of the product to

undergo the retro-Michael reaction. Besides this, the unsuccessful [^{18}F]AlF-complexation by **4.5** shows that the 1-hydroxyl group is potentially required for efficient [^{18}F]AlF-labelling.

In terms of the salen ligands, successful Al-complexation was achieved using $AlCl_3$ for both salphen **4.9** and salcyen **4.10**. For ligands without a cyclohexyl backbone, it was found that Et_2AlCl could be a viable alternative to avoid hydrolysis during aluminium complexation. It was also found that the Al-salen complexes are more stable towards hydrolysis compared to the free ligands, which meant that ^{18}F-labelling using pre-formed Al-salen complexes would be preferred. Although a new radioactive species was detected during ^{18}F-labelling of **salphen-AlCl**, further characterisation of this species was unsuccessful, and subsequent analysis by mass spectrometry did not provide evidence for the formation of an Al-F bond.

In summary, although the main aim of identifying a potential ligand for [^{18}F]AlF-labelling at room temperature and physiological pH was not achieved, the results from this study could provide a platform for further studies to be carried out, which is outlined briefly in the next section.

4.5 Future work

Firstly, the purification of **salalen-AlCl** could be investigated using alternative solvent combinations, or a more strongly coordinating solvent such as DMSO. Following that, the synthesis and isolation of aluminium complexes of salan **4.11** and saldien **4.12** could be attempted using Et_2AlCl to complete the series in **Figure 4.14**.

More importantly, the synthesis of pentadentate ligands could be attempted for the formation of a more stable [^{18}F]AlF complex. A potential route is outlined in **Scheme 4.7**, which was adapted from that used by Shitama *et al.*[80] To identify an optimal chelator, the additional coordination arm could be varied by using a different heteroaryl halide. Upon synthesis of the ligands, fluorination can then be investigated to determine the potential of Al-salen complexes in enabling ^{18}F-labelling under mild conditions.

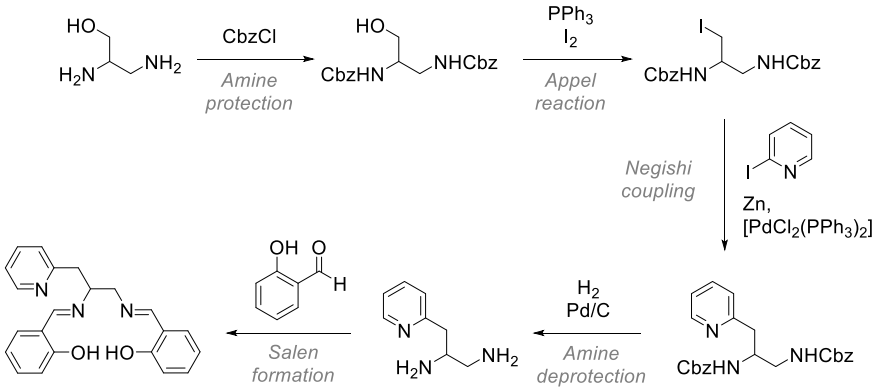

Scheme 4.7: Proposed synthetic route for pentadentate salen derivatives.

4.6 References

1 M. Kawahara and M. Kato-Negishi, *Int. J. Alzheimers. Dis.*, 2011, **2011**, Article ID 276393.

2 G. Crisponi, V. M. Nurchi, V. Bertolasi, M. Remelli and G. Faa, *Coord. Chem. Rev.*, 2012, **256**, 89–104.

3 R. G. Pearson, *J. Am. Chem. Soc.*, 1963, **85**, 3533–3539.

4 R. D. Hancock and A. E. Martell, *Chem. Rev.*, 1989, **89**, 1875–1914.

5 S. Schmitt and E. Moreau, *Coord. Chem. Rev.*, 2023, **480**, 215028-215062.

6 W. J. McBride, R. M. Sharkey, H. Karacay, C. A. D'Souza, E. A. Rossi, P. Laverman, C. H. Chang, O. C. Boerman and D. M. Goldenberg, *J. Nucl. Med.*, 2009, **50**, 991–998.

7 W. J. McBride, C. A. D'souza, R. M. Sharkey, H. Karacay, E. A. Rossi, C. H. Chang and D. M. Goldenberg, *Bioconjug. Chem.*, 2010, **21**, 1331–1340.

8 F. Cleeren, J. Lecina, E. M. F. Billaud, M. Ahamed, A. Verbruggen and G. M. Bormans, *Bioconjug. Chem.*, 2016, **27**, 790–798.

9 F. Cleeren, J. Lecina, M. Ahamed, G. Raes, N. Devoogdt, V. Caveliers, P. McQuade, D. J. Rubins, W. Li, A. Verbruggen, C. Xavier and G. Bormans, *Theranostics*, 2017, **7**, 2924–2939.

10 P. Laverman, W. J. McBride, R. M. Sharkey, A. Eek, L. Joosten, W. J. G. Oyen, D. M. Goldenberg and O. C. Boerman, *J. Nucl. Med.*, 2010, **51**, 454–461.

11 O. Happel and A. Seubert, *J. Chromatogr. A*, 2006, **1108**, 68–75.

12 M. Häring, M. M. Pérez-Madrigal, D. Kühbeck, A. Pettignano, F. Quignard and D. D. Díaz, *Mol. 2015, Vol. 20, Pages 4136-4147*, 2015, **20**, 4136–4147.

13 C. A. D'Souza, W. J. McBride, R. M. Sharkey, L. J. Todaro and D. M. Goldenberg, *Bioconjug. Chem.*, 2011, **22**, 1793–1803.

14 D. Shetty, S. Y. Choi, J. M. Jeong, J. Y. Lee, L. Hoigebazar, Y. S. Lee, D. S. Lee, J. K. Chung, M. C. Lee and Y. K. Chung, *Chem. Commun.*, 2011, **47**, 9732–9734.

15 E. Ruivo, K. Adhikari, F. Elvas, J. Fissers, C. Vangestel, S. Staelens, S. Stroobants, P. Van der Veken, L. Wyffels and K. Augustyns, *Nucl. Med. Biol.*, 2019, **76**–**77**, 36–42.

16 P. Laverman, C. A. D'Souza, A. Eek, W. J. McBride, R. M. Sharkey, W. J. G. Oyen, D. M. Goldenberg and O. C. Boerman, *Tumor Biol.*, 2012, **33**, 427–434.

17 J. H. Teh, M. Braga, L. Allott, C. Barnes, J. Hernández-Gil, M. X. Tang, E. O. Aboagye and N. J. Long, *Chem. Commun.*, 2021, **57**, 11677–11680.

18 L. Allott, C. Da Pieve, D. R. Turton and G. Smith, *React. Chem. Eng.*, 2017, **2**, 68–74.

19 S. Thompson, M. R. Kilbourn and P. J. H. Scott, *ACS Cent. Sci.*, 2016, **2**, 497–505.

20 S. H. Hausner, N. Bauer and J. L. Sutcliffe, *Nucl. Med. Biol.*, 2014, **41**, 43–50.

21 Y. Li, D. Zhang, Y. Shi, Z. Guo, X. Wu, J. L. Ren, X. Zhang and H. Wu, *Contrast Media Mol. Imaging*, 2016, **11**, 262–271.

22 T. Liu, C. Liu, X. Xu, F. Liu, X. Guo, N. Li, X. Wang, J. Yang, X. Yang, H. Zhu and Z. Yang, *J. Nucl. Med.*, 2019, **60**, 1284–1292.

23 E. Pauwels, F. Cleeren, T. Tshibangu, M. Koole, K. Serdons, L. Boeckxstaens, J. Dekervel, T. Vandamme, W. Lybaert, B. Van den Broeck, A. Laenen, P. M. Clement, K. Geboes, E. Van Cutsem, S. Stroobants, C. Verslype, G. Bormans and C. M. Deroose, *J. Nucl. Med.*, 2023, **64**, 632–638.

24 S. Piron, K. De Man, V. Schelfhout, N. Van Laeken, K. Kersemans, E. Achten, F. De Vos and P. Ost, *EJNMMI Res.*, 2020, **10**, 1–12.

25 J. Wu, S. Wang, X. Zhang, Z. Teng, J. Wang, B. C. Yung, G. Niu, H. Zhu, G. Lu and X. Chen, *J. Nucl. Med.*, 2018, **59**, 1809–1816.

26 F. L. Giesel, S. Adeberg, M. Syed, T. Lindner, L. D. Jiménez-Franco, E. Mavriopoulou, F. Staudinger, E. Tonndorf-Martini, S. Regnery, S. Rieken, R. El Shafie, M. Röhrich, P. Flechsig, A. Kluge, A. Altmann, J. Debus, U. Haberkorn and C. Kratochwil, *J. Nucl. Med.*, 2021, **62**, 201–207.

27 I. Dijkgraaf, S. Y. A. Terry, W. J. Mcbride, D. M. Goldenberg, P. Laverman, G. M. Franssen, W. J. G. Oyen and O. C. Boerman, *Contrast Media Mol. Imaging*, 2013, **8**, 238–245.

28 H. M. Yu, C. H. Chan, C. H. Yang, H. T. Hsia and M. H. Wang, *Appl. Radiat. Isot.*, 2020, **162**, 109199.

29 Y. Liu, X. Hu, H. Liu, L. Bu, X. Ma, K. Cheng, J. Li, M. Tian, H. Zhang and Z. Cheng, *J. Nucl. Med.*, 2013, **54**, 2132–2138.

30 D. Pan, Y. Yan, R. Yang, Y. P. Xu, F. Chen, L. Wang, S. Luo and M. Yang, *Contrast Media Mol. Imaging*, 2014, **9**, 342–348.

31 X. Gu, M. Jiang, D. Pan, G. Cai, R. Zhang, Y. Zhou, Y. Ding, B. Zhu and X. Lin, *J.*

Radioanal. Nucl. Chem., 2016, **308**, 851–856.

32 Y. Gai, L. Yuan, L. Sun, H. Li, M. Li, H. Fang, B. Altine, Q. Liu, Y. Zhang, D. Zeng and X. Lan, *J. Biol. Inorg. Chem.*, 2020, **25**, 99–108.

33 X. Shi, K. Gao, H. Huang and R. Gao, *Bioconjug. Chem.*, 2018, **29**, 250–254.

34 M. Wang, H. Zhang, H. Wang, H. Feng, H. Deng, Z. Wu, H. Lu and Z. Li, *Mol. Pharm.*, 2018, **15**, 3093–3100.

35 M. Li, H. Fang, Q. Liu, Y. Gai, L. Yuan, S. Wang, H. Li, Y. Hou, M. Gao and X. Lan, *Biomater. Sci.*, 2020, **8**, 1802–1814.

36 M. Lipowska, J. Klenc, D. Shetty, J. A. Nye, H. Shim and A. T. Taylor, *Nucl. Med. Biol.*, 2014, **41**, 248–253.

37 F. Basuli, X. Zhang, M. R. Williams, J. Seidel, M. V. Green, P. L. Choyke, R. E. Swenson and E. M. Jagoda, *Nucl. Med. Biol.*, 2018, **62**–**63**, 63–70.

38 L. Hoigebazar, J. M. Jeong, J. Y. Lee, D. Shetty, B. Y. Yang, Y. S. Lee, D. S. Lee, J. K. Chung and M. C. Lee, *J. Med. Chem.*, 2012, **55**, 3155–3162.

39 W. J. McBride, C. A. D'Souza, R. M. Sharkey and D. M. Goldenberg, *Appl. Radiat. Isot.*, 2012, **70**, 200–204.

40 J. Song, X. Peng, L. Li, F. Yang, X. Zhang, J. Zhang, J. Dai and M. Cui, *ACS Omega*, 2018, **3**, 13089–13096.

41 K. L. S. Chatalic, G. M. Franssen, W. M. Van Weerden, W. J. McBride, P. Laverman, E. De Blois, B. Hajjaj, L. Brunel, D. M. Goldenberg, J. A. Fehrentz, J. Martinez, O. C. Boerman and M. De Jong, *J. Nucl. Med.*, 2014, **55**, 2050–2056.

42 D. Shetty, J. M. Jeong, Y. J. Kim, J. Y. Lee, L. Hoigebazar, Y. S. Lee, D. S. Lee and J. K. Chung, *Bioorg. Med. Chem.*, 2012, **20**, 5941–5947.

43 E. A. Turolla, S. Valtorta, E. Bresciani, J. A. Fehrentz, L. Giuliano, S. Stucchi, S. Belloli, P. Rainone, F. Sudati, L. Rizzi, L. Molteni, P. Verdiè, J. Martinez, A. Torsello, R. M. Moresco and S. Todde, *Front. Pharmacol.*, 2018, **9**, 419184.

44 R. Beard, N. Singh, C. Grundschober, A. D. Gee and E. W. Tate, *Chem. Commun.*, 2018, **54**, 8120–8123.

45 D. Kang, U. Simon, F. M. Mottaghy and A. T. J. Vogg, *Pharmaceuticals*, 2021, **14**, 818.

46 Z. Zhang, G. Amouroux, J. Pan, S. Jenni, J. Zeisler, C. Zhang, Z. Liu, D. M. Perrin, F.

Bénard and K. S. Lin, *Mol. Pharm.*, 2016, **13**, 2823–2832.

47 C. Da Pieve, L. Allott, C. D. Martins, A. Vardon, D. M. Ciobota, G. Kramer-Marek and G. Smith, *Bioconjug. Chem.*, 2016, **27**, 1839–1849.

48 F. Cleeren, J. Lecina, J. Bridoux, N. Devoogdt, T. Tshibangu, C. Xavier and G. Bormans, *Nat. Protoc.*, 2018, **13**, 2330–2347.

49 E. L. Van der Veen, F. V. Suurs, F. Cleeren, G. Bormans, P. H. Elsinga, G. A. P. Hospers, M. N. Lub-De Hooge, E. G. E. De Vries, E. F. J. De Vries and I. F. Antunes, *J. Nucl. Med.*, 2020, **61**, 1355–1360.

50 L. Russelli, J. Martinelli, F. De Rose, S. Reder, M. Herz, M. Schwaiger, W. Weber, L. Tei and C. D'Alessandria, *ChemMedChem*, 2019, cmdc.201900652.

51 S. Lütje, G. M. Franssen, K. Herrmann, O. C. Boerman, M. Rijpkema, M. Gotthardt and S. Heskamp, *J. Nucl. Med.*, 2019, **60**, 1017–1022.

52 E. Al-Momani, I. Israel and S. Samnick, *Appl. Radiat. Isot.*, 2017, **130**, 102–108.

53 S. Boschi, J. T. Lee, S. Beykan, R. Slavik, L. Wei, C. Spick, U. Eberlein, A. K. Buck, F. Lodi, G. Cicoria, J. Czernin, M. Lassmann, S. Fanti and K. Herrmann, *Eur. J. Nucl. Med. Mol. Imaging*, 2016, **43**, 2122–2130.

54 J. Giglio, M. Zeni, E. Savio and H. Engler, *EJNMMI Radiopharm. Chem.*, 2018, **3**, 1–12.

55 K. Kersemans, K. De Man, J. Courtyn, T. Van Royen, S. Piron, L. Moerman, B. Brans and F. De Vos, *Appl. Radiat. Isot.*, 2018, **135**, 19–27.

56 Z. Liu, L. Yu, K. Cheng, Y. Feng, P. Qiu, Y. Gai and M. Zhou, *React. Chem. Eng.*, 2020, **5**, 1441–1449.

57 S. Piron, K. De Man, N. Van Laeken, Y. D'Asseler, K. Bacher, K. Kersemans, P. Ost, K. Decaestecker, P. Deseyne, V. Fonteyne, N. Lumen, E. Achten, B. Brans and F. De Vos, *J. Nucl. Med.*, 2019, **60**, 1736–1742.

58 S. J. Archibald and L. Allott, *EJNMMI Radiopharm. Chem.*, 2021, **6**, 1–28.

59 J. Díaz-Nido and J. Avila, *Neurosci. Lett.*, 1990, **110**, 221–226.

60 E. Gumienna-Kontecka, R. Silvagni, R. Lipinski, M. Lecouvey, F. Cesare Marincola, G. Crisponi, V. M. Nurchi, Y. Leroux and H. Kozlowski, *Inorganica Chim. Acta*, 2002, **339**, 111–118.

61 T. Bailly, R. Burgada, T. Prangé and M. Lecouvey, *Tetrahedron Lett.*, 2003, **44**, 189–192.

62 G. Crisponi, V. M. Nurchi, T. Pivetta, J. Gałezowska, E. Gumienna-Kontecka, T. Bailly, R. Burgada and H. Kozłowski, *J. Inorg. Biochem.*, 2008, **102**, 1486–1494.

63 E. Farkas, T. Fodor, F. K. Kálmán, G. Tircsó and I. Tóth, *React. Kinet. Mech. Catal.*, 2015, **116**, 19–33.

64 J. C. Pessoa and I. Correia, *Coord. Chem. Rev.*, 2019, **388**, 227–247.

65 J. Cheng, K. Wei, X. Ma, X. Zhou and H. Xiang, *J. Phys. Chem. C*, 2013, **117**, 16552–16563.

66 J. Cheng, X. Ma, Y. Zhang, J. Liu, X. Zhou and H. Xiang, *Inorg. Chem.*, 2014, **53**, 3210–3219.

67 C. Gou, S. H. Qin, H. Q. Wu, Y. Wang, J. Luo and X. Y. Liu, *Inorg. Chem. Commun.*, 2011, **14**, 1622–1625.

68 S. Samanta, B. Nath and J. B. Baruah, *Inorg. Chem. Commun.*, 2012, **22**, 98–100.

69 B. Saito, H. Egami and T. Katsuki, *J. Am. Chem. Soc.*, 2007, **129**, 1978–1986.

70 E. L. Whitelaw, G. Loraine, M. F. Mahon and M. D. Jones, *Dalton Trans.*, 2011, **40**, 11469–11473.

71 H. Y. Yin, J. Lai, J. Tang, Y. Shang and J. L. Zhang, *Inorganics*, 2018, **6**, 20.

72 D. Brodbeck, F. Broghammer, J. Meisner, J. Klepp, D. Garnier, W. Frey, J. Kästner and R. Peters, *Angew. Chem. Int. Ed.*, 2017, **56**, 4056–4060.

73 J. L. Viveros-Ceballos, L. A. Matías-Valdez, F. J. Sayago, C. Cativiela and M. Ordóñez, *Amino Acids*, 2021, **53**, 451–459.

74 C. E. McKenna, M. T. Higa, N. H. Cheung and M. C. McKenna, *Tetrahedron Lett.*, 1977, **18**, 155–158.

75 K. M. Błazewska, *J. Org. Chem.*, 2014, **79**, 408–412.

76 M. S. Ironside, M. J. Duer, D. G. Reid and S. Byard, *Eur. J. Pharm. Biopharm.*, 2010, **76**, 120–126.

77 D. W. Hutchinson and D. M. Thornton, *J. Organomet. Chem.*, 1988, **346**, 341–348.

78 E. M. Lewiecki, *Ther. Adv. Chronic Dis.*, 2010, **1**, 115.

79 P. Fan, C. Ge, X. Zhang, R. Zhang and S. Li, *Acta Crystallogr. Sect. E Struct. Reports Online*, 2011, **67**, o3399–o3399.

80 H. Shitama and T. Katsuki, *Chem. Eur. J.*, 2007, **13**, 4849–4858.

Chapter 5: π-clamp-mediated cysteine conjugation for site-selective [^{18}F]AlF-labelling of biomolecules

This chapter was done in collaboration with:

Thomas Tin Chi Yue (Chemical synthesis and ^{68}Ga-labelling)

5.1 Bioconjugation for ^{18}F-labelling of biomolecules

The use of ^{18}F-labelled small molecules has dominated the field of PET imaging in the past five decades. In particular, [^{18}F]FDG (2-[^{18}F]fluoro-2-deoxy-D-glucose) accounts for about 95% of PET scans due to its widespread diagnostic utility in oncology, cardiology and neurology.[1] First synthesised in 1968,[2] human studies of [^{18}F]FDG was documented as early as 1976 for mapping glucose metabolism in the brain.[1] Despite being the gold standard for PET imaging of many diseases,[3] the use of [^{18}F]FDG can be ineffective in cases where its uptake is not upregulated, such as in prostate,[4] neuroendocrine[5] and hepatic cancers.[6] This example highlights one of the limitations of small molecule probes, which can be restricted to cases with an observable difference in tracer metabolism between healthy and abnormal tissues.[7,8]

To overcome this, radiolabelled biomolecules such as peptides and proteins have been developed because of their high binding affinity and specificity for disease biomarkers.[8–11] However, due to the harsh reaction conditions typically employed for ^{18}F-labelling, the incorporation of ^{18}F into biomolecules is challenging as they are prone to degradation under these conditions.[8–11] Consequently, the first human study using an ^{18}F-labelled peptide, [^{18}F]FP-Gluc-TOCA (**Figure 5.1**), was only conducted in 2003 for imaging the somatostatin receptor (SSTR).[12,13] In this study, ^{18}F was incorporated using an amine-reactive prosthetic group, [^{18}F]NFP, where regioselective functionalisation of the N-terminal lysine was achieved by the use of an orthogonal Dde protecting group cleavable by hydrazine.[14] Subsequent PET imaging revealed high uptake of [^{18}F]FP-Gluc-TOCA in patients bearing sstr-positive tumours, demonstrating the diagnostic utility of ^{18}F-labelled peptides for cancer imaging.[13]

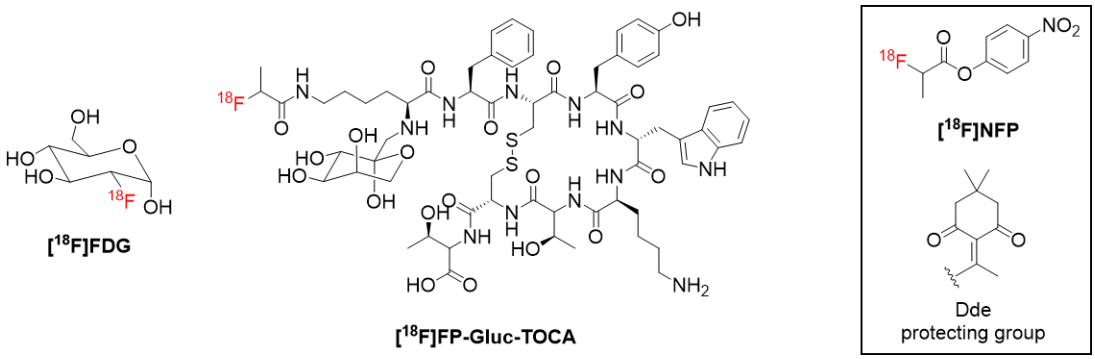

Figure 5.1: Structures of [^{18}F]FDG and [^{18}F]FP-Gluc-TOCA. Insert: structures of 4-nitrophenyl-2-[^{18}F]fluoropropionate, [^{18}F]NFP, and Dde protecting group for primary amines.

Apart from peptides, antibody fragments have also been identified as promising vectors for PET imaging due to their high specificity and affinity.[8,15] However, the bioconjugation of proteins incur additional complexities due to the increased availability of reactive amino acid residues, where non-selective conjugation strategies can result in the formation of

heterogenous mixtures or functionalisation of residues involved in the binding domain, affecting the binding affinity and pharmacokinetics of biomolecules.[16] Nevertheless, considerable successes have been achieved when ^{18}F-labelled biomolecules were used in PET imaging, highlighting the importance of the development of mild radiolabelling strategies for their functionalisation.[8]

In the next section, a brief overview of common methods for ^{18}F-labelling of biomolecules is described. Following this, site-selective conjugation methods are introduced, with a focus on methods that have been applied in ^{18}F-labelling. Finally, the *π*-clamp-mediated cysteine conjugation method is discussed before outlining the aims of this chapter.

5.1.1 Non-site-selective ^{18}F-labelling of biomolecules

Whilst a multitude of methods for bioconjugation are available for the modification of different amino acid residues,[17] traditional methods are based on reactions at nucleophilic residues, particularly lysine and cysteine.[18] In the same manner, prosthetic groups for non-site-selective ^{18}F-labelling of biomolecules can be divided into two broad categories: (A) amine-reactive prosthetic groups for the functionalisation of lysine residues and the N-terminus; and (B) thiol-reactive prosthetic groups for the functionalisation of cysteine residues.[8,9]

Amine-reactive prosthetic groups

Due to the availability of established methods for the chemoselective modification of primary amines, reactions at lysine residues are widely applied in peptide and protein functionalisation.[18] Common protocols include the use of activated esters to form amide bonds, isothiocyanates to form thiourea linkages, and aldehydes in reductive amination reactions (**Figure 5.2A**).[18] One potential drawback of the use of NHS esters is their susceptibility to hydrolysis,[19] where they have been shown to have a half-life of only 10 min at pH 8.6,[17] which could result in low reaction yields. In contrast, isothiocyanates are more resistant to hydrolysis under the same conditions.

Using these concepts, ^{18}F-labelled prosthetic groups featuring activated esters ([^{18}F]NFP and [^{18}F]SFB) and aldehydes ([^{18}F]FBA) have been developed to radiolabel biomolecules under mild conditions (**Figure 5.2B**).[12,20,21] Interestingly, despite the popularity of isothiocyanate groups for biomolecule functionalisation,[22] limited reports on ^{18}F-labelled isothiocyanate prosthetic groups are available,[23,24] presumably due to their slower reaction kinetics and longer reaction times.[25] Apart from prosthetic groups, it is also notable that lysine residues have often been used for attaching other reactive handles prior to ^{18}F-labelling, such as chelators for [^{18}F]AlF-labelling,[26,27] silyl ethers for ^{18}F-Si labelling,[28–30] and alkynes for copper-catalysed azide-alkyne cycloaddition with 2-[^{18}F]fluoroethyl azide (**Figure 5.2C**).[25]

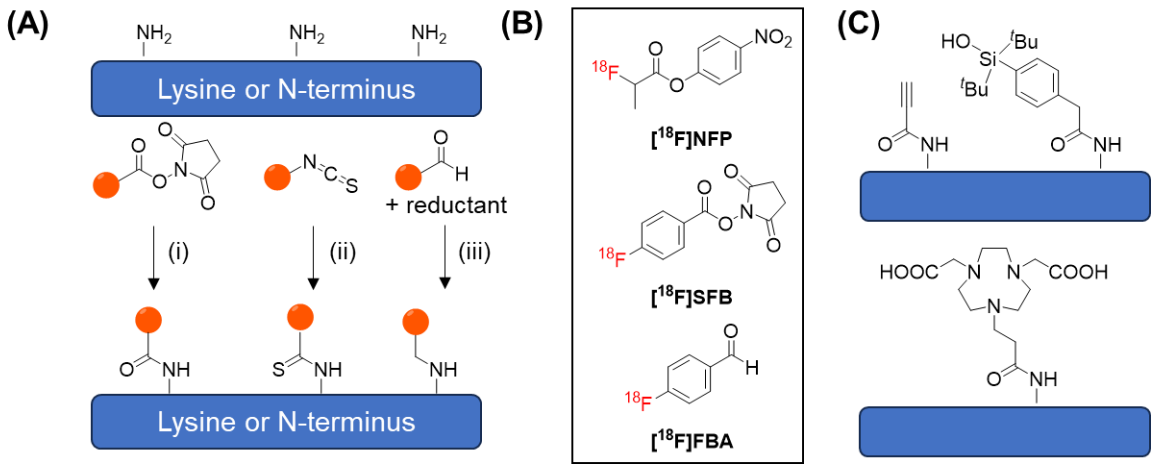

Figure 5.2: (A) Common methods for amine functionalisation: (i) activated esters such as *N*-hydrosuccinimide (NHS) esters for amide formation, (ii) isothiocyanates for thiourea formation, and (iii) aldehydes for reductive amination. (B) Common ^{18}F-labelled, amine-reactive prosthetic groups. (C) Amine modification with other functionalities for ^{18}F-labelling.

Thiol-reactive prosthetic groups

Thiol conjugation is an attractive choice for protein functionalisation due to the low natural abundance of cysteine residues (2.4 % in human proteins, *cf.* Lys: 5.0 %)[31] and strong nucleophilicity of the thiol side chain.[18,32,33] Chemoselective transformations at cysteine residues (pK_a ~ 8.5)[34] can be achieved by tuning the reaction conditions,[33,35] ideally between pH 6.5-7.5,[36,37] to reduce competing reactions at the lysine residues (pK_a ~ 10.5).[38] **Figure 5.3A** shows some of the methods used to achieve functionalisation at cysteine residues, which include the use of disulfides for cysteine-specific disulfide exchange, α-halocarbonyls for thiol alkylation, and maleimides as Michael acceptors.[18] Although maleimides have been most widely employed for thiol bioconjugation,[39] the resulting succinimide thioethers have been shown to be unstable to the retro-Michael reaction under physiological conditions, causing the release of the payload.[40] Due to the instability of thiol-succinimide adducts, alternative methods to construct stable bioconjugates at cysteine residues were developed, such as the use of mono-bromomaleimides, phenyloxadiazole methylsulfones, perfluoroaryls, palladium oxidative addition complexes (**Figure 5.3D**).[41–43]

Despite the wide range of chemistries available for cysteine conjugation, the modification of cysteine residues for PET imaging have largely been limited to the use of maleimides.[8,9,15,25] Interestingly, thiol-maleimide conjugations have often been referred to as 'site-specific' methods in multiple reports when used for ^{18}F-labelling, presumably due to the low abundance of cysteine residues on the biomolecules examined.[8,9,44–46] Of note, current thiol-reactive prosthetic groups all contain the maleimide functional group (**Figure 5.3B**),[9] and are synthesised from the corresponding amine-reactive prosthetic groups. **[^{18}F]FBAM** and

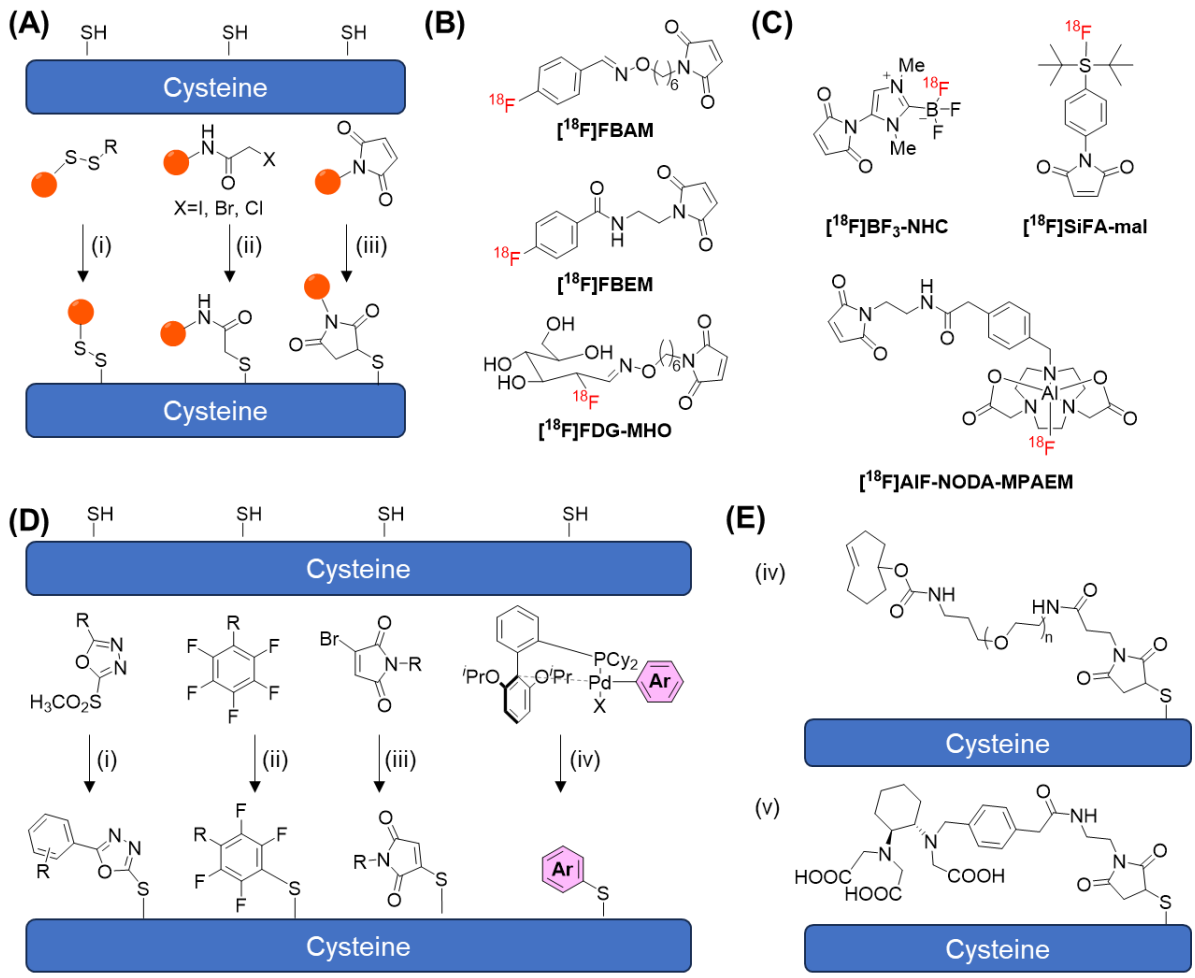

Figure 5.3: (A) Common methods for thiol functionalisation: (i) disulfides for disulfide exchange reactions, (ii) α-halocarbonyls for alkylation, and (iii) maleimides for Michael addition. (B) Common ^{18}F-labelled, thiol-reactive prosthetic groups. (C) Alternative thiol-reactive ^{18}F-labelled prosthetic groups that can be prepared by one-step ^{18}F-labelling. (D) Alternative methods for the formation of stable bioconjugates at cysteine residues using (i) phenyloxadiazole methyl sulfones, (ii) perfluoroaryls, (iii) mono-bromo maleimides, and (iv) palladium oxidative addition complexes. (E) Thiol modification with other functionalities for ^{18}F-labelling: (iv) *trans*-cyclooctene for IEDDA reaction and (v) RESCA chelator for [^{18}F]AlF-labelling.

[^{18}F]FDG-MHO are synthesised by formation of an oxime bond between *N*-(6-aminooxyhexyl)maleimide and [^{18}F]FBA and [^{18}F]FDG respectively.[44,47] In a similar manner, **[^{18}F]FBEM** is synthesised by amide coupling between *N*-(2-aminoethyl)maleimide and the corresponding ^{18}F-labelled 4-fluorobenzoate activated ester.[48] However, the multi-step synthesis required for ^{18}F-labelled, thiol-reactive prosthetic groups have limited their use due to the inconvenience and time-consuming aspects of their preparation.[25] To address this, inorganic approaches for milder ^{18}F-labelling have been used to simplify the preparation of

maleimide-containing prosthetic groups (**Figure 5.3C**), which includes the use of trifluoroborates and fluorosilanes for ^{18}F/^{19}F isotopic exchange reactions,[49,50] and chelators for [^{18}F]AlF-labelling.[51]

Apart from the use of ^{18}F-labelled maleimides, cysteines have also been modified with other reactive handles for ^{18}F-labelling of biomolecules (**Figure 5.3E**). For example, the modification of cysteines with *trans*-cyclooctene enables rapid conjugation to an ^{18}F-labelled tetrazine by the inverse-electron-demand Diels-Alder (IEDDA) reaction.[15,52] The functionalisation of cysteine residues with acyclic chelators such as RESCA also enables direct [^{18}F]AlF-labelling of biomolecules,[27] eliminating the use of prosthetic groups.

Whilst the use of these lysine and thiol conjugation strategies has enabled biomolecules to be radiolabelled and used in receptor-targeted PET imaging, their modification using these methods can lead to the formation of heterogeneous mixtures. Apart from poor reproducibility and challenges associated with precise characterisation of the modified biomolecules,[53] the use of stochastic conjugation methods can also affect the binding ability, pharmacokinetics, stability and toxicity of biomolecules.[16,32] To overcome this, site-selective conjugation strategies have been developed, which are discussed in the next section.

5.1.2 Site-selective ^{18}F-labelling of biomolecules

To overcome the issues associated with stochastic bioconjugation, a broad range of methods have been developed to achieve site-selective or site-specific bioconjugation. These methods can be broadly divided into two categories: chemo-enzymatic methods and chemical methods based on functional group reactivity.[53]

In brief, chemo-enzymatic methods rely on the introduction of a chemical tag, such as a peptide sequence, into the biomolecule. This tag is recognised by the enzyme of choice, which generates a reactive intermediate for further functionalisation. Whilst the use of chemo-enzymatic methods, such as sortase-mediated conjugations and transglutaminase-mediated conjugations,[54,55] represent powerful methods to site-specifically modify biomolecules, further discussion of these methods are not included since chemo-enzymatic methods for biomolecule functionalisation fall outside the scope of this thesis.

In terms of chemical methods, site-specific conjugation of biomolecules can be achieved by the introduction of non-canonical amino acids containing functionalities that are orthogonal to existing amino acids, such as alkynes, azides and aryl halides (**Figure 5.4A**).[18,32] In conjunction with these, ^{18}F-labelled prosthetic groups have also been developed for the site-specific labelling of biomolecules, with some examples shown in **Figure 5.4B**.[56–58] [^{18}F]FEA and **5.1** are widely employed in the copper-catalysed azide-alkyne cycloaddition (CuAAC)

reactions,[59–61] whereas the use of dibenzocyclooctyne (DBCO) **5.2** enables copper-free 'click' chemistry by strain-promoted azide-alkyne cycloaddition (SPAAC).[62] In addition, ^{18}F-labelled boronic acids have also been developed to enable site-specific conjugation of proteins with aryl halide handles.[57,63]

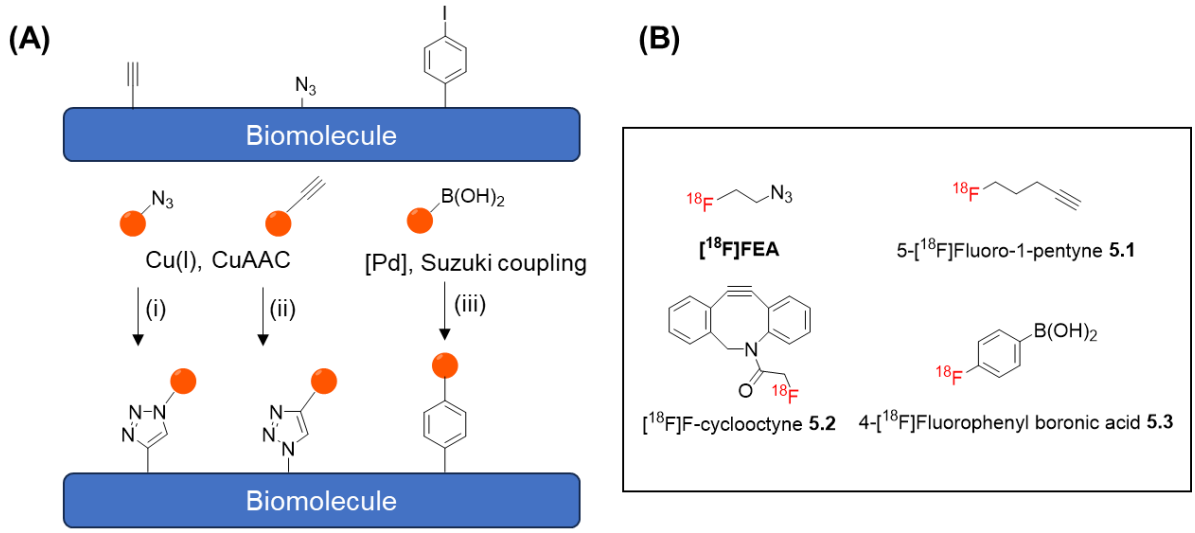

Figure 5.4: Chemical methods for site-specific bioconjugation of non-canonical amino acids: (i), (ii) copper-catalysed azide-alkyne cycloaddition, and (iii) Suzuki-Miyaura coupling between aryl iodide and boronic acids. (B) Selected examples of ^{18}F-labelled prosthetic groups for site-specific bioconjugation.

Apart from site-specific conjugation using bioorthogonal handles, which can be incorporated into biomolecules by genetic code expansion,[32] site-selective bioconjugation can also be achieved at native amino acids residues. One example is the modification of the N-terminus, which can be achieved through pH control or participation of the functional groups on its side chain residues (**Figure 5.5**). For pH controlled reactions, selective amine modification at the N-terminus instead of lysine residues is afforded due to the difference in pK_a between the α-amine of the N-terminus (pK_a = 6-8) and the ε-amines of lysine residues (pK_a ~10.5).[64] Although pH control does not provide exclusive site-selective modification, this method can reduce the heterogeneity of the resulting bioconjugates, and has been applied for the site-selective ^{18}F-labelling of peptides at the N-terminus using [^{18}F]SFB.[65,66]

In terms of the participation of side chain residues, native chemical ligation is likely the most well-developed method (**Figure 5.5B**),[64,67,68] which relies on transthioesterification followed by an intramolecular S- to N- acyl transfer to form a stable amide bond. However, this method has yet to be reported for the ^{18}F-labelling of biomolecules, presumably due to the lack of an ^{18}F-labelled thioester prosthetic group. Nevertheless, modification at N-terminal cysteines can also be achieved by condensation of 2-cyanobenzothiazole derivatives.[69] With a fast second

order rate constant of 9.19 M^{-1} s^{-1},[69] an ^{18}F-labelled prosthetic group, **[^{18}F]F-CBT** has been developed and applied in the site-selective ^{18}F-labelling of peptides and affibodies, providing high radiochemical conversions of up to 92% during the conjugation step.[46,70]

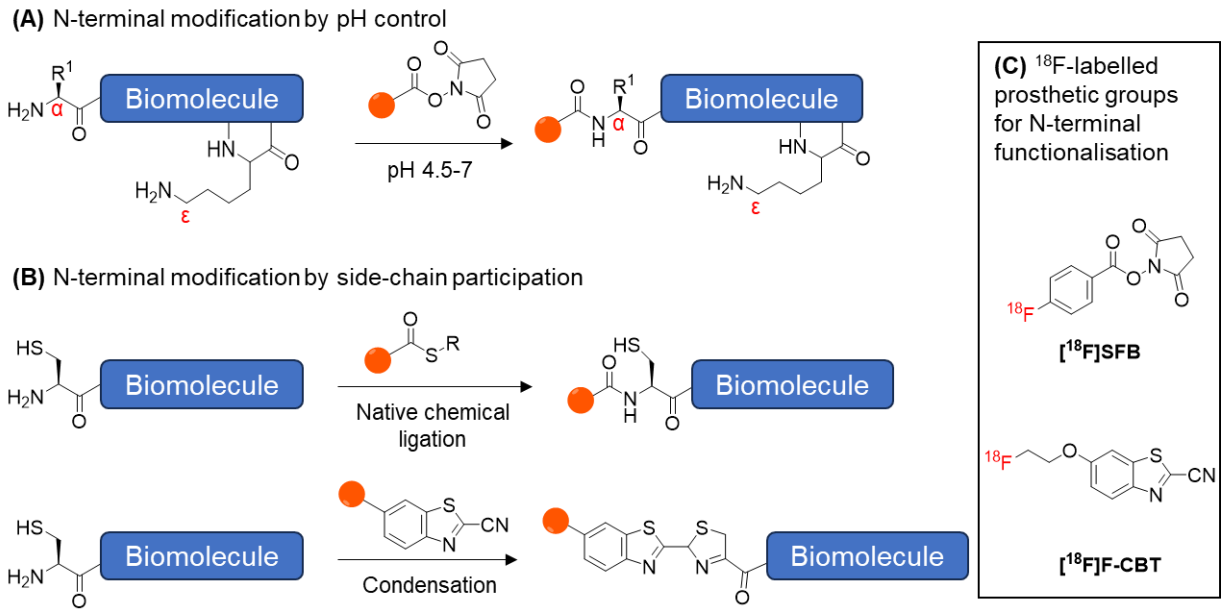

Figure 5.5: Site-selective modification of the N-terminus by (A) pH control and (B) side-chain participation.

Apart from the N-terminus, site-selective modification can also be achieved at other regions of biomolecules using chemoselective reactions (**Figure 5.6**). For example, in a seminal work reported by Lin *et al.* in 2017, oxaziridines were used for the selective functionalisation of methionine,[71] which is the second least abundant amino acid residue that is often located within the core of proteins.[72] The lack of solvent-exposed methionine residues enables more precise functionalisation of biomolecules, which led to the use of oxaziridine **5.3** (**Figure 5.6C**) to site-selectively functionalise peptides with an alkyne prior to radiolabelling by CuAAC using an ^{18}F-labelled azide.[73]

Besides this, site-selective modification of cysteine residues can also be achieved at the disulfide bridges of antibodies (**Figure 5.6B**).[35,74] Following reduction of the disulfide bonds, rebridging can be achieved using dibromomaleimides functionalised with a chelator, which enables radiolabelling by copper-64 and zirconium-89.[75] However, ^{18}F-labelling of antibodies using this approach has yet to be explored, presumably due to the mismatch in the half-life of fluorine-18 ($t_{1/2}$ = 109.8 min) and the long circulation time of antibodies (1-7 days). Apart from dibromomaleimides, dibromopyridazinedione **5.4** has also been used to functionalise antibodies with *trans*-cyclooctene,[76] which potentially allows pre-targeted PET imaging using an ^{18}F-labelled tetrazine.[77] In pre-targeted PET imaging, functionalised biomolecules with long

circulation times are first injected into animals prior to radiolabelling to allow accumulation at the target site and clearance from the systemic circulation. Following this, a radiotracer with the complementary bioorthogonal 'click' handle is administered to enable PET imaging of the target receptor, allowing biomolecules with long circulation times to be used in combination with short-lived radionuclides.[77–80]

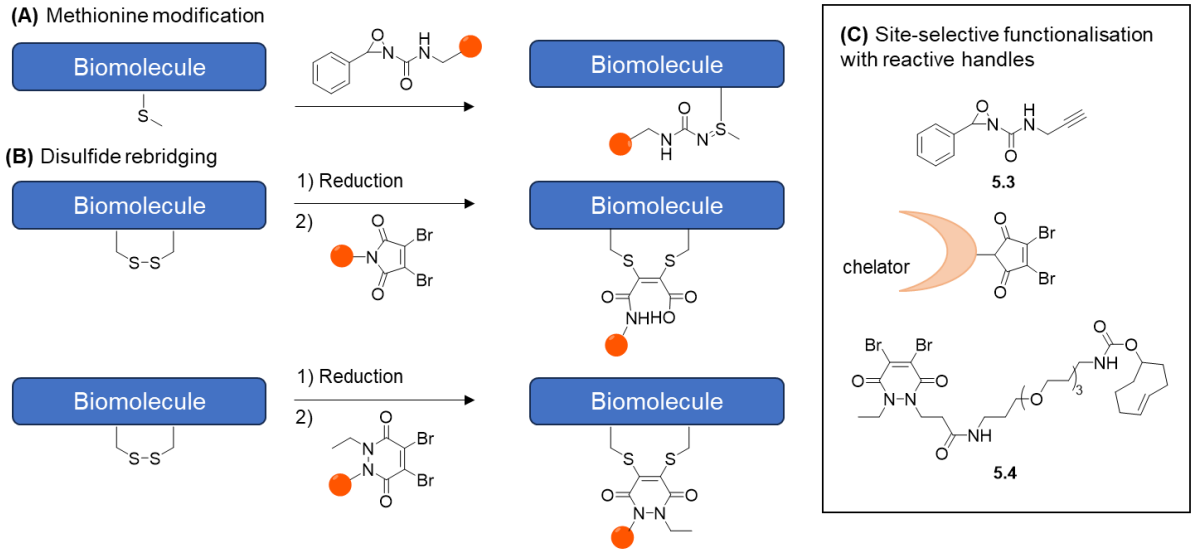

Figure 5.6: Examples of alternative methods to achieve site-selective modification of biomolecules by (A) methionine functionalisation and (B) disulfide rebriding. (C) Compounds used for site-selective functionalisation of biomolecules at methionine residues and disulfide bridges prior to radiolabelling.

In summary, while this section does not exhaustively discuss all the available methods for site-selective functionalisation of biomolecules, the use of site-selective bioconjugation has enabled the synthesis of biomolecules with improved pharmacokinetics and imaging capabilities.[32,53,68] Thus, the development of new methods to achieve site-selective functionalisation for ^{18}F-labelling would expand on the currently available strategies.

5.1.3 *π*-clamp mediated cysteine conjugation

In contrast to the use of maleimides, which generate thioethers that are prone to undergo retro-Michael addition reactions, the use of perfluoroaryl compounds for non-site-selective cysteine functionalisation has been shown to generate stable bioconjugates (**Figure 5.3**).[42] However, efficient arylation at cysteine residues by nucleophilic aromatic substitution (S_NAr) was only achievable in organic solvents such as DMF,[81] which precludes the use of this method for protein modification. Although rapid conjugation in aqueous conditions can be achieved with enzymes,[82,83] the ability to achieve one-step and catalyst-free site-selective cysteine conjugation in aqueous conditions was still unavailable.

To promote the reactivity of cysteines with **P**er**F**luoro**Bi****P**henyl (PFBP) reagents in aqueous conditions, Zhang *et al*. screened a library of peptides to identify peptide chains that can react quickly with these PFBP reagents.[84] Each peptide contained at least one cysteine (Cys) and one lysine (Lys) residue, and was reacted with a biotin-functionalised PFBP (**PFBP-biotin**, **Figure 5.7**). Upon completion, streptavidin beads were used to isolate the biotin-containing compounds. Subsequent analysis by liquid chromatography-tandem mass spectrometry (LC-MS/MS) revealed that a Phe-Cys-Pro-Trp sequence had reacted with the **PFBP-biotin**. To explain the increased reactivity of the cysteine residue to arylation, the authors hypothesised that the phenylalanine (Phe) and (Trp) residues interact with the PFBP moiety by *π*-stacking and termed this the '*π*-clamp'.

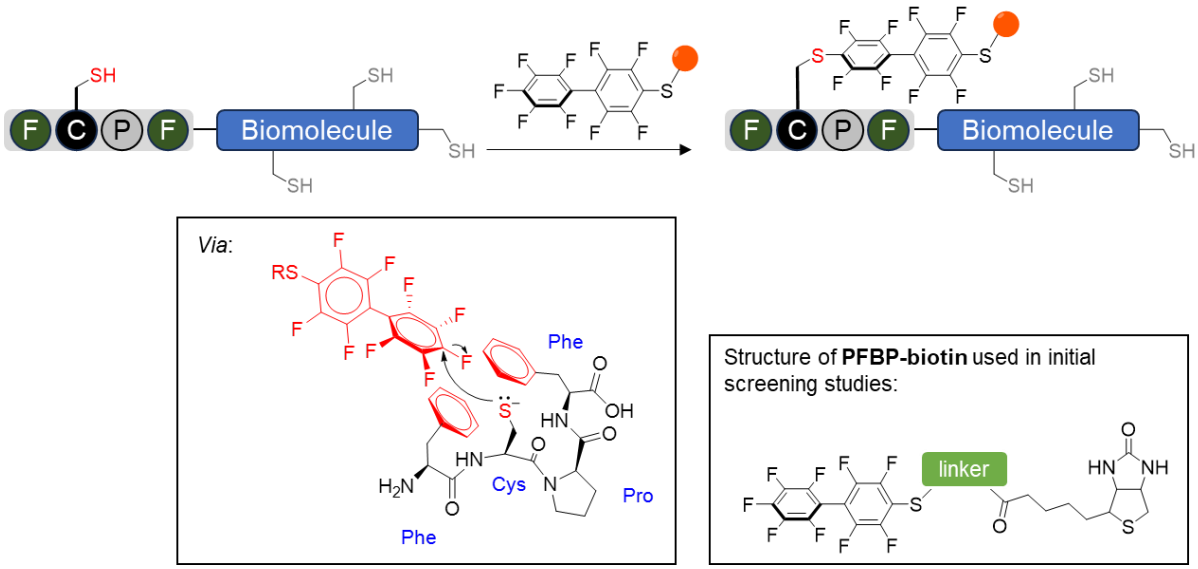

Figure 5.7: *π*-clamp-mediated cysteine conjugation using perfluorobiphenyl reagents. General scheme redrawn from Zhang *et al*.[84]

To better understand the increased reactivity of the *π*-clamp-mediated cysteine conjugation, the Phe and Trp residues were substituted with other aromatic residues (Phe, Trp and Tyr). In these cases, reactivity of the cysteine residue was preserved, with the Phe-Cys-Pro-Phe combination giving the fastest reaction (full conversion after 30 min). In contrast, changing the Phe and Trp residues to glycines (Gly) resulted in decreased reactivity, and changing the L-proline to D-proline also reduced reactivity, showing the importance of the proline residue in positioning the *π*-clamp. DFT calculations further revealed that the reaction between perfluorobiaryls and Phe-Cys-Pro-Phe were more favourable when compared to Gly-Cys-Pro-Gly both kinetically (3 kcal mol^{-1}) and thermodynamically (7 kcal mol^{-1}).[85]

Using this newly developed *π*-clamp-mediated cysteine conjugation, the authors were able to site-selectively functionalise antibodies to produce homogenously modified antibody-drug

conjugates. Following this, PFBP reagents functionalised with iridium(III) and rhenium(I) have also been reported for site-selective functionalisation of peptides for phototherapeutic and bioimaging applications.[86,87] Rhodamine-PFBP conjugates have also been synthesised to functionalise antibody fragments and proteins for fluorescent imaging, with the resulting bioconjugates showing preserved binding and cell penetrating abilities.[88,89]

In summary, compared to previous methods to achieve site-selective bioconjugation, such as bioorthogonal reactions and the use of enzymes as catalysts, site-selectivity is afforded by the *π*-clamp-mediated cysteine conjugation by the modulation of the chemical environment around the cysteine residue, which has the following advantages:

(i) No external catalyst is required.
(ii) Functionalisation is not limited to residues close to the N-terminus.
(iii) Only native amino acids are required, removing the need for genetic code expansion.
(iv) No protecting groups are required.
(v) The small size of the FCPF tag minimises disruption of the biomolecule function.

Given the advantages and operational simplicity of the *π*-clamp-mediated cysteine conjugation, it is envisioned that it could be used to achieve site-selective ^{18}F-labelling of biomolecules. The comparable reaction kinetics (second order rate constant k = 0.76 M^{-1} s^{-1}) to the SPAAC reaction (0.01-1 M^{-1} s^{-1}) also shows the potential of PFBP reagents to be used as prosthetic groups in ^{18}F-labelling.

5.1.4 Aims and objectives

The primary aim of this chapter is to evaluate the feasibility of applying the *π*-clamp-mediated cysteine conjugation for [^{18}F]AlF-labelling of biomolecules. Two strategies will be explored (**Figure 5.8**):

A. Prosthetic group approach, where an [^{18}F]AlF-labelled PFBP is used to radiolabel biomolecules under mild conditions.
B. Direct [^{18}F]AlF-labelling approach, where the biomolecule is functionalised with a PFBP-NODA conjugate prior to [^{18}F]AlF-labelling

It is envisioned that the prosthetic group approach would result in milder bioconjugation conditions, making it applicable to radiolabelling heat- and acid-sensitive biomolecules. In contrast, the direct [^{18}F]AlF-labelling approach would likely result in higher radiochemical yields since the conjugation step is eliminated from the radiosynthesis. Upon successful [^{18}F]AlF-labelling, evaluation of the stability and *in vitro* uptake of the resulting bioconjugates will be conducted.

To demonstrate the applicability of the *π*-clamp-mediated cysteine conjugation for radiolabelling approaches other than the [^{18}F]AlF method, a trimethylammonium-nicotinamide-functionalised PFBP will also be investigated as a potential prosthetic group (**Figure 5.9**), where this ^{18}F-labelling approach is used in the production of [^{18}F]SFB.[90–92]

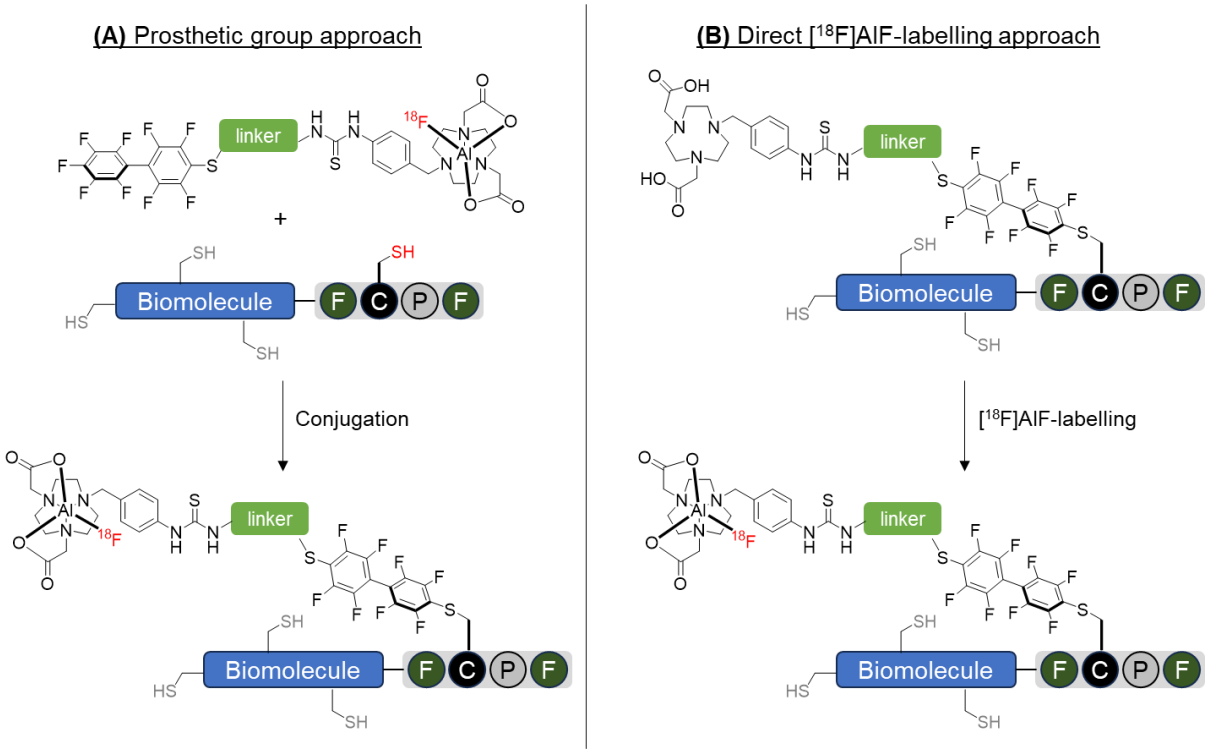

Figure 5.8: Development of the *π*-clamp-mediated cysteine conjugation for site-selective [^{18}F]AlF-labelling of biomolecules using (A) a prosthetic group approach and (B) a direct [^{18}F]AlF-labelling approach.

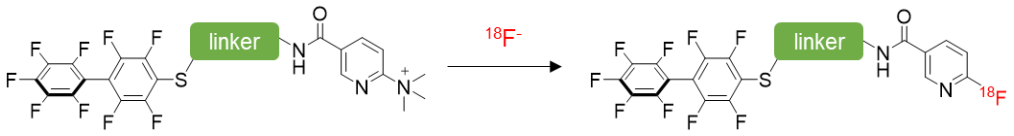

Figure 5.9: Site-selective ^{18}F-labelling using a trimethylammonium-nicotinamide-functionalised PFBP precursor.

5.2 Prosthetic group approach

In this study, octreotate was chosen as a model biomolecule due to the presence of competing cysteine residues, and its widespread application in targeting the somastostatin receptor subtype 2 (SSTR2) for imaging and treating neuroendocrine tumours.[93] A range of radiolabelled analogues of octreotate have also been synthesised with different radioisotopes such as ^{18}F, ^{68}Ga, ^{90}Y, ^{111}In and ^{177}Lu, demonstrating the utility of this peptide for nuclear imaging and therapy.[93–95] In this study, an FCPF tag was attached at the N-terminus of octreotate to enable cysteine functionalisation via the *π*-clamp approach (**Figure 5.10**).

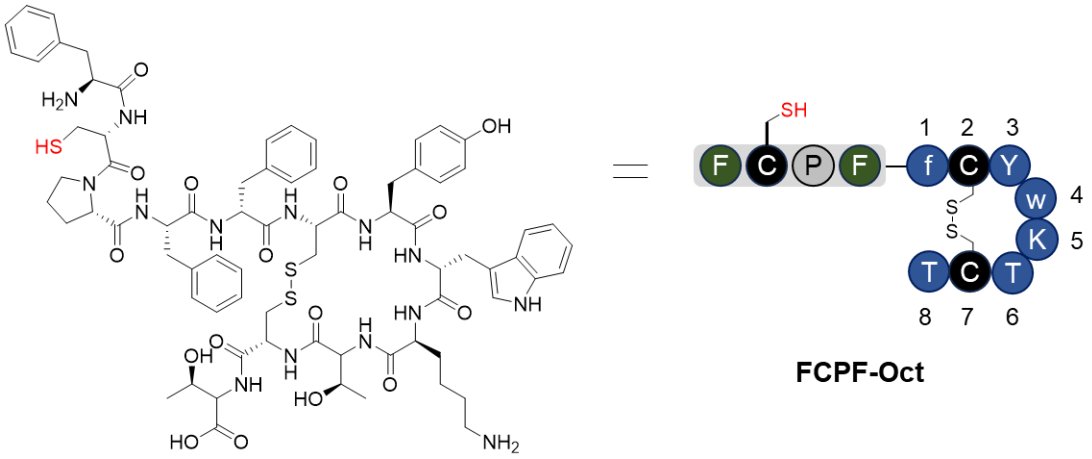

Figure 5.10: Structure of **FCPF-Oct** used in this study, where numbers of the amino acid residues on octreotate are shown for reference.

5.2.1 Synthesis of perfluorobiphenyl (PFBP) reagents

The synthesis of a NODA-functionalised perfluorobiphenyl (**PFBP-NODA**) for site-selective [^{18}F]AlF-labelling is shown in **Scheme 5.1**. Upon deprotection of 2-(tritylthio)ethanamine, **PFBP-NH$_2$** was synthesised in 20 % yield, which was reacted with a bifunctional isothiocyanate-functionalised NODA chelator to quantitatively afford **PFBP-NODA** for [^{18}F]AlF-labelling.

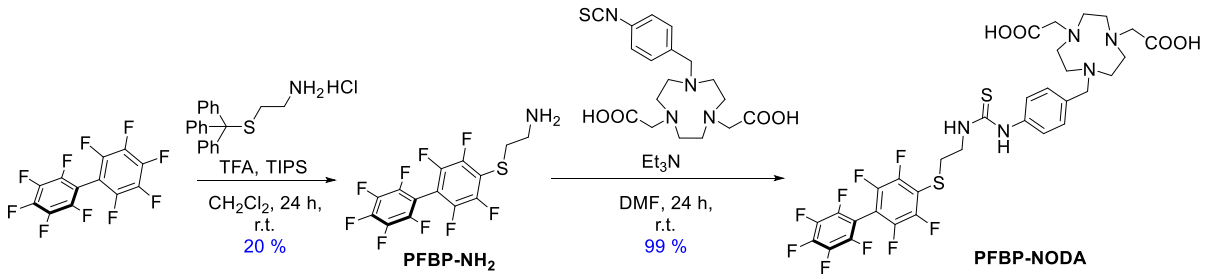

Scheme 5.1: Synthetic route of **PFBP-NODA**

Besides this, the synthesis of trimethylammonium-nicotinamide functionalised PFBP is outlined in **Scheme 5.2**. Dicylohexylcarbodiimide (DCC)-mediated coupling between **5.5** and 2,3,4,5-tetrafluorophenol generated **5.6** in 74% yield. Subsequent S_NAr with trimethylamine and counterion exchange with TMSOTf produced **5.7** in 64% yield. Finally, reaction of the activated ester with **PFBP-NH$_2$** generated **PFBP-Pyr-NMe$_3$**, ready for ^{18}F-labelling. A representative ^{19}F-NMR of the PFBP moiety is shown in **Figure 5.11**, where coupling between the aromatic fluorine atoms were observed.

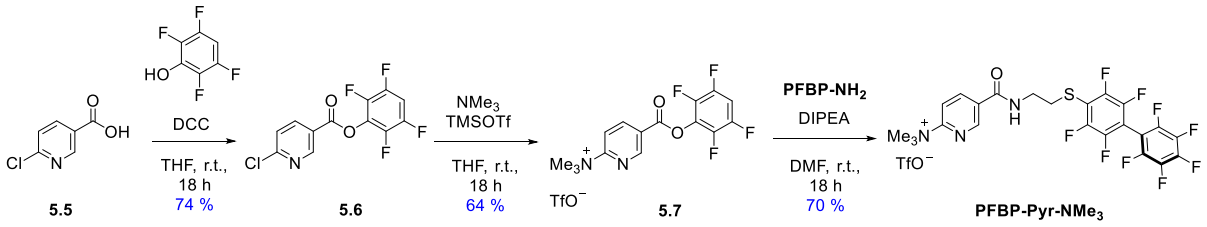

Scheme 5.2: Synthetic route of **PFBP-Pyr-NMe$_3$**

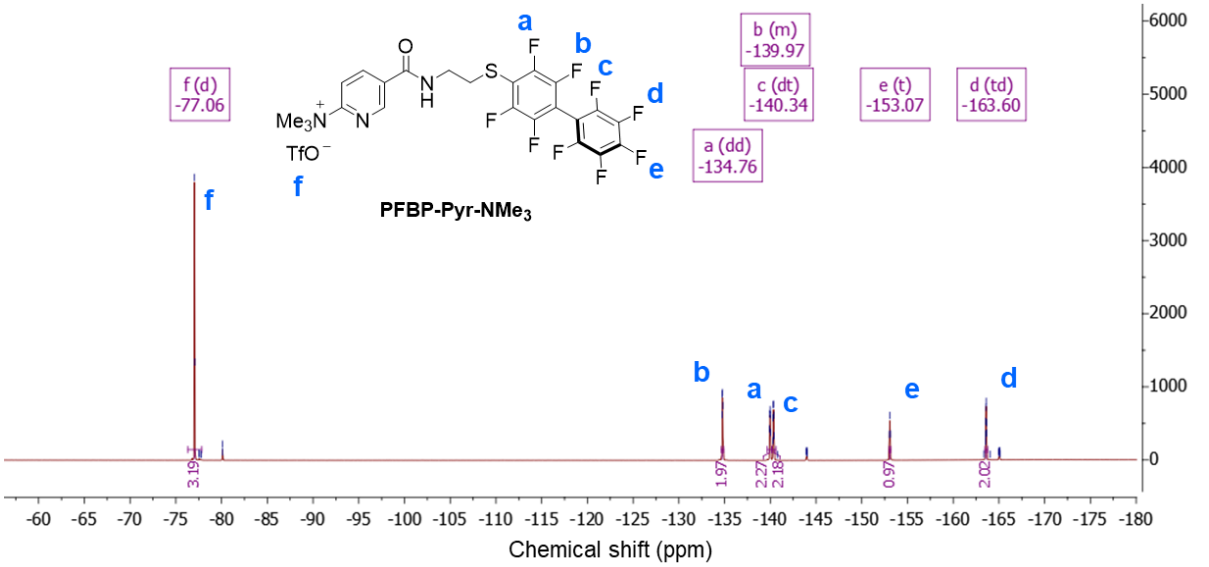

Figure 5.11: ^{19}F NMR of **PFBP-Pyr-NMe$_3$** in $CDCl_3$ at room temperature.

5.2.2 Conjugation efficiency of PFBP reagents

Upon synthesis of the PFBP-reagents, their specificity for the *π*-clamp-mediated cysteine conjugation was investigated using two tetrapeptides sequences: Phe-Cys-Pro-Phe (FCPF) and Gly-Cys-Pro-Gly (GCPG). The reaction of the FCPF *π*-clamp with **PFBP-NODA** successfully produced the desired product when analysed by LC-MS (**Figure 5.12**). In comparison, no reaction was observed for GCPG under the same conditions (**Figure 5.13**), confirming the results observed by Zhang *et al*. that perfluoroaryl reagents show poor reactivity with cysteines under aqueous conditions.[42,82–84]

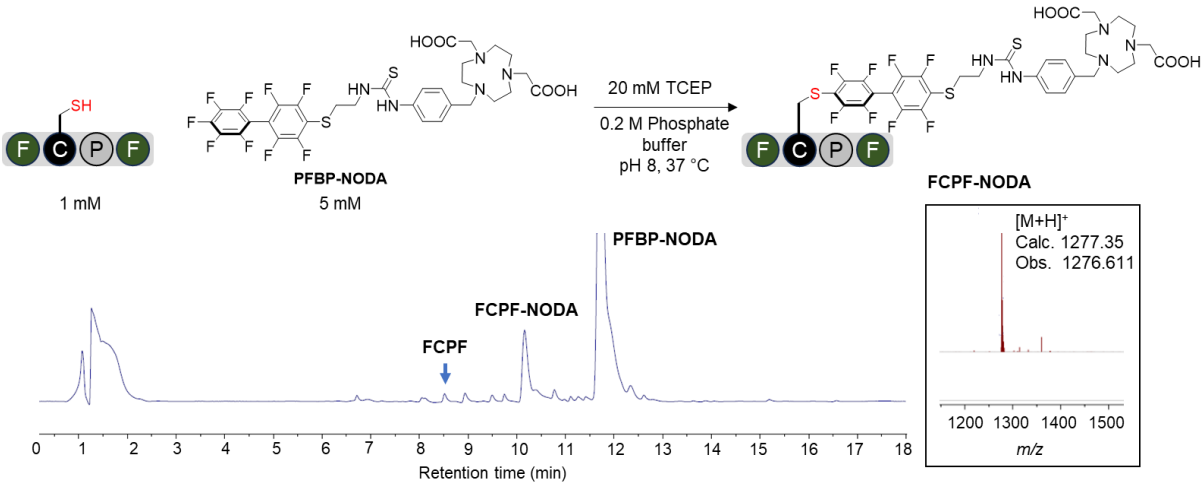

Figure 5.12: Reaction between FCPF and **PFBP-NODA**, where UV trace from the LC-MS analysis shows the formation of **FCPF-NODA**. Insert shows mass spectrum of the product.

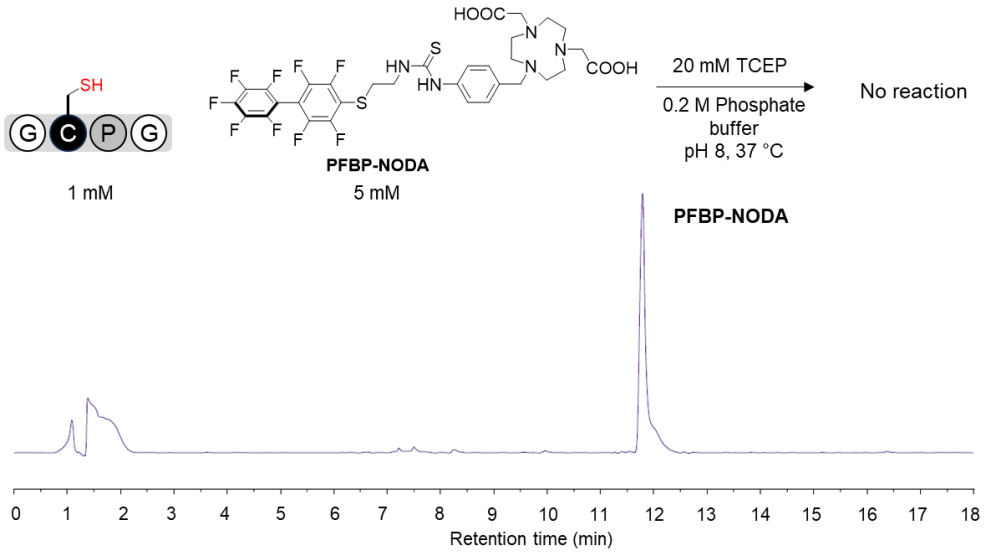

Figure 5.13: Reaction between GCPG and **PFBP-NODA**, where no cysteine arylation was observed.

After confirming the specificity and ability of **PFBP-NODA** to react with the *π*-clamp cysteine, its reactivity with **FCPF-Oct** was investigated (**Figure 5.14**). Although the formation of NODA-FCPF-Oct was observed after 30 min, the reaction did not proceed to completion even after 4 h, with **FCPF-Oct** still being detected. The slow reactivity was in contrast to that reported by Zhang *et al*., who obtained quantitative conversions after 30 min.[84] This could possibly be attributed to the poor aqueous solubility of **FCPF-Oct**. Interestingly, reaction of a second cysteine residue with **PFBP-NODA** was also detected after 2 h, which likely occurs at Cys-2 because it is adjacent to two aromatic residues (Phe-1 and Tyr-3) that could possibly adopt a configuration that is similar to *π*-clamp. Although this shows that octreotate is likely

not the ideal substrate for the development of site-selective cysteine conjugation for [^{18}F]AlF-labelling, perhaps it gives an indication on the limitations of this method in achieving site-selective conjugation.

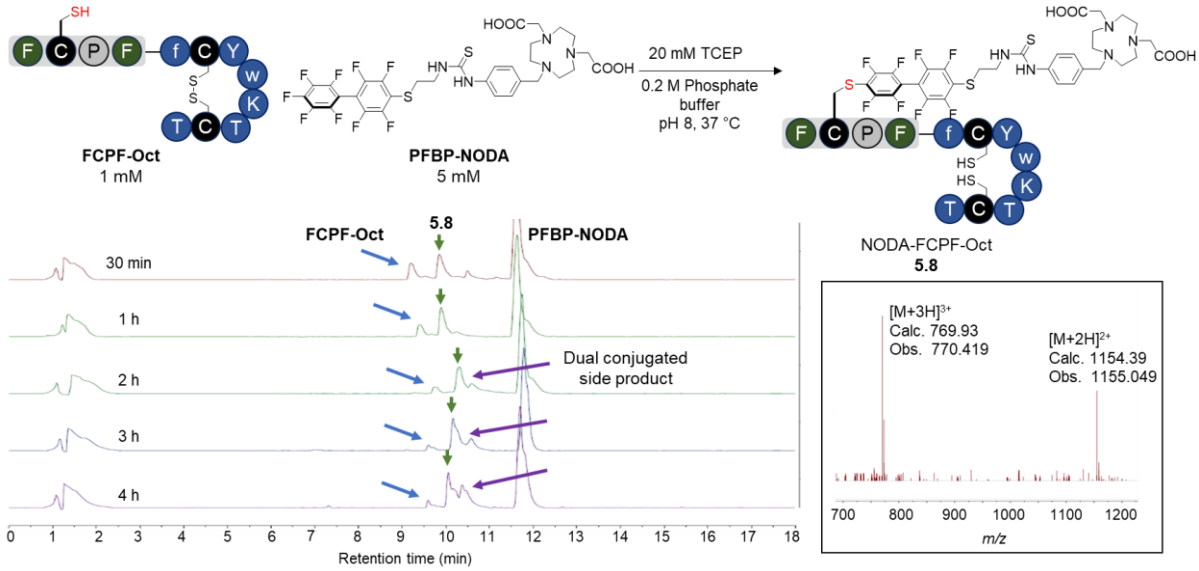

Figure 5.14: Reaction of **FCPF-Oct** with PFBP-NODA, where UV traces from LC-MS analysis show that the reaction was not complete after 4 h, and a dual conjugated side product was observed. Insert shows mass spectrum of **5.8**.

To minimise conjugation at the second cysteine residue, the reaction was repeated with a lower concentration of **PFBP-NODA** (2 mM). Subsequent analysis by LC-MS showed the formation of only NODA-PFBP-Oct **5.8** (**Figure 5.15**), affording site-selective conjugation at the desired cysteine residue. Expectedly, the reaction remained sluggish, where full conversion of FCPF-Oct to **5.8** was not achieved after 4 h. Precipitation was also observed during these reactions, potentially indicating the increased hydrophobicity of octreotate after modification with **PFBP-NODA**, leading to its decreased solubility in aqueous media.

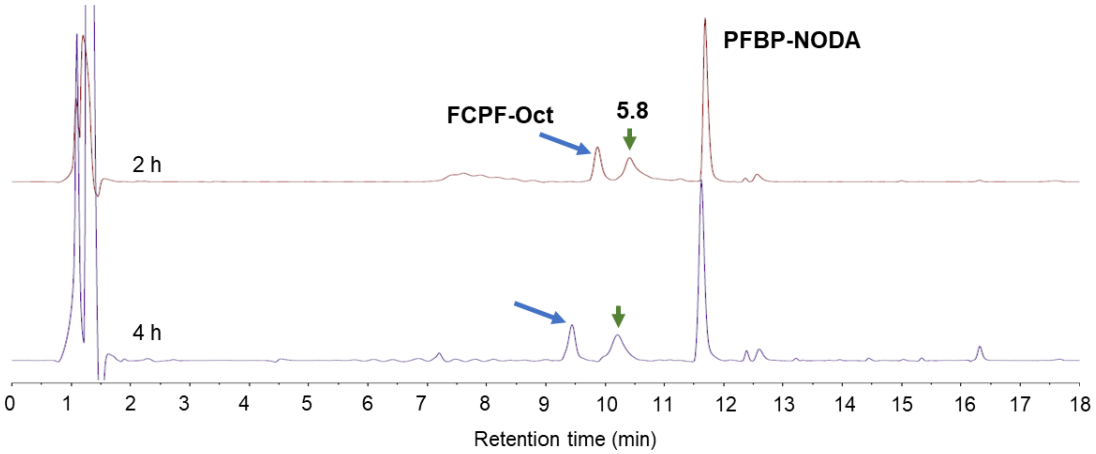

Figure 5.15: Reaction of FCPF-Oct with PFBP-NODA at a lower concentration (2 mM, 2 equiv.), where the dual-conjugated side product is not observed.

Compared to PFBP-NODA, the addition of PFBP-Pyr-NMe_3 resulted in instant precipitation. Subsequent analysis by LC-MS showed that both the desired NMe_3-Pyr-Oct **5.9** and the dual conjugated side products were formed after 10 min, indicating the increased reactivity of PFBP-Pyr-NMe_3 towards FCPF-Oct. Analysis of the reaction mixture at later time points proved challenging due to the poor solubility of the products, where reliable UV-HPLC chromatograms could not be obtained.

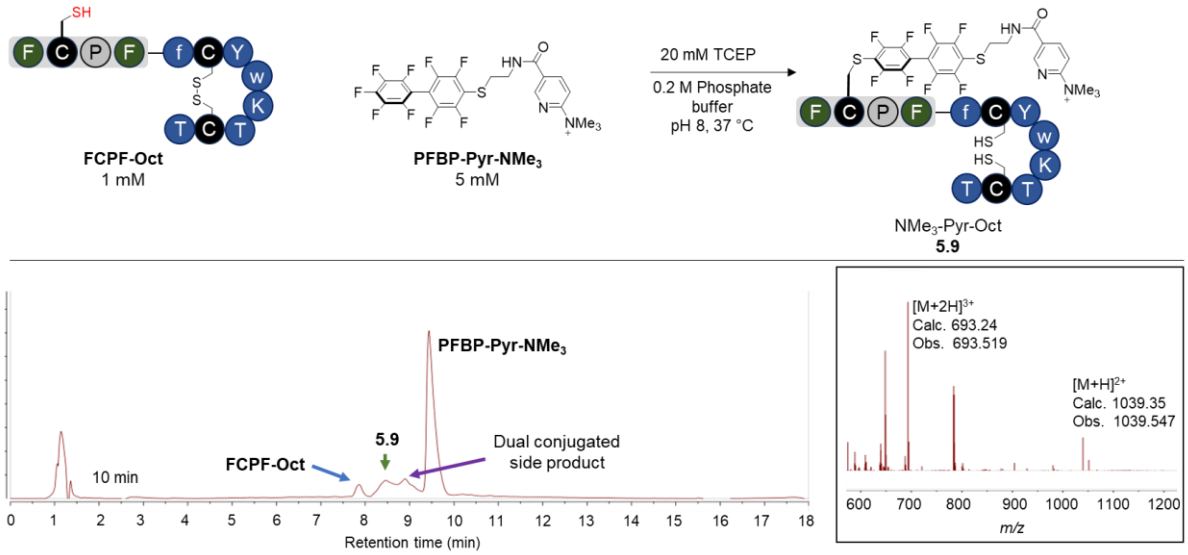

Figure 5.16: Reaction of **FCPF-Oct** with PFBP-Pyr-NMe_3, where UV traces from LC-MS analysis show the formation of the dual conjugated side product after 10 min. Insert shows mass spectrum of **5.9**.

5.2.3 [^{18}F]AlF-labelling of PFBP-NODA

Following the successful conjugation of PFBP-NODA to FCPF-Oct, [^{18}F]AlF-labelling of PFBP-NODA was conducted (**Figure 5.17A**), where >90% radiochemical conversion (RCC) was achieved after 15 min, consistent with the radiolabelling results obtained for [^{18}F]AlF-Tz (Chapter 2, section 2.3.2). After purification by solid-phase extraction (SPE) to remove unincorporated [^{18}F]fluoride, a decay-corrected RCY of 68 % was obtained in 30-35 min. The purified **[^{18}F]AlF-NODA-PFBP** had a radiochemical purity (RCP) of >90%, and was found to elute slightly later (t_R = 770 s, **Figure 5.17B**) than **PFBP-NODA** (t_R = 700 s).

After the isolation of [^{18}F]AlF-NODA-PFBP, its conjugation efficiency to FCPF-Oct was investigated. Using the same conditions for the conjugation of PFBP-NODA, a new peak was observed at t_R = 615 s in the radio-HPLC (**Figure 5.18**), corresponding to the formation of [^{18}F]AlF-NODA-Oct **5.10**. However, after 1 hour, only 21% RCC was achieved, which only increased slightly to 28% after 2 hours. Although the low conjugation efficiency was consistent with that observed in the previous section (Section 5.2.2), the combination of the poor RCC

and long reaction time required would result in a low isolated RCY of **5.10**. Ideally, an ^{18}F-labelled prosthetic group should result in high conversions and short reaction times of <30 min.[25,96] It was also found that during the purification of [^{18}F]AlF-NODA-PFBP prior to conjugation, washing the product with distilled water or phosphate buffered saline (PBS) to remove trace amounts of trifluoroacetic acid was essential for its conjugation to FCPF-Oct.

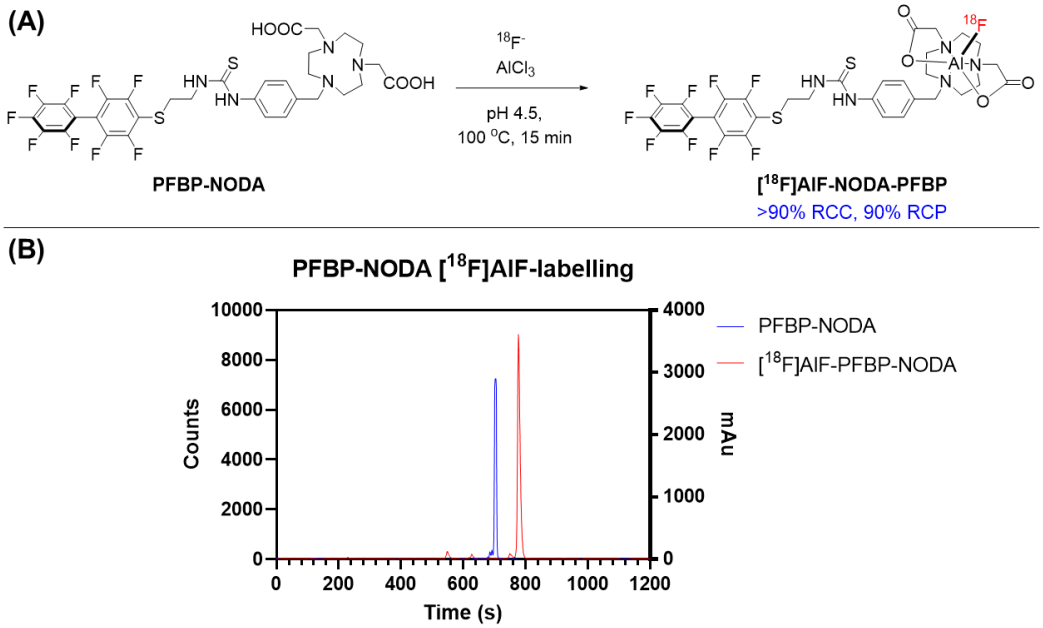

Figure 5.17: (A) [^{18}F]AlF-labelling of PFBP-NODA. (B) Stacked HPLC chromatogram of PFBP-NODA (t_R = 700 s) and the purified [^{18}F]AlF-NODA-PFBP (t_R = 770 s).

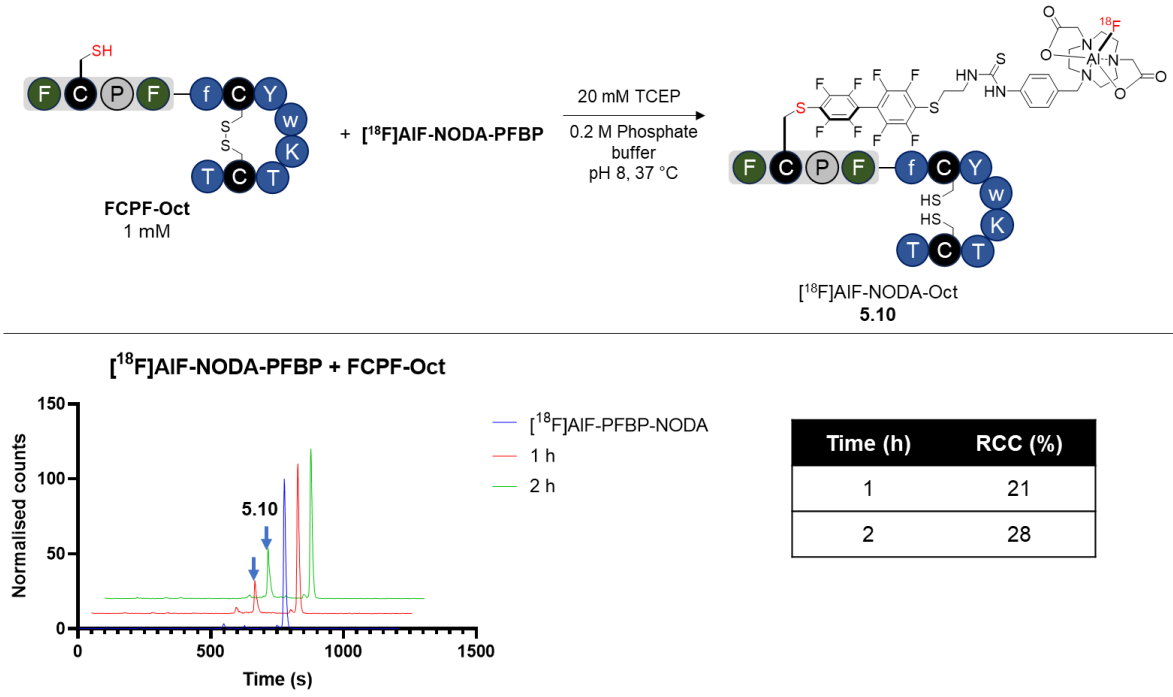

Time (h)	RCC (%)
1	21
2	28

Figure 5.18: Conjugation of [^{18}F]AlF-NODA-PFBP to FCPF octreotate, where a new peak corresponding to [^{18}F]AlF-NODA-Oct **5.10** is observed at t_R = 615 s, indicated by the blue arrows. Table shows radiochemical conversion (RCC) of [^{18}F]AlF-NODA-PFBP to **5.10**.

Since cysteine arylation reactions were reported to proceed more efficiently in organic solvents,[42,81] the use of an organic co-solvent was investigated to improve the reaction rate. The addition of an organic co-solvent also improved the solubility of FCPF-Oct, which was not fully soluble under aqueous conditions. Although the addition of DMF resulted in decreased conjugation efficiency (17% RCC after 1 h, **Figure 5.19**), it was found that using DMSO as a co-solvent improved conjugation efficiency to 34% after 1 h. Since this RCC was still relatively low, synthesis of a PFBP-NODA reagent with a polyethylene glycol (PEG) linker was attempted to improve its solubility and conjugation rate (Section 5.2.5).

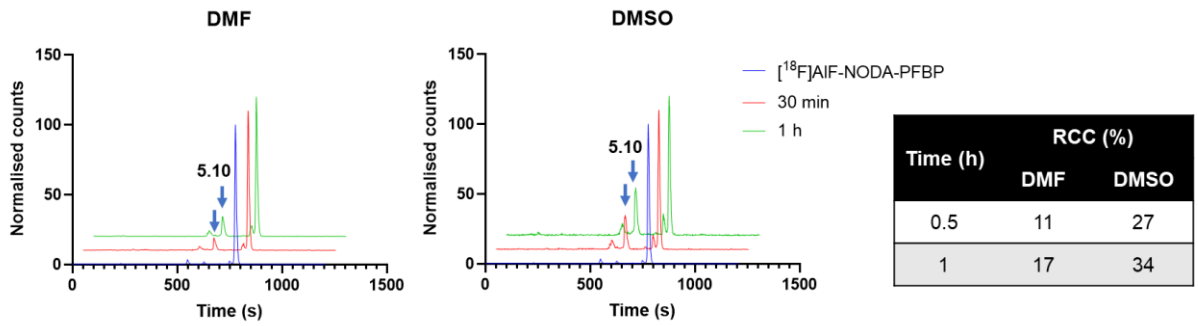

Time (h)	RCC (%)	
	DMF	DMSO
0.5	11	27
1	17	34

Figure 5.19: Addition of organic co-solvents (1:1 *v:v*) to improve conjugation efficiency, where blue arrows indicate the desired product **5.10**. The table summarises the conversions of [^{18}F]AlF-NODA-PFBP to [^{18}F]AlF-NODA-Oct **5.10**.

5.2.4 ^{18}F-labelling of PFBP-Pyr-NMe$_3$

As an alternative, ^{18}F-labelling of PFBP-Pyr-NMe$_3$ was also attempted (**Figure 5.20**). Radiolabelling was first investigated using the conditions reported by Olberg *et al*. for the [^{18}F]fluorination of a similar trimethylammonium-nicotinic acid tetrafluorophenyl ester,[96] which uses *tert*-butylammonium-[^{18}F]fluoride for the S_NAr reaction. However, conversion to the desired product was not observed by both radio-HPLC and radio-TLC, both only showing the unreacted precursor and [^{18}F]fluoride. To circumvent this, ^{18}F-labelling was investigated using the minimalist approach reported by Zlatopolskiy *et al*., which involves heating the trimethylammonium precursor with ^{18}F$^-$ in ethanol. To ensure a basic reaction medium, ^{18}F$^-$ was trapped and eluted using a quaternary ammonium (QMA) carbonate cartridge.[97] This produced **[^{18}F]F-Pyr-PFBP** in 34 % RCC when analysed by radio-TLC (**Figure 5.20B**), with a new non-radioactive species also observed in the UV-HPLC (**Figure 5.20C**, t_R = 935 s). Unreacted trimethyl ammonium precursor (PFBP-Pyr-NMe$_3$, t_R = 669 s) and ^{18}F$^-$ could be removed via SPE purification on a cationic exchange cartridge, and the purified **[^{18}F]F-Pyr-PFBP** being isolated with >95% RCP (**Figure 5.20D**).

However, due to the low radiochemical conversion, only 18 % RCY (decay corrected) was obtained after purification, where the radiosynthesis of **[18F]F-Pyr-PFBP** required 40-45 min. The radiochemical concentration of the isolated **[18F]F-Pyr-PFBP** was low (23 MBq/mL), which limited its use for subsequent conjugation with FCPF-Oct, which required a further 30-60 min was when using [18F]AlF-NODA-PFBP. Therefore, conjugation of **[18F]F-Pyr-PFBP** to FCPF-Oct was not attempted.

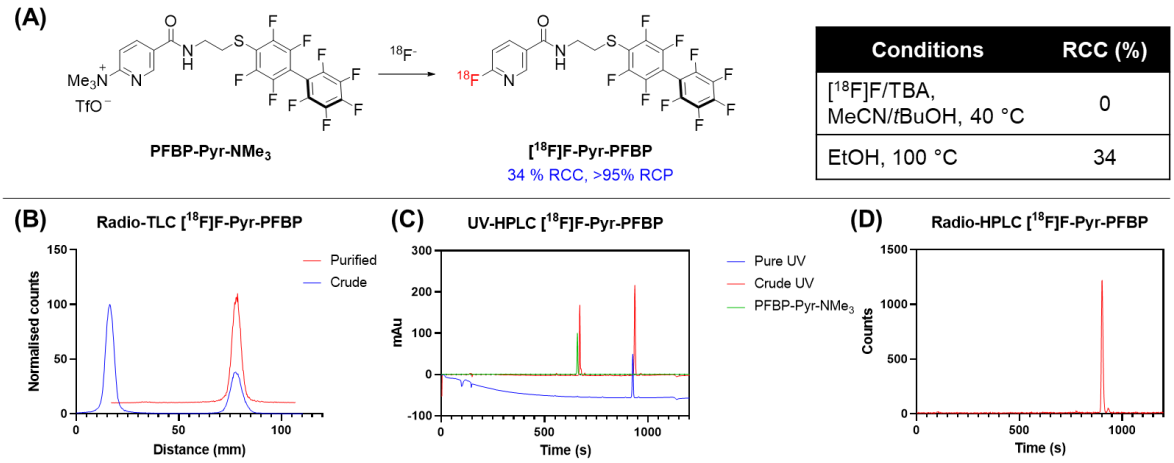

Conditions	RCC (%)
[18F]F/TBA, MeCN/*t*BuOH, 40 °C	0
EtOH, 100 °C	34

Figure 5.20: (A) ^{18}F-labelling of PFBP-Pyr-NMe$_3$ under two different conditions. (B) Radio-TLC chromatograms of crude and purified reaction, where product elutes at the solvent front. (C) UV-HPLC chromatograms of the crude and purified reaction. (D) Radio-HPLC chromatogram of purified [^{18}F]F-Pyr-PFBP, t_R = 900 s.

5.2.5 PEGylated PFBP reagents for improved hydrophilicity

Due to the poor water solubility of the observed octreotate-PFBP conjugates, syntheses of PFBP reagents with polyethylene glycol (PEG) linkers were carried out to improve their hydrophilicity.[98,99] A PEG$_4$ linker was used in this study, where both PFBP-PEG$_4$-Pyr-NMe$_3$ and PFBP-PEG$_4$-NODA were synthesised (**Figure 5.21**).

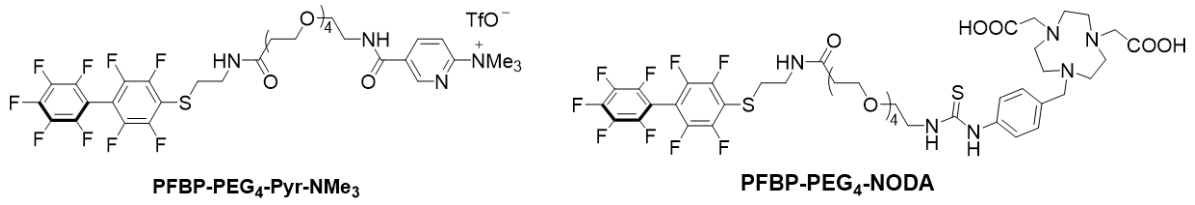

Figure 5.21: Structures of PFBP reagents with PEG linkers synthesised for improved hydrophilicity.

To evaluate the conjugation efficiency of the PEGylated compounds, PFBP-PEG$_4$-NODA was reacted with FCPF-Oct to form NODA-PEG$_4$-Oct **5.11** (**Figure 5.22**). However, similar to the

non-PEGylated version, the reaction was incomplete even after 4 h, where FCPF-Oct could still be observed when the reaction was analysed by LC-MS. In this case, the dual conjugated side product was formed as early as 30 min (*cf.* 2 h for PFBP-NODA), possibly indicating the increased reactivity of Cys-2 towards PFBP-PEG$_4$-NODA. This could potentially compromise the site-selectivity of the reaction when PFBP-PEG$_4$-NODA is used as a prosthetic group.

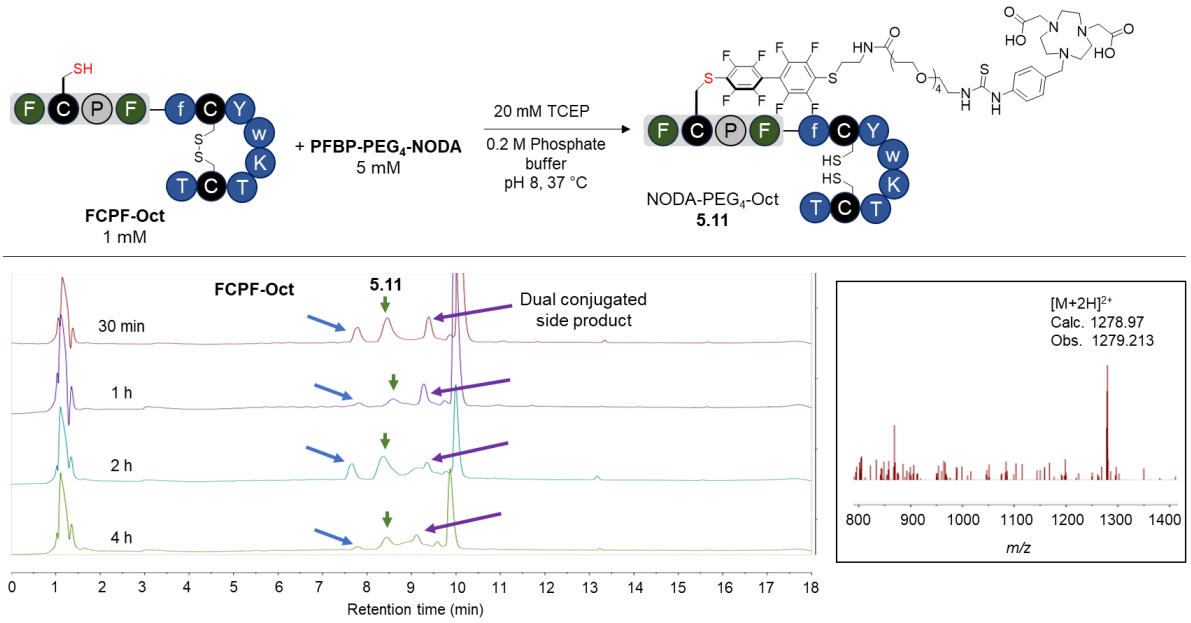

Figure 5.22: Reaction of **FCPF-Oct** with PFBP-PEG$_4$-NODA, where UV traces from LC-MS analysis show that the reaction was not complete after 4 h, and a dual conjugated side product was observed. Insert shows mass spectrum of **5.11**.

Nevertheless, upon conjugation of PFBP-PEG$_4$-NODA to FCPF-Oct, [^{18}F]AlF-labelling was attempted (**Figure 5.23**). Although an excellent RCC of >90 % could be achieved, a low RCP of 76 % was obtained for [^{18}F]AlF-NODA-PEG$_4$-PFBP **5.12,** t_R = 760 s. The stability of **5.12** was then evaluated in the conjugation media under reducing conditions, where it was found to be stable for up to 2 h (**Figure 5.23C**).

Upon confirmation that **5.12** was stable under the conjugation conditions, its reaction with FCPF-Oct was investigated (**Figure 5.24**), where DMSO was added as a co-solvent to improve solubility and reactivity. After 1 h, the formation of a new species with t_R = 600 s was observed (**Figure 5.24B**), comparable to that obtained using the non-PEGylated [^{18}F]AlF-NODA-PFBP (t_R = 615 s). This seemed to suggest that the addition of a PEG$_4$ chain did not significantly improve hydrophilicity. Nevertheless, oxidation of the product to reform the disulfide bond between Cys-2 and Cys-7 was conducted, where 2,2'-dipyridyl disulfide was added to the reaction after 1 h. Subsequent analysis of the crude reaction mixture at 1.5 h revealed an increase in RCC to 39 %, where the oxidised product seemed to have an identical

retention time. Following this, preparative HPLC was used to isolate **5.13**, where two peaks were observed at t_R = 592 s (37 %) and t_R = 615 s (63%) (**Figure 5.24D**). It is hypothesised that this could be due to the formation of stereoisomers, which has previously been observed for [^{18}F]AlF-labelled octreotate analogues.[100–102]

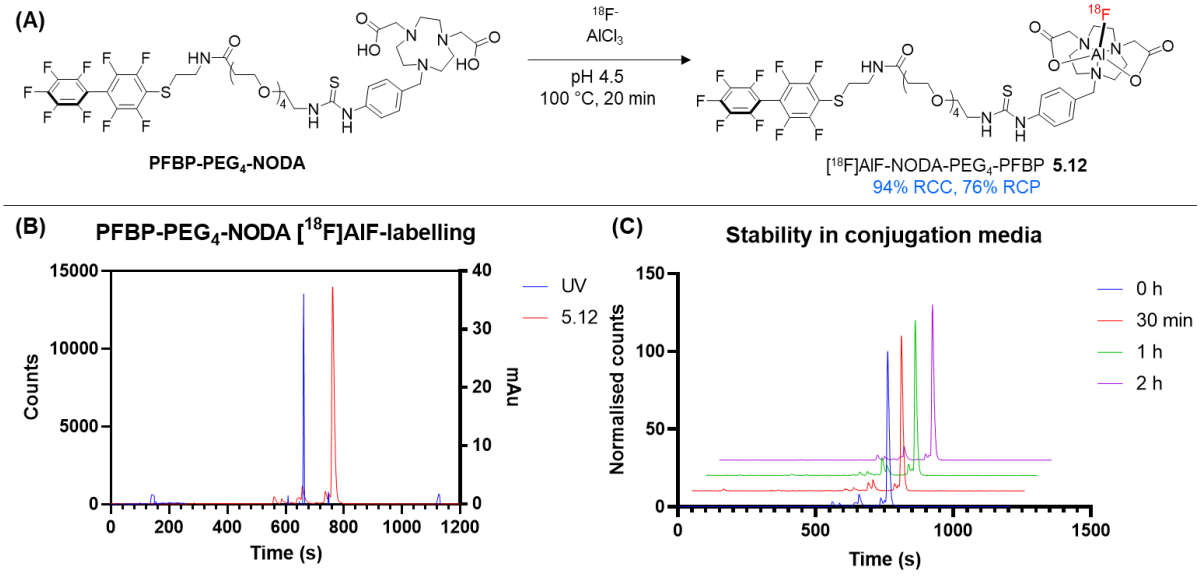

Figure 5.23: (A) [^{18}F]AlF-labelling of PFBP-PEG$_4$-NODA to form **5.12**. (B) Superimposed radio- and UV-HPLC chromatograms of purified **5.12**. (C) Stacked radio-HPLC chromatograms of **5.12** after incubation in 20 mM TCEP, 0.2 M phosphate buffer at pH 8.0.

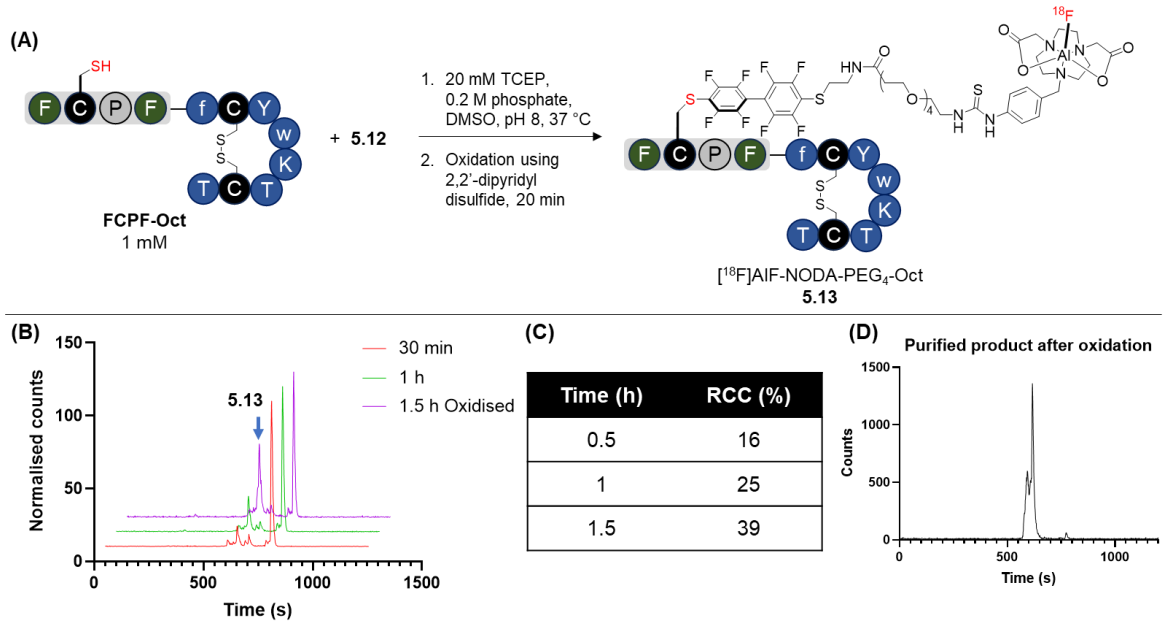

Figure 5.24: (A) Conjugation of **5.12** to FCPF-Oct. (B) Stacked radio-HPLC chromatograms the conjugation reaction. (C) Table summarising radiochemical conversion at different time points. (D) Radio-HPLC chromatogram of oxidised product after purification by prep-HPLC, showing two peaks at t_R = 592 s (37 %) and t_R = 615 s (63%).

In total, starting from PFBP-PEG$_4$-NODA, the radiosynthesis of **5.13** required 173 min, which could largely be attributed to the long conjugation duration (90 h) and purification by preparative HPLC (30-35 min). Using 420 MBq of [^{18}F]fluoride, only 5 MBq of **5.13** was obtained at the end of synthesis (3.6 % RCY, decay corrected), insufficient for further *in vitro* uptake experiments. Taken together, the poor conjugation kinetics seem to suggest that [^{18}F]AlF-PEG$_4$-PFBP would likely not perform well as a prosthetic group.

Since PFBP-Pyr-NMe$_3$ demonstrated fast conjugation to FCPF-Oct within 10 min (Section 5.2.2, **Figure 5.16**), radiolabelling of PFBP-Pyr-PEG$_4$-NMe$_3$ was attempted (**Figure 5.25A**). When the same conditions for ^{18}F-labelling of PFBP-Pyr-NMe$_3$ was used, no conversion was achieved. Gratifyingly, when DMSO was added as a co-solvent, a conversion of 52 % was observed (estimated by radio-HPLC). Upon isolation of [^{18}F]F-Pyr-PEG$_4$-PFBP **5.14**, a decay corrected RCY of 21 % was obtained, where the radiosynthesis was completed within 45 min. **5.14** had an earlier retention time (t_R = 840 s) compared to [^{18}F]F-Pyr-PFBP (t_R = 900 s), showing a slight increase in hydrophilicity with the incorporation of a PEG$_4$ linker. However, when the conjugation of **5.14** to FCPF-Oct was attempted, no reaction was observed after 1 h, and even when the temperature was raised to 42 °C (c.f. 37 °C previously). Due to time constraints, further investigation into the conjugation reaction was not carried out. Nevertheless, synthesis of a non-radioactive ^{19}F-Pyr-PEG$_4$-PFBP could potentially provide insight into the difference in reactivity observed when compared to the trimethylammonium precursor.

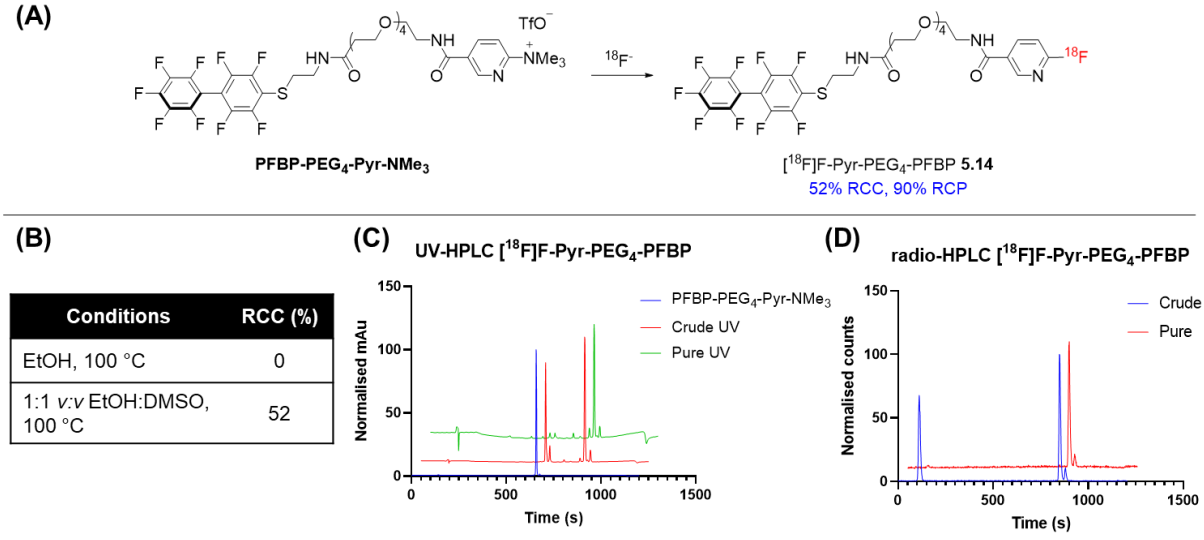

Figure 5.25: (A) ^{18}F-labelling of PFBP-PEG$_4$-Pyr-NMe$_3$ under two different conditions. (B) Table showing RCC obtained for the two conditions investigated (C) UV-HPLC chromatograms of the crude and purified reaction. (D) Radio-HPLC chromatogram of purified [^{18}F]F-Pyr-PEG$_4$-PFBP **5.14**, t_R = 840 s.

To evaluate the utility of the PFBP reagents as prosthetic groups, a comparison of their performance with commonly used ^{18}F-labelled prosthetic groups is provided in **Table 5.1** below, and is briefly discussed in the following page.

Table 5.1: Comparison of PFBP reagents with typical ^{18}F-labelled prosthetic groups. RCY: radiochemical yield; *k*: second order rate constant.

Prosthetic group functionality	**RCY of prosthetic group (%)**	**Conjugation parameters**				**Ref**
		k **(M^{-1} s^{-1})**	**RCY (%)**	**Time (min)**	**Conditions and comments**	
Halides or tosylates	50-80	-	15-89	5-15	Basic conditions with organic solvents, used widely for small molecule labelling	[25,103–105]
Activated esters, aldehydes	18-90	2-200	22-80	5-15	Basic aqueous conditions Mild temperatures	[8,9,25,96]
Maleimide	17-69	~100	43-58	10-30	Physiological reaction conditions	[8,9,33,44]
Alkyne-Azide CuAAC	64-99	10-100	54-99	10-20	Cu(I) catalyst, high temperatures might be required	[52]
SPAAC	21-42	0.01-1	19-98	20-30	Catalyst-free, aqueous or organic conditions possible	[52,62,106,107]
Tetrazine-TCO	12-95	100-1000	50-98	1-20	Catalyst-free, aqueous or organic conditions possible	[52]
Cyanobenzothiazole (CBT)	~20	9.19	3.5-10	20-30	60 °C, pH 7.5 Aqueous conditions	[46,70]
Perfluorobiphenyl (PFBP)	18-68	0.76	3.6	30-90	37 C, pH 8 1:1 *v:v* organic:aqueous	This work

In terms of ^{18}F-labelling of the prosthetic groups, the facile radiosynthesis of the PFBP reagents could make them an attractive choice, where they can be prepared in one step and purified by solid-phase extraction (SPE) methods. Without the need for preparative HPLC purification, the radiosynthesis can be completed within 30-45 minutes, comparable to that of the commonly used activated esters, aldehydes, alkynes and azides.[25,91] In comparison, ^{18}F-labelled maleimides and cyanobenzothiazoles (CBT) can require more extensive radiosynthesis, with preparation times exceeding 90 min.[45,46,48,70]

However, due to the relatively slow reaction of the ^{18}F-labelled PFBP compounds with FCPF-Oct as a model biomolecule, further optimisation of the conjugation step is required to demonstrate their applicability as prosthetic groups. Nevertheless, the similar second order rate constants (0.76 M^{-1} s^{-1}) observed for the *π*-clamp-mediated cysteine conjugation compared to SPAAC reactions (0.01-1 M^{-1} s^{-1}) show their potential to be used as prosthetic groups. In addition, the non-optimised RCY of [^{18}F]AlF-NODA-PEG$_4$-Oct **5.13** obtained in this study (3.6 % RCY) is similar to that obtained using **[^{18}F]F-CBT** (**Figure 5.5**) for the site-selective N-terminal functionalisation of biomolecules (3.5-10 % RCY).[46,70]

One potential modification for this study is to reduce the conjugation time to 30-45 min to potentially increase the isolated activity for further biological evaluations, at the expense of slightly lower conversions. Besides this, the use of higher starting activities on automated synthetic modules could also be investigated to enable sufficient amounts of **5.13** to be prepared. Jongho *et al*. and Xinhui *et al*. reported the use of 37 GBq of $^{18}F^-$ for the radiosynthesis of **[^{18}F]F-CBT**, more than 50-fold the amount used in the radiosynthesis of [^{18}F]AlF-NODA-PEG$_4$-PFBP (*ca*. 500 MBq).[46,70]

5.3 Direct labelling approach

Due to the relatively sluggish reaction kinetics observed when using ^{18}F-labelled PFBP reagents as prosthetic groups, a direct labelling approach was investigated using biomolecules functionalised with chelators prior to radiolabelling.

5.3.1 Site-selective conjugation of octreotate-FCPF

The synthesis of three analogues for three different radiolabelling approaches were attempted by the *π*-clamp-mediated cysteine conjugation (**Figure 5.26**): [^{18}F]AlF-labelling (**5.11**), ^{68}Ga-labelling (**5.15**) and ^{18}F-labelling (**5.16**). Although **5.11** and **5.15** were isolated and characterised by high resolution mass spectrometry, a sufficient quantity of **5.16** could not be obtained upon reoxidation for further analysis. Further confirmation of site-selective cysteine conjugation at the desired cysteine residue of **5.11** was obtained by liquid chromatography-tandem mass spectrometry (LC-MS/MS, data in Chapter 8, Appendix). The synthesis of **5.16**

was not attempted further due to the relatively large amounts of trimethyammonium precursors (*ca.* 10-20 µmol per reaction) required for ^{18}F-labelling,[96,97] which translates to 25-50 mg of peptide precursor.

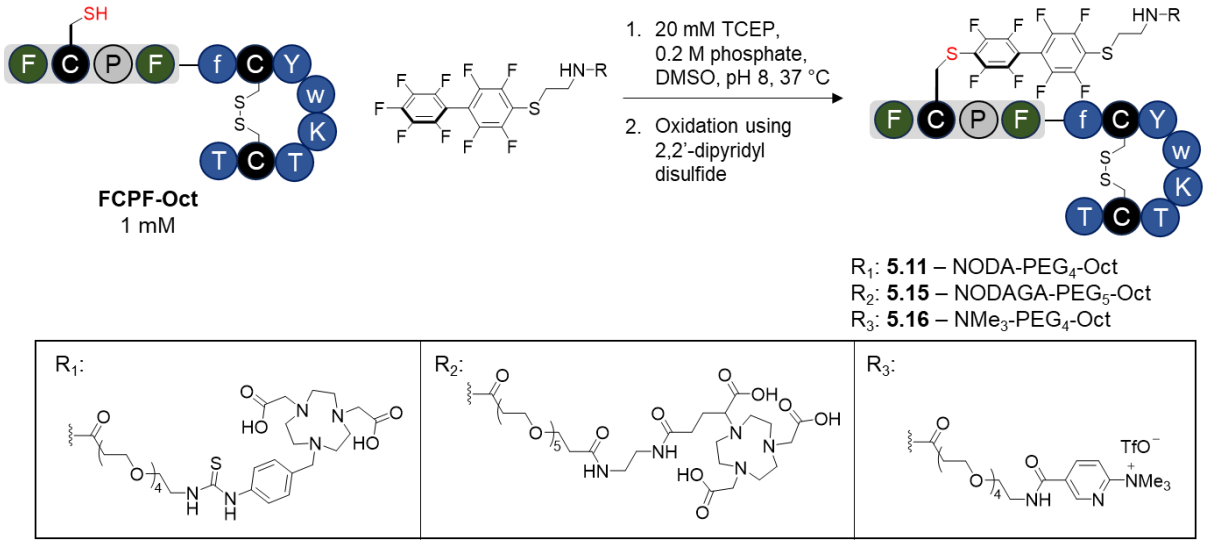

Figure 5.26: Site-selective conjugation of FCPF-Oct by PFBP reagents for three different radiolabelling approaches.

5.3.2 Radiolabelling by [^{18}F]AlF and ^{68}Ga

The labelling of **5.11** was conducted as shown in **Figure 5.27A**, where 74 % RCC was observed by radio-HPLC. Upon purification, [^{18}F]AlF-NODA-PEG$_4$-Oct **5.13** was isolated in 60 % RCY (decay-corrected) and 93 % RCP within 40-45 mins, with an apparent molar activity of 4.6 MBq/nmol. Interestingly, only one peak was obtained for the product at t_R = 615 s, in contrast to the two peaks obtained in **Figure 5.24D**. Since the retention time of **5.13** matched one of the peaks observed in **Figure 5.24D**, this suggests that peak at t_R = 592 s could potentially correspond to **5.13** in its reduced form (due to incomplete reoxidation). It is unlikely that the peak at t_R = 592 s corresponds to the formation of a dual-conjugated product, since this would be expected to have a longer retention time, as observed during the synthesis of **5.11** (**Figure 5.22**).

Upon isolation of **5.13**, its stability was evaluated in PBS, cell media and human serum (**Table 5.2**). Although **5.13** remained stable in cell media after 4 h, slow degradation was observed in PBS, where 85% remained after 4 h. In human serum, extensive degradation was observed as early as 1 h (**Figure 5.27D**), where only 49 % of **5.13** remained. This further decreased to 41 % at 2 h, where further time points were not sampled due to the low amount of **5.13** remaining. The instability of **5.13** in human serum was unexpected, since [^{18}F]AlF-NODA complexes have been reported to be highly stable in serum and *in vivo*,[108,109] and it corresponding ^{68}Ga-labelled analogue **5.17** was stable under the same conditions (vide infra,

Figure 5.28). Due to time constraints, further investigation on the stability of the compound and potential degradation products was not conducted. However, one potential experiment to identify whether the instability arises from the perfluorobiphenyl (PFBP) moiety is to examine the stability of [^{18}F]AlF-NODA-PEG$_4$-PFBP **5.12** in human serum. In addition, the stability of the *π*-clamp tetrapeptide FCPF after modification with **5.12** could also provide insight on the observed instability of **5.13**.

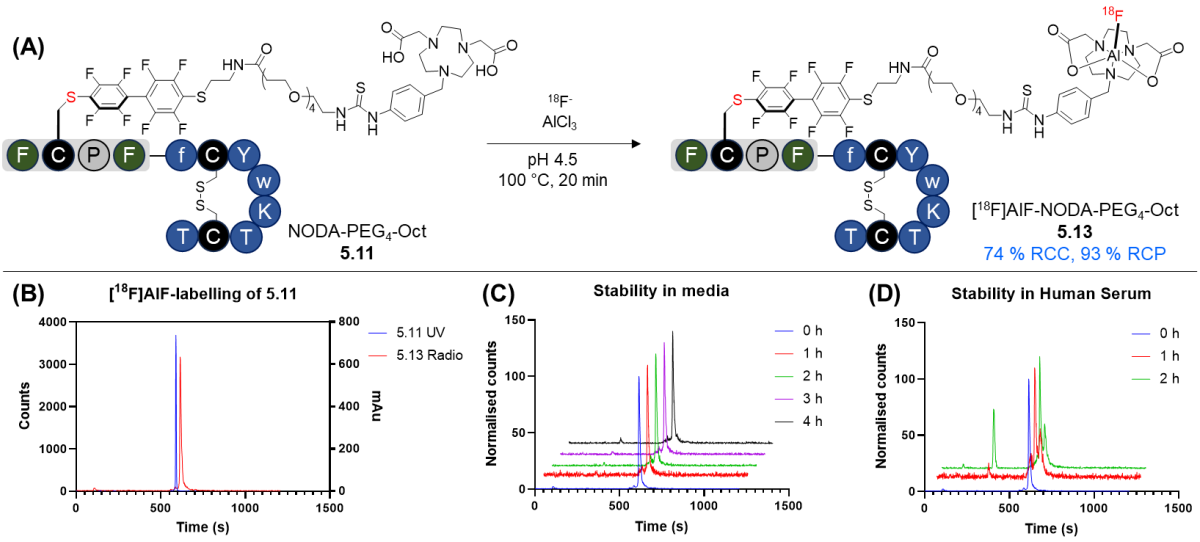

Figure 5.27: (A) Radiolabelling of **5.11** by the [^{18}F]AlF method. (B) Stacked HPLC chromatograms of **5.11** and **5.13** (t_R = 615 s). (C) Stacked radio-HPLC chromatograms of **5.13** in RPMI media. (D) Stacked radio-HPLC chromatograms of **5.13** in human serum.

Table 5.2: Stability of **5.13** in PBS, cell media and human serum.

Time (h)	Percentage of 5.13 remaining (%)		
	PBS	RPMI (cell media)	Human serum
1	99	99	49
2	-	99	41
3	91	99	-
4	85	98	-

In addition, ^{68}Ga-labelling was also conducted using NODAGA-PEG$_5$-Oct **5.15** (**Figure 5.28**), where complexation efficiency increased with increasing concentrations of the precursor (**Figure 5.28B**). Upon purification by SPE using a C18 cartridge, the [^{68}Ga]Ga-NODAGA-PEG$_5$-Oct **5.17** can be obtained with 68 % RCY (decay corrected) and >95% radiochemical purity. In contrast to the [^{18}F]AlF-labelled product, **5.17** showed excellent stability in human serum for up to 5 h (**Figure 5.28D**).

The octanol-water partition coefficients of radiotracers **5.13** and **5.17** was then determined to compare their hydrophilicity to existing [^{18}F]AlF- and ^{68}Ga-labelled octreotide analogues. It was found that both **5.13** and **5.17** had higher log $D_{7.4}$ values and were significantly more hydrophobic than existing octreotide analogues (**Table 5.3**), which was expected given their modification with the hydrophobic FCPF tag and PFBP functional group. In addition, the fact that [^{18}F]AlF-NODA-PEG$_4$-Oct **5.13** was more hydrophobic than its ^{68}Ga analogue also concurs with the observations obtained by Laverman *et al.*[110] However, the effect of the increased hydrophobicity of **5.13** and **5.17** on their *in vivo* pharmacokinetics and biodistribution is yet to be investigated, which will be the subject of future studies.

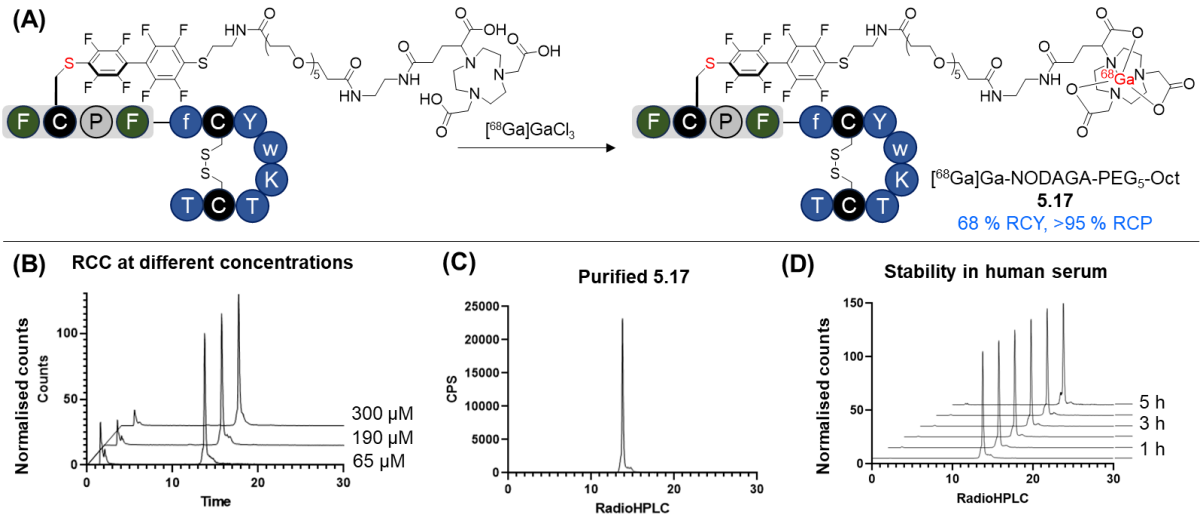

Figure 5.28: (A) Radiolabelling of **5.15** by ^{68}Ga. (B) Stacked HPLC chromatograms of ^{68}Ga-labelling at three different concentrations (C) Radio-HPLC chromatogram of purified **5.17**. (D) Stacked radio-HPLC chromatograms of **5.17** in human serum.

Table 5.3: Comparison of octanol-water partition coefficients (log $D_{7.4}$) of the radiotracers produced in this study to published octreotide derivatives with NOTA chelators.

Radiotracer	**log $D_{7.4}$**	**Ref.**
[^{18}F]AlF-NODA-PEG$_4$-Oct **5.13**	0.40 ± 0.10	-
[^{68}Ga]Ga-NODAGA-PEG$_5$-Oct **5.17**	-0.47 ± 0.08	-
[^{18}F]AlF-NOTA-NOC	-1.20	111
[^{18}F]AlF-IMP466	-2.44 ± 0.12	110
[^{68}Ga]Ga-NOTA-NOC	-1.29	111
[^{68}Ga]Ga-IMP466	-3.79 ± 0.07	110

5.4 Conclusions

A series of bifunctional perfluorobiphenyl (PFBP) reagents was synthesised, and their potential for site-selective conjugation to biomolecules was investigated using FCPF-Oct as a model. It was found that although conversion to the desired products could be observed within 30 min, the reactions remained incomplete after 4 h. Dual-conjugated side products were also observed, potentially at the Cys-2 residue of octreotate, which is also flanked by aromatic residues that could act as *π*-clamps.

When the PFBP reagents were investigated as prosthetic groups, a low RCY and radioactive concentration was obtained for [^{18}F]F-Pyr-PFBP, precluding its use in further conjugation reactions. In contrast, [^{18}F]AlF-NODA-PFBP could be isolated with 68 % RCY in 30-35 min. However, slow conjugation with FCPF-Oct was observed (21 % RCC after 1 h), which can be increased by the addition of DMSO as a co-solvent (34 % RCC after 1 h).

To improve the hydrophilicity and solubility of the resulting PFBP-functionalised octreotate, PEG_4 linkers were incorporated into the PFBP reagents. Although minimal change in hydrophilicity of the [^{18}F]AlF-labelled product was observed, [^{18}F]F-Pyr-PEG_4-PFBP had a shorter elution time when compared to [^{18}F]F-Pyr-PFBP. However, log $D_{7.4}$ values should be determined to obtain an accurate insight on the changes in hydrophilicity.

The PEGylated PFBP reagents demonstrated similar conjugation efficiencies to their non-PEGylated analogues. When used as a prosthetic group, [^{18}F]AlF-NODA-PEG_4-PFBP reacted with FCPF-Oct with 39 % RCC after 1.5 h. A decay-corrected RCY of 3.6 % was obtained, comparable to N-terminal functionalisation using 2-cyanobenzothiazole derivatives, demonstrating the potential of PFBP reagents to be used as prosthetic groups for the site-selective conjugation of biomolecules, though further optimisations are required.

Apart from this, direct [^{18}F]AlF- and ^{68}Ga-labelling of FCPF-Oct functionalised with NODA and NODAGA chelators was also conducted to provide a more simplified radiosynthesis route. Excellent radiochemical conversions could be achieved (up to 90 %), resulting isolated RCYs of 60-68 %. Although [^{68}Ga]Ga-NODAGA-PEG_5-Oct **5.17** was stable up to 5 h, its [^{18}F]AlF-labelled analogue **5.13** undergoes degradation in human serum, which requires further investigations. It was also found that both **5.13** and **5.17** were significantly more hydrophobic when compared to currently reported octreotate radiotracers, likely due to the incorporation of the FCPF-tag and PFBP functional group.

To conclude, these results show the potential of PFBP reagents to be used for site-selective radiolabelling of biomolecules, both as ^{18}F-labelled prosthetic groups, or as bifunctional chelators for the functionalisation of biomolecules prior to radiolabelling.

5.5 Future work

Prosthetic group approach: Optimisation of the conjugation time and conditions are likely vital for the development of the ^{18}F-labelled PFBP prosthetic groups. Reaction parameters such as reaction time, pH, co-solvent, and temperature could be tested to improve the low RCCs observed in this study. Although the use of harsher reaction conditions, such as increased temperature, could potentially result in decreased site-selectivity, the impact of this could likely be reduced since the dual-conjugated side products can be removed during purification by preparative HPLC.

Direct labelling approach: Further investigation on the stability of the [^{18}F]AlF-labelled FCPF-oct is required since it showed poor stability in human serum. This includes investigating the stability of [^{18}F]AlF-NODA-PEG$_4$-PFBP and potentially the radiolabelled tetrapeptide [^{18}F]AlF-NODA-PEG$_4$-PFBP (**Figure 5.29**). Nevertheless, since [^{18}F]AlF-NODA-PEG$_4$-Oct was stable in cell media, evaluation of its *in vitro* uptake with SSTR2-expressing cells can also be carried out.

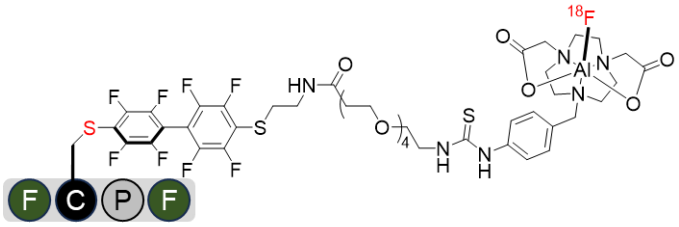

[^{18}F]AlF-NODA-PEG$_4$-FCPF

Figure 5.29: Structure of [^{18}F]AlF-NODA-PEG$_4$-FCPF that could be used for stability studies

5.6 References

1 D. Petroni, L. Menichetti and M. Poli, *J. Radioanal. Nucl. Chem.*, 2020, **323**, 1017–1031.

2 J. Pacák, Z. Toík and M. Erný, *J. Chem. Soc. D Chem. Commun.*, 1969, 77–77.

3 J. E. Shively, *J. Nucl. Med.*, 2007, **48**, 170–172.

4 G. Sanz, J. E. Robles, M. Giménez, J. Arocena, D. Sánchez, F. Rodriguez-Rubio, D. Rosell, J. A. Richter and J. M. Berián, *BJU Int.*, 1999, **84**, 1028–1031.

5 I. Kayani, B. G. Conry, A. M. Groves, T. Win, J. Dickson, M. Caplin and J. B. Bomanji, *J. Nucl. Med.*, 2009, **50**, 1927–1932.

6 K. H. Hwang, D. J. Choi, S. Y. Lee, M. K. Lee and W. Choe, *Appl. Radiat. Isot.*, 2009, **67**, 1195–1198.

7 C. Nanni, L. Fantini, S. Nicolini and S. Fanti, *Clin. Radiol.*, 2010, **65**, 536–548.

8 O. Morris, M. Fairclough, J. Grigg, C. Prenant and A. McMahon, *J. Label. Compd. Radiopharm.*, 2019, **62**, 4–23.

9 S. Richter and F. Wuest, *Molecules*, 2014, **19**, 20536.

10 H. S. Krishnan, L. Ma, N. Vasdev and S. H. Liang, *Chem. Eur. J.*, 2017, **23**, 15553-15577.

11 K. Kumar and A. Ghosh, *Bioconjug. Chem.*, 2018, 29, 953–975.

12 H. J. Wester, M. Schottelius, K. Scheidhauer, G. Meisetschläger, M. Herz, F. C. Rau, J. C. Reubi and M. Schwaiger, *Eur. J. Nucl. Med. Mol. Imaging*, 2003, **30**, 117–122.

13 G. Meisetschläger, T. Poethko, A. Stahl, I. Wolf, K. Scheidhauer, M. Schottelius, M. Herz, H. J. Wester and M. Schwaiger, *J. Nucl. Med.,* 2006, **47**, 566-573.

14 J. Jose Díaz-Mochó, L. Bialy and M. Bradley, *Curr. Opin. Biotechnol*, 1998, **37**, 6878.

15 R. Fu, L. Carroll, G. Yahioglu, E. O. Aboagye and P. W. Miller, *ChemMedChem*, 2018, **13**, 2466–2478.

16 A. M. Sochaj, K. W. Świderska and J. Otlewski, *Biotechnol. Adv.*, 2015, **33**, 775–784.

17 G. T. Hermanson, *Bioconjugate Techniques: Third Edition*, Elsevier Inc., 2013.

18 O. Boutureira and G. J. L. Bernardes, *Chem. Rev.*, 2015, **115**, 2174–2195.

19 G. P. Smith, *Bioconjug. Chem.*, 2006, **17**, 501–506.

20 S. Zijlstra, J. Gunawan and W. Burchert, *Appl. Radiat. Isot.*, 2003, **58**, 201–207.

21 S. M. Apana, R. J. Griffin, N. A. Koonce, J. S. Webber, R. P. M. Dings, K. H. Mayo and M. S. Berridge, *J. Label. Compd. Radiopharm.*, 2011, **54**, 708–713.

22 C. Wangler, R. Schirrmacher, P. Bartenstein and B. Wangler, *Curr. Med. Chem.*, 2010, **17**, 1092–1116.

23 P. Rosa-Neto, B. Wängler, L. Iovkova, G. Boening, A. Reader, K. Jurkschat and E. Schirrmacher, *ChemBioChem*, 2009, **10**, 1321–1324.

24 E. Hedberg and B. Långström, *Acta Chem. Scand.*, 1997, **51**, 1236–1240.

25 R. Schirrmacher, B. Wängler, J. Bailey, V. Bernard-Gauthier, E. Schirrmacher and C. Wängler, *Semin. Nucl. Med.*, 2017, **47**, 474–492.

26 P. T. Huynh, N. Soni, R. Pal, S. Sarkar, J. M. Jung, W. Lee and J. Yoo, *New J. Chem.*,

2019, **43**, 15389–15395.

27 F. Cleeren, J. Lecina, J. Bridoux, N. Devoogdt, T. Tshibangu, C. Xavier and G. Bormans, *Nat. Protoc.*, 2018, **13**, 2330–2347.

28 L. Mu, A. Höhne, P. A. Schubiger, S. M. Ametamey, K. Graham, J. E. Cyr, L. Dinkelborg, T. Stellfeld, A. Srinivasan, U. Voigtmann, U. Klar, L. Mu,] A Höhne, P. A. Schubiger, S. M. Ametamey, K. Graham, J. E. Cyr, L. Dinkelborg, T. Stellfeld, A. Srinivasan, U. Voigtmann, U. Klar and B. Schering, *Angew. Chemie Int. Ed.*, 2008, **47**, 4922–4925.

29 D. Connolly, J. J. Bailey, H. Ilhan, P. Bartenstein, C. Wängler, B. Wängler, M. Wuest, F. Wuest and R. Schirrmacher, *J. Vis. Exp.*, 2020, e60623, DOI:10.3791/60623.

30 R. Schirrmacher, V. Bernard-Gauthier, E. Schirrmacher, J. J. Bailey, K. Jurkschat, C. Wängler and B. Wängler, *Fluor. Life Sci. Pharm. Med. Diagnostics, Agrochem. Prog. Fluor. Sci. Ser.*, 2019, 551–574.

31 N. Echols, P. Harrison, S. Balasubramanian, N. M. Luscombe, P. Bertone, Z. Zhang and M. Gerstein, *Nucleic Acids Res.*, 2002, **30**, 2515–2523.

32 S. J. Walsh, J. D. Bargh, F. M. Dannheim, A. R. Hanby, H. Seki, A. J. Counsell, X. Ou, E. Fowler, N. Ashman, Y. Takada, A. Isidro-Llobet, J. S. Parker, J. S. Carroll and D. R. Spring, *Chem. Soc. Rev.*, 2021, **50**, 1305–1353.

33 F. J. Chen and J. Gao, *Chem. Eur. J.*, 2022, **28**, e202201843.

34 L. B. Poole, *Free Radic. Biol. Med.*, 2015, **80**, 148–157.

35 P. Akkapeddi, S. A. Azizi, A. M. Freedy, P. M. S. D. Cal, P. M. P. Gois and G. J. L. Bernardes, *Chem. Sci.*, 2016, **7**, 2954–2963.

36 G. Gorin, P. A. Martic and G. Doughty, *Arch. Biochem. Biophys.*, 1966, **115**, 593–597.

37 C. F. Brewer and J. P. Riehm, *Anal. Biochem.*, 1967, **18**, 248–255.

38 I. André, S. Linse and F. A. A. Mulder, *J. Am. Chem. Soc.*, 2007, **129**, 15805–15813.

39 J. M. J. M. Ravasco, H. Faustino, A. Trindade and P. M. P. Gois, *Chem. Eur. J.*, 2019, **25**, 43–59.

40 A. D. Baldwin and K. L. Kiick, *Bioconjug. Chem.*, 2011, **22**, 1946–1953.

41 P. M. S. D. Cal, G. J. L. Bernardes and P. M. P. Gois, *Angew. Chemie Int. Ed.*, 2014, **53**, 10585–10587.

42 C. Zhang, E. V. Vinogradova, A. M. Spokoyny, S. L. Buchwald and B. L. Pentelute,

Angew. Chemie Int. Ed., 2019, **58**, 4810–4839.

43 A. Chiotellis, F. Sladojevich, L. Mu, A. Müller Herde, I. E. Valverde, V. Tolmachev, R. Schibli, S. M. Ametamey and T. L. Mindt, *Chem. Commun.*, 2016, **52**, 6083–6086.

44 F. Wuest, M. Berndt, R. Bergmann, J. Den Van Hoff and J. Pietzsch, *Bioconjug. Chem.*, 2008, **19**, 1202–1210.

45 X. Yue, D. O. Kiesewetter, J. Guo, Z. Sun, X. Zhang, L. Zhu, G. Niu, Y. Ma, L. Lang and X. Chen, *Bioconjug. Chem.*, 2013, **24**, 1191–1200.

46 X. Su, K. Cheng, J. Jeon, B. Shen, G. T. Venturin, X. Hu, J. Rao, F. T. Chin, H. Wu and Z. Cheng, *Mol. Pharm.*, 2014, **11**, 3947–3956.

47 T. Kniess, M. Kuchar and J. Pietzsch, *Appl. Radiat. Isot.*, 2011, **69**, 1226–1230.

48 D. O. Kiesewetter, O. Jacobson, L. Lang and X. Chen, *Appl. Radiat. Isot.*, 2011, **69**, 410–414.

49 K. Chansaenpak, M. Wang, Z. Wu, R. Zaman, Z. Li and F. P. Gabbaï, *Chem. Commun.*, 2015, **51**, 12439–12442.

50 L. Iovkova, B. Wängler, E. Schirrmacher, R. Schirrmacher, G. Quandt, G. Boening, M. Schürmann and K. Jurkschat, *Chem. Eur. J.*, 2009, **15**, 2140–2147.

51 S. Lütje, G. M. Franssen, R. M. Sharkey, P. Laverman, E. A. Rossi, D. M. Goldenberg, W. J. G. Oyen, O. C. Boerman and W. J. McBride, *Bioconjug. Chem.*, 2014, **25**, 335–341.

52 B. L. Oliveira, Z. Guo and G. J. L. Bernardes, *Chem. Soc. Rev.*, 2017, 46, 4895–4950.

53 A. Sadiki, S. R. Vaidya, M. Abdollahi, G. Bhardwaj, M. E. Dolan, H. Turna, V. Arora, A. Sanjeev, T. D. Robinson, A. Koid, A. Amin and Z. S. Zhou, *Antib. Ther.*, 2020, **3**, 271–284.

54 M. W. Popp, J. M. Antos, G. M. Grotenbreg, E. Spooner and H. L. Ploegh, *Nat. Chem. Biol. 2007 311*, 2007, **3**, 707–708.

55 C. W. Lin and A. Y. Ting, *J. Am. Chem. Soc.*, 2006, **128**, 4542–4543.

56 X. Zhong, J. Yan, X. Ding, C. Su, Y. Xu and M. Yang, *Bioconjug. Chem.*, 2023, **34**, 457-476.

57 Z. Gao, V. Gouverneur and B. G. Davis, *J. Am. Chem. Soc.*, 2013, **135**, 13612–13615.

58 H. S. Gill, J. N. Tinianow, A. Ogasawara, J. E. Flores, A. N. Vanderbilt, H. Raab, J. M.

Scheer, R. Vandlen, S. P. Williams and J. Marik, *J. Med. Chem.*, 2009, **52**, 5816–5825.

59 J. Marik and J. L. Sutcliffe, *Tetrahedron Lett.*, 2006, **47**, 6681–6684.

60 M. Glaser and E. Årstad, *Bioconjug. Chem.*, 2007, **18**, 989–993.

61 S. H. Hausner, J. Marik, M. K. J. Gagnon and J. L. Sutcliffe, *J. Med. Chem.*, 2008, **51**, 5901–5904.

62 K. Kettenbach and T. L. Ross, *Medchemcomm*, 2016, **7**, 654–657.

63 J. M. Chalker, C. S. C. Wood and B. G. Davis, *J. Am. Chem. Soc.*, 2009, **131**, 16346–16347.

64 C. B. Rosen and M. B. Francis, *Nat. Chem. Biol. 2017 137*, 2017, **13**, 697–705.

65 Z. Miao, G. Ren, H. Liu, R. H. Kimura, L. Jiang, J. R. Cochran, S. S. Gambhir and Z. Cheng, *Bioconjug. Chem.*, 2009, **20**, 2342–2347.

66 S. Richter, V. Bouvet, M. Wuest, R. Bergmann, J. Steinbach, J. Pietzsch, I. Neundorf and F. Wuest, *Nucl. Med. Biol.*, 2012, **39**, 1202–1212.

67 P. E. Dawson, T. W. Muir, I. Clark-Lewis and S. B. H. Kent, *Science*, 1994, **266**, 776–779.

68 I. S. Carrico, *Chem. Soc. Rev.*, 2008, **37**, 1423–1431.

69 H. Ren, F. Xiao, K. Zhan, Y. P. Kim, H. Xie, Z. Xia and J. Rao, *Angew. Chem. Int. Ed.*, 2009, **48**, 9658–9662.

70 J. Jeon, B. Shen, L. Xiong, Z. Miao, K. H. Lee, J. Rao and F. T. Chin, *Bioconjug. Chem.*, 2012, **23**, 1902–1908.

71 S. Lin, X. Yang, S. Jia, A. M. Weeks, M. Hornsby, P. S. Lee, R. V Nichiporuk, A. T. Iavarone, J. A. Wells, F. D. Toste and C. J. Chang, *Science*, 2017, **355**, 597–602.

72 M. H. Stipanuk, *Annu. Rev. Nutr.*, 2004, **24**, 539–577.

73 D. Lin, M. Wallace, A. J. Allentoff, D. J. Donnelly, E. Gomes, K. Voronin, S. Gong, R. Y. C. Huang, H. Kim, J. Caceres-Cortes and S. Bonacorsi, *Bioconjug. Chem.*, 2020, **31**, 1908–1916.

74 M. Morais and M. T. Ma, *Drug Discov. Today. Technol.*, 2018, **30**, 91.

75 M. Farleigh, T. T. Pham, Z. Yu, J. Kim, K. Sunassee, G. Firth, N. Forte, V. Chudasama, J. R. Baker, N. J. Long, C. Rivas and M. T. Ma, *Bioconjug. Chem.*, 2021, **32**, 1214–

1222.

76 A. N. Marquard, R. Weissleder and R. Weissleder, *Bioconjug. Chem.*, 2020, **31**, 1616.

77 J.-P. Meyer, J. L. Houghton, P. Kozlowski, D. Abdel-Atti, T. Reiner, N. V. K. Pillarsetty, W. W. Scholz, B. M. Zeglis and J. S. Lewis, *Bioconjug. Chem.*, 2016, **27**, 298–301.

78 E. M. F. Billaud, S. Belderbos, F. Cleeren, W. Maes, M. Van De Wouwer, M. Koole, A. Verbruggen, U. Himmelreich, N. Geukens and G. Bormans, *Bioconjug. Chem.*, 2017, **28**, 2915–2920.

79 C. A. Maitz, S. Delaney, B. E. Cook, A. R. Genady, R. Hoerres, M. Kuchuk, G. Makris, J. F. Valliant, S. Sadeghi, J. S. Lewis, H. M. Hennkens, J. N. Bryan and B. M. Zeglis, *Mol. Pharm.*, 2022, **19**, 3153–3162.

80 D. M. Goldenberg, C. H. Chang, E. A. Rossi, W. J. McBride and R. M. Sharkey, *Theranostics*, 2012, **2**, 523–540.

81 A. M. Spokoyny, Y. Zou, J. J. Ling, H. Yu, Y. S. Lin and B. L. Pentelute, *J. Am. Chem. Soc.*, 2013, **135**, 5946–5949.

82 C. Zhang, P. Dai, A. M. Spokoyny and B. L. Pentelute, *Org. Lett.*, 2014, **16**, 3652–3655.

83 C. Zhang, A. M. Spokoyny, Y. Zou, M. D. Simon and B. L. Pentelute, *Angew. Chemie*, 2013, **125**, 14251–14255.

84 C. Zhang, M. Welborn, T. Zhu, N. J. Yang, M. S. Santos, T. Van Voorhis and B. L. Pentelute, *Nat. Chem. 2015 82*, 2015, **8**, 120–128.

85 P. Dai, J. K. Williams, C. Zhang, M. Welborn, J. J. Shepherd, T. Zhu, T. Van Voorhis, M. Hong and B. L. Pentelute, *Sci. Reports 2017 71*, 2017, **7**, 1–11.

86 P. K. K. Leung, L. C. C. Lee, T. K. Y. Ip, H. W. Liu, S. M. Yiu, N. P. Lee and K. K. W. Lo, *Chem. Commun.*, 2021, **57**, 11256–11259.

87 L. C. C. Lee, A. W. Y. Tsang, H. W. Liu and K. K. W. Lo, *Inorg. Chem.*, 2020, **59**, 14796–14806.

88 M. D. Lee, W. Y. Tong, T. Nebl, L. A. Pearce, T. M. Pham, A. Golbaz-Hagh, S. Puttick, S. Rose, T. E. Adams and C. C. Williams, *Bioconjug. Chem.*, 2019, **30**, 2539–2543.

89 J. A. Baccile, P. J. Voorhees, A. J. Chillo, M. Berry, R. Morgenstern, T. J. Schwertfeger, F. M. Rossi and C. D. S. Nelson, *ChemBioChem*, 2021, **22**, 3037–3041.

90 P. Mäding, F. Füchtner and F. Wüst, *Appl. Radiat. Isot.*, 2005, **63**, 329–332.

91 G. Tang, X. Tang and X. Wang, *J. Label. Compd. Radiopharm.*, 2010, **53**, 543–547.

92 H. K. Kim, M. R. Javed, S. Chen, K. A. Zettlitz, J. Collins, A. M. Wu, C. J. Kim, R. Michael Van Dam and P. Y. Keng, *RSC Adv.*, 2019, **9**, 32175–32183.

93 S. W. J. Lamberts, L. J. Hofland Octreotide, S. W. J. Lamberts and L. J. Hofland, *Eur. J. Endocrinol.*, 2019, **181**, R173–R183.

94 Z. Liu, L. Yu, K. Cheng, Y. Feng, P. Qiu, Y. Gai and M. Zhou, *React. Chem. Eng.*, 2020, **5**, 1441–1449.

95 E. Pauwels, F. Cleeren, T. Tshibangu, M. Koole, K. Serdons, L. Boeckxstaens, J. Dekervel, T. Vandamme, W. Lybaert, B. Van den Broeck, A. Laenen, P. M. Clement, K. Geboes, E. Van Cutsem, S. Stroobants, C. Verslype, G. Bormans and C. M. Deroose, *J. Nucl. Med.*, 2023, **64**, 632–638.

96 D. E. Olberg, J. M. Arukwe, D. Grace, O. K. Hjelstuen, M. Solbakken, G. M. Kindberg and A. Cuthbertson, *J. Med. Chem.*, 2010, **53**, 1732–1740.

97 B. D. Zlatopolskiy, J. Zischler, P. Krapf, R. Richarz, K. Lauchner and B. Neumaier, *J. Label. Compd. Radiopharm.*, 2019, **62**, 404–410.

98 G. Lin, X. Zhang, S. R. Kumar and J. E. Mark, *Silicon*, 2009, **1**, 173–181.

99 T. Tedeschini, B. Campara, A. Grigoletto, M. Bellini, M. Salvalaio, Y. Matsuno, A. Suzuki, H. Yoshioka and G. Pasut, *J. Control. Release*, 2021, **337**, 431–447.

100 T. Tshibangu, C. Cawthorne, K. Serdons, E. Pauwels, W. Gsell, G. Bormans, C. M. Deroose and F. Cleeren, *EJNMMI Radiopharm. Chem. 2020 51*, 2020, **5**, 1–23.

101 S. Ahenkorah, C. Cawthorne, E. Murce, C. M. Deroose, T. Cardinaels, Y. Seimbille, G. Bormans, M. Ooms and F. Cleeren, *Nucl. Med. Biol.*, 2023, 108338.

102 P. Laverman, C. A. D'Souza, A. Eek, W. J. McBride, R. M. Sharkey, W. J. G. Oyen, D. M. Goldenberg and O. C. Boerman, *Tumor Biol.*, 2012, **33**, 427–434.

103 B. W. Schoultz, B. J. Reed, J. Marton, F. Willoch and G. Henriksen, *Molecules,* 2013, **18**, 7271–7278.

104 D. Y. Chi, M. R. Kilbourn, J. A. Katzenellenbogen and M. J. Welch, *J. Org. Chem.*, 1987, **52**, 658–664.

105 T. Kniess, M. Laube, P. Brust and J. Steinbach, *Medchemcomm*, 2015, **6**, 1714–1754.

106 S. Arumugam, J. Chin, R. Schirrmacher, V. V. Popik and A. P. Kostikov, *Bioorg. Med.*

Chem. Lett., 2011, **21**, 6987–6991.

107 L. S. Campbell-Verduyn, L. Mirfeizi, A. K. Schoonen, R. A. Dierckx, P. H. Elsinga and B. L. Feringa, *Angew. Chem. Int. Ed.*, 2011, **50**, 11117–11120.

108 S. J. Archibald and L. Allott, *EJNMMI Radiopharm. Chem.*, 2021, **6**, 1–28.

109 S. Schmitt and E. Moreau, *Coord. Chem. Rev.*, 2023, **480**, 215028-215062.

110 P. Laverman, W. J. McBride, R. M. Sharkey, A. Eek, L. Joosten, W. J. G. Oyen, D. M. Goldenberg and O. C. Boerman, *J. Nucl. Med.*, 2010, **51**, 454–461.

111 J. H. Dam, N. Langkjær, C. Baun, B. B. Olsen, A. Y. Nielsen and H. Thisgaard, *Molecules*, 2022, **27**, 6818.

Chapter 6: Conclusions and future work

6.1 Conclusions

In this thesis, the development and application of the [^{18}F]AlF method for radiolabelling a range of biomolecules were explored, demonstrating the robustness and versatility of this method. It is hoped that the work completed in this thesis will improve the scope of the [^{18}F]AlF method, facilitating its use in radiolabelling more diverse systems, which could potentially contribute to the development of new radiotracers for molecular imaging.

This began with the design and synthesis of an [^{18}F]AlF-labelled tetrazine prosthetic group, [^{18}F]AlF-Tz. Upon optimisation, the operationally simple radiosynthesis afforded [^{18}F]AlF-Tz in high radiochemical yields (>90 %) and purity (>95 %) within a short duration of 30-35 min. In comparison, currently available methods to produce ^{18}F-labelled tetrazines by C-F bond formation through S_N2, S_NAr and copper-mediated radiofluorinations result in relatively lower RCYs (up to 24 %) and require more involved radiosyntheses taking up to 90 min.[1–4]

Upon isolation of [^{18}F]AlF-Tz, its utility in radiolabelling nano- and micron-sized particles were demonstrated by successful production of [^{18}F]AlF-labelled nanobubbles and microbubbles. This was achieved by the efficient inverse-electron-demand Diels-Alder (IEDDA) reaction between tetrazines and *trans*-cyclooctene, enabling production of the radiolabelled particles with up to 30 % RCY. To further demonstrate the applicability of the [^{18}F]AlF method in enabling operationally simple radiolabelling procedures, a kit-based approach to producing [^{18}F]AlF-labelled microbubbles was also developed, potentially improving the accessibility of radiolabelled microbubbles.

The potential of the [^{18}F]AlF-labelled microbubbles ([^{18}F]AlF-MBs) to be used in molecular imaging was then investigated by the incorporation of a T140 peptide for targeting CXCR4 in cancer. Although the targeted microbubbles demonstrated poor specificity, where binding to CXCR4-negative cells was observed, the increased binding compared to non-targeted microbubbles and blocking controls revealed that improved targeting was achieved, thus suggesting that optimisation of the targeting functionality is required. While this work did not result in the successful development of a new targeted microbubble formulation, it instead revealed the utility of radiolabelled microbubbles in providing insight on the targeting capabilities of newly developed formulations.

Apart from molecular imaging, the [^{18}F]AlF-MBs were further applied to study the effects of sonoporation during ultrasound-mediated microbubble destruction (UMMD). Consistent with other reported microbubble formulations, high radioactive uptakes were observed in the liver, spleen, bladder and lungs, corresponding to microbubble elimination pathways. Importantly, when UMMD was carried out, an increased radioactive uptake was observed in tumours

compared to control experiments without UMMD. Although the overall tumour uptake was low, this study demonstrates the utility of the [^{18}F]AlF-MBs in studying drug delivery by UMMD, pointing towards the further optimisation of sonication parameters and microbubble formulation for improved delivery of radioactivity.

Besides demonstrating the utility of the [^{18}F]AlF method in radiolabelling microbubbles and studying drug delivery, improvement of the currently available [^{18}F]AlF-labelling methodologies was also of interest in this work. This first encompassed the development of new chelators, where bisphosphonates and salen ligands were explored. Although preliminary studies showed the potential of alendronic acid to complex [^{18}F]AlF^{2+}, limited success was achieved using this class of ligands due to the lack of synthetic routes identified. In comparison, the wide range of literature available on salen ligands in aluminium complexation offered more flexibility for tuning the chelator structure. Leveraging on this, the synthesis of salen, salan, and salalen ligands was explored for [^{18}F]AlF-complexation. It was found that salen ligands without a cyclohexyl backbone were prone to imine hydrolysis, but the imine bond could be stabilised upon complexation to aluminium. Thus, the synthesis of pre-formed Al-salen complexes was attempted to investigate their ability to form AlF complexes when exposed to a fluoride source under aqueous conditions. However, evidence of Al-F bond formation was not obtained, where analysis by mass spectrometry revealed the coordination of solvent molecules, instead of fluoride ions, to the aluminium centre. This suggests that further optimisation of the ligand structure was necessary to enable [^{18}F]AlF-labelling using salen ligands.

Finally, the development of new methods to achieve site-selective [^{18}F]AlF-labelling of biomolecules was explored using the *π*-clamp-mediated cysteine conjugation. Two approaches were investigated, (i) a prosthetic group approach and (ii) a direct [^{18}F]AlF-labelling approach, each with their own advantages and disadvantages. Whilst the prosthetic group approach (i) enables site-selective [^{18}F]AlF-labelling of biomolecules under milder conditions, this required more extensive radiosynthesis (2-3 steps, preparative HPLC purification, 175 min) and resulted in lower yields (3.6 % RCY). Nevertheless, these parameters were comparable to a reported site-selective ^{18}F-labelling approach for N-terminal cysteine functionalisation,[5] demonstrating that further optimisation of the conjugation step could enable the application of perfluorobiphenyl reagents as prosthetic groups in ^{18}F-labelling. In comparison, direct [^{18}F]AlF-labelling resulted higher radiochemical yields (60 %) and facile labelling procedures (one-step, 40-45 min). However, this approach would be less feasible for radiolabelling heat- or acid-sensitive biomolecules due to the harsh [^{18}F]AlF-labelling steps (typically pH 4-5, 90-110 °C).

In summary, the work presented in this thesis demonstrates the versatility and utility of the [^{18}F]AlF method for enabling the facile radiolabelling of different biomolecules and particles, which can lead to improved accessibility of ^{18}F-labelled tracers for studying various biological phenomena such as sonoporation, receptor binding and disease progression. Whilst the [^{18}F]AlF method is by no means the ideal strategy for the ^{18}F-labelling of molecules, the work presented herein would represent an advancement in the currently available knowledge for radiolabelling using the fluorine-18 isotope. Since its inception in 2009, the [^{18}F]AlF method has transformed the landscape of ^{18}F-labelling, where it combines the convenience of radiometal-based chemistry with the favourable decay characteristics of ^{18}F. Therefore, it represents an important addition to the radiolabelling toolkit, and the continued development of methods for [^{18}F]AlF-labelling would certainly be beneficial towards the development of new radiopharmaceuticals.

6.2 Future work

Each of the projects discussed had avenues for further development, which are discussed in this section. Due to the diverse range of work presented in this thesis, where each chapter focused on the development and application of the [^{18}F]AlF method for different purposes, future work relating to this thesis will be separated into discrete sections based on each chapter.

6.2.1 Future Work Related to Chapter 2

The primary goal of this chapter was to develop facile methods for radiolabelling microbubbles and their subsequent use for molecular imaging. Although a kit-based method was developed to radiolabel microbubbles, the targeted microbubbles produced did not show sufficient specificity and sensitivity when investigated *in vitro*. Therefore, one potential improvement is to change the targeting vector that was incorporated into the microbubbles. Instead of T140, Pentixafor could be used, since radiolabelled Pentixafor analogues showed higher affinities to CXCR4-expressing cells when compared to T140.[6–8] Therefore, synthesis of a Pentixafor-functionalised lipid (**Figure 6.1**) for incorporation into microbubbles could perhaps enable more efficient targeting of CXCR4. This can be achieved by the conjugation of the amine functionality of the ornithine residue on the Pentixafor scaffold to DSPE-PEG$_{2000}$-iso.[9] Since this residue is used for the attachment of chelators in Pentixafor analogues, its functionalisation likely has minimal impact on CXCR4-binding.

If CXCR4-targeting proves to be unfeasible using the [^{18}F]AlF-MBs, validation of the ability to incorporate targeting functionalities could also be assessed using known vascular biomarkers

such as vascular endothelial growth factor receptors (VEGFR), vascular cell adhesion molecule-1 (VCAM-1), or $\alpha_v\beta_3$ integrins.[10–15]

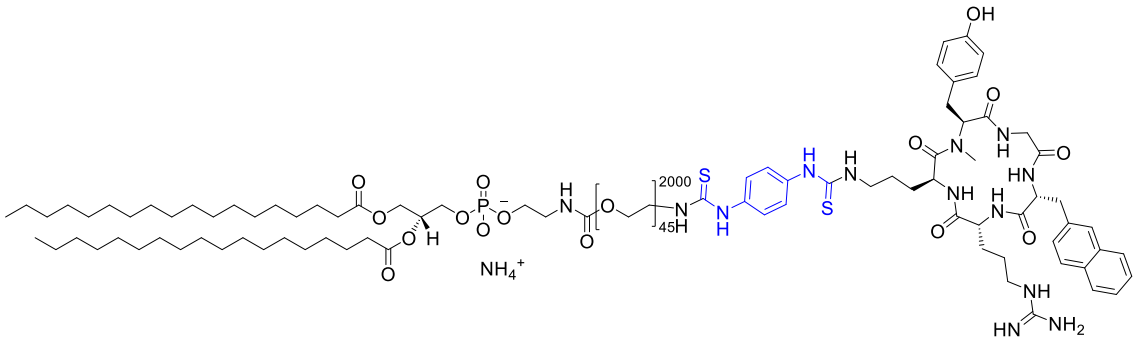

Figure 6.1: Structure of lipid functionalised with Pentixafor scaffold.

Apart from targeting, further optimisation and validation of the generation of [^{18}F]AlF-labelled nanobubbles ([^{18}F]AlF-NBs) could also be carried out. The present procedure generated [^{18}F]AlF-NBs in low RCYs of approximately 5 %, presumably due to the concurrent formation of microbubbles. Several variations, such as decreasing the amount of ethanol, varying the amount of lipids, or varying the composition of lipids could potentially improve the RCYs obtained by favouring nanobubble formation. The recent development of nanobubbles represent an exciting prospect, since these have significantly longer circulation half-lives than microbubbles, and have the ability to extravasate through leaky tumour vasculatures.[16–19] Therefore, the development of radiolabelled nanobubbles can allow improved understanding of their whole-body pharmacokinetics and distribution, potentially facilitating the development of new formulations.

6.2.2 Future Work Related to Chapter 3

Upon synthesis of the [^{18}F]AlF-MBs, chapter 3 investigated their use for studying the increase in radioactive accumulation in tumours after ultrasound-mediated microbubble destruction (UMMD). Whilst a significant increase in radioactive accumulation was observed, the overall deposition of radioactivity was low. Therefore, the logical next step would be to investigate the ability to increase the delivery of radioactivity to tumours. It is envisioned that this can be potentially achieved using three approaches:

(i) Changing the ultrasound destruction methodology, where a 3-dimensional sonication probe, such as that used by Chung *et al.*,[20] is used to maximise the effects of UMMD.

(ii) Modifying the [^{18}F]AlF-MBs with targeting functionalities to increase their accumulation at the tumour.

(iii) Changing the method of administration of radioactivity to enable better extravasation, which can be achieved by the co-administration of microbubbles and radiolabelled liposomes (**Figure 6.1**), explained further below.

For point (iii), radiolabelled lipids currently incorporated into the [^{18}F]AlF-MBs, which have relatively large sizes (1.98 ± 1.55 µm diameter) and short circulation times (3-20 min). In comparison, pore sizes generated by UMMD typically have diameters of 110 nm to 2 µm, and reseal within 12 min,[21–23] which likely meant that only the radiolabelled lipids from microbubbles that had undergone destruction could extravasate into the tumour. Therefore, the amount of radioactivity delivered to tumours can potentially be increased by co-administering radiolabelled liposomes with microbubbles, which have smaller sizes (50-500 nm) and longer circulation times (up to a few hours), potentially offering increased extravasation upon UMMD.[24] Alternatively, radiolabelled nanobubbles could also be tested.

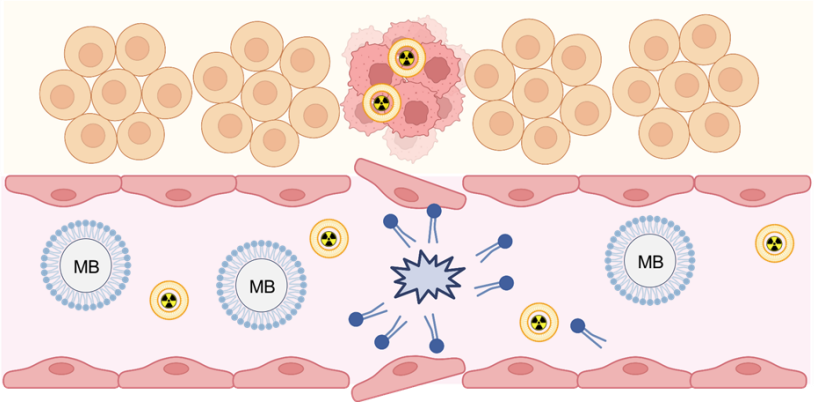

Figure 6.2: Graphical illustration of microbubbles co-injected with liposomes.

Approach (i) represents the method that can be achieved under the shortest time frame, since new formulations of radiotracers need not be developed. In addition, approach (i) should be prioritised since it can be carried forward for approaches (ii) and (iii). Lastly, should a sufficient radioactive dose be delivered to the tumour, incorporation of a therapeutic radionuclide such as ^{177}Lu could be investigated for targeted radiotherapy.

6.2.3 Future Work Related to Chapter 4

Apart from utilising the [^{18}F]AlF method to radiolabel biomolecules, this thesis also explored the possibility of expanding on the currently available methods for [^{18}F]AlF-labelling. Chapter 4 was focussed on the identification of new chelators to enable [^{18}F]AlF-labelling under milder conditions. Further work will be described for the salen chelators since these showed a greater potential for modification and improvement.

Given that the salalen-AlCl complexes were not fully purified, investigation of the purification of these complexes by recrystallisation in different solvent combinations can be attempted. The use of diethylaluminium chloride for the formation of aluminium complexes for ligands prone to hydrolysis would also offer access to salen-Al complexes that are potentially stable for ^{18}F-labellning.

Nevertheless, since the primary goal for this project was to identify ligands that could enable the formation of stable [^{18}F]AlF complexes, the synthesis of pentadentate ligands should likely be prioritized. A potential synthetic scheme was outlined in Chapter 4 and is reproduced below.

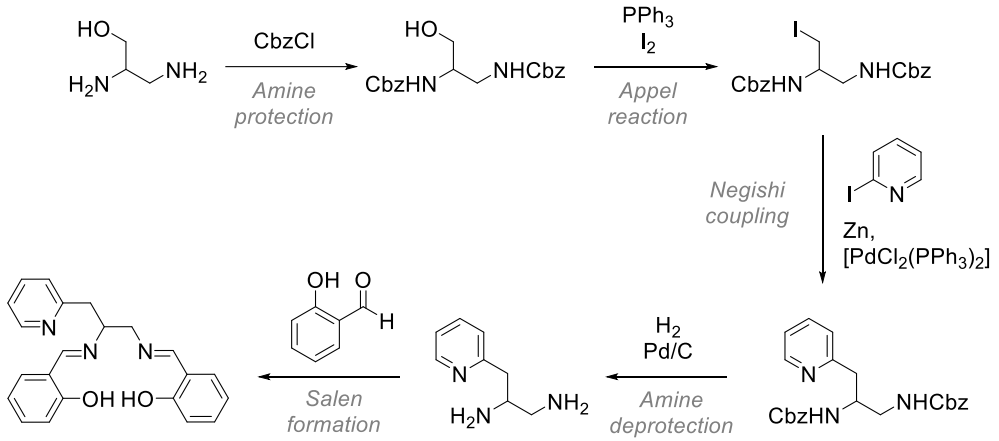

Scheme 6.1: Proposed synthetic route for pentadentate salen derivatives, adapted from that used by Shitama *et al.*[25]

6.2.4 Future Work Related to Chapter 5

Following on with the theme of expanding the currently available methodologies for [^{18}F]AlF-labelling, chapter 5 looks at the use of the *π*-clamp-mediated cysteine conjugation for achieving site-selective [^{18}F]AlF-labelling. In terms of the prosthetic group approach, the immediate follow up would be the optimisation of the radiosynthesis procedure to allow a higher amount of radioactivity to be isolated for biological evaluations. This could be in terms of decreasing the conjugation time to enable a shorter radiosynthesis duration, or increasing the peptide concentration to enable higher conversions to be achieved. Following this, determination of the molar activity of the isolated product should also be conducted to demonstrate the utility of this approach in synthesising radiotracers that are applicable for evaluating biological processes.

In terms of the direct [^{18}F]AlF-labelling approach using chelator-functionalised biomolecules, the immediate concern is the investigation of the stability of [^{18}F]AlF-NODA-PEG$_4$-Oct in human serum. Following this, *in vitro* uptake of the radiolabelled octreotate analogues will be evaluated to demonstrate that the binding ability of radiotracers produced using this approach remains unaffected.

Finally, in the long term, extension of this methodology to functionalise and radiolabel larger biomolecules, such as affibodies or nanobodies, could be investigated to further demonstrate the applicability of the *π*-clamp-mediated cysteine conjugation for achieving site-selective radiolabelling.

6.3 References

1 C. Denk, D. Svatunek, T. Filip, T. Wanek, D. Lumpi, J. Fröhlich, C. Kuntner and H. Mikula, *Angew. Chem. Int. Ed.*, 2014, **53**, 9655–9659.

2 U. M. Battisti, K. Bratteby, J. T. Jørgensen, L. Hvass, V. Shalgunov, H. Mikula, A. Kjær and M. M. Herth, *J. Med. Chem.*, 2021, **64**, 15297–15312.

3 R. García-Vázquez, U. M. Battisti, J. T. Jørgensen, V. Shalgunov, L. Hvass, D. L. Stares, I. N. Petersen, F. Crestey, A. Löffler, D. Svatunek, J. L. Kristensen, H. Mikula, A. Kjaer and M. M. Herth, *Chem. Sci.*, 2021, **12**, 11668–11675.

4 R. García-Vázquez, J. T. Jørgensen, K. E. Bratteby, V. Shalgunov, L. Hvass, M. M. Herth, A. Kjær and U. M. Battisti, *Pharmaceuticals*, 2022, **15**, 245.

5 X. Su, K. Cheng, J. Jeon, B. Shen, G. T. Venturin, X. Hu, J. Rao, F. T. Chin, H. Wu and Z. Cheng, *Mol. Pharm.*, 2014, **11**, 3947–3956.

6 J. Kuil, T. Buckle and F. W. B. van Leeuwen, *Chem. Soc. Rev.*, 2012, **41**, 5239–5261.

7 A. Poschenrieder, M. Schottelius, M. Schwaiger, H. Kessler and H. J. Wester, *EJNMMI Res.*, 2016, **6**, 1–8.

8 G. P. C. George, E. Stevens, O. Åberg, Q. D. Nguyen, F. Pisaneschi, A. C. Spivey and E. O. Aboagye, *Bioorg. Med. Chem.*, 2014, **22**, 796–803.

9 O. Demmer, I. Dijkgraaf, M. Schottelius, H. J. Wester and H. Kessler, *Org. Lett.*, 2008, **10**, 2015–2018.

10 D. B. Ellegala, H. Leong-Poi, J. E. Carpenter, A. L. Klibanov, S. Kaul, M. E. Shaffrey, J. Sklenar and J. R. Lindner, *Circulation*, 2003, **108**, 336–341.

11 H. Leong-Poi, J. Christiansen, A. L. Klibanov, S. Kaul and J. R. Lindner, *Circulation*, 2003, **107**, 455–460.

12 A. L. Klibanov, *J. Nucl. Cardiol.*, 2007, **14**, 876-884.

13 A. S. Wadajkar, S. Santimano, M. Rahimi, B. Yuan, S. Banerjee and K. T. Nguyen, *Biotechnol. Adv.*, 2013, 31, 504–513.

14 A. L. Klibanov, *J. Cardiovasc. Transl. Res.*, 2013, **6**, 729–739.

15 F. Moccetti, C. C. Weinkauf, B. P. Davidson, J. T. Belcik, E. R. Marinelli, E. Unger and J. R. Lindner, *Ultrasound Med. Biol.*, 2018, **44**, 1155–1163.

16 H. Wu, N. G. Rognin, T. M. Krupka, L. Solorio, H. Yoshiara, G. Guenette, C. Sanders,

N. Kamiyama and A. A. Exner, *Ultrasound Med. Biol.*, 2013, **39**, 2137–2146.

17 C. Counil, E. Abenojar, R. Perera, A. A. Exner, C. Counil, E. Abenojar, R. Perera and A. A. Exner, *Small*, 2022, **18**, 2200810.

18 R. H. Perera, C. Hernandez, H. Zhou, P. Kota, A. Burke and A. A. Exner, *Wiley Interdiscip. Rev. Nanomedicine Nanobiotechnology*, 2015, **7**, 593–608.

19 R. H. Perera, E. Abenojar, P. Nittayacharn, X. Wang, G. Ramamurthy, P. Peiris, I. Bederman, J. P. Basilion and A. A. Exner, *Nanotheranostics*, 2022, **6**, 270–285.

20 Y. H. Chung, P. H. Hsu, C. W. Huang, W. C. Hsieh, F. T. Huang, W. C. Chang, H. Chiu, S. T. Hsu and T. C. Yen, *Mol. Pharm.*, 2014, **11**, 3904–3914.

21 B. Helfield, X. Chen, S. C. Watkins and F. S. Villanueva, *Proc. Natl. Acad. Sci. U. S. A.*, 2016, **113**, 9983–9988.

22 Y. Zhou, R. E. Kumon, C. X. Deng and J. Cui, *Proc. - IEEE Ultrason. Symp.*, 2008, 558–561.

23 Y. Z. Zhao, Y. K. Luo, C. T. Lu, J. F. Xu, J. Tang, M. Zhang, Y. Zhang and H. D. Liang, *J. Drug Target.*, 2008, **16**, 18–25.

24 L. Sercombe, T. Veerati, F. Moheimani, S. Y. Wu, A. K. Sood and S. Hua, *Front. Pharmacol.*, 2015, **6**, 163819.

25 H. Shitama and T. Katsuki, *Chem. Eur. J.*, 2007, **13**, 4849–4858.

Chapter 7: Experimental

7.1 General considerations

Reagents: Anhydrous solvents were obtained under a nitrogen atmosphere from a PureSolv multiple dispensing solvent drying system and degassed for >30 minutes before use. Anhydrous DMF and DMSO were purchased from Sigma Aldrich. Flash column chromatography was performed using Geduran® Si 60 Silicagel (Merck). All phospholipids were purchased from Avanti Polar Lipids. All other reagents and solvents were used as purchased unless otherwise specified.

Instruments and characterisation: ^{1}H, $^{13}C\{^{1}H\}$, ^{19}F and ^{31}P NMR spectra were recorded using Bruker Avance 400 spectrometers, and chemical shifts (δ) are reported in ppm relative to residual undeuterated solvent signals ($CDCl_3$ δH = 7.26 ppm, δC = 77.16 ppm; DMSO-d_6 δH = 2.50 ppm, δC = 39.52 ppm; D_2O δH = 4.79 ppm; CD_3OD δH = 3.31 ppm, δC = 49.00 ppm, CD_3CN δH = 1.94 ppm, δC = 1.32, 118.26 ppm). Multiplicities are designated by the following abbreviations: s = single, d = doublet, t = triplet, q = quartet, m = multiplet, quint = quintet, br = broad. Coupling constants (J) are reported in hertz (Hz). NMR spectra were analysed using MESTRELAB MestReNova software.

High resolution mass spectrometry (HRMS) analyses were carried out by Dr Lisa Haigh and Malgorzata Puchnarewicz from the Imperial College Department of Chemistry Mass Spectrometry service. MALDI mass spectra were obtained using a MALDI micro MX-TOF mass spectrometer from Waters. Samples were spotted 1:1 *v:v* with a matrix solution (matrix indicated in text) and measured in linear mode. Liquid chromatography-mass spectrometry (LC-MS) analyses were conducted on a Waters LC-MS system: Waters 2767 autosampler for samples injection and collection; Waters 515 HPLC pump to deliver the mobile phase to the source; Waters 3100 mass spectrometer with ESI; and Waters 2998 Photodiode Array (detection at 200-600 nm), equipped with XBridge C_{18} reverse-phase columns with dimensions 4.6 mm × 100 mm. Liquid chromatography-tandem mass spectrometry (LC-MS/MS) was performed by Thomas Tin Chi Yue on an Agilent 6545XT AdvanceBio LC/Q-TOF system. Crystallographic analysis was performed by Dr Andrew White from the Imperial College Department of Chemistry crystallography service.

Analytical HPLC chromatograms were obtained using an Agilent 1200 series instrument equipped with a flow-ram detector (Lablogic, Sheffield, UK), and integrated using Laura 6 software (Lablogic, Sheffield, UK). Semi-preparative HPLC was performed using a Waters HPLC or Agilent 1260 Infinity II Preparative LC System. Analytical radio-HPLC chromatograms were obtained using an Agilent 1200 series instrument equipped with a flow-ram detector (Lablogic, Sheffield, UK). Radio-HPLC chromatograms were integrated using Laura 6 software (Lablogic, Sheffield, UK). Columns, flow rate, and mobile phases are

indicated in the text. Reverse-phase purifications were carried out in a Isolera™ Spektra System using Biotage® SNAP Ultra C18 cartridges (12 g), and gradients are indicated throughout the text.

Thin Layer Chromatography (TLC) was performed using TLC silica gel 60 F_{254} (aluminium sheets 20 × 20 cm for analytical runs and glass plates 20 × 20 cm for preparative TLC purifications of phospholipids. Phospholipids were visualised by charring with 5% primuline in acetone : water (8 : 2 *v:v*), with lipids appearing as yellow spots under 365 nm irradiation.

7.2 Experimental for Chapter 2

Part of the data from this section has been published.[1]

7.2.1 Synthetic chemistry

N,N',N"-tritosyldiethylene triamine, *N,N',N"*-tritosyl-1,4,7-triazacyclononane and 1,4,7-triazacyclononane (tacn) was synthesized as described by Lippard *et al.*[2] **NODA** was synthesised as described by Shetty *et al*.[3] Tetrazine **2.2** was synthesised as described by Yang *et al*.[4]

NODA-tetrazine conjugates:

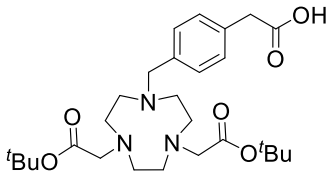

NODA^{t}Bu-MPAA:[5] A suspension of 4-(bromomethyl)phenylacetic acid (0.62 mmol, 141.00 mg) in acetonitrile (4 mL) was added dropwise to a suspension of 1,4-bis(*tert*-butoxycarbonylmethyl)-1,4,7-triazacyclononane (NODA, 0.56 mmol, 200.00 mg) and K_2CO_3 (1.12 mmol, 154.00 mg) in acetonitrile (8 mL). The resulting yellow suspension was stirred at 25 °C for 24 hours. Reaction progress was monitored by TLC (CH_2Cl_2/MeOH; 9/1). When completed, the mixture was filtered and concentrated *in vacuo*. The product was purified by flash chromatography using an Isolera™ Spektra System (Biotage® SNAP Ultra C18 cartridge (12 g), A: H_2O with 0.1% TFA, B: CH_3CN with 0.1% TFA. Gradient: 0-100% B, product eluted at 25-30% CH_3CN), and the collected fractions were lyophilized to give a pale-yellow solid (110 mg, 39%).

^{1}H NMR (400 MHz, $CDCl_3$, *δ*): 8.22 (1H, br s), 7.49 (2H, d, $^3J_{HH}$ = 7.6 Hz), 7.34 (2H, d, $^3J_{HH}$ = 7.6 Hz), 4.36 (2H, s), 3.68 (2H, s), 3.55-2.81 (16H, m), 1.45 (18H, s); ^{13}C NMR (101 MHz, $CDCl_3$, *δ*): 174.4, 170.0, 136.6, 131.0, 130.6, 128.9, 82.9, 60.3, 57.0, 51.4, 50.4, 48.1, 40.8, 28.1; HRMS (ES$^+$, TOF): *m/z* $[M+H]^+$ calc. for $C_{27}H_{44}N_3O_6$ 506.3230, found 506.3222.

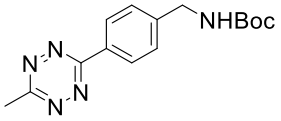

***Tert*-butyl (4-(6-methyl-1,2,4,5-tetrazin-3-yl)benzyl)carbamate**:[6] In a high pressure reaction tube, *tert*-butyl (4-cyanobenzyl)carbamate (2.00 mmol, 464 mg), CH_3CN (20.00 mmol, 1050 µL), nickel(II)trifluoromethanesulfonate (1.00 mmol, 356.00 mg) and hydrazine monohydrate (100.00 mmol, 6.2 mL) were added. The tube was sealed and heated at 60 °C for 72 hours, following which sodium nitrite (40.00 mmol, 2.82 g) in H_2O (10 mL) was added dropwise to the mixture. 1 M HCl was then added dropwise until the pH reached 3 and gases stopped evolving, at which point the mixture had turned bright red. The product was extracted with EtOAc (3 x 40 mL), and the combined organic layers were washed with H_2O (3 x 20 mL), dried over $MgSO_4$, filtered and concentrated *in vacuo*. The crude pink solid was purified by flash column chromatography (CH_2Cl_2/Et_2O gradient 100:0 *v:v* to 96:4 *v:v*) to give a dark pink solid (261 mg, 43%).

^{1}H NMR (400 MHz, $CDCl_3$, *δ*): 8.55 (2H, d, $^3J_{HH}$ = 8.3 Hz), 7.50 (2H, d, $^3J_{HH}$ = 8.3 Hz), 4.99 (1H, br s), 4.43 (2H, d, $^3J_{HH}$ = 6.1 Hz), 3.09 (3H, s), 1.48 (9H, s); ^{13}C NMR (101 MHz, $CDCl_3$, *δ*): 167.2, 163.9, 155.9, 144.0, 130.8, 128.2, 128.1, 79.8, 44.4, 28.4, 21.2; HRMS (ES^+, TOF): *m/z* $[M+H]^+$ calc. for $C_{15}H_{20}N_5O_2$ 302.1617, found 302.1621.

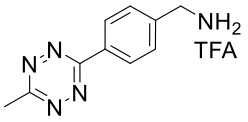

(4-(6-Methyl-1,2,4,5-tetrazin-3-yl)benzylamine:[6] To *tert*-butyl (4-(6-methyl-1,2,4,5-tetrazin-3-yl)benzyl)carbamate (0.15 mmol, 45.00 mg), TFA/CH_2Cl_2 (1:1,*v:v*, 4 mL) was added and stirred at room temperature for 2 h. The solvent was removed *in vacuo* to give the TFA salt of 4-(6-methyl-1,2,4,5-tetrazin-3-yl)benzylamine as a pink solid (41.70 mg, 88% yield).

^{1}H NMR (400 MHz, CD_3OD, *δ*): 8.63 (2H, d, $^3J_{HH}$=8.4 Hz), 7.72 (2H, d, $^3J_{HH}$ = 8.4 Hz), 4.26 (2H, s), 3.06 (3H, s); ^{13}C NMR (101 MHz, CD_3OD, *δ*): 167.7, 163.5, 137.4, 133.0, 129.4, 128.0, 42.5, 19.7); ^{19}F NMR (377 MHz, CD_3OD, *δ*): -73.5; HRMS (ES^+, TOF): *m/z* $[M+H]^+$ calc. for $C_{10}H_{12}N_5$ 202.1087, found 202.1096.

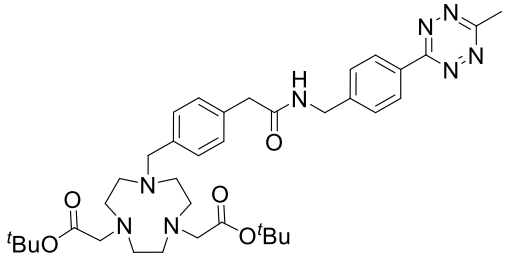

NODA^{t}Bu-MPAA-Tz: Under a nitrogen atmosphere, NODA^{t}Bu-MPAA (0.12 mmol, 60.00 mg) and HBTU (0.14 mmol, 53.7 mg) were dissolved in anhydrous DMF (1 mL). Triethylamine (0.12 mmol, 16.50 µL) was added and the pale yellow suspension was stirred at 40 °C for 15 mins. (4-(6-Methyl-1,2,4,5-tetrazin-3-yl)benzylamine (0.12 mmol, 23.70 mg) in anhydrous CH_2Cl_2 (1 mL) and triethylamine (0.16 mmol, 23.50 µL) were added, and the resulting pink solution was stirred at 40 °C for 24 hours. Completion of the reaction was monitored by TLC (90:10 CH_2Cl_2:MeOH). The resulting solution was concentrated *in vacuo* to give a pink solid, which was purified by flash column chromatography (CH_2Cl_2/MeOH gradient 100:0 *v:v* to 80:20 *v:v*), and washed with Et_2O to give a dark pink solid (50.05 mg, 60%).

^{1}H NMR (400 MHz, $CDCl_3$, *δ*): 8.46 (2H, d, $^3J_{HH}$ = 8.4 Hz), 7.53 (2H, d, $^3J_{HH}$ = 8.1 Hz), 7.44 (2H, d, $^3J_{HH}$ = 8.4 Hz), 7.37 (2H, d, $^3J_{HH}$ = 8.1 Hz), 6.36 (1H, t, $^3J_{HH}$ = 6.1 Hz), 4.50 (2H, d, $^3J_{HH}$ = 6.1 Hz), 4.40 (2H, s), 3.65 (2H, s), 3.33-3.17 (8H, m), 3.07 (3H, s), 3.07-3.00 (2H, m), 2.80-2.59 (6H, m), 1.45 (18H, s); ^{13}C NMR (101 MHz, $CDCl_3$, *δ*): 170.7, 170.5, 167.2, 163.9, 143,4, 137.1, 131.2, 130.7, 130.4, 129.5, 128.4, 128.1, 82.3, 65.8,z 59.4, 56.7, 51.6, 50.4, 47.4, 43.5, 43.3, 28.1, 21.2, 15.3; HRMS (ES$^+$, TOF): *m/z* [M+H]$^+$ calc. for $C_{37}H_{53}N_8O_5$ 689.4139, found 689.4163.

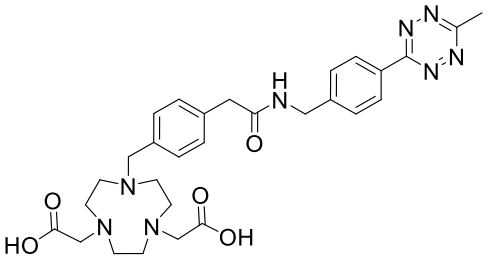

NODA-MPAA-Tz: NODA^{t}Bu-MPAA-Tz (0.017 mmol, 12.30 mg) was treated with TFA/CH_2Cl_2 (1:1,*v:v*, 2 mL) and stirred at room temperature for 5 h. The solvent was removed *in vacuo,* and the crude product was purified by flash chromatography using an Isolera™ Spektra System (Biotage® SNAP Ultra C18 cartridge (12 g), A: H_2O with 0.1% TFA, B: CH_3CN with 0.1% TFA. Gradient: 0-100% B) The fractions were lyopholized to give the desired product as a pink solid (10.50 mg, 99%).

^{1}H NMR (400 MHz, CD_3OD, *δ*): 8.50 (2H, d, $^3J_{HH}$ = 8.4 Hz), 7.61 (2H, d, $^3J_{HH}$ = 8.1 Hz), 7.51 (2H, d, $^3J_{HH}$ = 8.4 Hz), 7.46 (2H, d, $^3J_{HH}$ = 8.1 Hz), 4.51 (2H, s), 4.44 (2H, s), 3.67 (2H, s), 3.54-3.40 (2H, m), 3.27-3.11 (8H, m), 3.05 (3H, s), 2.86-2.64 (6H, m); ^{13}C NMR (101 MHz, CD_3OD, *δ*): 172.8, 168.5, 164.7, 144.6, 138.6, 132.2, 131.8, 131.3, 130.7, 129.2, 128.7, 59.4, 55.5, 51.8, 50.4, 47.3, 43.8, 43.1, 21.4; HRMS (ES$^+$, TOF): *m/z* [M+H]$^+$ calc. for $C_{29}H_{37}N_8O_5$ 577.2880, found 577.2884.

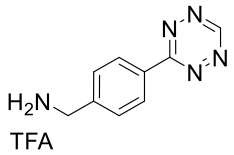

(4-(1,2,4,5-tetrazin-3-yl)phenyl)methanamine (2.3):[7] *Tert*-butyl-(4-(1,2,4,5-tetrazin-3-yl)benzyl)carbamate (**2.2**, 0.15 mmol, 43.10 mg) was treated with TFA/CH_2Cl_2 (1:1,*v:v*, 4 mL) and stirred for 2 h at room temperature. The solvent was removed *in vacuo* to give the TFA salt of (4-(1,2,4,5-tetrazin-3-yl)phenyl)methanamine (45.10 mg, 99% yield).

^{1}H NMR (400 MHz, CD_3OD, *δ*): 10.37 (1H, s), 8.67 (2H, d, $^3J_{HH}$=8.4 Hz), 7.74 (2H, d, $^3J_{HH}$ = 8.4 Hz), 4.27 (2H, s); ^{13}C NMR (101 MHz, CD_3OD, *δ*): 167.3, 159.5, 139.3, 134.2, 130.9, 129.8, 43.9; ^{19}F NMR (377 MHz, CD_3OD, *δ*): -73.5.

Phospholipid synthesis:

DSPE-PEG_{200}-TCO was synthesised as described by Hernandez *et al*.:[6]

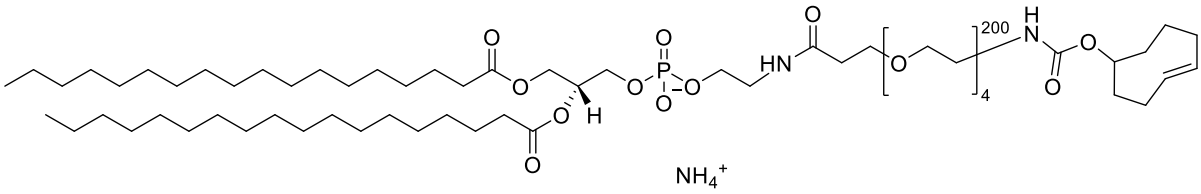

DSPE-PEG_{200}-TCO: 18:0 PE-NH_2 (10 mg, 13.3 µmol) was dissolved in a mixture of anhydrous $CHCl_3$:MeOH (0.56:0.44 *v:v*) and triethylamine (50 µL). A solution of TCO-PEG_4-NHS (10 mg, 19.43 µL in 0.3 mL $CHCl_3$) was added, and the solution was stirred at room temperature for 5 h. The solvent was removed *in vacuo*, and the product was purified by preparative TLC ($CHCl_3$: MeOH: H_2O 8:2:0.2 *v:v:v*) to give an off-white solid (7.2 mg, 48%).

^{1}H NMR (400 MHz, CD_3OD, *δ*): 5.64–5.52 (1H, m), 5.48–5.37 (1H, m), 5.23 (1H, m), 4.41–4.35 (1H, m), 4.30–4.23 (1H, m), 4.21–4.14 (1H, m,), 4.00 (4H, m), 3.84–3.38 (18H, m), 3.02 (2H, m), 2.52–2.41 (2H, m), 2.40-2.33 (2H, m), 2.30–2.25 (4H, m), 2.04-1.70 (12H, m), 1.64–1.55 (6H, m), 1.26 (58H, m), 0.88 (6H, t, $^3J_{HH}$ = 6.5 Hz); MALDI (matrix: 4-nitroaniline); m/z for $[C_{62}H_{122}N_3O_{16}PN]^+$ ([M + NH4 + CH3OH]+) expected: 1195.9, found: 1195.4.

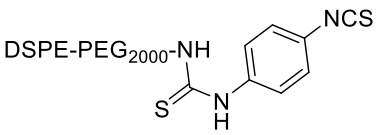

DSPE-PEG_{2000}-iso: Under a nitrogen atmosphere, *p*-phenylene diisothiocyanate (26.6 µmol, 5.00 mg) was dissolved in anhydrous $CHCl_3$ (1 mL). DSPE-PEG_{2000}-NH_2 (4.6 µmol, 13.00 mg) in a solution of anhydrous $CHCl_3$ (0.5 mL) and triethylamine (50 µmol) was added dropwise to

the solution, and the reaction was stirred for 24 hours at room temperature. Completion of the reaction was monitored by TLC (CH_2Cl_2 : MeOH 90:10 *v:v*). The crude was concentrated *in vacuo*, and purified by preparative TLC, and lyophilized to obtain a white foamy solid (12.3 mg, 80%). R_f = 0.46 (CH_2Cl_2:MeOH 90:10 *v:v*). MALDI (matrix: 4-nitroaniline): *m/z* for $[C_{140}H_{270}N_5O_{54}PS_2 + NH_4 + H]^+$ expected = 2981.8, found 2981.1.

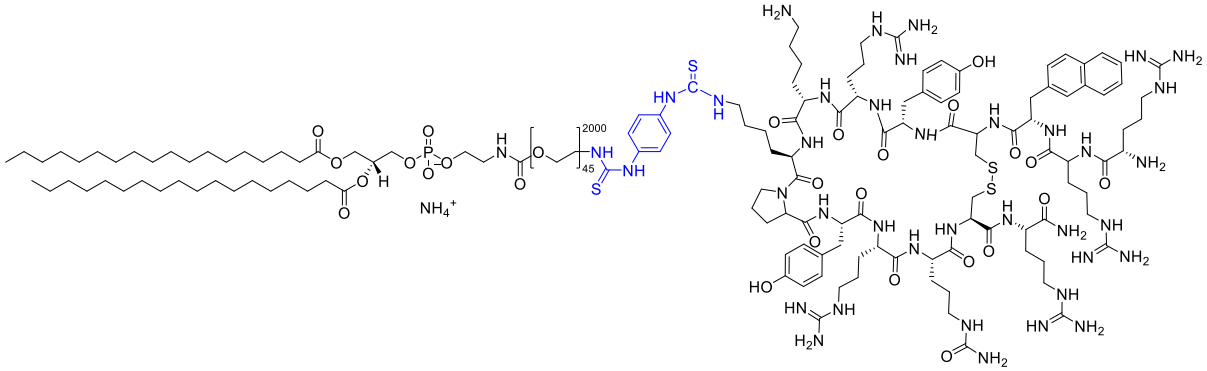

DSPE-PEG$_{2000}$-iso-T140 (2.7): Under a nitrogen atmosphere, DSPE-PEG$_{2000}$-iso (4.10 µmol, 12.3 mg) and T140 peptide (RR-2Nal-(CYRKkPYR-Cit-C)R-NH_2 4.1 µmol, 8.25 mg) was dissolved in anhydrous DMF (0.7 mL). Et_3N (50 µL) was added, and the solution was stirred at room temperature for 24 hours. The reaction was lyopholized and the crude product was purified by preparative HPLC (Gradient: 5:95 to 95:5 0.1 % HCOOH in H_2O:MeOH, 0.8 mL/min, Column: phenomenex, Luna 5 µm C8 4.6 x 75 mm, 100 Å). Subsequent lyopholization gave a white solid (4.3 mg, 20%). t_R = 20:02 min:s (Gradient: 5:95 to 95:5 H_2O:MeOH, 0.8 mL/min, column: phenomenex, Luna 5 µm C8 4.6 x 75 mm, 100 Å). MALDI (matrix: 4-nitroaniline): *m/z* for $[C_{230}H_{412}N_{39}O_{71}PS_4 + DMF + K]^+$ expected = 5128.4, found 5128.3.

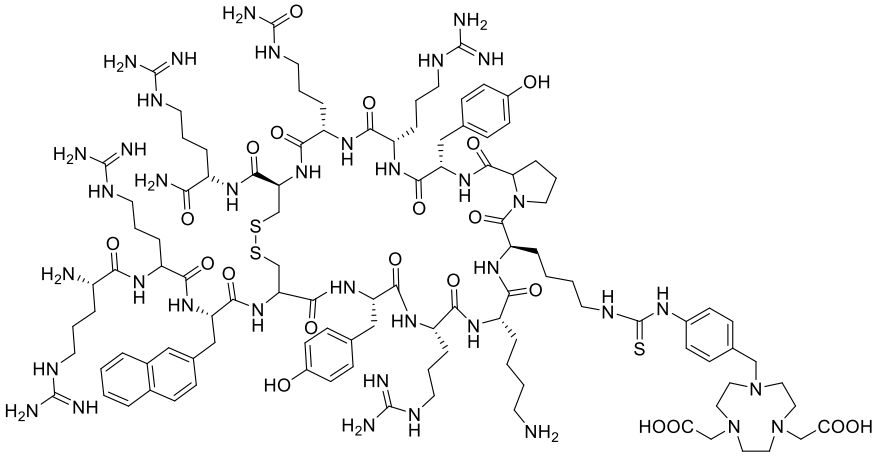

T140-NODA: Under a nitrogen atmosphere, T140 peptide (10 mg, 4.9 µmol) and NODA-MP-NHS (2 mg, 4.9 µmol) were dissolved in anhydrous DMF (3 mL). Et_3N (20 µL) was added, and the reaction was stirred at room temperature for 24 hours. Upon completion, the solvent was

removed *in vacuo* and the reaction was purified by preparative HPLC (phenomenex C18 column, gradient: 0.1% TFA in water:MeOH 5:95 to 95:5 in 30 mins) and lyophilised to give a white solid (4 mg, 33%). MALDI-TOF (matrix: 4-nitroaniline), calc. for $[M+Et_3N+H]^+$ $C_{114}H_{182}N_{39}O_{21}S_3$ = 2529.4, found: 2529.5.

7.2.2 Radiochemistry

[^{18}F]FBox-Tz was synthesised according to a previously reported protocol.[8]

Prior to usage, $^{18}F^-$ was purified using a Sep-PAK Accell Plus QMA light cartridge (Cl^- form, Waters, WAT023525) and eluted with 0.9% *w:v* NaCl solution.

Radiosynthesis of [^{18}F]AlF-Tz

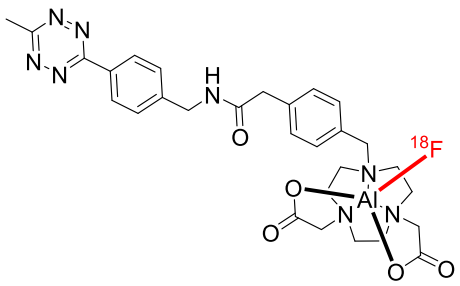

A mixture of **NODA-MPAA-Tz** in MeCN (12.5 µL, 100 nmol), $AlCl_3$ (2 mM in 0.5 M sodium acetate at pH 4.2, 50 µL, 100 nmol), [^{18}F]fluoride (100-350 MBq, 150 µL) and MeCN (200 µL) was heated at 100 °C for 20 min. Upon completion, the reaction was diluted in 0.1 % TFA in water (20 mL), trapped on an Oasis® HLB (30 mg) Light cartridge, washed with 0.1 % TFA in water (5 mL), and eluted with ethanol (400 µL). Analytical RP-HPLC (Gradient: 0.1% TFA H_2O:MeCN 95:5 *v:v* to 5:95 *v:v*, column: phenomenex, Gemini 5 µm C18 110 Å, 1 mL/min flow rate): t_R [^{18}F]AlF-Tz = 8 min 48 s.

Stability test

[^{18}F]AlF-Tz (200-300 MBq) in 500 µL ethanol was left to stand at room temperature. Aliquots of the solution was analysed by radio-HPLC at 1, 2, 3 and 4 h time points.

[^{18}F]AlF-Tz + DSPE-PEG$_{200}$-TCO reaction

To purified [^{18}F]AlF-Tz in ethanol (300 µL) was added PE-PEG$_{200}$-TCO (100 nmol) in ethanol (10 µL). The reaction was incubated at 60 °C unsealed, allowing ethanol to evaporate. Completion of the reaction was monitored by radio-TLC (2 M NH_4OAc:MeOH 1:1 *v:v* – lipid remains at baseline, [^{18}F]AlF-Tz moves with solvent front). Radio-HPLC (Gradient: 0.1% SDS in 200 mM NH_4OAc:MeOH 50:50 *v:v* to 5:95 *v:v*, 1 mL/min flow rate, column: phenomenex Aeris™ 3.6 µm WIDEPORE C4 200 Å 250 x 4.6 mm). t_R ([^{18}F]AlF-lipid)= 7:35 min:s.

Automated synthesis of [^{18}F]AlF-Tz

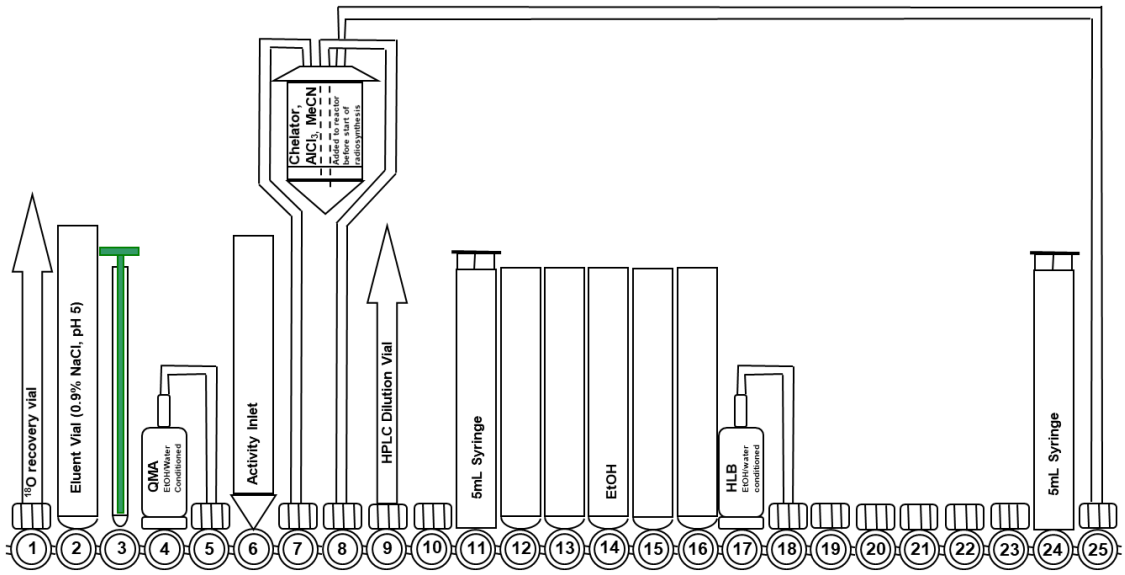

Cassette position	
1	^{18}O water recovery vial
2	Eluent vial (1000 µL 0.9% saline)
3	1 mL syringe
4/5	QMA cartridge
6	Activity inlet
7/8	Reaction vessel
9	Dilution vial: water (25 mL)
10	HPLC loop
11	5 mL syringe
12	Empty
13	Empty
14	5 mL ethanol
15-16	Empty
17/18	Oasis® HLB (30 mg) Light cartridge
19-23	Empty
24	5 mL syringe
25	Reaction vessel (vac line)

A standard FASTlab synthesis manifold with silicone tubing was used. Purification cartridges were conditioned with EtOH (5 mL), water (10 mL) and dried with air (10 mL) prior to use. Aqueous [^{18}F]fluoride in enriched ^{18}O-water was delivered to the FASTlab™ radiosynthesis module and trapped onto a Waters Accell™ Plus QMA cartridge (Cl^- form, WAT023525) using

the syringe at position 1. The [^{18}F]fluoride was eluted in 0.9% saline (pH 5, 1 mL) into the reaction vessel pre-loaded with NODA-MPAA-Tz (25 µL, 8 mM in MeCN), $AlCl_3$ (100 µL, 2 mM in pH 4.2 NaOAc buffer), and MeCN (1 mL) at position 7/8. The reaction vessel was then heated at 100 °C for 20 mins, where nitrogen is bubbled through the reaction solution for mixing. After which, the reaction solution was diluted in 0.1% TFA H_2O (25 mL) at position 9, then passed through an Oasis® HLB (30 mg) Light cartridge. The product was eluted with ethanol (0.5 mL), giving 450-550 MBq of activity in 60-66% RCY in 45-50 min.

Radiosynthesis of [^{18}F]AlF-NODA-T140

A mixture of **T140-NODA** in DMSO (12.5 µL, 100 nmol), $AlCl_3$ (2 mM in 0.5 M sodium acetate at pH 4.2, 50 µL, 100 nmol), [^{18}F]fluoride (100-350 MBq, 150 µL) and MeCN (200 µL) was heated at 100 °C for 20 min. Upon completion, the reaction was diluted in 0.1 % TFA in water (20 mL), trapped on an Oasis® HLB (30 mg) Light cartridge, washed with 0.1 % TFA in water (5 mL), and eluted with ethanol (400 µL). Analytical RP-HPLC (Gradient: 0.1% TFA H_2O:MeCN 95:5 *v:v* to 5:95 *v:v*, column: phenomenex, Gemini 5 µm C18 110 Å, 1 mL/min flow rate): t_R [^{18}F]AlF-NODA-T140 = 7 min 11 s.

7.2.3 Microbubble and nanobubble production

The lipid-coated, decafluorobutane-filled microbubbles (MBs) were produced using a modified formulation.[6] Hernandez *et al*. prepared MBs containing 85 mol% 1,2-dipalmitoyl-*sn*-glycero-3-phosphocholine (DPPC), 10 mol% PE-PEG_4-TCO, and 5 mol% 1,2-dipalmitoyl-*sn*-glycero-3-phosphoethanolamine-*N* [methoxy(polyethylene glycol)-2000] (DSPE-PEG_{2000}-NH_2). In this project, MBs with 75 mol% DPPC, 10 mol% DPPA, 10 mol% PE-PEG_4-TCO, and 5 mol% DSPE-PEG_{2000}-NH_2 were prepared. The total lipid concentration was between 0.85-0.88 mg/mL. For [^{18}F]AlF-T140-microbubbles, DSPE-PEG_{2000}-NH_2 was replaced with an equal amount (mol%) of T140-lipid **2.7**. The lipids were first dissolved in chloroform, transferred to a 2 mL glass vial, dried over nitrogen gas, and then dried overnight *in vacuo* to remove residual solvent. T140-lipid **2.7** was dissolved in $CHCl_3$:EtOH (1:1 *v:v*) due to its low solubility in $CHCl_3$ alone. Then, propylene glycol (150 µL), phosphate-buffered saline (PBS) (800 µL), and glycerol (50 µL) were added in order. For the preparation of DiI-stained microbubbles, 1 µL of a solution of DiI in DMSO (2 mg/mL) was added after the glycerol addition step. This created a lipid suspension, which was stirred for 10 mins at room temperature, then left to stand for 10 mins. The vials were then sealed, and the headspace purged with decafluorobutane. The microbubbles were produced *via* mechanical agitation (5000 rpm, 30 s, two cycles) to yield a cloudy solution.

Microbubble compositions are as follow:

Non-targeted MBs (NT-MBs):

Reagent	**MW (g/mol)**	**mol (nmol)**	**mole fraction (%)**	**Mass (mg)**
DPPC	734.039	753	81.9	0.5525
DPPA	670.873	79.2	8.6	0.0531
DSPE-PEG_{2000}-NH_2	2790.486	87.6	9.5	0.2444

TCO-MBs:

Reagent	**MW (g/mol)**	**mol (nmol)**	**mole fraction (%)**	**Mass (mg)**
DPPC	734.039	753	76.4	0.5525
DPPA	670.873	79.2	8.0	0.0531
DSPE-PEG_{2000}-NH_2	2790.486	87.6	4.4	0.1222
TCO-lipid	1188.38	109	11.1	0.1300

T140-TCO-MBs:

Reagent	**MW (g/mol)**	**mol (nmol)**	**mole fraction (%)**	**Mass (mg)**
DPPC	734.039	753	73.2	0.5525
DPPA	670.873	79.2	7.7	0.0531
DSPE-PEG_{2000}-NH_2	2790.486	43.8	4.3	0.1222
TCO-lipid	1188.38	109	10.6	0.1300
T140-lipid **2.7**	5036.86	43.8	4.3	0.2206

Microbubble characterisation: Microbubble sizing and concentration were obtained using a bright-field microscope (Nikon Eclipse 50i, 40x objective) according to previously reported protocol.[9] Zeta potentials were recorded using a 1:100 diluted sample in PBS using a Malvern Nano ZetaSizer.

	T140-MBs	**TCO-MBs**
Concentration (MB/mL)	4.12×10^8	4.32×10^8
Mean diameter (μm)	2.07 ± 1.52	1.98 ± 1.52
Range (μm)	0.50 – 9.97	0.50 – 9.97
Zeta potential (mV)	-1.5	+7

[^{18}F]AlF-MB or [^{18}F]FBox-MB (Stepwise production)

[^{18}F]AlF-Tz or [^{18}F]FBox-Tz in ethanol (300 µL) was added to a vial containing DSPE-PEG$_4$-TCO (0.13 mg, 0.11 µmol). The reaction vial was heated at 60 °C for 20 mins. After that, the volume of the reaction was reduced to approximately 100 µL, and this was added to a solution containing the rest of the lipids (DPPC 0.553 mg, DPPA 0.053 mg, DSPE-PEG$_{2000}$-NH$_2$ 0.1222 mg) dissolved in 1 mL of a solution of propylene glycol, glycerol, and phosphate-buffered saline (PBS) (15:5:80 *v:v/v*). The vial was sealed and purged with perfluorobutane, and the microbubbles were produced by mechanical agitation (5000 rpm for 30 s, two cycles). The microbubble suspension was then centrifuged for purification.

[^{18}F]AlF-MB or [^{18}F]FBox-Tz (kit-based production)

[^{18}F]AlF-Tz or [^{18}F]FBox-Tz in ethanol/reaction solution (80 µL) was added to a vial containing PE-PEG$_4$-TCO (0.13 mg, 0.11 µmol) and the rest of the lipids (DPPC - 0.553 mg, DPPA - 0.053 mg, DSPE-PEG$_{2000}$-NH$_2$ - 0.1222 mg) dissolved in 1 mL of a solution of propylene glycol, glycerol, and phosphate-buffered saline (PBS) (15:5:80 *v:v:v*). The vial was sealed and purged with perfluorobutane, and the microbubbles were produced by mechanical agitation (5000 rpm for 30 s, two cycles). The microbubble suspension was left to stand for 5 mins, and then centrifuged for purification.

[^{18}F]AlF-T140-MBs were prepared using the stepwise production method, but with 25 µL of [^{18}F]AlF-Tz being added to the vial containing the rest of the lipids (DPPC 0.553 mg, DPPA 0.053 mg, DSPE-PEG$_{2000}$-NH$_2$ 0.1222 mg and T140-lipid 0.2206 mg).

Nanobubbles

Nanobubbles were produced by mechanical agitation using a previously described procedure,[10] described below:

TCO-NBs

To a 3 mL vial, lipids including TCO-lipid (0.13 mg), DBPC (6 mg), DPPA (1 mg), DPPE (2 mg), and mPEG-DSPE (1 mg) were added. Propylene glycol (100 µL), glycerol (100 µL) and PBS (800 µL) were added. The vial was sealed and purged with C_4F_{10}. Next, the vial was placed on a dental HL-AH High Speed Digital Amalgamator Amalgam Capsule Blend Mixer, and mechanical agitation was used to drive bubble self-assembly (4000 rpm for 45 s). Nanobubbles were isolated by centrifugation at 50 *g* for 5 min with the vial inverted. 500 µL of nanobubbles were obtained from the vial.

Nanobubbles were characterised using a Malvern Nano ZetaSizer. Dynamic light scattering was performed at a scattering angle of 173 at 25 °C. The refractive index of the material was

set to 1 in accord with air. The refractive index of the sample was set to 1.333 in accord with water.

[^{18}F]AlF-NB

[^{18}F]AlF-Tz in ethanol (300 µL) was added to a vial containing DSPE-PEG$_4$-TCO (0.13 mg, 0.11 µmol). The reaction vial was heated at 60 °C for 20 mins. After that, the volume of the reaction was reduced to approximately 100 µL, and this was added to a solution containing the rest of the lipids: DBPC (6 mg), DPPA (1 mg), DPPE (2 mg), and mPEG-DSPE (1 mg) dissolved in 1 mL of a solution of propylene glycol, glycerol, and phosphate-buffered saline (PBS) (10:10:80 *v:v/v*). The vial was sealed and purged with perfluorobutane, and the nanobubbles were produced by mechanical agitation (5000 rpm for 30 s, two cycles). Unincorporated [^{18}F]AlF-Tz and [^{18}F]AlF-lipid were removed by purification using a Cytiva NAP-5 column, eluting with H_2O in 500 µL fractions. The [^{18}F]AlF-NBs were obtained in fractions 2 and 3.

7.2.4 In vitro studies

Cell culture

MDA-MB-231 cell line was obtained from PerkinElmer (Waltham, MA, USA). MDA-MB-231 shCXCR4 and MDA-MB-231 shSC were obtained from Dr Marta Braga.[11] All cells were cultured in Roswell Park Memorial Institute Medium 1640 (RPMI) (Sigma-Aldrich), supplemented with 10% Foetal Calf Serum (FCS) and 1% penicillin-streptomycin-glutamine (Sigma-Aldrich) in a humidified atmosphere of 5% CO_2 at 37 °C.

Binding studies with fluorescent T140-MBs

MDA-MB-231 shCXCR4, MDA-MB-231 shSC or C4-2B cells (10x10^6) in media (25 mL) were plated in Petaka G3^{TM} LOT (Low Oxygen Transfer) for adherent cells plates (Life Science Production) for 24-48 hours in a humidified atmosphere of 5% CO_2 at 37 °C. Following this, media was removed, and microbubbles with approximately 1x10^6 MB/mL in media (25 mL) was introduced and incubated for 15 mins at 37 °C. The plates were flipped to maximise contact between the cells and microbubbles. After incubation, the plates were flipped to the original position, and allowed to rest for 5 mins before evaluation to allow unbound microbubbles to float to the top of the plate. Fluorescence evaluation was carried out using DiI-modified microbubbles. Images were acquired using a 10x UPlanAPO objective lens on an Olympus BX-51 wide-field microscope.

Dox-treatment of MDA-MB-231 shCXCR4 cells to induce CXCR4-knockdown: Doxycycline hyclate (98%, Sigma-Aldrich) was dissolved in DMSO, filtered through a 0.22 µm sterile

syringe filter, and made up to 0.5 µg/mL in media. After plating the cells in Petaka G3™ LOT (Low Oxygen Transfer) for adherent cells plates (Life Science Production) for 24 h, the media was removed and replaced with the 0.5 µg/mL Doxycycline media, and the cells were incubated for a further 24 h. Subsequent binding procedures are the same as described above.

Radioactive uptake studies with [^{18}F]AlF-T140-MBs and [^{18}F]AlF-T140-NODA

MDA-MB-231 cells were plated at 2.5 × 10^5 cells per well in 6-well plates. After 24 h, cells were treated with doxycycline hyclate (0.5 µg/mL) in media for 24 h. On the day of the radioactive uptake experiment, fresh media containing 0.74 MBq of [^{18}F]AlF-T140-NODA was added to the individual wells (1 mL per well. For [^{18}F]AlF-T140-MB, 0.5 mL was added per well to form a thin film so that microbubbles could come in contact with the cells for binding. Cells were incubated with the radiotracers for 30 min at 37 °C in a humidified condition of 5% CO_2. Cells were then washed two times with warm PBS and lysed in RIPA buffer (1 mL per well). The radioactivity of 800 µL lysate from each sample was counted on a Wizard 2480 Automatic Gamma Counter (Perkin Elmer). Data were expressed as a percentage of incubated radioactive dose (ID), normalised to total cellular protein (%ID per mg) as measured by bicinchoninic acid (BCA) assay.

Western blot was carried out as described by Braga *et al*.[11]

For the evaluation of CXCR4 expression, cells were placed on ice, washed with ice-cold PBS (3 times) and lysed on ice for 10 min using RIPA buffer (Sigma-Aldrich) supplemented with protease and phosphatase inhibitor cocktail (100X Pierce™, Thermo Fisher Scientific). The lysed cells were centrifuged at 500 rpm at 4 °C for 5 min, and the supernatant was transferred to new Eppendorf® tubes. The protein content was measured using BCA assay. Lysates were then denatured using NuPage® LDS loading buffer and reducing agent (Invitrogen™) at 70 °C for 10 min. The proteins (30 µg) were then separated by gel electrophoresis for 15 min at 290 V using 4-15% Mini-PROTEAN® TGX™ gels (Bio-Rad). Subsequently, the Trans-Blot® Turbo system was used to transfer the gels to PVDF membranes (Trans-Blot Turbo Transfer Packs, Bio-Rad). Membranes were then blocked with 5 % milk in PBS containing 0.1% v:v Tween®20 (PBST) for 1 h at room temperature. After blocking, membranes were incubated with rabbit anti-human CXCR4 clone UMB2 antibodies (1:1000 dilution, ab124824, Abcam) in 5 % milk-PBST at 4 °C overnight. After washing with PBST (3 times), membranes were incubated with goat anti-rabbit Immununoglobin G (IgG) horseradish peroxidase (IgG-HRP) (1:2000 dilution, ab109809, Abcam) in 5 % milk-PBST at room temperature for 1 h. Visualisation of signals was carried out using the Amersham enhanced chemiluminescence (ECL) Plus Western Blotting Detection Reagent kit and Amersham Hyper-film (GE Healthcare Life Sciences).

7.2.5 Statistical tests

Data were presented as mean ± SD. Comparisons were made using unpaired two-tailed *t*-tests using the GraphPad Prism 9.0 software. A significant difference was considered when $p < 0.05$. Significance levels were expressed as: ns = no significance, * $p < 0.05$, ** $p < 0.01$, *** $p < 0.001$, and **** $p < 0.0001$

7.3 Experimental for Chapter 3

Ultrasound imaging and data processing were performed by Kai Riemer and Laura Taylor from the Department of Bioengineering, Imperial College London. Animal experiments were performed together with Ala Amgheib and Joel Abrahams from the Department of Surgery and Cancer, Imperial College London.

7.3.1 Cell culture

The U2932 cell line was purchased from Deutsche Sammlung von Mikroorganismen and Zellkulturen GmBH, and cultured in Roswell Park Memorial Institute Medium 1640 (RPMI), supplemented with 10% Foetal Calf Serum (FCS), 2 mM L-glutamine (Invitrogen™), and 100 U/mL penicillin-streptomycin (Invitrogen™) in a humidified atmosphere of 5% CO_2 at 37 °C.

7.3.2 Animal and tumour models

In accordance with the UK Home Office Guidance on the Operation of the Animal Scientific Procedures Act (ASPA) 1986, all animal experiments were performed by licensed researchers. The guidelines of outlined by the UK National Cancer Research Institute Committee on Welfare of Animals in Cancer research were also adhered to.[12] Experiments were performed under Project License number 1780377; approval was granted by the UK Home Office on 01-08-2020.

Female NOD SCID mice (Charles River) aged 6-8 weeks old, with weights between 20 ± 2 g were used in this study. Mice were allowed at least 7 days to acclimatize before use. To generate the tumour xenografts, mice were anesthetized with 2-2.5% isoflurane/O_2, placed on a heating mat, and subcutaneously injected with U2932 cells (5 x 10^6 cells in 100 µL of 50% Matrigel and 50% PBS) in the upper flank. Tumour dimensions were measured by calliper, and their volumes were calculated using the ellipsoid formula: $Volume\ (mm^3) = \frac{\pi}{6} \times a \times b \times c$, where *a, b* and *c* represent the three orthogonal axes of the tumour. Tumours reached appropriate volumes of approximately 100 mm^3 after 4-5 weeks.

7.3.3 Microbubble dosage

Microbubbles were made fresh prior to each injection to ensure consistency in the quality and number of microbubbles injected, and sufficient radioactive dose for PET scanning. 1.2-3.1 MBq of activity in 70-120 µL of PBS, corresponding to ~4.5 x 10^7 microbubbles, were injected per mice to ensure sufficient radioactivity and microbubbles were present for detection by both PET and ultrasound. The catheter was flushed with 50 µL of PBS, and then removed to measure residual activity for calculation of the injected dose. Injected dose was reported as the total activity in the syringe and needle before injection minus the residual activity in syringe, needle and catheter.

7.3.4 *In vivo* PET/CT imaging and experiment set up

PET/CT imaging was conducted using a Siemens Inveon small-animal multimodality PET/CT system (Siemens Medical Solutions).

Each animal served as its own control to minimize animal numbers. The control experiment without ultrasound destruction sequence was carried out one day before the experiment with the destruction sequence to allow sufficient time for ^{18}F decay. Prior to MB injection, mice were anesthetized with 2-2.5% isoflurane/O_2 and placed on a heating mat. [^{18}F]AlF-MBs (70-120 µL, 1.2-3.1 MBq, 4.5 x 10^8 MB/mL) was injected *via* lateral tail vein cannula. Ultrasound imaging was carried out using a Verasonics research platform for 3 mins post-injection (parameters specified in section 7.3.5 below), with the ultrasound probe was placed directly above the tumour. Following this, animals then transferred to the PET/CT scanner. CT images were obtained immediately after transfer for 10-15 mins, whereas PET scans was started 30 mins post-injection to ensure consistency. Dynamic PET scans were acquired for 20 mins in a list-mode format to give decay-corrected values of radioactivity accumulation in tissues. The collected data was reconstructed as 0.55 mm sinogram bins and 20 time-frames using the 2D-ordered subsets expectation maximization (2D-OSEM) algorithm with CT-based attenuation correction. Frame durations were 12 × 5 s, 4 × 15 s, 6 × 30 s and 11 x 300 s.

The Inveon Research Workspace software (Siemens Healthcare Molecular Imaging) was used to analyse the images. CT and PET images were co-registered, and used to draw 3D regions of interests (ROIs) over the relevant tissues to obtain time-activity curves (TACs). Data for the tissues were normalised to muscle uptake for analysis.

7.3.5 Ultrasound imaging

A Verasonics Vantage 256 research ultrasound system (Verasonics, USA) with the (i) L22-14vx, (ii) L11-4v and (iii) L12-3v broadband probes were used. Three different ultrasound imaging protocols were performed to (i) visualize the distribution of contrast agents inside the tumour region; (ii) to quantify perfusion without and with a single microbubble destruction sequence; and (iii) to quantify perfusion without and with repeated microbubble destruction sequence. The mechanical indices (MI) were derated based on an attenuation coefficient α = 0.3 dB/(MHz·cm) and calibrated in a water tank with a 0.2 mm needle hydrophone (Precision Acoustics, UK).

(i) Visualization of the spatial distribution of microbubbles was achieved using the L22-14vx with a transmit frequency of 15 MHz, 5 angles and a frame rate of 500 Hz. The total number of frames was 2500 for a total of 5 s of acquisition with two half cycles in transmission and MI<0.08.

(ii) A single sequence microbubble destruction interleaved with imaging before and after the destruction was done with the L11-4v. A total of 5000 frames were acquired at a transmit frequency of 8 MHz with two half cycles, 3 angles, MI<0.1, a frame rate of 25 Hz for a total of 200 s of acquisition. Focusing was performed after 40 s with a transmit frequency of 4 MHz, 20 half cycles, MI<1.5 with two focal depth and 30 transmissions, repeated 3 times.

(iii) To quantify the perfusion without microbubble destruction ultrasound images were acquired with the L12-3v probe and a frame rate of 800 Hz yielding 3 angles, an angle range of 12° degree, and two half cycles in transmission for a total of 0.5 seconds. Imaging was repeated over the course of 180 seconds. The transmit frequency was 11 MHz with a MI<0.1.

For ultrasound-mediated microbubble destruction, the imaging and destruction sequence were interleaved. The same imaging parameters were used to record 400 frames followed by focused transmission and another 400 imaging frames equalling 1 second of acquisition. For the microbubble destruction, along two manually selected focus depth, 30 focal points were selected, and microbubbles were destroyed repeatedly 10 times. The number of half cycles per transmission was 20 with a MI<1.2. The radiofrequency data were delay and sum beamformed and further analysis was performed in MATLAB (The Math-Works Inc., USA).

(i) To visualize the spatial distribution of microbubbles, Singular Value Decomposition based clutter filtering was used. (ii) Quantification was not achieved due to the poor image resolution obtained. (iii) To quantify the contrast uptake and tumour perfusion a square region of interest encapsulating the entire tumour was manually selected. For each mouse the region was kept

the same size. The mean intensity of the region of interest was calculated for each acquisition from the B-Mode images.

Illustrations of the images obtained using the three different ultrasound imaging setups are shown in **Figure 7.1**, which were used to (i) visualize the distribution of contrast agents inside the tumour region, (ii) to quantify perfusion without and with a single microbubble destruction sequence and (iii) to quantify perfusion without and with repeated microbubble destruction sequence. Images are displayed with a dynamic range of 40 dB. Yellow rectangle marks the tumour region.

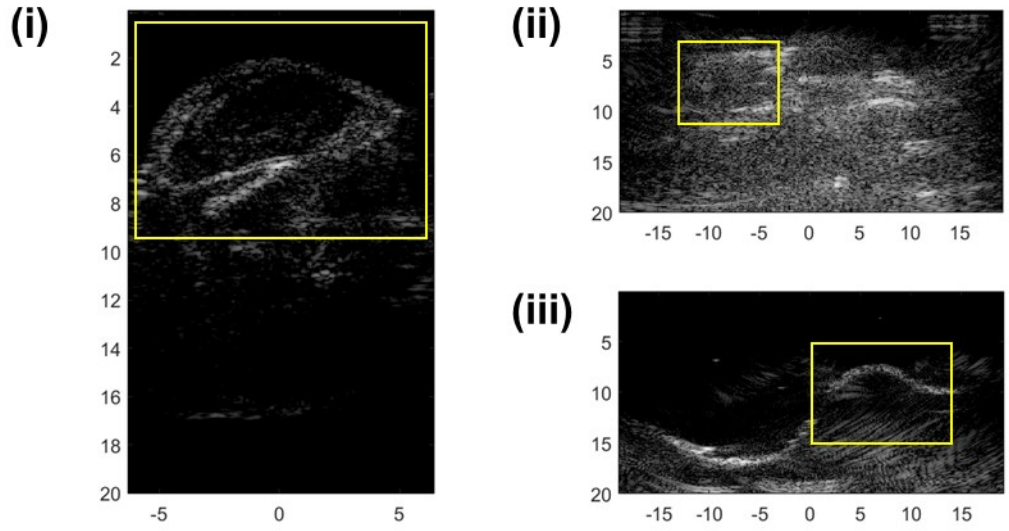

Figure 7.1: Representative images obtained using each ultrasound probe

7.3.6 *Ex vivo* Biodistribution

Ex vivo biodistribution studies were conducted with the same animals that underwent the imaging procedures. Immediately after the PET scan, mice were sacrificed by exsanguination via cardiac puncture. Selected tissues were then dissected and counted in a gamma-counter (Wizard 2480 Automatic Gamma Counter, Perkin Elmer). Data were expressed as a percentage of injected dose (%ID) normalised by tissue weight (%ID/g). Part of the tumour was preserved in formalin (10 % in water, Sigma-Aldrich) for paraffin embedding.

7.3.7 Statistical test

Data were presented as mean ± SD. Comparisons were made using paired two-tailed *t*-tests using the GraphPad Prism 9.0 software. A significant difference was considered when $p < 0.05$. Significance levels were expressed as: ns = no significance, * $p < 0.05$, ** $p < 0.01$, *** $p < 0.001$, and **** $p < 0.0001$.

7.3.8 Histology

The preserved U2932 tumours were processed by the Imperial College London Research Histology Facility (IRD section). Tissue microarrays obtained were stained with Haematoxylin & Eosin, and were visualised using a 40X UPanAPO objective lens on a Olympus BX-51 wide-field microscope.

7.4 Experimental for Chapter 4

7.4.1 Synthetic chemistry

Bisphosphonate chelators:

Tetraethyl Aminomethyl-bis(phosphonate) **4.1** was prepared as described by Kubícek *et al*.[13] Tetraethyl ethenylidenebisphosphonate was synthesised according to the procedure reported by Katrin *et al*.[14]

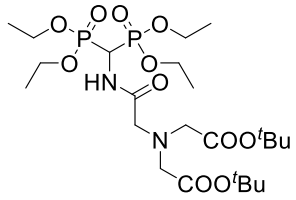

Bisphosphonate **4.3**: Under a nitrogen atmosphere, bis(2-(*tert*-butoxy)-2-oxoethyl)glycine **4.2** (0.33 mmol, 100.00 mg) and HBTU (0.36 mmol, 137.50 mg) were dissolved in anhydrous DMF (4.6 mL). *N,N*-diisopropylethylamine (0.83 mmol, 140 µL) was added and the pale brown solution was stirred at 40 °C for 15 mins. **4.1** (0.36 mmol, 110.00 mg) in anhydrous DMF (2 mL) and DIPEA (0.83 mmol, 140 µL) were added, and the resulting solution was stirred at 40 °C for 24 hours. Completion of the reaction was monitored by LC-MS (Gradient: 0.1% HCOOH in H_2O:MeCN 80:20 *v:v* to 5:95 *v:v*, column: XBridge C_{18} reverse-phase 4.6 mm × 100 mm,flow rate: 1.2 mL/min).

^{1}H NMR (400 MHz, $CDCl_3$, *δ*): 8.26 (2H, d, $^3J_{HH}$ = 10.4 Hz), 5.04 (1H, td, $^2J_{HP}$ = 22.1, $^3J_{HH}$ = 10.4 Hz), 4.31-4.04 (8H, m), 3.45 (2H, s), 3.43 (4H, s), 1.45 (18H, s), 1.33 (12H, q, $^3J_{HH}$ = 6.9 Hz); ^{13}C NMR (101 MHz, $CDCl_3$, *δ*): 170.7, 170.3, 81.7, 63.6 (dt, *J* = 6.4, 3.0 Hz, -O<u>C</u>$H_2$$CH_3$), 58.1, 56.1, 43.9 (t, $^1J_{CP}$ = 147.1 Hz, -<u>C</u>P_2-), 28.3, 16.5 (q, *J* = 3.4 Hz, -OCH_2<u>C</u>H_3); ^{31}P NMR (162 MHz, $CDCl_3$, *δ*): 16.34; HRMS (ES^+, TOF): *m/z* $[M+H]^+$ calc. for $C_{23}H_{47}N_2O_{11}P_2$ 589.2655, found 589.2646.

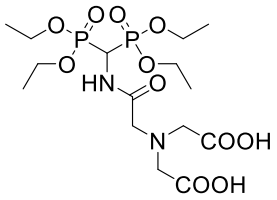

Bisphosphonate **4.4**: To **4.3** (0.09 mmol, 51.00 mg) was added CH_2Cl_2 (2 mL) and trifluoroacetic acid (1 mL). The solution was stirred at room temperature for 24 h. Upon completion, the solvent was removed *in vacuo* and the crude product was purified by flash chromatography using an Isolera™ Spektra System (Biotage® SNAP Ultra C18 cartridge (12 g), A: H_2O with 0.1% TFA, B: CH_3CN with 0.1% TFA. Gradient: 0-100% B) The fractions were lyopholized to give the desired product as a colourless oil (35.80 mg, 77 %).

^{1}H NMR (400 MHz, CD_3OD, δ): 5.04 (1H, t, $^2J_{HP}$ = 22.6), 4.30-4.15 (8H, m), 3.82 (6H, s), 1.35 (12H, td, $^3J_{HH}$ = 7.0, 5.3 Hz); ^{13}C NMR (101 MHz, CD_3OD, δ): 171.2, 169.9, 63.9 (d, J = 12.4 Hz), 56.7, 54.4, 43.5 (t, J = 149.6 Hz), 15.33-15.26 (m); ^{31}P NMR (162 MHz, CD_3OD, δ): 16.1; HRMS (ES$^+$, TOF): *m/z* [M+H]$^+$ calc. for $C_{15}H_{31}N_2O_{11}P_2$ 477.1403 found 477.1392.

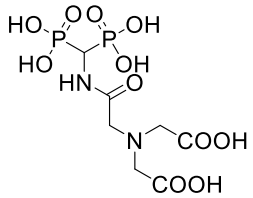

Bisphosphonate **4.5**: Under a nitrogen atmosphere, to **4.3** (0.08 mmol, 49.00 mg) in anhydrous MeCN (1.5 mL) was added TMSBr (0.99 mmol, 152 mg). The yellow was heated at 36 °C for 24 h. Upon completion, the solvent was removed *in vacuo*, and MeOH:H_2O 4:1 *v:v* was added. The resulting suspension was stirred for 1 h, after which the solvent was removed *in vacuo*, and the crude product was triturated with CH_2Cl_2 (5 mL, 3 times) to give a white solid (26.1 mg, 87 %), with approximately 10% impurities observed in the ^{1}H NMR.

^{1}H NMR (400 MHz, CD_3OD, δ): 4.79 (1H, t, $^2J_{HP}$ = 21.5), 4.43-4.32 (4H, m), 4.32-4.20 (2H, s); ^{13}C NMR (101 MHz, CD_3OD, δ): 169.0, 168.5, 57.33, 55.5, $\underline{C}P_2$ not detected; ^{31}P NMR (162 MHz, CD_3OD, δ): 14.0; HRMS (ES$^+$, TOF): *m/z* [M+K]$^+$ found 403.1623.

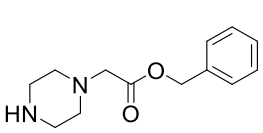

Benzyl 2-(piperazin-1-yl)acetate

Under a nitrogen atmosphere, to piperazine (1 g, 11.6 mmol), K_2CO_3 (641 mg, 4.64 mmol) in anhydrous MeCN (20 mL) was added dropwise benzyl-2-bromoacetate (532 mg, 2.32 mmol).

The mixture was stirred at room temperature for 24 h, filtered, and concentrated *in vacuo*. The product was purified by flash chromatography using an Isolera™ Spektra System (Biotage® SNAP Ultra C18 cartridge (12 g), A: H_2O with 0.1% TFA, B: CH_3CN with 0.1% TFA. Gradient: 0-100% B) The fractions were lyopholized to give the desired product as a white solid (256 mg, 47%).

^{1}H NMR (400 MHz, $CDCl_3$, *δ*): 7.34-7.29 (5H, m), 5.13 (2H, s), 3.21 (2H, s), 2.90-2.87 (4H, m), 2.52-2.50 (4H, m); ^{13}C NMR (101 MHz, $CDCl_3$, *δ*): 170.2, 135.7, 128.6, 128.4, 126.9, 66.4, 59.9, 54.2, 45.8.

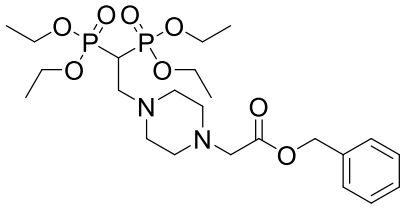

Bisphosphonate **4.8**: (Not isolated) Tetraethyl ethenylidenebisphosphonate (0.25 mmol, 75.00 mg) and benzyl 2-(piperazin-1-yl) acetate (0.45 mmol, 105.00 mg) were dissolved in $CDCl_3$ (0.5 mL) and heated at 45 °C for 30 min. The reaction was then analysed by ^{1}H and ^{31}P NMR spectroscopy. ^{1}H NMR (400 MHz, $CDCl_3$, *δ*): 7.44-7.19 (5H, m), 5.10 (2H, s), 4.24-3.97 (9H, m), 3.19 (2H, s), 2.86 (2H, td, $^3J_{HP}$ = 14.9, $^3J_{HH}$ = 6.2 Hz), 2.58-2.47 (8H, m), 1.28 (12H, t, $^3J_{HH}$ = 7.1); ^{31}P NMR (162 MHz, $CDCl_3$, *δ*): 22.5.

Salen chelators:

Salphen **4.9** and **salphen-Al-Cl** were synthesised as described by Yin *et al*.[15] Salcyen **4.10** and salcyan **4.11** were synthesised as described by Yeori *et al*.[16] Saldien **4.12** was synthesised as described by Wei Wang *et al*.[17]

Salalen ligands were synthesised using a modified procedure from Whitelaw *et al*.[18]

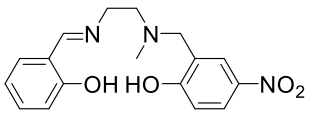

Nitro salalen **4.13**: methylene diamine (10.00 mmol, 1.02 g) and salicylaldehyde (10.00 mmol, 1.12 g) in methanol were stirred at room temperature for 24 h. Upon completion, the solvent was removed *in vacuo* and the resulting yellow oil was used in the next step without further purification. To the yellow oil (3.44 mmol, 1.00 g) was added 2-hydroxy-5-nitrobenzyl bromide (3.44 mmol, 798 mg), Et_3N (3.44 mmol, 0.48 mL) and THF (20 mL). The resulting suspension was heated at reflux for 3 h, after which the reaction was cooled and left at -20 °C overnight.

The solid was filtered, then recrystallised in MeOH (*ca*. 10 mL) at -20 °C, resulting in a bright yellow solid (554 mg, 49 %).

^{1}H NMR (400 MHz, $CDCl_3$, *δ*): 8.40 (1H, s), 8.08 (1H, dd, *J* = 9.0, 2.8 Hz), 7.94 (1H, d, *J* = 2.8 Hz), 7.33 (1H, td, *J* = 7.7, 1.7 Hz), 7.29-2.23 (1H, m), 6.98 (1H, d, *J* = 8.6 Hz), 6.90 (1H, t, *J* = 7.7 Hz), 6.83 (1H, d, *J* = 8.6 Hz), 3.87 (1H, s), 3.81 (2H, t, *J* = 6.2 Hz), 2.92 (2H, t, *J* = 6.2 Hz), 2.41 (3H, s); ^{13}C NMR (101 MHz, $CDCl_3$, *δ*): 166.8, 164.4, 161.0, 140.2, 132.8, 131.7, 125.6, 124.7, 121.6, 119.0, 118.7, 117.2, 116.8, 61.0, 57.6, 57.1, 41.9; HRMS (ES^+, TOF): *m/z* $[M+H]^+$ calc. for $C_{17}H_{20}N_3O_4$ 330.1454, found 330.1453.

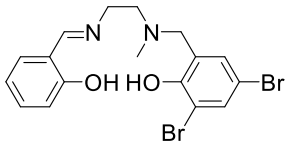

Dibromo salalen **4.14**: Using the same yellow oil from nitrosalalen **4.13**, to the yellow oil (2.08 mmol, 0.60 g) was added 2-hydroxy-5-nitrobenzyl bromide (2.08 mmol, 0.72 g), Et_3N (2.08 mmol, 0.29 mL) and THF (12 mL). The resulting suspension was heated at reflux for 3 h, after which the reaction was cooled and left at -20 °C overnight. The solid was filtered, then recrystallised in MeOH (*ca*. 10 mL) at -20 °C, resulting in bright yellow crystals (214 mg, 23 %), which was suitable for X-ray diffraction studies.

^{1}H NMR (400 MHz, $CDCl_3$, *δ*): 8.38 (1H, s), 7.54 (1H, d, *J* = 2.3 Hz), 7.32 (1H, ddd, *J* = 8.4, 7.2, 1.7 Hz), 7.26 (1H, dd, *J* = 7.6, 1.7 Hz) 7.04 (1H, d, *J* = 2.3 Hz), 6.96 (1H, d, *J* = 8.4 Hz), 6.89 (1H, t, *J* = 7.6 Hz), 3.79 (2H, t, *J* = 6.6 Hz), 3.76 (2H, s), 2.89 (2H, t, *J* = 6.6 Hz), 2.40 (3H, s); ^{13}C NMR (101 MHz, $CDCl_3$, *δ*): 166.7, 161.0 154.3, 134.4, 132.7, 131.7, 130.2, 124.2, 118.9, 118.7, 117.1, 111.2, 110.7, 61.1, 57.5, 57.4, 42.2; HRMS (ES^+, TOF): *m/z* $[M+H]^+$ calc. for $C_{17}H_{19}N_2O_2Br_2$ 442.9793, found 442.9792.

Complexation reactions with $AlCl_3$ was carried out as described by Yin *et al*.[15] A general procedure is as follow:

Under a nitrogen atmosphere, salen ligand (0.50 mmol) and $AlCl_3$ (0.5 mmol, 68.00 mg) in MeCN (20 mL) were heated at reflux overnight. The reaction was filtered, and the residue was washed with MeCN (20 mL, 3 times) to yield the product.

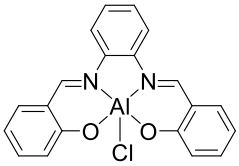

Salphen-AlCl:[15] ^{1}H NMR (400 MHz, DMSO-d_6, δ): 9.31 (2H, s), 8.14 (2H, dt, J = 7.3, 3.7 Hz), 7.70 (2H, dd, J = 7.9, 1.8 Hz), 7.59-7.48 (4H, m), 6.98 (2H, d, J = 8.4 Hz), 6.90-6.82 (2H, m); ^{13}C NMR (101 MHz, DMSO-d_6, δ): 165.5, 161.5, 137.5, 136.9, 135.8, 128.8, 121.5, 119.6, 117.1, 116.7; HRMS (ES$^+$, TOF): *m/z* [M - Cl + 2 DMSO]$^+$ found 382.1096.

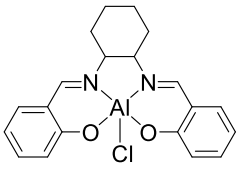

Salcyen-AlCl: ^{1}H NMR (400 MHz, DMSO-d_6, δ): 8.38 (2H, s), 7.53 (2H, dd, J = 7.8, 1.9 Hz), 7.38 (2H, td, 7.5, 1.8 Hz), 6.86 (2H, d, J = 8.3 Hz), 6.74 (2H, t, J = 7.4 Hz), 3.35 (2H, masked by H_2O peak, assigned from HMQC), 2.56 (2H, d, J = 10.8 Hz), 1.95 (2H, d, J = 7.7 Hz), 1.51-1.28 (4H, m); ^{13}C NMR (101 MHz, DMSO-d_6, δ): 164.3, 163.3, 135.0, 134.8, 121.1, 63.2, 26.9, 23.4; HRMS (ES$^+$, TOF): *m/z* [M – Cl + MeCN]$^+$ calc. 388.1606, found 388.1600.

7.4.2 Radiochemistry

Prior to usage, $^{18}F^-$ was trapped on a Sep-PAK Accell Plus QMA light cartridge (Cl^- form, Waters) and eluted with 0.9% *w:v* NaCl solution.

[^{18}F]AlF-labelling of alendronic acid:

To an Eppendorf® tube with alendronic acid in H_2O (12.5 µL, 100 nmol) was added $AlCl_3$ (2 mM in 0.5 M sodium acetate at pH 4.2, 50 µL, 100 nmol), and [^{18}F]fluoride (100-350 MBq, 150 µL). The reaction was heated at 37 °C for 20-60 min, and analysed by radio-TLC (TLC silica gel 60 F_{254}, eluting with 1:1 *v:v* MeOH, 2 M NH_4OAc), where a new species was observed on the baseline. However, further characterisation of the species was unsuccessful.

[^{18}F]AlF-labelling of salphen-AlCl

To an Eppendorf® tube with salphen-AlCl in DMSO:H_2O 1:1 *v:v* (10 µL, 100 nmol) was added [^{18}F]fluoride (30-35 MBq, 50 µL) and mixed at 37-100 °C for 20-60 min. The reaction was heated at 37 °C for 20-60 min, and analysed by radio-TLC (TLC silica gel 60 F_{254}, eluting with 1:1 *v:v* MeOH, 2 M NH_4OAc), where a new species was observed on the baseline. However, further characterisation of this species was unsuccessful.

7.5 Experimental for Chapter 5

Peptides (FCPF, GCPG and FCPF-Oct) were purchased from PeptideSynthetics, Peptide Protein Research Ltd, UK. NCS-MP-NODA was purchased from CheMatech. Synthetic chemistry and peptide conjugations were performed by Thomas Tin Chi Yue.

7.5.1 Synthetic chemistry

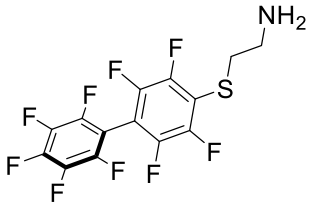

PFBP-NH_2: To a solution of 2-(tritylthio)ethylamine hydrochloride (1.41 mmol, 0.50 g) and triisopropylsilane (1.69 mmol, 0.35 mL) in CH_2Cl_2 (5 mL) was added trifluoroacetic acid (2 mL) dropwise. The solution was stirred at room temperature for 1 h, after which analysis by ^{1}H NMR showed complete deprotection of the trityl group. Volatile compounds were first removed by evaporation using a stream of N_2 gas, and the reaction was subsequently concentrated *in vacuo*. The resulting residue was dissolved in DMF (5 mL). To this, decafluorobiphenyl (11.20 mmol, 3.75 g) and *N,N*-diisopropylethylamine (11.20 mmol, 1.5 mL) were added, and the resulting solution was stirred at room temperature for 1 h. Upon completion, the reaction was quenched with 1 M HCl and concentrated *in vacuo*. The residue was triturated with MeCN:H_2O 7:7 *v:v*, filtered, and the filtrate was dried *in vacuo.* The crude product was purified by flash chromatography using an Isolera™ Spektra System (Biotage® SNAP Ultra C18 cartridge (12 g), A: 0.1 M NH_4OAc, B: 10% 0.1 M NH_4OAc in MeCN. Gradient: 20-100% B), and the collected fractions were lyophilized to give a white solid (120 mg, 20 %).

^{1}H NMR (400 MHz, $CDCl_3$, *δ*): 4.11 (br s, 2H), 3.15 (t, 2H), 2.95 (t, 2H); ^{13}C NMR (101 MHz, $CDCl_3$, *δ*): 148.5, 146.1, 145.5, 143.2, 142.9, 139.2, 136.7, 39.2, 33.8.; ^{19}F NMR (377 MHz, $CDCl_3$, *δ*): -132.42 to -132.56 (2F, m), -137.05 to -137.22 (2F, m), -137.39 to -137.58 (2F, m), -149.73 to -149.93 (1F, m), -160.21 to -160.42 (2F, m); HRMS (ES^+, TOF): *m/z* $[M+H]^+$ calc. for $C_{14}H_7F_9NS$ 392.0150, found 392.0140.

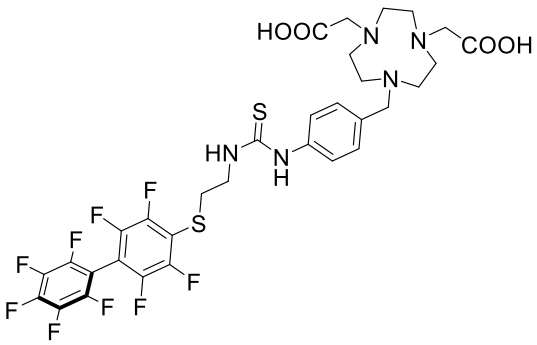

PFBP-NODA: Under a nitrogen atmosphere, PFBP-NH_2 (30.6 µmol, 13.8 mg) and NCS-MP-NODA (25.0 µmol, 10.0 mg) were dissolved in anhydrous DMF (1 mL). *N,N*-diisopropylethylamine (50 µL) was added, and the reaction was stirred at room temperature for 24 h. Upon completion, the solvent was removed *in vacuo*, and the crude product was purified by flash chromatography on an Isolera™ Spektra System (Biotage® SNAP Ultra C18 cartridge (12 g), A: H_2O with 0.1% TFA, B: CH_3CN with 0.1% TFA. Gradient: 0-100% B), and the collected fractions were lyophilized to give a white solid (TFA salt, 23 mg, 86 %).

^{1}H NMR (400 MHz, CD_3CN, *δ*): 8.53 (2H, br s), 7.08 (2H, br s), 4.30 (2H, s) 3.76 (2H, d, *J* = 6.1 Hz), 3.52-3.33 (6H, m), 3.33 (2H, t, *J* = 6.6 Hz), 3.25-2.94 (8H, m), 2.74 (4H, s), 2.71-2.61 (2H, m); ^{19}F NMR (377 MHz, CD_3CN, *δ*): -76.66 (TFA), -133.99 (2F, dd, *J* = 25.3, 12.9 Hz), -139.38 (2F, dd *J* = 25.3, 11.9 Hz), -139.59 to -140.18 (2F, m), -152.59 (1F, t, *J* = 22.0 Hz), -161.39 to -164.63 (2F, m); HRMS (ES$^+$, TOF): *m/z* $[M+H]^+$ calc. for $C_{32}H_{31}F_9N_5S_2O_4$ 784.1674, found 784.1672.

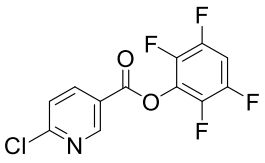

Compound **5.6**: To a solution of 6-chloronicotinic acid (6.35 mmol, 1.00 g) dissolved in THF (25 mL), *N,N'*-dicyclohexylcarbodiimide (9.52 mmol, 1.96 g) was added. The white suspension was stirred at room temperature for 5 min, and 2,3,5,6-tetrafluorophenol (7.62 mmol, 1.26 g) in THF (10 mL) was added dropwise. The resulting white suspension was stirred at room temperature for a further 18 h. The white suspension was filtered, and the filtrate was concentrated *in vacuo*. Purification by flash column chromatography (Hexane:EtOAc 8:2) yields a white powder (1.45 g, 75 %)

^{1}H NMR (400 MHz, $CDCl_3$, *δ*): 9.16 (1H, dd, *J* = 2.4, 0.7 Hz), 8.40 (1H, dd, *J* = 8.4, 2.4 Hz), 7.54 (1H, dd, *J* 8.3, 0.7 Hz), 7.09 (1H, tt, *J* = 9.9, 7.1 Hz); ^{13}C NMR (101 MHz, $CDCl_3$, *δ*): 162.5-156.2 (m), 151.9, 147.7-144.5 (m), 142.2-139.0 (m), 140.3, 129.6-128.46 (m), 124.7, 122.4, 103.8 (t, *J* = 22.8 Hz), 78.0-76.3 (m); ^{19}F NMR (377 MHz, $CDCl_3$, *δ*): -138.38 to -138.59

(m), -152.42 to – 152.92 (m); HRMS (ES$^+$, TOF): *m/z* [M+H]$^+$ calc. for $C_{12}H_5ClF_4NO_2$ 305.9939, found 305.9939.

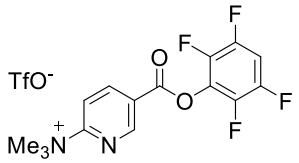

Compound **5.7**: Under a nitrogen atmosphere, **5.6** (3.27 mmol, 1.00 g) was dissolved in anhydrous THF (5 mL). Triethylamine (2 M in THF, 8 mL) was added, and the solution was stirred at room temperature overnight. The solid was collected by suction filtration and dried *in vacuo*. Under a nitrogen atmosphere, the product in Cl^- counterion form was suspended in CH_2Cl_2 (50 mL) with vigorous stirring. Trifluoromethanesulfonate (5.89 mmol, 1.06 mL) was added over 5 min, and the resulting solid was obtained by filtration. The residue was washed with diethyl ether (25 mL × 2), and dried *in vacuo* to yield a white powder (1.09 g, 70 %).

^{1}H NMR (400 MHz, CD_3CN, *δ*): 9.34 (1H, dd, *J* = 2.3, 0.8 Hz), 8.84 (1H, dd, *J* = 8.7, 2.3 Hz), 8.06 (1H, dd, *J* = 8.8, 0.8 Hz), 7.43 (1H, tt, *J* = 10.5, 7.3 Hz); ^{13}C NMR (101 MHz, CD_3CN, *δ*): 160.1, 160.1, 150.8, 146.2 (dtd *J* = 246.8, 12.0, 4.1 Hz), 143.2, 140.6 (dd, *J* = 250.9, 15 Hz), 128.8 (t, *J* = 14.3 Hz), 125.9, 115.8, 104.6 (t, *J* = 23.4 Hz), 55.2; ^{19}F NMR (377 MHz, CD_3CN, *δ*): -79.32 (2F, s), -140.30 (2F, dd, *J* = 20.7, 9.5 Hz), -154.27 (2F, dd, *J* = 20.7, 9.5 Hz); HRMS (ES$^+$, TOF): *m/z* [M]$^+$ calc. for $C_{15}H_{13}F_4N_2O_2$ 329.0908, found 329.0915.

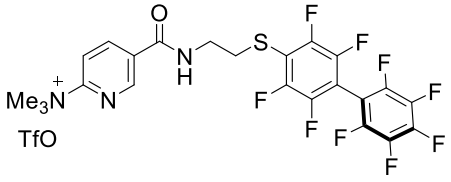

PFBP-Pyr-NMe$_3$: To a solution of PFBP-NH_2 (0.21 mmol, 102.00 mg) and **5.7** in DMF (5 mL), *N,N*-diisopropylethylamine (0.63 mmol, 111 µL) was added, and the pale yellow solution was stirred at room temperature for 18 h. The reaction was concentrated *in vacuo*, and the solid was purified by flash chromatography on an Isolera^{TM} Spektra System (Biotage® SNAP Ultra C18 cartridge (12 g), A: H_2O with 0.1% TFA, B: CH_3CN with 0.1% TFA. Gradient: 20-100% B), and the collected fractions were lyophilized to give a white solid (103 mg, 69 %).

^{1}H NMR (400 MHz, CD_3OD, *δ*): 9.02 (1H, d, *J* = 2.3 Hz), 8.55 (1H, dd, *J* = 8.7, 2.3 Hz), 8.15, (1H, dd, *J* = 8.7, 2.9 Hz), 3.77-3.71 (m, 9H), 3.68 (2H, t, *J* = 6.6 Hz), 3.39 (2H, t, *J* = 6.6 Hz); ^{19}F NMR (377 MHz, CD_3OD, *δ*): -77.06 (3F, s), -134.76 (2F, dd, *J* = 22.4, 11.0 Hz), -139.97 (2F, dt, *J* = 19.1, 10.1 Hz), -140.34 (2F, dt, *J* = 20.1, 10.1 Hz), -153.07 (1F, t, *J* = 20.1

Hz), -163.47 to -163.75 (2F, m); HRMS (ES$^+$, TOF): *m/z* [M]$^+$ calc. for $C_{23}H_{17}F_9N_3OS$ 554.0943, found 554.0948.

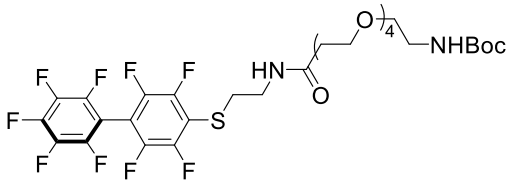

PFBP-PEG$_4$-NHBoc: Under a nitrogen atmosphere, to BocNH-PEG$_4$-COOH (0.24 mmol, 92.00 mg) was added HBTU (0.27 mmol, 101.15 mg), anhydrous DMF (5 mL), and *N,N*-diisopropylethylamine (0.60 mmol, 106 µL). The reaction was stirred at room temperature for 10 min, after which PFBP-NH_2 (0.27 mmol, 124 mg) and *N,N*-diisopropylethylamine (1.08 mmol, 190 µL) in anhydrous DMF (3 mL) was added. The reaction was stirred for a further 18 h at room temperature. The solvent was removed *in vacuo*, and the crude product was purified by flash chromatography on an Isolera™ Spektra System (Biotage® SNAP Ultra C18 cartridge (12 g), A: H_2O with 0.1% TFA, B: CH_3CN with 0.1% TFA. Gradient: 20-100% B), and the collected fractions were lyophilized to give a white solid (111 mg, 59 %).

^{1}H NMR (400 MHz, CD_3CN, *δ*): 3.65 (2H, t, *J* = 5.9 Hz), 3.61-3.52 (12H, m), 3.45 (2H, t, *J* = 5.6 Hz), 3.40 (2H, q, *J* = 6.4 Hz), 3.22-3.12 (4H, m), 2.40 (2H, t, *J* = 6.0 Hz), 1.39 (9H, s); ^{19}F NMR (377 MHz, CD_3CN, *δ*): -132.66 to -136.34 (2F, m), -139.37 to -139.59 (2F, m), -139.81 to -140.04 (2F, m), -152.60 (1F, t, *J* = 20.2 Hz), -160.50 to -165.45 (2F, m); HRMS (ES$^+$, TOF): *m/z* [M+Na]$^+$ calc. for $C_{30}H_{35}F_9N_2O_7SNa$ 761.1919, found 761.1907.

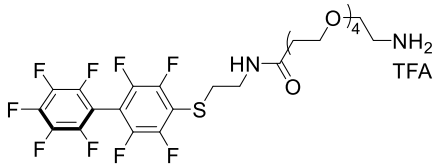

PFBP-PEG$_4$-NH$_2$: To PFBP-PEG$_4$-NHBoc (0.15 mmol, 111.00 mg) was added TFA (0.5 mL) and CH_2Cl_2 (1 mL). The solution was stirred at room temperature for 3 hours and concentrated *in vacuo* to afford the product. (118 mg, 100 %)

^{1}H NMR (400 MHz, CD_3CN, *δ*): 3.77-3.73 (2H, m), 3.69-3.63 (4H, m), 3.63-3.54 (10H, m), 3.39 (2H, q, *J* = 6.3 Hz), 3.20-3.04 (4H, m), 2.41 (2H, t, *J* = 5.6 Hz); ^{19}F NMR (377 MHz, CD_3CN, *δ*): -76.56 (TFA), -134.19 to -134.46 (2F, m), -139.51 (2F, ddt, *J* = 23.3, 9.2, 5.1 Hz), -139.90 (2F, dt, *J* = 21.0, 10.5 Hz), -152.54 (1F, td, *J* = 20.5, 3.8 Hz), -162.70 to -163.03 (2F, m); HRMS (ES$^+$, TOF): *m/z* [M+H]$^+$ calc. for $C_{25}H_{28}F_9N_2O_5S$ 639.1575, found 639.1537.

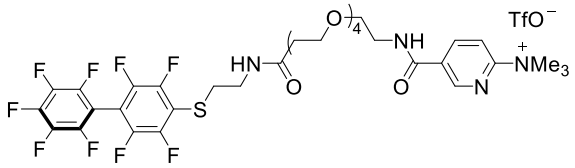

PFBP-PEG$_4$-Pyr-NMe$_3$: Under a nitrogen atmosphere, PFBP-PEG$_4$-NH$_2$ (49 µmol, 31.00 mg) was dissolved in anhydrous DMF (2 mL). *N,N*-diisopropylethylamine (0.19 mmol, 34 µL) and **5.7** (42 µmol, 20 mg) were added, and the reaction was stirred at room temperature for 18 h. Upon completion, the solvent was concentrated *in vacuo*, and the product was purified by flash chromatography on an Isolera™ Spektra System (Biotage® SNAP Ultra C18 cartridge (12 g), A: H_2O with 0.1% TFA, B: CH_3CN with 0.1% TFA. Gradient: 20-100% B). The collected fractions were lyophilized to give the product (40.6 mg, 100 %).

^{1}H NMR (400 MHz, CD_3CN, *δ*): 9.00 (1H, d, *J* = 2.2 Hz), 8.53 (1H, dd, *J* = 8.6, 2.4 Hz), 8.10 (1H, t, *J* = 5.5 Hz), 7.93 (1H, d, *J* = 8.6 Hz), 7.07 (1H, t, *J* = 6 Hz), 3.78-3.47 (27H, m), 3.34 (2H, q, *J* = 6.3 Hz), 3.13 (2H, t, *J* = 6.6 Hz), 2.3 (2H, t, *J* = 6 Hz); ^{19}F NMR (377 MHz, CD_3CN, *δ*): 76.15 (OTf), -134.30 (2F, dd, *J* = 23.1, 11.5 Hz), -139.47 (2F, d, *J* = 24.5 Hz), -140.00 (2F, dt, *J* = 22.9, 11.2 Hz), -152.57 (1F, t, *J* = 20.3 Hz), -162.63 to -163.07 (2F, m); HRMS (ES$^+$, TOF): *m/z* [M+H]$^+$ calc. for $C_{34}H_{38}F_9N_4O_6S$ 801.2368, found 801.2382.

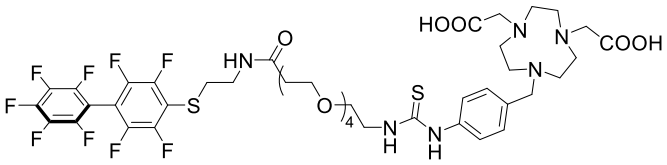

PFBP-PEG$_4$-NODA: Under a nitrogen atmosphere, to a solution of PFBP-PEG$_4$-NH$_2$ (60 µmol, 38 mg) and NCS-MP-NODA (50 µmol, 20 mg) in anhydrous DMF (3 mL) was added *N,N*-diisopropylethylamine (200 µmol, 35 µL). The reaction was stirred at room temperature for 24 h. Upon completion, the solvent was removed *in vacuo* and the reaction was purified by flash chromatography on an Isolera™ Spektra System (Biotage® SNAP Ultra C18 cartridge (12 g), A: H_2O with 0.1% TFA, B: CH_3CN with 0.1% TFA. Gradient: 20-100% B). The collected fractions were lyophilized to give the product (37.9 mg, 73 %).

^{1}H NMR (400 MHz, CD_3CN, *δ*): 7.57 (2H, d, *J* = 8.1 Hz), 7.47 (2H, d, *J* = 8.1 Hz), 7.05 (1H, t, *J* = 6.0 Hz), 4.28 (2H, s), 3.72 (2H, s), 3.65-3.51 (16H, m), 3.43 (2H, s), 3.39-3.31 (4H, m), 3.14 (4H, t, *J* = 6.6 Hz), 3.09-2.94 (4H, m), 2.74 (4H, s), 2.70-2.59 (2H, m), 2.34 (2H, t, *J* = 6.0 Hz); ^{19}F NMR (377 MHz, CD_3CN, *δ*): -76.42 (TFA), -133.25 to -136.50 (2F, m), -139.41 (2F, dtq, *J* = 19.1, 8.9, 5.0 Hz), -139.81 to -140.00 (2F, m), -152.55 (1F, tt, *J* = 20.5, 3.3 Hz), -162.43 to -163.11 (2F, m); HRMS (ES$^+$, TOF): *m/z* [M+H]$^+$ calc. for $C_{43}H_{52}F_9N_6O_9S_2$ 1031.3094, found 1031.3138.

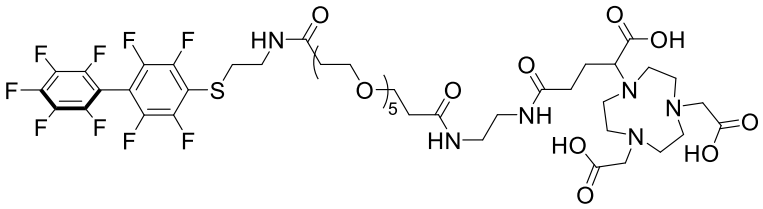

PFBP-PEG$_5$-NODAGA: Under a nitrogen atmosphere, PFBP-NH$_2$ (95 µmol, 37 mg) and *N,N*-diisopropylethylamine (249 µmol, 43 µL) were dissolved in anhydrous DMF (3 mL). This was slowly transferred over 30 min to a solution of Bis(NHS)PEG$_5$ (83 µmol, 44 mg) in anhydrous DMF (3 mL). The resulting solution was stirred at room temperature for 18 h. Upon completion, a solution of NH$_2$-NODA-GA (108 µmol, 45 mg) and *N,N*-diisopropylethylamine (332 µmol, 57 µL) in anhydrous DMF (2 mL) was added. The reaction was stirred at room temperature overnight, quenched with 0.1 % TFA in water (3 mL), concentrated *in vacuo* and purified by flash chromatography on an Isolera^{TM} Spektra System (Biotage® SNAP Ultra C18 cartridge (12 g), A: H$_2$O with 0.1% TFA, B: CH$_3$CN with 0.1% TFA. Gradient: 20-100% B). The collected fractions were lyophilized to give the product (29.8 mg, 33 %).

^{1}H NMR (400 MHz, CD$_3$CN, *δ*): 7.30 (1H, br s), 7.03 (1H, br s), 6.92 (1H, br s), 3.89 (2H, s), 3.69-3.62 (6H, m), 3.59-3.51 (16H, m), 3.38 (2H, q, *J* = 6.5 Hz), 3.16 (6H, t, *J* = 6.5 Hz), 3.03-2.92 (7 H, br m), 2.84-2.78 (8H, br m), 2.43 (2H, t, *J* = 6.0 Hz), 2.35 (2H, t, *J* = 6.0 Hz), 2.33-2.28 (2H, m); ^{19}F NMR (377 MHz, CD$_3$CN, *δ*): -76.44 (TFA), -134.27 (2F, dd, *J* = 24.5, 11.3 Hz), -139.16 to -139.71 (2F, m), -139.94 (2F, dt, *J* = 21.9, 10.9 Hz), -152.57 (1F, t, *J* = 20.4 Hz), -162.83 (2F, t, *J* = 19.5 Hz); HRMS (ES$^+$, TOF): *m/z* [M+H]$^+$ calc. for $C_{45}H_{60}F_9N_6O_{14}S$ 1111.3745, found 1111.3789.

7.5.2 Peptide conjugation

The following stock solutions were prepared for use throughout the conjugation reactions:

PFBP reagents: PFBP-NODA: 10 mM in MeCN; PFBP-Pyr-NMe$_3$: 10 mM in MeCN; PFBP-PEG$_4$-NODA: 30 mM in DMSO; PFBP-PEG$_4$-Pyr-NMe$_3$: 40 mM in DMSO; PFBP-PEG$_5$-NODAGA: 50 mM in DMF

Peptides: FCPF: 20 mM in H$_2$O; GCPG: 10 mM in H$_2$O; FCPF-Oct: 10 mM in H$_2$O.

Buffers: 0.2 M phosphate buffer at pH 8.0, 200 mM TCEP in 0.2 M phosphate pH 8.0.

General procedure for PFBP conjugation reactions:

Reactions were carried out with a total volume of 100 µL in Eppendorf® tubes. Appropriate volumes of each reagent were added to achieve a final reaction concentration of **FCPF peptide** (1 mM), **PFBP reagent** (5 mM) and **TCEP** (20 mM), where the remaining volume was

made up to 100 µL by addition of 0.2 M phosphate buffer at pH 8. Reactions were incubated at 37 °C on an Eppendorf® ThermoMixer and monitored by LC-MS at the appropriate time points of 0.5, 1, 2, 3 and 4 h.

Syntheses of NODA-PEG_4-Oct and NODAGA-PEG_5-Oct for the direct labelling approach were carried out using the same protocol, but on a larger scale. In brief, FCPF-Oct (5 mg) was reacted with 5 equiv. of the respective PFBP reagents at 37 °C for 24 h. The reactions were then purified by preparative HPLC on an Agilent 1260 Infinity II Preparative LC System (Column: Agilent Pursuit XRs C18 250 × 10 mm, 5 µm; Gradient: A: H_2O with 0.1% TFA, B: CH_3CN with 0.1% TFA. Gradient: 5-95% B).

NODA-PEG_4-Oct: HRMS (ES^+, TOF): *m/z* $[M+2H]^{2+}$ calc. 1277.9631, found 1277.9601.

NODAGA-PEG_5-Oct: HRMS (ES^+, TOF): *m/z* $[M+2H]^{2+}$ calc. 1317.9959, found 1318.00161.

7.5.3 Radiochemistry

Prosthetic group approach:

The following stock solutions were used for the [^{18}F]AlF-labelling reactions:

PFBP-NODA: 10 mM in MeCN, PFBP-PEG_4-NODA: 10 mM in MeCN, FCPF-Oct: 32.3 mM in DMSO, 0.2 M phosphate buffer at pH 8.0 and 200 mM TCEP in 0.2 M phosphate pH 8; 2,2'-dipyridyl disulfide 500 mM in MeOH.

[^{18}F]AlF-PFBP

A mixture of PFBP-NODA in MeCN (10 µL, 100 nmol), 2 mM $AlCl_3$ in 0.5 M sodium acetate at pH 4.2 (50 µL, 100 nmol), QMA purified [^{18}F]fluoride (400-500 MBq, 150 µL) and MeCN (200 µL) was incubated in a sealed Eppendorf® tube at 100 °C for 20 min. Upon completion, the reaction was then diluted in water (15 mL), trapped on a Sep-Pak tC18 Plus Light Cartridge (145 mg sorbent), washed with PBS pH 7.4 (5 mL), and eluted with MeCN (500 µL). Analytical RP-HPLC (0.1% TFA H_2O:MeCN 95:5 *v:v* to 5:95 *v:v* gradient, phenomenex, Gemini 5u C18 110 Å column, 1 mL/min flow rate): t_R [^{18}F]AlF-PFBP = 770 s.

[^{18}F]AlF-PEG_4-PFBP: The same procedure was used but with PFBP-PEG_4-NODA as the precursor. t_R [^{18}F]AlF-PEG_4-PFBP = 760 s.

[^{18}F]F-Pyr-PFBP

On a Sep-Pak Accell Plus QMA carbonate light cartridge, preconditioned with H_2O (1 mL), non-purified [^{18}F]fluoride (500-700 MBq) was loaded from the male side. The cartridge was then flushed with EtOH (1 mL) from the male side, and then eluted with a solution of

PFBP-Pyr-NMe_3 (5 mg in DMSO:EtOH 1:1 *v:v*) into an Eppendorf® tube. The reaction was sealed and heated at 100 °C for 20-30 min, following which it was cooled and diluted with H_2O (3 mL). Precipitation was observed when H_2O was added. The product was then trapped on an Oasis MCX Plus Short Cartridge (225 mg Sorbent, preconditioned with 5 mL EtOH followed by 5 mL H_2O), rinsed with H_2O (5 mL), and eluted with water:MeCN (2:8 *v:v*, 2.1 mL). Analytical RP-HPLC (0.1% TFA H_2O:MeCN 95:5 *v:v* to 5:95 *v:v* gradient, phenomenex, Gemini 5u C18 110 Å column, 1 mL/min flow rate): t_R [^{18}F]F-Pyr-PFBP = 900 s.

[^{18}F]F-Pyr-PEG$_4$-PFBP: The same procedure was used but with PFBP-PEG_4-Pyr-NMe_3 as the precursor.): t_R [^{18}F]F-Pyr-PFBP = 840 s

Peptide conjugation reactions were performed with a final concentration of:

Peptide 1 mM and TCEP 20 mM. PFBP reagent: since the amount of ^{18}F-labelled compound is usually negligible compared to their non-radioactive counterparts (13 GBq is approximately 0.2 nmol of fluorine-18), it was not possible to achieve a concentration of 5 mM for the ^{18}F-labelled PFBP reagent.

Conjugation protocol: To a 1.5 mL Eppendorf® tube, FCPF-Oct (100 nmol, 3.1 µL), ^{18}F-labelled PFBP (50 µL in MeCN, 50-60 MBq), TCEP (100 mM in 0.2 M phosphate, 20 µL), 0.2 M phosphate buffer (27 µL) were added. The reaction was incubated on a ThermoMixer at 37 °C at 450 rpm. For optimisations, DMF or DMSO (50 µL) was added. Analysis was carried out by radio-HPLC at the appropriate time points with the following parameters: Gradient: 0.1% TFA H_2O:MeCN 95:5 *v:v* to 5:95 *v:v*; Column: phenomenex Gemini 5u C18 110 Å, 1 mL/min flow rate.

t_R [^{18}F]AlF-NODA-Oct **5.10** = 615 s; t_R [^{18}F]AlF-NODA-PEG_4-Oct **5.13** = 615 s. Conjugations were unsuccessful when **[^{18}F]F-Pyr-PFBP** and **[^{18}F]F-Pyr-PEG$_4$-PFBP** were investigated

For the isolation of [^{18}F]AlF-NODA-PEG_4-Oct **5.13**:

After 1 h of conjugation, 2,2'-dipyridyl disulfide (8 µL) was added for disulfide reoxidation, and the reaction was incubated for a further 30 min. Following which, [^{18}F]AlF-NODA-PEG_4-Oct **5.13** was purified by semi-preparative HPLC (Shimadzu LC20-AT pump attached to a custom-built system, Column: Agilent Eclipse XDB-C18, 5 µm, 250 x 9.4 mm; Mobile phase: 2:8 *v:v* MeCN:H_2O with 0.1% H_3PO_4 for 20 mins, followed by 44:56 *v:v* MeCN/H_2O with 0.1% H_3PO_4. [^{18}F]AlF-NODA-PEG_4-Oct **5.13** eluted at 28 mins.

Direct labelling approach

A stock solution of NODA-PEG_4-Oct in DMSO (5 mM) was used for [^{18}F]AlF-labelling; NODAGA-PEG_5-Oct in DMSO (0.38 mM) was used for ^{68}Ga-labelling.

[^{18}F]AlF-NODA-PEG_4-Oct 5.13

A mixture of NODA-PEG_4-Oct **5.11** in DMSO (5 µL, 25 nmol), 2 mM $AlCl_3$ in 0.5 M sodium acetate at pH 4.2 (12.5 µL, 100 nmol), QMA purified [^{18}F]fluoride (400-500 MBq, 100 µL) and DMSO (150 µL) was incubated in a sealed Eppendorf® tube at 100 °C for 20 min. Upon completion, the reaction was then diluted in water (15 mL), trapped on a Sep-Pak tC18 Plus Light Cartridge (145 mg sorbent, preconditioned with 5 mL EtOH followed by 5 mL H_2O), washed with H_2O (5 mL), and eluted with EtOH (500 µL). Analytical RP-HPLC (0.1% TFA H_2O:MeCN 95:5 *v:v* to 5:95 *v:v* gradient, phenomenex, Gemini 5u C18 110 Å column, 1 mL/min flow rate): t_R [^{18}F]AlF-NODA-PEG_4-Oct **5.13** = 615 s.

[^{68}Ga]Ga-NODAGA-PEG_5-Oct 5.17

NODAGA-PEG_5-Oct (150 µL, 57 nmol), [^{68}Ga]$GaCl_3$ (125 µL, 56 MBq) and 2 M NH_4OAc at pH 6 (62.5 µL) were incubated at 37 °C for 15 min. Upon completion, the reaction was diluted in water (15 mL), trapped on a Sep-Pak tC18 Plus Light Cartridge (145 mg sorbent, preconditioned with 5 mL EtOH followed by 5 mL H_2O), washed with H_2O (5 mL), and eluted with EtOH (500 µL).

Stability tests

Radiotracer **5.13** or **5.17** (3-5 MBq) was incubated in 500 µL of the respective media (PBS, human serum or RPMI) at 37 °C. Aliquots of the solutions were sampled at 1, 2, 3, 4 and 5 hours, and diluted in H_2O for analysis by radio-HPLC using the conditions indicated above. For samples in human serum and RPMI, the diluted solutions were centrifuged at 13 000 *g* for 5 min prior to injection. Diluted solutions from PBS were injected directly.

Determination of $LogP_{7.5}$

To a 1.5 mL Eppendorf® tube, PBS (500 µL) and octanol (500 µL) were added, and shaken on a ThermoMixer at 37 °C for 15 min. Radiotracer **5.13** or **5.17** (3-5 MBq) was diluted in PBS to <5% EtOH. The diluted radiotracer (50 µL) was added to the octanol/water mixture, shaken at 37 °C for 30 min, and then centrifuged (13 000 *g*, 5 min). Aliquots from the PBS and octanol layers (3 × 100 µL each) were removed and placed in separate gamma counting tubes. Radioactivity was measured a γ-counter (Wizard 2480 Automatic Gamma Counter, Perkin Elmer). $LogP_{7.5}$ was calculated using the formula $LogP_{7.5} = \log_{10}$ [Oct]/[PBS]. The data were presented as mean ± SD, *n* = 6-9).

7.6 References

1 J. H. Teh, M. Braga, L. Allott, C. Barnes, J. Hernández-Gil, M. X. Tang, E. O. Aboagye and N. J. Long, *Chem. Commun.*, 2021, **57**, 11677–11680.

2 R. Cao, P. Müller and S. J. Lippard, *J. Am. Chem. Soc.*, 2010, **132**, 17366–17369.

3 D. Shetty, S. Y. Choi, J. M. Jeong, J. Y. Lee, L. Hoigebazar, Y. S. Lee, D. S. Lee, J. K. Chung, M. C. Lee and Y. K. Chung, *Chem. Commun.*, 2011, **47**, 9732–9734.

4 J. Yang, M. R. Karver, W. Li, S. Sahu and N. K. Devaraj, *Angew. Chem. Int. Ed.*, 2012, **51**, 5222–5225.

5 C. A. D'Souza, W. J. McBride, R. M. Sharkey, L. J. Todaro and D. M. Goldenberg, *Bioconjug. Chem.*, 2011, **22**, 1793–1803.

6 J. Hernández-Gil, M. Braga, B. I. Harriss, L. S. Carroll, C. H. Leow, M.-X. Tang, E. O. Aboagye and N. J. Long, *Chem. Sci.*, 2019, **10**, 5603–5615.

7 N. K. Devaraj, R. Weissleder and S. A. Hilderbrand, *Bioconjug. Chem.*, 2008, **19**, 2297–2299.

8 L. Allott, A. Amgheib, C. Barnes, M. Braga, D. Brickute, N. Wang, R. Fu, S. Ghaem-Maghami and E. O. Aboagye, *React. Chem. Eng.*, 2021, **6**, 1070–1078.

9 S. Li, S. Lin, Y. Cheng, T. O. Matsunaga, R. J. Eckersley and M. X. Tang, *Ultrasound Med. Biol.*, 2015, **41**, 1422–1431.

10 C. Counil, E. Abenojar, R. Perera, A. A. Exner, C. Counil, E. Abenojar, R. Perera and A. A. Exner, *Small*, 2022, **18**, 2200810.

11 M. Braga, C. H. Leow, J. H. Gil, J. H. Teh, L. Carroll, N. J. Long, M. X. Tang and E. O. Aboagye, *PLoS One*, 2021, **16**, e0260186.

12 P. Workman, E. O. Aboagye, F. Balkwill, A. Balmain, G. Bruder, D. J. Chaplin, J. A. Double, J. Everitt, D. A. H. Farningham, M. J. Glennie, L. R. Kelland, V. Robinson, I. J. Stratford, G. M. Tozer, S. Watson, S. R. Wedge, S. A. Eccles, V. Navaratnam and S. Ryder, *Br. J. Cancer 2010 10211*, 2010, **102**, 1555–1577.

13 J. Šimeček, M. Schulz, J. Notni, J. Plutnar, V. Kubíček, J. Havlíčková and P. Hermann, *Inorg. Chem.*, 2012, **51**, 577–590.

14 K. Hochdörffer, K. Abu Ajaj, C. Schäfer-Obodozie and F. Kratz, *J. Med. Chem.*, 2012, **55**, 7502–7515.

15 H. Y. Yin, J. Lai, J. Tang, Y. Shang and J. L. Zhang, *Inorganics*, 2018, **6**, 20.

16 A. Yeori, S. Groysman, I. Goldberg and M. Kol, *Inorg. Chem.*, 2005, **44**, 4466–4468.

17 W. Wang, Q. Wen, Y. Zhang, X. Fei, Y. Li, Q. Yang and X. Xu, *Dalton Trans.*, 2013, **42**, 1827–1833.

18 E. L. Whitelaw, G. Loraine, M. F. Mahon and M. D. Jones, *Dalton Trans.*, 2011, **40**, 11469–11473.

Chapter 8: Appendix

8.1 Stability of [^{18}F]AlF-Tz

Table 8.1: Radio-HPLC analysis of stability of [^{18}F]AlF-Tz with time, showing slow degradation of 2-3% per hour, where the appearance of a new peak with a shorter retention time than the product was observed

Time	Decomposition	Radio-HPLC chromatogram
1 h	7%	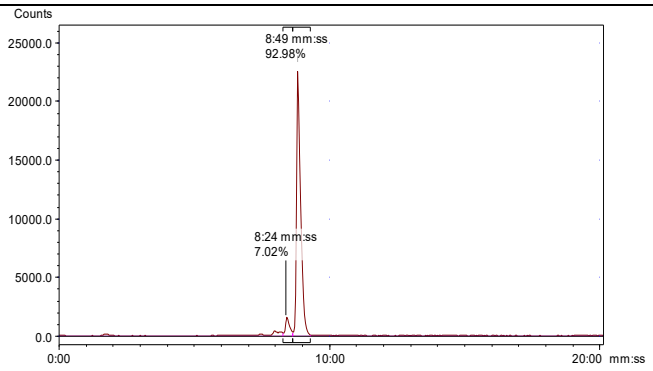
2 h	9%	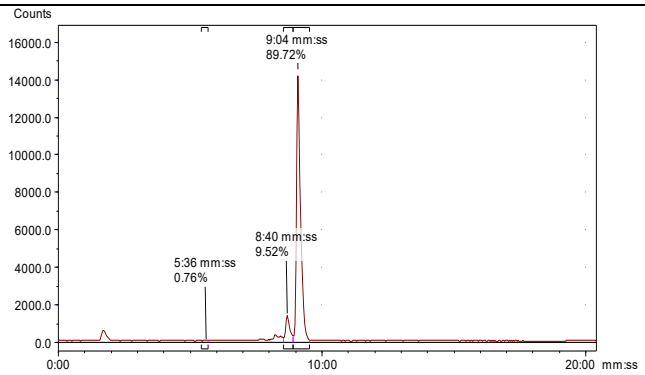
3 h	11%	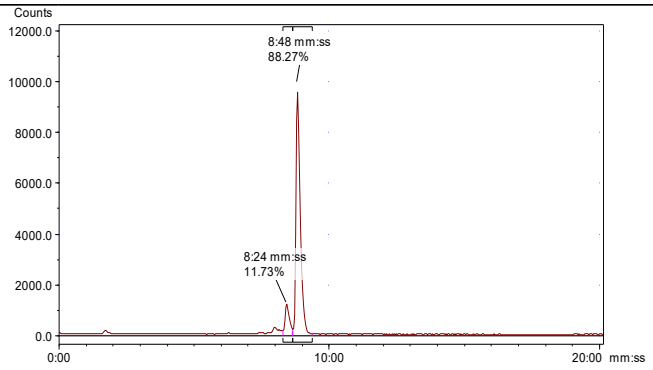
4 h	13%	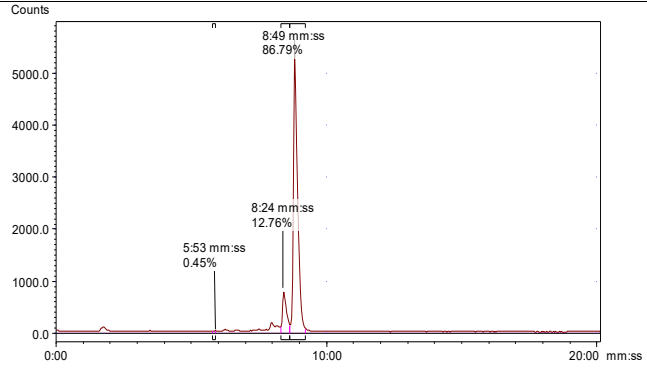

8.2 X-ray Crystallography Data

This section includes the experimental data for salalen **4.14**, which includes a full list of bond lengths (Å) and angles (°). The structure was obtained and solved by Dr Andrew White from the Department of Chemistry, Imperial College London.

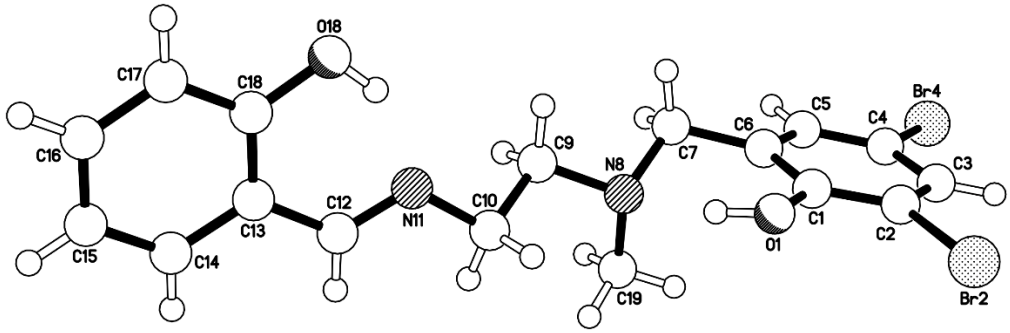

Identification code	NL2310	
Formula	C17 H18 Br2 N2 O2	
Formula weight	442.15	
Temperature	173(2) K	
Diffractometer, wavelength	Agilent Xcalibur 3 E, 0.71073 Å	
Crystal system, space group	Triclinic, P-1	
Unit cell dimensions	a = 9.2943(4) Å	a = 69.725(5)°
	b = 9.8340(5) Å	b = 79.334(4)°
	c = 10.7938(6) Å	g = 73.645(4)°
Volume, Z	883.77(8) $Å^3$, 2	
Density (calculated)	1.662 Mg/m^3	
Absorption coefficient	4.596 mm^{-1}	
F(000)	440	
Crystal colour / morphology	Pale yellow blocks	
Crystal size	0.399 x 0.174 x 0.092 mm^3	
q range for data collection	2.526 to 28.268°	
Index ranges	-12<=h<=11, -12<=k<=12, -14<=l<=13	
Reflns collected / unique	11430 / 3736 [R(int) = 0.0309]	
Reflns observed [F>4s(F)]	2947	
Completeness to theta(full)	0.996 to 25.242 deg	
Absorption correction	Analytical	
Max. and min. transmission	0.668 and 0.311	
Refinement method	Full-matrix least-squares on F^2	

Data / restraints / parameters	3736 / 2 / 217
Goodness-of-fit on F^2	1.024
Final R indices [F>4s(F)]	R1 = 0.0322, wR2 = 0.0593
R indices (all data)	R1 = 0.0486, wR2 = 0.0641
Largest diff. peak, hole	0.480, -0.513 $eÅ^{-3}$
Mean and maximum shift/error	0.000 and 0.001

Bond lengths [Å] and angles [°] for NL2310.

O(1)-C(1)	1.357(3)	C(3)-C(2)-Br(2)	119.5(2)
C(1)-C(2)	1.392(3)	C(1)-C(2)-Br(2)	118.85(18)
C(1)-C(6)	1.399(4)	C(4)-C(3)-C(2)	118.0(2)
C(2)-C(3)	1.383(3)	C(3)-C(4)-C(5)	122.1(2)
C(2)-Br(2)	1.893(3)	C(3)-C(4)-Br(4)	119.71(19)
C(3)-C(4)	1.368(4)	C(5)-C(4)-Br(4)	118.2(2)
C(4)-C(5)	1.378(3)	C(4)-C(5)-C(6)	120.1(2)
C(4)-Br(4)	1.910(2)	C(5)-C(6)-C(1)	119.1(2)
C(5)-C(6)	1.384(3)	C(5)-C(6)-C(7)	120.8(2)
C(6)-C(7)	1.510(3)	C(1)-C(6)-C(7)	120.1(2)
C(7)-N(8)	1.474(3)	N(8)-C(7)-C(6)	111.4(2)
N(8)-C(19)	1.469(3)	C(19)-N(8)-C(9)	111.8(2)
N(8)-C(9)	1.471(3)	C(19)-N(8)-C(7)	110.5(2)
C(9)-C(10)	1.513(4)	C(9)-N(8)-C(7)	110.8(2)
C(10)-N(11)	1.463(3)	N(8)-C(9)-C(10)	111.1(2)
N(11)-C(12)	1.270(3)	N(11)-C(10)-C(9)	110.3(2)
C(12)-C(13)	1.455(3)	C(12)-N(11)-C(10)	118.0(2)
C(13)-C(18)	1.395(4)	N(11)-C(12)-C(13)	122.1(3)
C(13)-C(14)	1.400(4)	C(18)-C(13)-C(14)	118.5(2)
C(14)-C(15)	1.375(4)	C(18)-C(13)-C(12)	121.6(2)
C(15)-C(16)	1.383(4)	C(14)-C(13)-C(12)	119.9(2)
C(16)-C(17)	1.379(4)	C(15)-C(14)-C(13)	121.1(3)
C(17)-C(18)	1.390(4)	C(14)-C(15)-C(16)	119.4(3)
O(18)-C(18)	1.350(3)	C(17)-C(16)-C(15)	120.9(3)
O(1)-C(1)-C(2)	119.6(2)	C(16)-C(17)-C(18)	119.7(3)
O(1)-C(1)-C(6)	121.3(2)	O(18)-C(18)-C(17)	118.7(3)
C(2)-C(1)-C(6)	119.1(2)	O(18)-C(18)-C(13)	121.0(2)
C(3)-C(2)-C(1)	121.7(2)	C(17)-C(18)-C(13)	120.3(3)

8.3 Liquid chromatography-tandem mass spectrometry (LC-MS/MS) data

The following data was obtained by Thomas Tin Chi Yue, Department of Chemistry, Imperial College London

Biomolecule Summary

Biomol	Seq Loc	Mods	Var Mods	Score (Bio)	RT	Height	Mass	Tgt Mass	Diff (ppm)
18	A(8-12)				5.523	130934	637.2885	637.2894	-1.37
9	A(9-12)				5.523	203079	451.2097	451.2101	-0.80
25	A(4-12)				5.523	106650	1197.4963	1197.4987	-1.99
28	A(6-12)				5.523	97567	903.3614	903.3619	-0.50
1	A(1-12)		1*PFBP-PEG-NODA		5.523	4240826	2554.9204	2554.9244	-1.55
27	A(7-12)				5.523	98607	800.3531	800.3527	0.44
16	A(5-12)				5.524	132751	1050.4288	1050.4303	-1.48
10	A(3-12)				5.524	186146	1294.5499	1294.5515	-1.19